Title

Nanocapsule-based Platforms for Protein Delivery and Protein Therapy

Permalink

https://escholarship.org/uc/item/38v229v5

Author

Liu, Yang

Publication Date

2016

UNIVERSITY OF CALIFORNIA

Los Angeles

Nanocapsule-based Platforms for Protein Delivery and Protein Therapy

A dissertation submitted in partial satisfaction of the

requirements for the degree Doctor of Philosophy

in Chemical Engineering

by

Yang Liu

2016

ABSTRACT OF THE DISSERTATION

Nanocapsule-based Platforms for Protein Delivery and Protein Therapy

by

Yang Liu

Doctor of Philosophy in Chemical Engineering

University of California, Los Angeles, 2016

Professor Yunfeng Lu, Chair

In living organisms, numerous biochemical reactions occur synergistically, allowing the organisms to grow and reproduce, convert food to energy, maintain the structure, and response to the environment – all activities that we called "life". As one of the most important types of molecules for any living organism, protein controls and mediates all these biological processes; malfunction of protein often induces the body to an abnormal state namely disease. Viewed from the perspective of disease mechanisms, protein therapy, which treats diseases by delivering therapeutic proteins directly to redress disorders, represents a tremendous opportunity to alleviate many incurable diseases. However, intrinsic problems, including low stability, low permeability, and high immunogenicity, hamper the clinic application of proteins. Development of advanced protein delivery

systems, which can properly address these issues, has been considered as a practical solution that could enable the therapeutic use of a wide scope of proteins in disease treatments.

In this dissertation, novel delivery systems have been developed based on the protein nanocapsule technology, providing several practical methods to overcome essential issues that hinder the application of therapeutic proteins, but have not yet been properly resolved by current protein delivery systems. These common issues include the efficiency of protein intracellular delivery, co-delivery of multiple proteins, and the plasma half-life and immunogenicity of proteins when delivering systemically. Based on these issues, the dissertation research can be outlined briefly with the following three topics:

1. Intracellular delivery of any protein(s) with optimal efficiency. This part of work demonstrated a polymer-based nano-carrier that was constructed by utilizing multiple weak interactions, which offers the feasibility of loading and delivering proteins without any chemical modification, as well as finely tuning the surface properties of the nano-carriers to achieve optimal delivery efficiency. The intracellular delivery capability of this nano-carrier was first demonstrated by delivering bioactive transcription factors into cells (Chapter 3). Combining with single-protein nanocapsule and microfluidic platform, any protein can be intracellularly delivered using this nano-carrier and the delivery efficiency can be optimized with a high-throughput systhesis and screening system (Chapter 5), providing a fundamental platform for researches on stem cell reprogram and regenerative medicine.

2. Co-delivery of multiple proteins that function synergistically. In eukaryotic cells, most biological processes are accomplished by multiple enzymes or proteins, which are usually spatially confined with precise ratio control in order to function correctly and optimally.

Demonstrated in this part of work (Chapter 1), defined types and amount of enzymes were assembled and co-encapsulated into enzyme nanocomplex, which ensures those enzyme functioning effectively no mater being delivered into local tissues or diluted system like blood stream. This strategy provides a feasible method to construct protein-based multi-functional nanostructure as needed without engineering protein sequence. From the perspective of developing protein therapeutics, this system offers a practical method to detoxify the by-product of many enzymes, enabling safe use of them for therapeutic purposes.

3. Prolong circulation time and reduce immunogenicity of therapeutic proteins. One major problem of most therapeutic proteins is the fast clearance by immune system, which significantly reduces or completely diminish their therapeutic effects. In this part (Chapter 3), we designed a general method that can prolong the plasma half-life of most proteins significantly by minimizing their interactions with serum proteins, blood cells, tissues and organs with a protein-adsorption-resistant polymer shell. With this method, the overall therapeutic effect was enhanced after systemic administration, which was demonstrated with uricase as model therapeutic protein. This strategy also inhibits immune responses against exogeneous proteins, which can broaden the scope of proteins with therapeutic potentials.

Overall, this dissertation research established various methods to endow new surface properties to proteins and enzymes as needed. Based on these work, one can expect that increasing number of protein therapeutics will be developed and widely applied for curing diseases in the near future.

The dissertation of Yang Liu is approved.

Selim M. Senkan

Harold G. Monbouquette

Qibing Pei

Yunfeng Lu, Committee-Chair

University of California, Los Angeles

2016

Table of Contents

List of Figures

xxiii

for the 2nd category: RGD-MFNPs; Black dots (125 data points) for 3rd category: MFNPs. b)

A set of synthetic parameters that resulted in high (★) delivery performance (see the

fluorescence micrographs that reflect transfection/transduction outcomes) were chosen for

scale-up preparation (200 droplets, 40 μL for each set) of the respective RGD/TAT-MFNPs.

c) Transmission electron microscopy (TEM) was employed to examine the morphology and

sizes of the RGD/TAT-MFNPs, scale bars: 400 nm. d) Dynamic light scattering (DLS) was

employed to measure MFNPs hydrodynamic sizes in PBS buffer. The distinct MFNP size of

100 ± 4 nm was obtained from the chosen synthetic parameters. Error bars are based on the

standard deviation of three independent experimental results. e) A colorimetric assay was

employed for quantifying intracellular enzymatic activity of HRP delivered by the MFNPs

using o-Dianisidine (3,3'-dimethoxybenzidine) (50 mM) as chromogenic substrates and H$_2$O$_2$

as an oxidizer. Different concentrations of 100-nm RGD/TAT-MFNPs with encapsulated

HRP amounts from 0 to 500 nM were added into individual wells in a 96-well plate. The

orange color indicated that the HRP remained its biological activity after transduction. f) The

time-dependent in vitro co-delivery performance of the optimal 100-nm RGD/TAT-MFNPs

were monitored in parallel by quantifying fluorescent signals associated with EGFP

expression and colorimetric readouts correlated to HRP activity, respectively. The highest co-

delivery performance was achieved after treatment of cells for 24-48 h. g) Fluorescence

images of U87-EGFP cells before (i) and after (ii) transduction with MFNPs containing

siRNA silencing enhanced green fluorescence protein, BSA-Cy5 and HRP-RhB. Intense

cellular fluorescence signals from HRP-RhB and BSA-Cy5, as well as significantly reduced

green fluorescence intensity due to the silencing of EGFP expression by siRNA, suggest

successful demonstration of simultaneous delivery of gene and proteins. h) Quantification of

List of Tables

Acknowledgement

First and foremost, I would like to express my special appreciation and thanks to my advisor Professor Yunfeng Lu. He has been supportive since the first day I came to UCLA. I would like to thank him not only for encouraging my research and for allowing me to grow as a research scientist, but also for teaching me to enjoy the joy of doing research. He always told me "Research is art.", and said "Life is good" for countless times during our discussion and even in his conference talk and lectures. I believe I would never understand the true meaning of those simple words without these 5-year tough but fruitful research journey with him.

I would also like to thank Prof. Selim Senkan, Prof. Harold Monbouquette, and Prof. Qibing Pei for serving as my committee members. I want to thank them for their help with my research work and dissertation. I would also like to thank my formal doctoral committee member Prof. Tatiana Segura for all her help with my research over these years.

Nowadays, high level research cannot be done without good collaborators. I would especially like to thank Prof. Hsian-Rong Tseng from UCLA and Prof. Cheng Ji from USC for their generous support on my research work. I also learned many skills and knowledge through the collaboration, which will be priceless for my future career.

I would like to express my appreciation to Dr. Ming Yan and Dr. Juanjuan Du, who are the key inventors of protein encapsulation technology that is the fundamental of all my Ph.D. research. They also offered me great help at the beginning, which ensured a smooth start of my research in this field. I would also like to thank Dr. Qiangfeng Xiao, Dr. Chih-ning Pao, Dr. Ding Weng, Dr.

Vita

Education:

2002-2006   Department of Chemistry, Nankai University, China

                       Bachelor in Chemistry, July, 2006

2006-2009   Institute of Polymer Chemistry, Nankai University, China

                       Master of Science, July, 2009;

                       Advisor: Prof. Linqi Shi; Emphasis: Macromolecular self-assembly

Publications:

1. Y. Liu, J. Du, M. Yan, M.-Y. Lau, J. Hu, H. Han, O. O. Yang, S. Liang, W. Wei, H. Wang, J. Li, X. Zhu, L. Shi*, W. Chen*, C. Ji*, Y. Lu*. "Biomimetic enzyme nanocomplexes and their use as antidotes and preventive measures for alcohol intoxication" *Nature Nanotechnol.*, 2013, *8*, 187-192.

2. Y. Liu, H. Wang, K. Kamei, M. Yan, K.-J. Chen, Q. Yuan, L. Shi, Y. Lu*, H.-R. Tseng*. "Delivery of intact transcription factor by using self-assembled supramolecular nanoparticles" *Angew. Chem. Int. Ed.*, 2011, *123*, 3114-3118.

3. Y. Liu, J. Du, J. Choi, K.-J. Chen, S. Hou, M. Yan, W.-Y. Lin, K. Chen, T. Ro, G. S. Lipshutz, L. Wu, L. Shi, Y. Lu*, H.-R. Tseng*, H Wang*. "A High-Throughput Platform for Formulating and Screening Multifunctional Nanoparticles Capable of Simultaneous Delivery of Genes and Transcription Factors". *Angew. Chem. Int.l Ed.*, 2016, *55*, 169.

4. Y. Liu, S. Liang, X. Jin, G. Liu, J. Wen, L. Zhang, J. Li, X. Yuan, I. S.Y. Chen, W. Chen, H. Wang, L. Shi, X. Zhu, Y. Lu*. "Phosphorylcholine polymer nanocapsules prolong the

circulation time and reduce the immunogenicity of therapeutic proteins". *Nano Research,* 2016, doi: 10.1007/s12274-016-0991-3

5. Y. Liu, J. Li, Y. Lu*. "Enzyme therapeutics for systemic detoxification" *Adv. Drug Deliv. Rev.,* 2015, *90,* 24.

6. J. Li, X. Jin, Y. Liu, F. Li, L. Zhang, X. Zhu*, Y Lu*. "Robust Enzyme-Silica Composites Made from Enzyme Nanocapsules", Chem. Comm., 2015, published online, doi: 10.1039/C5CC02053K

7. J. Jin, W. Wei, J. Du, Y. Liu, J. Li, Z. Lu*, Y. Lu*. "Development of a self-crosslinking targeting polymer for rapid gene delivery" *J. Controlled Release*, 2013, *172,* e107-e108

8. M. Yan, M. Liang, J. Wen, Y. Liu, Y Lu*, I.S.Y. Chen*. "Single siRNA nanocapsules for enhanced RNAi delivery" *J. Am. Chem. Sci.,* 2012, *134,* 13542-13545

9. Q. Xiao, M. Gu, H. Yang, B. Li, C. Zhang, Y. Liu, F. Liu, F. Dai, L. Yang, Z. Liu, X. Xiao, G. Liu, P. Zhao, S. Zhang, C. Wang, Y. Lu, M. Cai* "Inward Lithium-ion Breathing of Hierarchically Porous Silicon Anodes". *Nature Communication*, 2015, doi: 10.1038/ncomms9844

Patents:

1. Y. Lu, M. Yan, Y. Liu, Multiple-EnzymeNanocomplexes, Publication No.: WO 2013/006762; Application No.: PCT/US2012/045690

2. O. O.Yang, Y. Lu, C. Ji, M. Yan,Y. Liu, Oral Delivery of Enzymes by Nanocapsules for Targeted Metabolism of Alcohol or Toxic Metabolites, Publication No.: WO 2013/006763; Application No.: PCT/US2012/045692

Chapter 1. Protein therapeutics and protein delivery

1.1 Protein therapy and therapeutic proteins

Proteins have the most dynamic and diverse role of any macromolecule in the body, catalyzing biochemical reactions, forming receptors and channels in membranes, providing intracellular and extracellular scaffolding support, and transporting molecules within a cell or from one organ to another.[1] Viewed from the perspective of disease mechanisms, protein therapy, which treats diseases by delivering therapeutic proteins directly, represents a tremendous opportunity to alleviate many incurable diseases including chronic diseases, inherited diseases and cancers, as disease often results from mutations or other abnormalities of one or several proteins, or an abnormal concentration of any protein.[2] Although one can argue which molecules are most important for life and they all are, currently the proteins as therapeutics are the most important biologicals in terms of their clinical utility. To date, more than 150 different proteins, including monoclone antibodies (mAbs), enzymes, cytokines, growth factors and others, have been approved by the US Food and Drug Administration (FDA) for clinical use, and many more are in development. In contrast, we still have to wait for the first approved DNA-based therapeutic.[3]

According to the functions or the mechanisms, protein therapeutics can be grouped in several different ways. Based on their pharmacological activity, they can be divided into five groups: (a) replacing a protein that is deficient or abnormal, (b) augmenting an existing pathway, (c) providing a novel function or activity, (d) interfering with a molecule or organism, and (e) delivering other compounds or proteins, such as a radionuclide, cytotoxic drug, or effector proteins.[2] Protein therapeutics can be also grouped based on their molecular mechanism of function. In this way, protein

therapeutics can be divided into three groups: (a) specific noncovalent binders, (b) proteins affecting covalent bonds, and (c) others. By 2011, the first group of proteins approved by the European Union or the USA for clinical use consists of 73 unmodified proteins including 29 mAbs, the second group includes 21 enzymes; and the third group has only one representative, human serum albumin, which is used to increase plasma osmolarity. The largest and currently most selling therapeutic protein group is the first group protein therapeutics, especially mAbs and Fc fusion proteins. In 2010, sales of mainly recombinant therapeutic proteins and antibodies exceeded US$ 100 billion, where therapeutic mAbs accounted for almost half (48%) of the sales.[4–6]

In term of sales, therapeutic mAbs and Fc fusion proteins are more successful than therapeutic proteins other than mAbs and Fc fusion proteins, which are almost all enzymes and albumin.[2] Several major differences between these proteins and antibody-based therapeutics may explain why on average the approved mAbs and Fc fusion proteins are more successful. Firstly, the Fc portion of antibody confers them with long half-life by binding to the FcRn and effector functions including antibody-dependent cell-mediated cytotoxicity (ADCC) and complement. No other proteins are capable to perform those functions simultaneously. Secondly, Fabs can bind to large number of targets to keep their Ig-based scaffold, which often results a desired bio-distribution and better therapeutic index. The third advantage is that antibodies have evolved to fight diseases and are usually in high concentration in the blood without significant side effects. Therefore, mAbs and Fc fusion proteins on average present less toxic than other protein therapeutics.

Towards the development of wider scope of protein therapeutics, various methodologies have been used to engineer proteins to resemble some of the properties which mAbs already have through their Fc or Fabs. Such properties include long plasma half-life, low toxicity and immunogenicity,

2

targeting capability to specific tissues and organs, as well as high membrane permeability for intracellular protein delivery. During the past several decades, tremendous efforts have been devoted into this field, resulting three major types of approaches to endow one or several abovementioned features to engineered proteins. The traditional approach is achieved by mutation and direct evolution of therapeutic proteins. Although it is still the most widely used method to develop protein therapeutics, it is a very time-consuming process and the properties of the resulted proteins are usually hard to predict. Modern approaches for protein engineering and protein delivery mostly focus on tuning the surface properties of therapeutic proteins. This could be achieved by either modifying protein surface structures through restricted chemical reactions, or encapsulating therapeutic proteins and delivering them through artificial vectors. To date, the conjugation methods, especially PEGylation, which conjugates poly(ethylene glycol) onto therapeutic proteins to prolong their circulation time, have achieved massive success; 7 types of PEGylated enzymes and interferons (Table 1-1) have been approved by FDA for clinical use by Year 2010 and several more are under clinical trials. However, recent researches have reported the discovery of anti-PEG antibodies from all patients received PEGylated drugs and 25% polulation of normal people. Such antibody can quickly identify PEGylated therapeutics and help immune system to clear them from the blood circulation effectively, leading to poor therapeutic index of PEGylated proteins and reduced therapeutic effects.[7,8] For this type of protein engineering method, new materials have to be invented to avoid the immune clearance in the future development of protein therapeutics.

Table 1-1 PEGylated protein therapeutics approved by FDA by Year 2010

Name	Company	Therapeutic Protein	Diseases	Approved Year
Adagen®	Sigma-Tau Pharmaceuticals, Inc.	adenosine deaminase	severe combined immunodeficiency caused by	1990

			the deficiency of adenosine aminase	
Neulasta®	Amgen	granulocyte colony stimulating factor	neutropenia	2002
Pegasys®	Genentech	Interferon-α2a	hepatitis C	2002
Peg-Intro®	Merck	Interferon-α2b	hepatitis C	2001
Somavert®	Pfizer	a modified version of human growth hormone designed to bind to and block the growth hormone receptor	acromegaly	2003
Oncaspar®	Enzon Pharmaceuticals, Inc.	L-asparaginase	acute lymphoblastic leukemia	2006
Krystexxa®	Savient Pharmaceuticals, Inc.	uricase	chronic gout, hyperuricemia	2010

Vector-based protein delivery methods, which deliver proteins by carrying them using synthesized vehicles, have attracted attentions from both material scientists and biologists. Instead of direct modification of the protein surface, vector-based method uses polymers or other synthesized materials to encapsulate therapeutic proteins, which effectively provides a new surface to the protein without altering the chemical structure of the protein. Compared to the conjugation method, the major advantage of vector-based delivery system is well preservation of the original structure of the encapsulated protein, which effectively avoids the change, reduce or complete loss of the biological function of the therapeutic proteins. Another advantage of vector-based delivery strategies is the ease of surface engineering with desired physic-chemical properties due to the wide choices of materials and methods for constructing the delivery vectors and less concern about the damage to the protein's function. Currently, vector-based protein delivery systems are under heavy development and some of them have entered clinical trials. Recent advances in the

protein delivery vectors, especially for intracellular delivery and systemic delivery of proteins, will be discussed in the following section.

1.2 Systemic delivery of proteins

For the therapeutic purposes, most therapeutic proteins do not need to be delivered into cells. Instead, most therapeutics need to function extracellularly, including all mAbs and most enzymes. For the latter one, most therapeutic enzymes need to stay in the blood circulation long enough to allow them functioning effectively. This type of application can be generalized as enzyme-based systemic detoxification, which use therapeutic enzymes to convert toxicants introduced externally or produced by malfunctioning biological process to non-toxic ones, or use enzymes to correct the level of certain substances so as to redress metabolic disorders. Compared to traditional detoxification agents, enzyme-based detoxification agents possess several advantages: (1) high substrate selectivity – enzymes can decompose toxic substances without affecting other biochemical molecules, resulting in less side effects; (2) high catalytic efficiency – enzymes usually catalyze the conversion of their substrates with fast kinetics, which is crucial for making effective antidotes for acute intoxication; (3) the most direct method to treat intoxications caused by metabolic disorders – enzymes can be delivered to replace the dysfunctional ones to redress metabolic disorders. Because of these advantages, many enzymes have been discovered and developed for decomposing toxic substances.[9–17] However, native enzymes barely show any detoxification effects, while some of them even caused severe immune responses when administrating systemically. Particularly, exogenous enzymes generally exhibit high immunogenicity and low circulating ability, which result in fast clearance after the administration.[18–24]

5
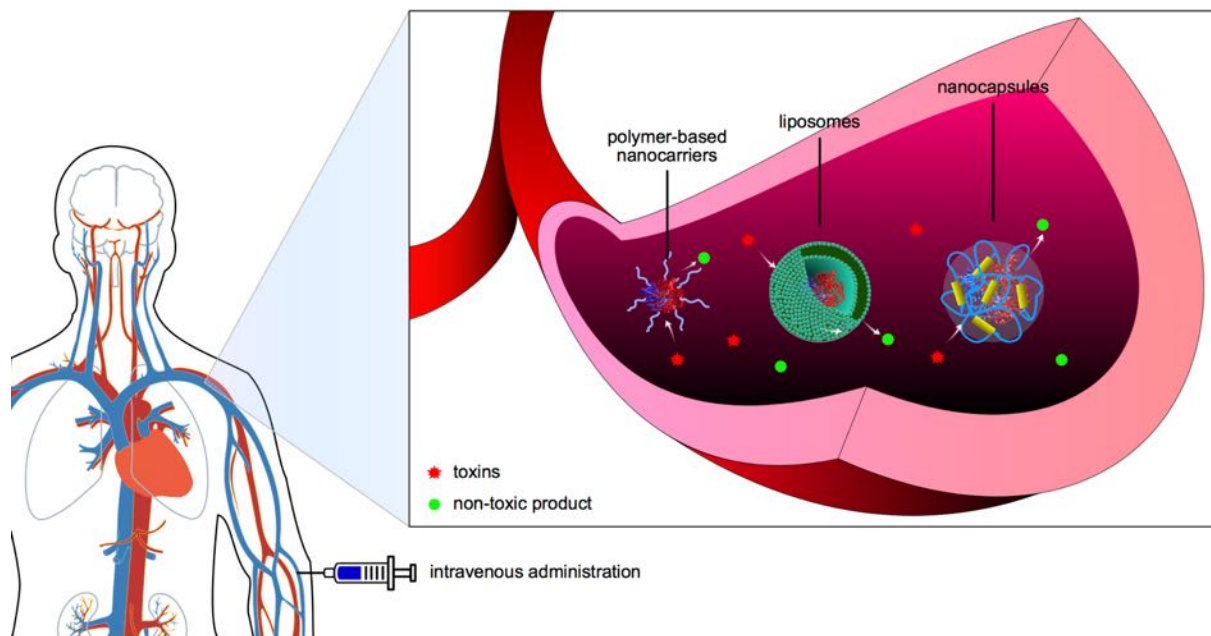
Figure 1-1 A schematic illustration of the three major types of enzyme-nanocarrier architectures for detoxification through intravenous delivery.

To circumvent these limitations, nanocarriers were extensively developed, affording a large number of protein therapeutics with improved efficacy and reduced side effects.[25–29] To date, various enzyme-nanocarrier architectures have been explored, some of which have been used clinically.[25,30] Such enzyme-nanocarrier architectures mainly include liposome-wrapped enzymes, polymer-conjugated enzymes, and polymer-encapsulated enzymes (Figure 1-1). In the following sections, these three architectures will be discussed from the perspective of detoxification achieved through systemic administration. Examples of enzyme-based antidotes and therapeutics will be provided (Table 1-2) and perspectives in future development of enzyme-based antidotes will be also provided.

Table 1-2 Enzyme therapeutics for systemic detoxification purposes

Enzyme	Related Disease	Carrier	Development Status	References

Uricase	Hyperuricemia and gout	PEG	FDA approved in 2010 (Krystexxa™, Savient Pharmaceuticals, Inc.)	[10,11,18,31–37]
		Dextran	Preclinical study	[38]
		PVP	Preclinical study	[39,40]
		PAcM	Preclinical study	[39–41]
		Liposome	Preclinical study	[42,43]
		Erythrocyte	Preclinical study	[44,45]
Glucose oxidase	Diabetes	Liposome	Preclinical study	[46]
		Erythrocyte	Preclinical study	[47,48]
		Nanocapsule	Preclinical study	[49]
Adenosine deaminase	ADA deficient SCID	PEG	FDA approved in 1990 (Adagen®, Sigma-tau Pharmaceuticals Inc.)	[13,50]
Phenylalanine hydroxylase	Phenylketonuria	PEG	Preclinical study	[51]
Phenylalanine ammonia lyase	Phenylketonuria	PEG	Phase I clinical trial	[7,52]
		Gelatin capsule	Preclinical study	[53]
		Cellulose capsule	Preclinical study	[54]
Superoxide dismutase & catalase	ROS related disease	PEG	Preclinical study	[55,56]
		Dextran	Preclinical study	[57–59]
		PVP	Preclinical study	[60]
		Block copolymer	Preclinical study	[61–63]
		Liposome	Preclinical study	[64–74]
Rhodanese	Cyanide intoxication	Liposome	Preclinical study	[75,76]
		Erythrocyte	Preclinical study	[77]
		Dendritic polymer	Preclinical study	[78]
Phosphotriesterase	Organophosphate intoxication	PEG	Preclinical study	[79]
		Liposome	Preclinical study	[80–84]
		Erythrocyte	Preclinical study	[85,86]
		Dendritic polymer	Preclinical Study	[78,87]
		Pluronic micelle	Preclinical study	[88]
		Nanocapsule	Preclinical study	[89]
		Liposome	Preclinical study	[90]

Alcohol dehydro-genase & Alde-hyde dehydro-genase	Alcohol intoxica-tion	Erythrocyte	Preclinical study	[91–93]
Alcohol oxidase	Alcohol intoxica-tion	Erythrocyte	Preclinical study	[94]
		Nanocapsule	Preclinical study	[49]
L-Asparaginase	Acute lympho-blastic leukemia	PEG	FDA approved in 2006 (Oncaspar®, Enzon Pharmaceu-ticals, Inc.)	[95–101]
		Liposome	Preclinical study	[102–104]
		Erythrocyte	Preclinical study	[105–108]
		Poly(lactide-co-glycolide)	Preclinical study	[109]
Arginase	T-cell acute lym-phoblastic leuke-mia	PEG	Preclinical study	[12,110]
		Dextran	Preclinical study	[111]
Plasminogen acti-vators	Vascular clot	PEG	Preclinical study	[112–118]
		Liposome	Preclinical study	[119]

1.2.1 Liposomes

Liposomes have been used as pharmaceutical carriers during the past 30 years.[25] Liposomes are nano-sized artificial vesicles, which can be produced from natural or synthetic phospholipids. Enzymes are typically located in the aqueous core, while other hydrophobic molecules can be dissolved within the bilayers of liposomes.[120] Liposomes provide many advantages for detoxification, including: 1) liposomes are biocompatible; 2) liposomes can stabilize the encapsulated enzymes; 3) hydrophobic toxins can be entrapped into liposomes facilitating their degradation; 4) the size, charge and surface properties of liposomes can be readily turned by introducing desired lipid moieties such as PEG-conjugated lipids, where PEG stands for poly(ethylene glycol).

8
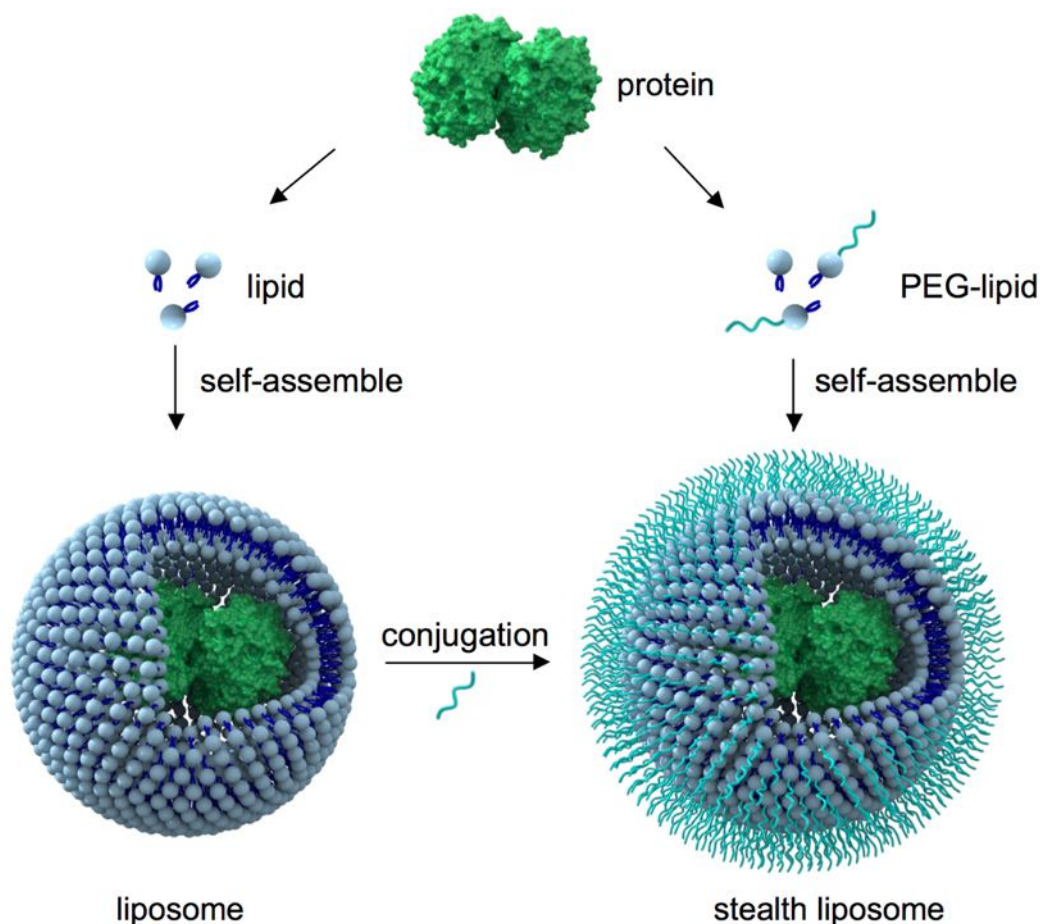
Figure 1-2 A schematic illustration of preparing liposomes and "stealth liposomes" through self-assembly of lipids or a mixture of lipids and PEG-lipids, respectively. Stealth liposomes could also be prepared by conjugating PEG chains onto the liposome surface.

A potential problem with liposome-wrapped enzymes, particularly when delivered intravenously, is the rapid removal from the circulation by the reticuloendothelial system.[121] To enhance their circulation half life, "stealth liposomes" have been designed by coating the liposomes with PEG.[122] This could be achieved either by constructing liposomes using PEG-conjugated lipids (PEG-lipid) or by post-conjugating PEG on the liposome surface (Figure 1-2). Klibanov et al. first reported the preparation of PEGylated liposomes, which increased the circulation half life from less than 30 min to 5 h compared to their non-pegylated counterparts.[123] The prolonged circulation time is

9

attributed to the large hydrodynamic volume of the PEG chains, which shield around the liposomes and mask the liposomes from immune and metabolic systems.[64] Based on a similar mechanism, other hydrophilic polymers were also used to construct long-circulating liposomes, including poly[N-(2-hydroxypropyl) methacrylamide]],[124] poly-N-vinylpyrrolidones,[125] L-amino-acid based polymers,[126] and polyvinyl alcohol[127]. However, conjugating with these polymers often decreases the liposome stability, because conjugation of hydrophilic polymers reduces the glass-transition temperature of the liposomes. To maintain necessary stability for these liposome, only a limited amount of polymers could be conjugated, leading to low density of the surface-grafted polymeric layer, which reduce their effects in prolonging the circulation time of liposomes.

To date, various enzymes have been encapsulated into liposomes for detoxification or therapeutic purposes. For example, uricase has been successfully encapsulated within liposomes. Studies showed that liposome-wrapped uricase exhibits more effective management of the uric-acid level than native uricase in hyperuricemia rat model due to the higher uricolytic activity.[42,43] Consistently, L-asparaginase has also been encapsulated within liposomes, resulting in liposome-wrapped L-asparaginase with prolonged circulating time, abrogation of acute toxicity and better retained in vivo antitumor activity.[103,104] For systemic detoxification, Petrikovics et al. co-encapsulated rhodanese and a sulfur donor (thiosulfate) for the detoxification of cyanide. By optimizing their compositions, these liposomes exhibit high encapsulation efficiency, as well as good fluidity for effective cyanide penetration and conversion.[75,76] Promising results have been demonstrated in the detoxification of organophosphates (OPs), in which organophosphorus acid anhydrolase (OPAA) and phosphotriesterase were encapsulated within liposomes and delivered intravenously to eliminate diisopropylfluorophosphate (DFP) and paraoxon in the blood circulation.[80–82,128] Because their ease of preparation and excellent biocompatibility, liposomes have been extensively

explored as delivery carriers for many therapeutic enzymes; however, despite the improved circulating time and therapeutic effects, the delivery efficiency is still far from optimal.

1.2.2 Polymeric vectors

Due to versatility and easy control of the physiochemical properties, conjugating therapeutic enzymes with polymer has been broadly adapted for the development of therapeutic or detoxifying agents. The polymers may shield the enzymes from undesired interactions, improve the enzyme stability, reduce immune activation, and prolong the circulation time. Such shielding effects are highly dependent on the physiochemical properties of the polymers, such as hydrophilicity, chain length, chain architecture (i.e., linear versus branched) and biocompatibility, which are elaborated in detail below.[129]

PEG is the most commonly used polymer for the preparation of polymer-enzyme conjugates. Covalently attaching PEG to the enzymes, also termed as PEGylation, is generally achieved by reacting PEG with the reactive motifs of enzymes. Commonly, PEGylation is achieved through reacting the ε-amino groups of lysine residues. This process often results in the formation of conjugated isomers containing various PEG chains attached at different sites,[28] and further purification process is required for FDA approval. To circumvent this limitation, site-specific PEGylation reactions have also been developed,[130] such as the methods of N-terminal PEGylation and cysteine-specific PEGylation, where the conjugation is occurred at the N-terminal α-amino groups and the residue cysteines (or cleaved disulfide bond), respectively.[131–133] Other site-specific PEGylation methods were also developed, such as conjugating PEG-alkylamine reagent onto glutamine resi-

dues by transglutaminase,[134,135] and reacting (sialic acid)-PEG with the hydroxyl groups of a gly-cosylated protein.[136] These site-specific strategies lead to more defined conjugating structure, fa-cilitating their transition for clinic use.

The shielding effect of PEG is mainly attributed from its hydrogen bonding with water, though the backbone of the molecule is hydrophobic. When dispersed in aqueous solution, the PEG chains form hydrogen bonds with the surrounding water molecules. Such hydrated layers effectively shield the enhzymes from their surrounding, affording the enzymes with improved bioavailability, prolonged circulation time, and reduced immunogenicity and toxicity (Figure 1-3). Consistently, PEG with longer chain length and higher density offers longer circulation life. In addition, PEG chain architecture also influences the pharmacokinetics of PEGylated enzymes, and branched PEG generally exhibits longer circulation half life than linear ones with similar molecular weight.[137] However, such shielding layers may block active sites of the PEGylated enzymes, resulting in reduced or even completely loss of the enzyme activity. Although the improved pharmacokinetics may compensate the reduced enzyme activity in certain degree, [138,139] reduced enzyme activity remains as a main drawback of PEGylation.

PEGylated enzymes have been extensively studied for both in vitro and in vivo eliminations of hazardous chemicals, some of which have been approved for therapeutic use.[30] Adagen (pegada-mase) represents the first enzyme therapeutic approved for inherited disease,[140] followed by the approval of Oncaspar (pegaspargase),[95] both of which use PEG succinimidyl succinate as a random PEGylation reagent. Krystexxa, a PEGylated recombinant uricase was also prepared by random conjugation of PEG p-nitrophenyl carbonate ester to the lysine residues of uricase.[141] Other en-

zymes, such as arginine deiminase (ADI), phenylalanine ammonia-lyase and organophoshpate hydrolase (OPH), were also conjugated with PEG, resulting in significantly extended residence time of days in comparison with their native enzyme counterparts with resident time of hours.[7,142] However, there are increasing number of reports on the formation of anti-PEG antibodies when PEGylation therapeutics was used as intravenous agents.[7,8] Developing alternative shielding layers that can further evade the immune system is essential but challenging.
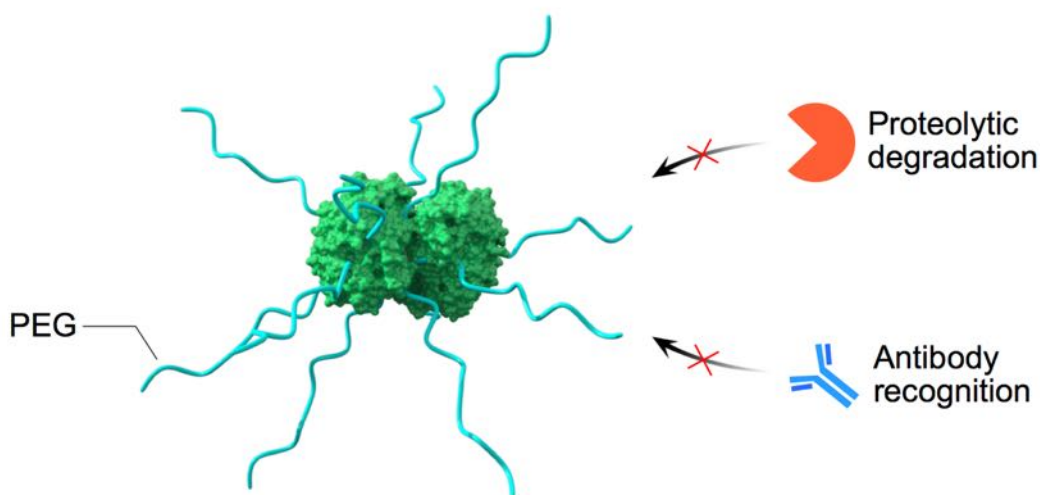
Figure 1-3 A schematic illustration of a PEGylated protein. The PEG chains are conjugated on an enzyme, which could protect the protein from proteolysis and help to evade the immune system.

Dextran, a natural and biodegradable polysaccharide, has been widely employed for decades as a plasma volume expander, peripheral flow promoter, and antithrombolytic agents.[143] Recently, dextran has also been investigated as carriers for delivery of drugs and proteins, which are mainly achieved through conjugating dextran with the therapeutic agents.[144] Similar to PEG, conjugation with dextran endows the therapeutic agents with prolonged circulating time, increased protein stability and reduced in vivo immunogenicity. For example, Wileman et al. prepared asparaginase-

dextran conjugates with significantly improved plasma half-life in both immune and non-immune rabbits.[145] Similarly, dextran-conjugated uricase exhibits significantly prolonged circulation time, which is over ten times of the native enzyme counterpart (7h vs 0.6h).[38] Carboxypeptidase G2 (CPG), which can enzymatically deplete an essential nutrient (folate) for the tumor cells, has only 3.1 h plasma half-life. Conjugating CPG with dextran with 40, 70, 110 or 150 kDa molecular weight results in a plasma half-life of 14.3, 16.3, 17.5 and 45.6 h in normal mice, respectively.[146] However, it has been reported that intravenous administration of dextran with high molecular weight may cause life-threatening anaphylaxis.[147]

Amphiphilic block copolymers are another class of polymers used as nanocarriers. Particularly, Pluronic triblock copolymers have been extensively studied due to their biocompatibility, biodegradability, low toxicity and prolonged circulation time when conjugated with proteins.[148,149] Pluronic copolymers are composed with poly(ethylene oxide) (PEO) and poly(propylene oxide) (PPO) with a general formula of $EO_xPO_yEO_x$, where x and y represent the number of EO or PO repeat units in the copolymer. In aqueous solution, Pluronic copolymers can self-assemble into micelles with a hydrophobic core formed with PPO and a hydrophilic shell composed with PEO. Pluronic copolymers have been used for delivering enzymes for detoxification. For example, Pluronic F127 ($EO_{100}PO_{65}EO_{100}$) and OPH was conjugated, and the resulting conjugates could self-assemble into a micelle structure with a hydrophobic PPO core and OPH on the surface. These hydrophobic cores can attract lipophilic OP molecules and the OPH on the surface facilitates its degradation. Such conjugates form micelles in solution exhibiting excellent stability, which are of great interest for OP-detoxification for both military and civilian applications.[88] Pluronic P85 ($EO_{26}PO_{40}EO_{26}$) and L81 ($EO_6PO_{43}EO_6$) were also conjugated with superoxide dismutase (SOD), which could be used to inhibit intraneuronal superoxides.[150]

14

Besides Pluronic triblock copolymers, other block copolymers have also been studied. One example is vinyl sulfone (VS)-terminated block copolymers of poly(propylene sulfide) (PPS) and PEG (PPS-PEG-VS), which forms micelles with vinyl sulfone groups. SOD could be readily conjugated to the micelle surface through the Michael-type addition. The conjugated SOD could effectively eliminate superoxides, while PPS (mainly located within the micelle cores) can scavenge the toxic hydrogen peroxide produced by the SOD-mediated reactions. Such a synergic effect is also observed in a cascade reactions mediated by SOD and catalase.[63]

Poly(vinylpyrolidone) (PVP) is a synthetic polymer used in large quantities as a blood expander, and is known for its negligible toxicity, low immunogenicity and antigenicity.[151,152] Similar to PEG, PVP has also been used to form enzyme-PVP conjugates, which were generally synthesized by a two-step process. First, a single (monofunctional) or multiple reactive (polyfunctional) groups, which can conjugate with the amino-acid residues on enzymes, are created for PVP to form the activated PVP. Activated PVP is then incubated with enzymes to form enzyme-PVP conjugates.[60,153] Using these methods, PVP-conjugated SOD was prepared with increased circulation time, reduced antigenicity and immunogenicity, and enhanced thermal stability. PVP-uricase conjugates were also prepared; however, 2-folds higher of antigenicity than the native uricase was observed.[39] Similar issue was also observed in the PVP-enzyme conjugates made with N-acetyl-beta-D-hexosaminidase.[154]

Poly(N-acryloylmorpholine) (PAcM), an amphiphilic and nontoxic polymer, was also explored as plasma substitutes and transdermal carriers.[155] For example, poly(AcM-co-NAS) made by copolymerizing N-acryloylmorpholine (AcM) and N-acryloxysuccinimide (NAS) inherits the water solubility and biocompatibility from PAcM, and the ability to conjugate with amino groups from

poly(NAS). Such copolymer has been used to form conjugates with catalase and ribonuclease A without compromising their enzyme activities.[156,157] Similar to PVP, reactive groups can be also generated within PAcM to enable protein conjugation.[158] PAcM-uricase conjugates, for example, exhibit dramatically reduced antigenicity and suppressed immunogenicity.[39] Nevertheless, more extensive studies in toxicity, immunogenicity, antigenicity, and clearance mechanism of PAcM-based conjugates are required to understand their therapeutic potentials.

1.3 Intracellular delivery of proteins

Intracellular protein de- livery is considered to be the most direct, fastest and safest approach for curing gene-deficiency diseases, enhancing vaccination, triggering cell trans-differentiation process, inducing the formation of pluripotent stem cells, and other applications. In contrast to gene delivery, intracellular protein delivery avoids permanently altering the genomic information of host cells, circumventing the concerns of potential mutagenesis associated with the delivered genes. To date, various vectors have been explored to facilitate intra- cellular delivery of proteins, such as liposomes, polymers, gold nanoparticles, mesoporous silica particles, carbon nanotubes, and natural vectors such as cell-penetrating peptides, antibodies and other biomolecules. This dissertation will focus on synthesized nano-carriers including liposomes, polymer-based systems, and cell penetration structures.

1.3.1 Liposomes

Liposomes have been widely used for drug delivery purposes since first observation several decades ago. In a liposomal delivery system, proteins are wrapped with in a hollow sphere composed by lipid bilayer, which facilitates translocation of the encapsulated proteins into lysosomes or cytoplasm. Table 1-3 lists three types of commonly used lipids, including cationic lipids, neutral

lipids, and pH-responsive lipids. Particularly for pH-responsive lipids, liposomes formed with these lipids can be protonated and deprotonated in response to the change of pH, resulting the release of the encapsulated protein in different micro-environments.

Table 1-3 Commonly used lipid structures for protein delivery

Type	Name	Structure
Cationic lipids	SAINT-2	
	DODAP	
	DODAPL	
	DOGS	
Neutral lipids	DOPE	
	DOPC	
pH-responsive lipids	CHEMS	

DOSG	
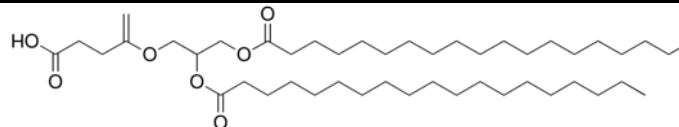
Since most liposomes enter cells through endocytosis process, enhancement of cell-uptake efficiency of liposomes is essential for an effective protein delivery. To achieve this goal, cationic lipids are usually employed to form liposomes with a positively charged surface, which enhances the electrostatic interactions between liposome and cell membranes effectively. For example, intracellular delivery of β-galactosidase and caspase was reported by using cationic liposomes synthesized with DODAPL and DOPE.[159,160] However, most cationic liposomes show poor compatibility with serum due to undesired non-specific absorption of serum proteins, which highly restricts their application in clinic. To improve the serum stability, a new type of cationic lipid, SAINT-2, was developed recently. Cell uptake efficiency of liposomes formed with this lipid was not influenced by the size or charge of the liposomes.[161] However, most cationic liposome have shown certain degree of cytoxicity, which could be attributed to the apoptosis induced by the cationic moieties of the lipids.[162] To overcome this issue, cell penetrating structures, including cell penetrating peptides (CPPs), antibodies,[163–165] folic acid,[166] and transferrin[165–167] can be conjugated to the surface of liposome to facilitate cell internalization without using cationic lipids. In this case, TAT, a CPP derived from HIV virus, was one of the most commonly used structures due to its low molecular weight, wide availability, and ease of conjugation. To date, proteins including bovine serum albumin (BSA), β-galactosidase, and IgG have been reported to be delivered intracellularly with TAT-conjugated liposomes.[168,169] Liposome conjugated with both TAT and antibody on the surface was also constructed to achieve targeted delivery, where TAT enhanced the endocytosis efficiency significantly.[170]

1.3.2 Polymer-based systems

Polymeric protein delivery systems rely on the formation of micrometer- or nanometer- size polymer particles containing protein cargo. Based on their synthetic process and structure, such systems can be classified into non-covalent and covalent delivery systems. In the first category, current polymer-based systems achieved intracellular delivery of proteins by adsorbing proteins onto polymer particles or dendrimers. For example, GTPase rhoG was delivered into PC12 cells by first adsorbing proteins onto poly(butylcyano- acrylate) (PCBA) nanoparticles, which could trigger cell internalization via lipoprotein receptor-mediated endocytosis.[171] Dendrimers such as hyper-branched polyhydroxyl (HBPH) polymers were also employed to deliver proteins including glutathione S-transferase (GST) luciferase, antibodies, and cytochrome C.[172,173] One major advantages for using dendrimers is the ease to conjugate functional groups to confer unique features to the carrier. Exemplified by conjugation of folic acid onto HBPH, such modified dendrimer could target and translocate the protein cargo (cytochrome C) into cancer cell selectively, which demonstrates a strategy of protein cancer therapy.[173]

 In addition to polymer particles and dendrimers, non-covalent delivery systems constructed by self-assembly of protein and macromolecules have also been studied. Such assembly process can be driven by electrostatic interactions, hydrophobic interactions, host-guest interaction and others, which are usually determined by the structure of polymers. In particular to protein intracellular delivery, forming a protein-polymer complex with cationic block copolymer is a very common approach. In such cases, protein was loaded into the assembled structure via electrostatic interaction, or hydrophobic interaction. [174–176] The result protein-polymer structures usually have cationic polymer chains exposed on the surface, which enables cell internalization. Similar to liposomal

delivery systems, such cationic polymer chains can be also replaced by cell internalization moieties or antibodies in order to incorporate desired functions such as targeting ability.

Viewed from material science perspective, polymer-based systems provide endless potential for the development of more advanced delivery system due to the wide variety of materials and interactions that can be employed compared to liposomal systems. However, the construction of non-covalent systems relies on self-assembly process, which is a dynamic state that is only stable under certain condition. As the environment changes, for example, administration of such protein-polymer complex into blood, such steady state cannot be maintained, resulting the dissociation of the protein-polymer complex and release of the protein.[177] To overcome this problem, crosslinking process of polymer can be applied after the formation of protein-polymer complex to enhance the serum stability.[178] Such crosslinking structure can be also constructed with cleavable bonds and structures (e.g., disulfide bond), which can be degraded after entering into cells, resulting a more effective release of the protein cargo.

In addition to non-covalent polymer systems, intracellular protein delivery has also been achieved by covalently conjugating protein and polymers together. Early attempts in this field mainly focus on conjugating proteins with cationic polymer, especially polyethylenimine. In this method, proteins including enhanced green florescent protein (EGFP) and ribonuclease (RNase) were conjugated chemically with PEI, which significantly enhanced their cell penetrating capability.[179] However, the chemical conjugation approach often result in denaturation of the protein, leading to the further exploration of non-permanent conjugation methods. Intracellular degradable structures such as disulfide bonds and biotin-avidin interactions were employed for the delivery of β-catenins

and p53.[180,181] After endocytosis, proteins dissociated from the polymer carriers and refolded into their original structures, therefore, functioned normally inside the cell.

Recently, our group developed a platform technology for protein delivery by incorporate single protein molecule into a polymeric nanocapsule. With this method, high efficient intracellular delivery of functional proteins can be achieved. This will be discussed in detail in Section 1.4 .

1.3.3 Inorganic delivery systems

Due to the high biocompatibility of organic materials, organic carriers such as liposomes and polymer systems were widely studied for intracellular protein delivery. However, certain inorganic materials are also non-toxic and highly biocompatible, which have potential to be designed for protein delivery purposes. To date, studies on using inorganic carriers for intracellular protein delivery mainly focus on a few systems, including gold nanoparticles (GNPs), mesoporous silica, and carbon nanotubes.

Gold nanoparticle has been widely explored for its biological applications due to its bio-inertness, imaging capability, and ease of synthesis and morphology control.[182–184] Due to its high surface energy, GNPs can be uptake by cells, which has been documented for common cell-lines.[185] For protein delivery, GNP can adsorb proteins onto its surface so as to mediate their cell-uptake. One advantage of using GNP for protein delivery is the ease of surface engineering of GNP. Thiol-group-containing ligands can be easily conjugated onto the surface of GNP, which can change the surface properties of GNP significantly. Several proteins including β-glycosidase was delivered into cells with this method without observation of significant cytotoxicity.[186]

Mesoporous silica nanoparticles (MSNs) have recently been explored as potential nanocarriers for bioactive molecules due to their unique properties, such as high surface area, tunable pore size, and ease of surface functionalization.[187] The mechanism of intracellular delivery of protein with MSNs is similar to GNP-based delivery systems. The first protein delivery achieved with MSN-based vectors was the delivery of cytochrome C, which was successfully translocate into HeLa cells and released from the MSN-based vector.[188] One unique feature of MSN-based vector is the capability of loading and controlled releasing of small molecules simultaneously during the protein delivery due to the porous structure.[189–194] This feature offers a potential method to co-delivery of small molecules, genes, and proteins together into cells to allow them functioning synergistically.

The last inorganic carrier is single-walled carbon nanotubes (SWNT), which has recently been shown to shuttle various molecular cargos into living cells including proteins, short peptides, and nucleic acids.[195–201] The cell internalization pathway of SWNT was believed to achieve via energy-dependent endocytosis, which was recently observed by Dai's group in the research of delivering several proteins (<80 kDa) with SWNT into different cells.[202] One big concern of using SWNT is the toxicity and biocompatibility, although it has been consistently reported that well processed water-soluble nanotubes are biocompatible and nontoxic at the cellular level.

1.4 Protein nanocapsule

Recently, Lu group has developed a novel encapsulation method, where a thin polymer network is formed *in situ* around a single enzyme or enzyme complex, leading to the formation of enzyme nanocapsules containing an enzyme core and a thin polymer shell. Such nanocapsule platform has been used for systemic delivery of proteins.[49,89,203,204] The synthesis of the protein nanocapsule

involves two steps. (Figure 1-4) Proteins were first conjugated with amine-reactive acrylate molecules to attach polymerizable groups onto the proteins. *In-situ* polymerization is then initiated in aqueous solution, yielding a thin polymer shell around each of the protein molecule with several advantages: 1) the crosslinked polymer shells offer enhanced stability against proteolysis and non-physiological environments; while the shells are so thin (nanometer scale) allowing effectively transport of small-size molecular substrates crossing the shells. 2) The physicochemical properties of the nanocapsules can be easily controlled by judicious choice of monomers and crosslinkers with desired charge (neutral, positive and negative charge), degradability, and hydrophilicity. 3) In most cases, only one single protein molecule is encapsulated within each nanocapsule, resulting in small particle size (~ 20 nm) favorable for systemic circulation[205–207]. All of these advantages make enzyme nanocapsules ideal nanocarriers for enzyme-based detoxification.
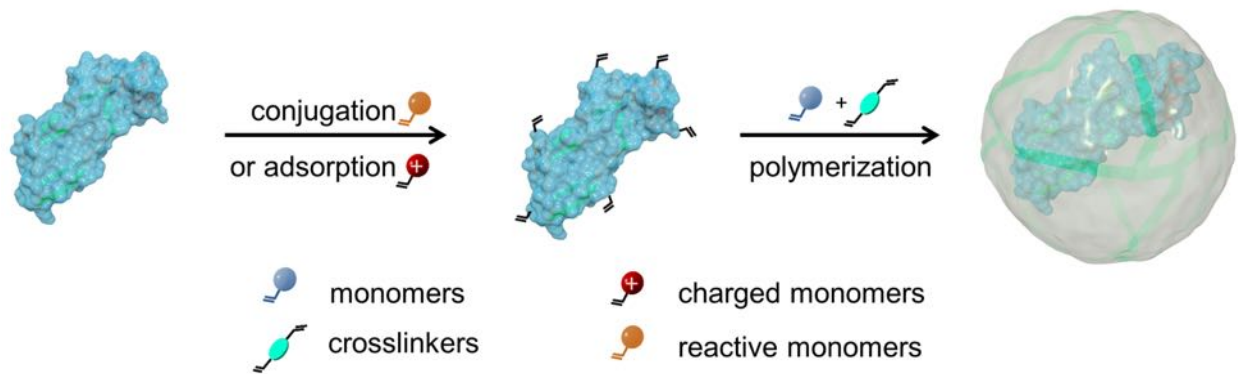
Figure 1-4 Schematic representing the preparation of single enzyme nanocapsule via in situ *synthesis of crosslinked polymer shell on the enzyme surface. Enzyme nanocapsule is synthesized by firstly conjugating or adsorbing unsaturated molecules onto the protein surface, followed by the initiation of* in situ *polymerization reaction to form the polymer shell.*

Since the modification of the enzymes prior to their encapsulation may decrease the enzyme activity, a revised encapsulation protocol was also developed.[208,209] Instead of conjugating acrylate

groups to the enzyme surface, monomers and crosslinkers are adsorbed and enriched around the enzyme molecules spontaneously through electrostatic or hydrogen-bonding interactions. Subsequent polymerization yields enzyme nanocapsules with a similar core-shell structure. With the revised protocol, enzymes can retain as their intact form with highly preserved activity. This encapsulation approach become a platform technology for the encapsulation of proteins with different sizes, surface charges, and structures without compromising their biological activity.

The enzyme nano-encapsulating platform provides a highly powerful tool towards the development of enzyme therapeutics and antidotes. The antidote application was first demonstrated by the decomposition, decontamination and detoxification of OPs. OPH is vulnerable to harsh conditions and proteolytic environment; Wei *et al.* used this approach to prepare robust and highly active OPH nanocapsules that can effectively decompose OP under extreme conditions like elevated temperature and presence of proteases. The enhanced stability allow the OPH nanocapsules for broad military and civilian applications, ranging from antidotes to prophylactics for OP-poisoning.[210] Moreover, the activity of OPH could be enhanced by manipulating the local chemical environment, while the thermal stability could be precisely tuned by controlling the amount of crosslinkers used to construct the shells. Preliminary *in vivo* study also reveals that two out of three mice with native OPH injection survived from the paraoxon poisoning, and all of them displayed poisoning symptoms within the first 2 hrs. For comparison, all the mice administrated with the OPH nanocapsules survived from OP-poisoning without any toxic symptoms throughout 24 hrs.

Naturally existed detoxification systems in our body generally require cascades reactions to work synergistically to decompose toxic substances (e.g. phase I and phase II detoxification). In this

context, ability to deliver two or more enzymes with synergic functions is essential for effective detoxification. Exemplified with alcohol detoxification, during the metabolism, alcohol is converted to acetaldehyde and acetic acid sequentially by alcohol dehydrogenase and acetaldehyde dehydrogenase, respectively. Administrating alcohol dehydrogenase or alcohol oxidase alone reduces the blood alcohol concentration, however, generates toxic intermediates acetaldehyde and hydrogen peroxide, respectively. To address this problem, a multiple-enzyme nanocapsule system was developed during my Ph.D. research to mimic the physiological alcohol detoxification process, where alcohol oxidase and catalase are co-delivered to eliminate the toxic intermediate hydrogen peroxide.[49] This part of work will be discussed in detail in Chapter 1.

Another general requirement for all protein therapeutics is the overall stability in blood circulation. This stability includes several important aspects, such as the capability to maintain the original structure and bio-functions, as well as avoiding being indentified and cleared by immune proteins, cells and organs. Currently strategy to enhance the plasma stability of therapeutic proteins is achieved by conjugating proteins with PEG (aka PEGylation), which intrinsically achieves by shielding the surface of protein with PEG chains. With the protein nanocapsule technique, proteins are wrapped completely by a thin layer of polymer shell, which interacts with outer environment (e.g., serum proteins, immune cells, organs) instead of the original surface of the encapsulated protein. Taking advantage of this unique structure, we designed a protein-adsorption-resistant polymer shell with zwitterionic polymer to encapsulate proteins. With this non-fouling polymer shell, the plasma half-life of the encapsulated protein was significantly prolonged. Moreover, because of the minimal protein adsorption, immune proteins and cells cannot recognize and identify the wrapped proteins, resulting the failure in activation of immune clearance and immune responses. This strategy provides a practical method for the in vivo use of any exogenous proteins, which

significantly broaden the scope of potential candidates of therapeutic proteins. This work will be discussed in detail in Chapter 3.

1.5 Therapeutic applications of protein delivery

1.5.1 Enzyme therapeutics for redressing metabolic disorders

Several diseases are caused by metabolic disorders due enzyme deficiency or dysfunction. Enzyme therapeutics could treat these diseases by delivering the enzymes to restore the missing functions. Various enzyme therapeutics have been developed or under development aiming to treat metabolic diseases, such as hyperuricemia, hyperglycemia, phenylketonuria and overproduction of reactive oxygen species. Recent advances in the development of enzyme therapeutics for these diseases will be discussed in the following paragraphs.

1.5.1.1 Hyperuricemia and gout

Hyperuricemia is an abnormally high level of serum uric acid, which may crystallize at locations with low body temperature. Increased levels of serum uric acid predispose for gout, which is a medical condition usually characterized by recurrent attacks of acute inflammatory arthritis, and eventually results in other serious syndromes due to bone erosion.[211] Traditional strategies to manage gout involve the treatments with nonsteroidal anti-inflammatory drugs, steroids or colchicine, which cannot reduce the serum uric acid level despite improving symptoms.[212] Xanthine oxidase inhibitors like allopurinol can effectively decrease the production of uric acid, therefore, reduce the serum uric acid level.[213] However, those inhibitors interfere with the normal purine metabolism and cause side effects.[214] An ideal treatment for hyperuricemia and gout should be able to directly convert excess amount of uric acid in the blood to highly soluble substances without bringing side effects.

Uricase (urate oxidase, EC 1.7.3.3, UOx) is an enzyme that catalyzes the oxidation of uric acid to 5-hydroxyisourate, which is a more soluble product that is readily excreted in urine. Unfortunately, unlike most mammals, human lacks functional uricase, resulting a much higher serum uric acid concentration. Treatment with administration of uricase can lower the uric acid concentration significantly; however, direct use of uricase results low therapeutic efficacy due to its low stability and high immunogenicity.[18]

Great efforts have been devoted to overcoming these limitations. One major type of approaches is to conjugate uricase with polymers. [39–41,215] It was found that conjugating uricase with neutral and hydrophilic polymers significantly reduces its immunogenicity and organ accumulation after intravenous administration.[41] Among all types of polymer-uricase conjugates, PEGylated uricase shows a prolonged blood circulating half-life, good biocompatibility and positive therapeutic effect in the management of hyperuricemia. [10,11,18,31–33] Decades of efforts in this field eventually result in a PEGylated form of recombinant mammalian uricase, which was developed jointly by Mountain View Pharmaceuticals, Inc. and Duke University. [37] In 2010, FDA approved this PEG-uricase (Krystexxa™, Savient Pharmaceuticals, Inc.) as a clinic therapeutic for the management of chronic gout. In the meantime, other encapsulated uricase have also been explored, such as by loading uricase into human erythrocytes[44,45,216] or liposomes.[43,217] Overall, the common goal is focused on developing uricase-based structure with sufficient circulating half-life and minimal immune responses. Since treatment of chronic gout usually span several months and need repetitive administrations of therapeutics, low immunogenicity is of particular importance.

1.5.1.2 Adenosine deaminase deficiency

Adenosine deaminase (ADA, EC 3.5.4.4), an enzyme that is needed for the breakdown of adenosine from food, plays essential roles in purine metabolism. The deficiency of ADA is one major cause of severe combined immunodeficiency (SCID), making the patients extremely vulnerable to infectious diseases.[218] Although bone marrow transplantation is an effective therapy for a minority of patients,[219] other treatments are being sought, including non-curative methods such as enzyme replacement therapy.[220] Initially, ADA replacement was achieved using transfusion of irradiated erythrocytes from healthy donors.[221] Despite the decrease in immunogenicity, the response was often inadequate or unsustained, with an increasing risk of iron overload and viral infection.[222] Hershfield *et al* introduced PEG-ADA, which was prepared by conjugating mono-methoxy-poly(ethylene glycol) (Mw=5000) to bovine intestinal ADA. The PEG-ADA serves as an alternative therapeutic for ADA replacement, demonstrating effectiveness with two SCID patients.[50] The PEG-ADA also showed an extended plasma half-life of 48 to 72 hours, and neither toxic effects nor hypersensitivity reactions were observed. By maintaining the plasma ADA activity *via* weekly dosing, the principle biochemical consequences of ADA deficiency in patients were completely reversed, indicating the effectiveness of PEG-ADA treatment. PEG-ADA was approved by FDA in 1990 (Adagen®, Sigma-tau Pharmaceuticals Inc.) as the first successful enzyme replacement therapy for an inherited disease,[223] and has been used to treat hundreds ADA-deficient SCID patient worldwide.[13]

1.5.1.3 Phenylalanine hydroxylase deficiency and phenylketonuria

Phenylalanine hydroxylase (PAH, EC 1.14.16.1) is an enzyme that catalyzes the hydroxylation of phenylalanine (Phe) to generate tyrosine. Deficiency in PAH results in the accumulation of Phe, which is eventually converted into neurotoxic phenylpyruvate that causes phenylketonuria (PKU),

leading to intellectual disability, seizures, and other serious medical problems if leaving untreated. Currently, the major treatment of PKU is achieved with low Phe diet for lifetime. Other forms of therapies are now being explored, including enzyme replacement therapy using PAH. Because of the complex structure of native PAH, truncated forms of PAH are often used in order to stabilize the structure and increase the activity.[224] Additionally, PEG conjugation is also employed to lower the immune response of PAH and improve the pharmacokinetics,[51] which shows promise as an alternative treatment to PKU.

In addition to the PAH replacement therapy, phenylalanine ammonia-lyase (PAL, EC 4.3.1.24) was also widely explored as a substitution to PAH in the treatment of PKU. PAL catalyzes the conversion of Phe to ammonia and trans-cinnamic acid, therefore, has the potential to manage the accumulation of Phe. Since it's widely existed in plants, yeasts and fungi, PAL is much easier to obtain than PAH and no complicated cofactors are required for PAL to function. However, proper protections are required because PAL is vulnerable to proteolytic degradation and also highly immunogenic. Initial attempts in PAL substitution therapy were achieve by immobilizing PAL in semipermeable cellulose microcapsule and packing inside gelatin capsules, resulting in significant plasma Phe reduction in both mice and human.[53,54] Another common approach is achieved by conjugating PAL with PEG. Studies have shown that conjugation of PAL with a 20 kDa linear PEG could abolish its immunogenicity without compromising its activity.[52] Recently, Phase I clinic trail on PEG-PAL has been initiated, and the treatment seems to be effective at reducing blood Phe levels in all five participants who received the highest dose of PEG-PAL. However, all 25 participants had developed antibodies against PEG at the end of the trial, which may significantly reduce the therapeutic effect since repetitive dosing is required for PEG-PAL.[7] Thus, new

materials need to be developed to replace PEG to avoid antibody genesis in order to achieve an effective and low-cost PAL-conjugates for the treatment of PKU.

1.5.2 Enzyme therapeutics in the antagonism of exogenous toxins

1.5.2.1 Cyanide poisoning

Cyanide poisoning occurs when exposed to a compound that produces cyanide ions. Because cyanide ions can inhibit cytochrome c oxidase, exposure to cyanide halts the cell inspiration. and a high concentration of cyanide could cause rapid death. Antidotes against cyanide poisoning requires rapid restore of the normal function of cytochrome c oxidase, which can be achieved by binding with the cyanide to release cytochrome c oxidase, or converting the cyanide to nontoxic forms directly. Current treatments usually use nitrites or 4-dimethylaminophenol for acute cyanide poisoning. These two drugs can convert hemoglobin to methemoglobin, which binds avidly with cyanide thus release cytochrome c oxidase.[225] These antidotes usually take effects rapidly, which makes them valuable for treating acute cyanide poisoning. However, since methemoglobin cannot carry oxygen and has to be converted back to hemoglobin with additional treatments, these drugs are not suitable to use as preventive measurements for chronic cyanide exposure.

Rhodanese (Rh, EC 2.8.1.1) is one of the sulfurtransferases related to the biotransformation of cyanide to the less toxic thiocyanate in the presence of a sulfur donor. Initial attempts with direct administration of free Rh and sulfur donors were mostly failed due to the fast clearance of the enzyme by the body's immune system.[19,21,226] The first effort to overcome this limitation was achieved by loading Rh and sodium thiosulfate into mouse erythrocytes, resulting the increase in the protection against the lethal effects of cyanide by approximately two-fold in mice.[77] However, the necessary prior blood typing rendered the erythrocyte carriers less useful for detoxification

purposes. In order to address this problem, liposomal encapsulated Rh systems were developed as more practical cyanide antidotes.[75] In one study, mice administrated with a liposomal encapsulated DTO-rhodanese-thiosulfate antidotal systems achieved 100% survival rate against 20 mg/kg cyanide, and maximum antidotal protection against cyanide intoxication could reach 15x LD_{50}.[76] Considering the necessity of sulfur donor, further development of Rh-based cyanide antidotes should choose carriers that are capable of co-delivery of Rh and sulfur donor molecules together. Particularly to Rh-based cyanide antidotes, liposome is still the preferred carriers, because most sulfur donors are small molecules and liposome is capable to co-encapsulate enzymes as well as small molecules.

1.5.2.2 Organophosphate (OP) poisoning

OP compounds are acetylcholinesterase (AChE) inhibitors and exert their toxicity by causing an excessive accumulation of the neurotransmitter, acetylcholine, and subsequent disruption of cholinergic nervous transmission. Formerly developed as chemical warfare agents, OP compounds are now widely used as pesticides and insecticides. Unfortunately, many of them are still exceedingly toxic, which may cause acute intoxication or even lethality if exposure without protection. Phosphotriesterases, which are divided as aryldialkylphosphatase (EC 3.8.1.1) and diisopropylfluorophosphatase (DFPase, EC 3.8.1.2) by the hydrolyzed bond types, are a family of enzymes that are highly efficient in hydrolysis of certain OP compounds. Back in 1957, Cohen and Warringa have attempted to use these exogenous enzymes in OP antagonism.[20] However, the severe immunogenic reactions rendered these enzymes ineffective when injecting in the form of purified free enzymes.

This problem is partially addressed by the development of nanocarrier systems. Pei *et al.* firstly confirmed that the paraoxon (an OP-based pesticide) could diffuse across the erythrocyte membrane and the encapsulated phosphotriesterases were still capable to hydrolyze paraoxon rapidly. [85,86] As an artificial replacement of erythrocytes, liposomal carriers were also employed for the delivery of phosphotriesterases. Several different phosphotriesterases, including OPAA,[80] OPH, [81,83] and paraoxonase-1 (PON1),[84] were stabilized by liposomal encapsulation, resulting in extended circulating half-life and enhanced protection against the lethal effect of paraoxon. However, several reports indicated that the activity of encapsulated enzymes appeared a first order kinetics, suggesting that the diffusion limitation of OP compounds caused by the liposome may weaken the detoxification effects of these enzymes.

To overcome the diffusion limitation, another class of carriers based on biocompatible polymers was applied to the construction of OP antidotes. By conjugating OPH with branched PEG, significant reduction of anti-OPH antibody was observed compared to the direct administration of free OPH *in vivo*.[79] Other branched or dendritic polymers, including branched poly(ethylene imine)[227] and dendritic polyoxazoline,[78,87] were also employed to stabilize the OPH, OPAA and DFPase. Compared to the traditional detoxification method using pralidoxime and atropine (60x LD$_{50}$), OPH/dendrimer complex showed a more dramatic protection (780x LD$_{50}$) against paraoxon intoxication in mice,[87] leading to a more effective OP antidote approach to combat soldiers and agricultural workers.

Recently, various nanocarriers have been developed to enhance OPH stability thus increase its detoxifying efficiency. By assembly with Pluronic F127 micelles, OPH could survival from the

thermal denaturation at 70°C, allowing manufacture of such formulation under flexible conditions.[88] Our group also have explored the potential of OPH in OP-detoxification by enhancing it with the single-protein encapsulation method.[89] Significant stability enhancement was observed from the OPH nanocapsules, which is capable to retain its enzymatic activity after repetitive freeze-thaw and long-term thermal denaturation. More importantly, the OPH nanocapsules could effectively decompose OP compounds in present of high concentration of proteases, which ensures them function normally after administrating into animal circulation. Animal studies revealed that the OPH nanocapsules represented stronger protective effects than native OPH against paraoxon intoxication in mice, indicating the potential of OPH nanocapsules as an effective antidote and preventive measurements for chronic OP exposure.

1.5.3 Other enzyme therapeutics for circulatory system diseases

1.5.3.1 L-Asparaginase and arginase based therapeutics

L-Asparaginase (EC 3.5.1.1) is an enzyme that catalyzes the hydrolysis of asparagine to aspartic acid. Since the first successful demonstration of lymphomas growth inhibition by administration of the enzyme in guinea pigs,[228] L-asparaginase has become an important agent in the therapy of acute lymphoblastic leukemia (ALL). In order to minimize its adverse effects like allergic or hypersensitivity reaction, various strategies have been developed for the delivery of L-asparaginase. Initial attempts mainly focused on extending the blood circulation time by encapsulating the enzyme with erythrocytes[105–107] and liposomes.[102–104,108] It was reported that the encapsulation could preserve most of the activity of asparaginase, as well as enhance its stability in the serum.[102] *In vivo* studies confirmed that the encapsulation of asparaginase with erythrocytes[105] and liposomes[104] could prolong the blood circulation time significantly, resulting in obvious therapeutic effects in the treatment of ALL.[229] A recent report showed an up to 44% improvement in survival rate by the

33

administration of RBC-encapsulated asparaginase, when challenging the mice with lymphoma cells.[108]

Several other methods such as conjugation with poly(d,l-lactide-co-glycolide) nanospheres[109] and immobilization on agarose beads[230] also showed improvement in the pharmacokinetics of asparaginase. However, such technologies are still in early stage and their preparations are less practical compared to that of PEGylated asparaginase (pegaspargase). Pegaspargase was invented to overcome the obvious hypersensitivity reactions in the direct use of asparaginase *in vivo*. This modification was shown in animal models to reduce antibody formation compared to native L-asparaginase and to markedly extend the effective period of the drugs.[96,97] Initial clinical trials showed that the pegaspargase achieved a mean half-life of 357 h, which is 10x longer than the native L-asparaginase.[231] Despite the adverse responses observed in patients with high dose,[99] pegaspargase maintained an effective plasma concentration of >100 units/l for over one week with a low dose of 500 units/m^2.[100] Further clinical studies indicated that pegaspargase represented comparable therapeutic effects to free L-asparaginase expressed with *E coli.* in the treatment of ALL, but with less hypersensitivity reactions.[101] Additionally, the long blood circulating half-life of pegaspargase allowed significantly less frequency of drug administration, which is obviously more convenient than the repetitive injection required by the native enzyme therapy. In 2006, US FDA granted approval to pegaspargase (Oncaspar®, Enzon Pharmaceuticals, Inc.) for the first-line treatment of patients with ALL as a component of a multi-agent chemotherapy regimen.[95]

Arginase (EC 3.5.3.1), which is an enzyme that catalyzes the hydrolysis of arginine to ornithine, represents therapeutic effects in inhibiting the proliferation of arginine-requiring cancers like T-cell acute lymphoblastic leukemia (T-ALL). For an effectively enzymatic depletion of arginine *in*

vivo, arginase requires a carrier to allow it staying long enough in the blood circulation. By administrating the arginase conjugated with soluble dextran, Sherwood *et al.* achieved 9 times longer blood circulating half-life and significantly lower blood arginine concentration compared to the mice administrated with native arginase.[111] Recent studies indicated that the anti-T-ALL effects could be induced by the administration of PEG-arginase, suggesting a safe and effective therapeutic for T-ALL treatments.[12,110]

1.5.3.2 Plasminogen activators based therapeutics

A blood clot (thrombus) developed in the circulatory system can cause vascular blockage leading to serious consequences including death. Clinical intervention consisting of intravenous administration of thrombolytic agents is needed to control the development of clot. Plasminogen activators are serine proteases which convert plasminogen to plasmin, thus promoting thrombolysis or fibrinolysis. There are two plasminogen activators occurred naturally in blood, including tissue-type plasminogen activator (tPA) and urokinase (uPA or UK), which are already used in clinical intervention. However, their circulation behavior is poor ($t_{1/2}$ is around several minutes) partially due to the enzyme degradation. To enhance their therapeutic effects, one major type of approach was achieved by conjugating tPA or UK with PEG-based polymers. For instance, conjugating UK with PEG (Mw=5000) extended its plasma half-life to 6 hours in beagle, resulting a strong activation of fibrinolysis.[112] Further studies confirmed the modification with PEG-based polymers could enhance the stability of UK against proteolysis without altering its original biological functions.[113,114] Similar effects were also observed in PEG-conjugated tPA, with the extension of half-life from 5 min (native tPA) to 60 min (PEG-tPA).[115] However, systemic infusion of UK or tPA increases the risk of bleeding complications significantly. Thus, carriers that are capable of responsive release were designed to overcome this problem. By incorporating the enzymes with

nanogel, UK and tPA could be released under external ultrasonic stimulation and enzyme degradation respectively, allowing them only functioning at desired location.[232,233]

Streptokinase (SK) is a microbial sourced enzyme that can also bind and activate human plasminogen to induce fibrinolysis. Compared with UK and tPA, streptokinase is the least expensive but immunogenic. Since UK and tPA are short-lived *in vivo*, comparative clinical trials and cost-effectiveness considerations suggest that streptokinase is the drug of choice for thrombolytic therapy.[234,235] Due to its intrinsic problems, researches of SK mainly focused on reducing its antigenicity and prolonging its blood circulation. After conjugating with PEG, SK could still retain its protease activity, but its binding ability with serum proteins disappeared, suggesting that PEG-SK could be less antigenic than its native form.[116] Further investigation of PEG-SK in animal studies confirmed that the antigenicity could be largely reduced after PEGylation, which also endowed SK with significantly prolonged circulation half-life.[117,118] Additionally, liposomal carriers have also been developed to deliver SK. In one study, using PEG-liposomal SK achieved 16-fold longer blood circulating half-life than direct use of native SK in rats.[119] With continuous efforts in elimination of the antigenicity, extension of the circulation time, and improvement of the plasminogen activation, SK could become an ideal thrombolytic agent for the treatment against blood clotting.

1.6 Summary

In a biochemical perspective, disease describes an abnormal state, in which certain proteins are dysfunction, resulting in the activation of undesired biochemical process or normal processes are disrupted. This can be corrected by direct delivery of a protein that functions correctly to replace malfunctioning ones, or delivery of a protein that can rapidly remove of the toxic substances, in order to restore normal biochemical processes. Proteins with high specificity and efficiency are

therefore the most effective therapeutic agents. Through constructing suitable protein delivery system, various protein therapeutics can be rapidly developed to treat many diseases, including chronical diseases, inherited diseases, and cancers.

Towards the development of an effective protein therapeutics, several issues have not yet been resolved properly, which hamper the wide application of therapeutic protein in clinic drastically. For intracellular protein delivery, a general and effective delivery platform is still needed for the intracellular delivery of various proteins and transcription factors into different host cells. A platform that is capable of delivery of multiple proteins intracellularly is also highly demanded in the field of stem cell reprogramming and regenerative medicine. For systemic protein delivery, enhanced plasma stability and reduced immunogenicity are still two of the essential aspects for a successful protein delivery. Although PEG has set a golden standard for enzyme delivery, an increasing population of people has developed or will develop (after the first administration) anti-PEG antibodies, which results in a rapid clearance of PEGylated therapeutics. New shielding materials are needed to achieve the similar therapeutic effects without the activation of antibody genesis. Similar to many metabolic processes, detoxification may require synergistic actions of multiple enzymes. Although liposome and polymer encapsulation have shown certain merit to build multiple enzyme system in defined space, confining synergistic enzymes in a single nanostructure with precise control in the types, ratios and positions of enzymes remains challenging. Targeting delivery has been the ultimate goal for the broad field of nanomedicine. Since toxicants may not evenly distribute among the tissues and organs, targeting capability could lead to better detoxification performance and fewer side effects. Despite more targeting sites being discovered, targeted nanocarriers are still far from clinical applications. Fundamental studies are required to better

understand the highly complicated behaviors of the therapeutics or detoxification agents after systemic administration, which may provide insight towards the design of nanocarriers with targeting ability.

My Ph.D. research projects mainly focused on addressing the challenges that are described above in protein delivery. Specifically, my research tried to overcome four common issues existed in both intracellular protein delivery and systemic protein delivery through the design of novel delivery systems based on protein nanocapsule technology. In this thesis, the researches on following aspects are discussed in detail accordingly.

- Design and synthesis of protein nanocapsules that can deliver multiple proteins and ensure them function synergistically. (Chapter 2)

- Design a non-fouling protein nanocapsule that can prolong the plasma half-life and reduce immunogenicity of any protein. (Chapter 3)

- Intracellular delivery of sensitive proteins without changing their original structures or compromising their biological activities. (Chapter 4)

- Design a general platform that can synthesize and screen vectors that deliver multiple proteins intracellularly with high efficiency. (Chapter 5)

Chapter 2. Biomimetic enzyme nanocomplexes and their use as antidotes and preventive measures for alcohol intoxication

2.1 Introduction

Enzymes are exquisite biocatalysts mediating every biological process in living organisms. In eukaryotic cells, most enzymes do not freely diffuse within the cytosols, but are spatially defined within subcellular organelles or closely co-localized as enzyme complexes along with other enzymes.[236–238] In consecutive reactions catalysed by multiple enzymes, such close confinement minimizes the diffusion of intermediates among the enzymes, enhancing overall reaction efficiency and specificity.[239–243] Meanwhile, toxic intermediates generated during a metabolic process are promptly eliminated by the proximate enzymes co-localized within the confined structures.[244,245] Peroxisome, as an example, harbours a variety of oxidases with important metabolic and catabolic functions.[246,247] Toxic intermediates, such as hydrogen peroxide (H_2O_2), are also produced during the enzymatic reactions in peroxisome; nature circumvents this dilemma by incorporating catalase (Cat) within the peroxisomes. Catalase is highly active and specific in decomposing H_2O_2, preventing its escape from the peroxisomes and subsequent damage to other cellular components.[248]

Inspired by the natural multi-enzyme architectures, researchers have long been devoted to constructing enzyme complexes with synergic and complimentary functions, which is mainly based on co-entrapment, co-immobilization, template assembly or fusion-protein techniques. The former two approaches enable co-entrapment or co-immobilization of multiple enzymes within liposomes or solid particles.[249,250] However, it is difficult to control the number, type, and spatial arrangement of the enzymes within the liposomes and particles. The latter two approaches enable

the formation of enzyme complexes with significantly improved compositional and spatial controls but still with limitations, such as inadequate translational capability of the host cells and insufficient enzyme stability against proteolysis and non-physiological environments.[251]

In this chapter, we demonstrate a general design of robust enzyme nanocomplexes with well-controlled enzyme composition and spatial arrangement. This is achieved by assembling or conjugating enzymes with synergic or complementary functions to form a nanocomplex, followed by encapsulating the nanocomplex within a crosslinked polymer nanocapsule. Exemplified by the synthesis of a triple-enzyme nanocomplex (Figure 2-1), inhibitors for each enzyme are respectively conjugated to a single-strand DNA with designed sequence; complementary assembly of the DNA molecules forms a DNA-inhibitor scaffold linked with the three inhibitors; specific binding of the inhibitors and the enzymes enables the construction of a triple-enzyme nanocomplexes (Step **I**). Subsequent *in-situ* polymerization grows a thin layer of polymer network around each nanocomplex, leading to the formation of nanocapsules containing a triple-enzyme core and a permeable shell (Step **II**). Finally, removal of the DNA-inhibitor scaffolds creates highly robust enzyme nanocomplexes denoted as **n(Enzymes),** where **Enzymes** within the parentheses refer to the enzymes within the core of the nanocapsules (Step **III**). It is important to point out that, without a significant compromise of the enzyme activity, encapsulating the enzymes within the nanocapsules effectively stabilizes them in non-physiological environment and against protease attack. Furthermore, the nanocomplexes can be readily functionalized to acquire desired surface properties and targeting capability.
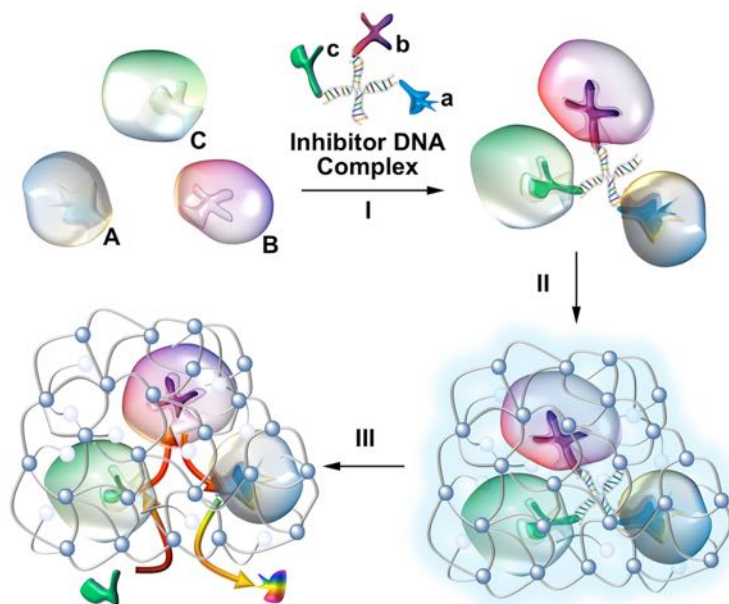
*Figure 2-1 **Synthesis of Enzyme Nanocomplexes.** Schematic illustration of a synthesis of a model triple-enzyme nanocomplex by DNA-directed assembly and nano-encapsulation. **I,** Spontaneous assembly of (A) invertase (Inv), (B) glucose oxidase (GOx), and (C) horseradish peroxidase (HRP) with an inhibitor-DNA scaffold containing their respective competitive inhibitors: (a) lactobionic acid, (b) glucosamine, and (c) 4-dimethylaminoantipyrine leading to the formation of a triple-enzyme architecture. **II,** Confinement and stabilization of the triple-enzyme architecture by in-situ growth of a thin network polymer around the enzyme nanocomplex. **III,** Removal of the DNA scaffold leading to the formation of triple-enzyme nanocomplexes with significantly enhanced stability and close-proximity definition. Such a close-proximity architecture enables active transport of their reaction intermediates among the enzymes, leading to significantly enhanced reaction efficiency and complementary function such as the capability to eliminate toxic intermediates.*

2.2 Methods, experiments, and characterizations

2.2.1 Materials and Instruments

Reagents and solvents were purchased from Sigma-Aldrich (St. Louis, MO) and used as received without further purification unless otherwise noted. HeLa cells were purchased from American Type Culture Collection (ATCC). The Dulbecco's Modified Eagle Medium (DMEM) growth medium and Penicillin/streptomycin were obtained from Invitrogen (Carlsbad, CA). Fetal Bovine

Serum (FBS) was obtained from Lonza Walkerrsville Inc. (Walkerrsville, MD). CellTitra Blue cell viability kit was purchased from Promega (Madison, WI). Mono-sulfo-N-hydroxy-succinimido Au-nanoparticles was purchased from NanoProbe, NY. Fluorescence dyes including Rhodamine B isothiocyanate and Fluorescein isothiocyanate were obtained from Sigma-Aldrich (St. Louis, MO). Enzymes including horseradish peroxidase, glucose oxidase, invertase, catalase and alcohol oxidase were purchased from Sigma-Aldrich (St. Louis, MO). Male C57B6 mice were purchased from Jackson Laboratory (Bar Harbor, ME). Alcohol liquid diet AIN76A was obtained from Dyets, Inc. Ethanol Assay Kit was purchased from BioVision (Mountain View, CA) or from Analox Instruments (IL, USA). H&E and fluorescent TUNEL staining kits were purchased from Roche. 1,2-distearoyl-sn-glycero-3-phosphoethanolamine-N-[methoxy(polyethylene glycol)-2000] (ammonium salt) (PEG2000-DSPE) and L-α-phosphatidylcholine, hydrogenated (Soy) (HSPC) were obtained from Avanti Polar Lipids (Alabaster, AL), and cholesterol was purchased from Sigma-Aldrich. Acrylic acid, N-hydroxylsuccinimide ester, acrylamide, N,N'-methylenebisacrylamide, ammonium persulfate, and N,N,N',N'-tetramethylethylenediamine were purchased from Sigma-Aldrich and used without further purification. Sepharose-6B, Superdex-75 and Sephadex G-25 were purchased from Sigma-Aldrich. Single strand DNAs (ssDNAs) were purchased from Sigma-Aldrich with sequences described below.

Table 2-1 Sequences of DNA oligomers for the construction of DNA-enzyme complex

Name	Sequence
ssDNA-1	5'-*[Phos]*ATACGAATTCTAC-3'
ssDNA-1'	5'-*[ThiC6]*ATACGAATTCTAC-3'
ssDNA-2	5'-*[Phos]*AGTAGAATTCGTA-3'
ssDNA-2'	5'-*[ThiC6]*AGTAGAATTCGTA-3'
ssDNA-I	5'-*[Phos]*ATGGTTGAGGAAGTC-3'

ssDNA-II	5'-*[Phos]*AGACTTCCGCTATCG-3'
ssDNA-III	5'-*[AmC6T]*ACGATAGCATGTGTA-3'
ssDNA-IV	5'-ATACACATTCAACCA-3'

UV-Visible spectra were acquired with a GeneSys 6 spectrometer (Thermo Scientific). Fluorescence spectra were obtained with a QuantaMaster Spectrofluorimeter (Photon Technology International). Dynamic light scattering (DLS) studies of the enzyme nanocomplexes was measured on Zetasizer Nano instrument (Malvern Instruments Ltd., United Kingdom) equipped with a 10 mW helium-neon laser (λ = 632.8 nm) and thermoelectric temperature controller. Transmission electron microscope (TEM) images were obtained on Philips CM120 electron microscope operating with an acceleration voltage of 120 kV. Fluorescence intensities were measured with a Fujifilm BAS-5000 plate reader. Mass spectra were acquired with an Applied Biosystem Voyager-DE-STR MALDI-TOF mass spectrometer. Tissue sections were observed and photographed with a Nikon TE2000S inverted fluorescent microscope.

2.2.2 Preparation of enzyme nanocomplexes (ENs) and nanocapsules

2.2.2.1 Synthesis of DNA-inhibitor scaffolds

The syntheses of DNA-inhibitor scaffolds were achieved by combining the conjugation and self-assembly technologies. Briefly, single strand DNAs were first conjugated with reversible enzyme inhibitors or substrate derivatives to afford various single-strand-DNA-derived enzyme inhibitors (ssDNA inhibitors). After the conjugation, different ssDNA inhibitors were mixed and heated to 37°C for 10 min. After cooling to room temperature, ssDNA-inhibitors spontaneously assembled with their complementary strand(s), forming the DNA-inhibitor scaffolds.

As illustrated in Figure 2-2, 13 mg of 1-ethyl-3-(3-dimethylaminopropyl)carbodiimide hydrochloride) (EDAC) was firstly added into a micro-centrifuge tube; then 75 uL of ssDNA solution that

contains 150 nmol 5' phosphate ssDNA or 5' amine modified ssDNA was added. Then 50 uL of

0.2 M inhibitor compound (4-aminoantipyrine, Figure 2-2a; glucosamine, Figure 2-2b; or lactobi-

onic acid, Figure 2-2c), which was dissolved in 0.1 M imidazole (pH 6.0), was added into the

ssDNA-EDAC solution immediately. The solution was then mixed by vortexing and centrifuged

at 10,000 rpm for 5 min. After further conjugation reactions at room temperature for 30 min,

ssDNA inhibitors were purified by the gel filtration technique on desalting resin (Sephadex G-25,

Sigma-Aldrich, St. Louis, MO) using a solution containing 10 mM sodium phosphate, 0.15 M

NaCl and 10 mM EDTA at pH 7. Using this general protocol, ssDNA inhibitors for horseradish

peroxidase (HRP), glucose oxidase (GOx) and Invertase (Inv) was synthesized as illustrated in

Figure S1a, b, and c, respectively.
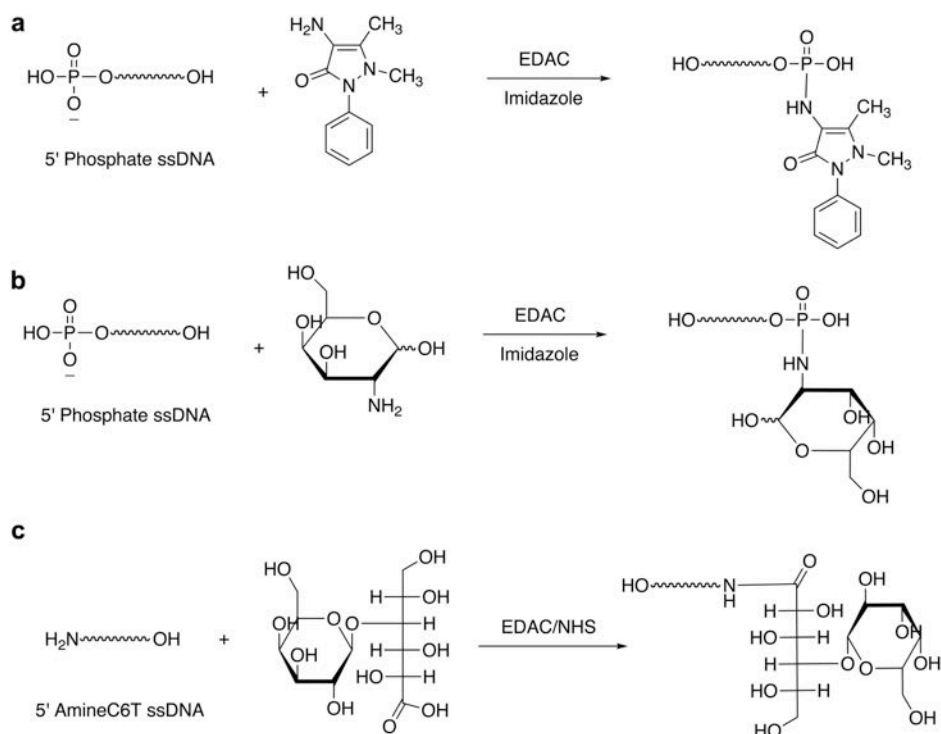
*Figure 2-2 Schematic illustration of the syntheses of ssDNA inhibitors for HRP (**a**), GOx (**b**), and Inv (**c**).*

2.2.2.2 MALDI-TOF characterizations of ssDNA-inhibitors

Successful conjugation of ssDNA-inhibitors was demonstrated by monitoring their molecular weight increase via MALDI-TOF spectra. Ultrapure 3-hydroxypicolinic acid (3-HPA) was used as matrix for the following measurements. Unconjugated ssDNAs were used as controls for MALDI-TOF characterizations. Resulted spectra of ssDNA before (black) and after (red) conjugating with enzyme inhibitors were shown in Figure 2-3.
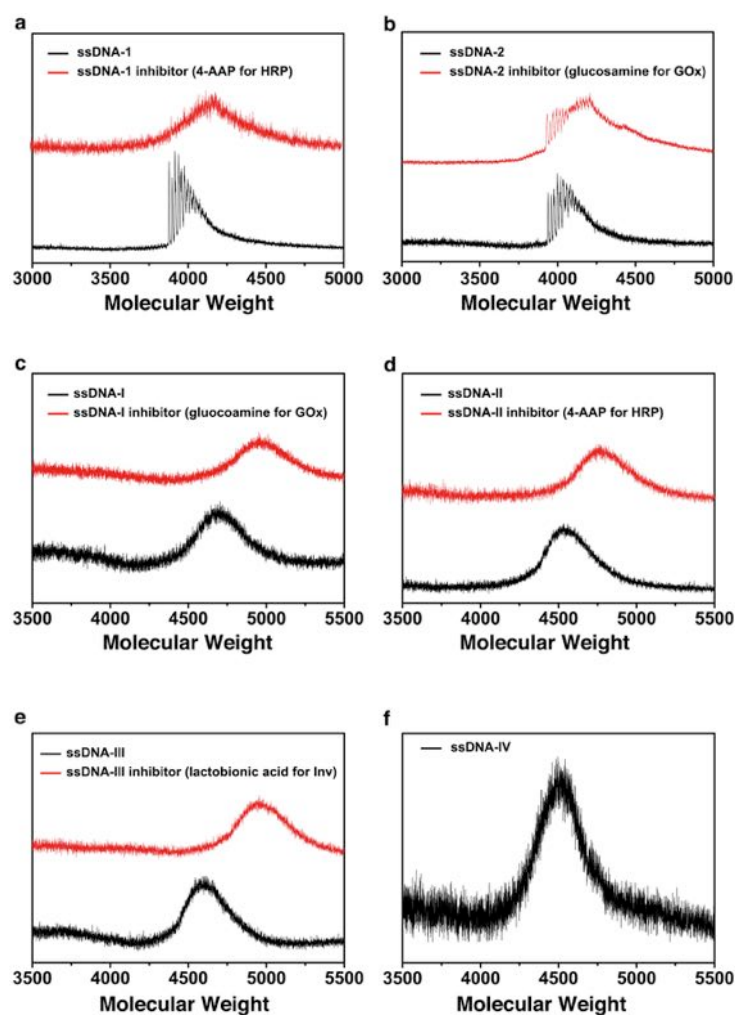
Figure 2-3 MALDI-TOF mass spectra of DNAs before (black) and after (red) 5'-modification with inhibitors. *(a)* *ssDNA-1 and 4-Aminoantipyrine (4-AAP) modified ssDNA-1.* *(b)* *ssDNA-2 and glucosamine modified ssDNA-2.* *(c)* *ssDNA-I and glucosamine modified ssDNA-I.* *(d)* *ssDNA-II and 4-AAP modified ssDNA-II.* *(e)* *ssDNA-III and lactobionic acid modified ssDNA-III.* *(f)* *ssDNA-IV. As shown in the mass spectra (a-*

*e), the molecular weights of ssDNAs increased after conjugating with enzyme inhibitors. Moreover, the increases between conjugated ssDNAs and their native counterparts are accordant with the molecular weights of corresponding enzyme inhibitors, respectively. (**a.** $\Delta Mw_{ssDNA-I} \approx 200$, $Mw_{4-AAP} = 203.4$; **b.** $\Delta Mw_{ssDNA-2} \approx 210$, $Mw_{gulcosamine} = 180.1$; **c.** $\Delta Mw_{ssDNA-I} \approx 200$, $Mw_{glucosamine} = 180.1$; **d.** $\Delta Mw_{ssDNA-II} \approx 250$, $Mw_{4-AAP} = 203.4$; **e.** $\Delta Mw_{ssDNA-III} \approx 400$, $Mw_{lactobionic\ acid} = 358.3$)*

2.2.2.3 Acryloxylation of enzymes

Before polymerization, enzymes were first conjugated with N-acryloxysuccinimide (NAS) to attach acryloyl groups onto their surfaces. A typical procedure for the conjugation is described as follow. Enzyme (~ 10 mg/mL) was first dialyzed against sodium carbonate buffer (20 mM, pH 8.5) to remove any ammonium sulfate that usually exists in enzyme powder. After dialysis, enzyme solution was diluted to 5 mg/mL with sodium carbonate buffer (20 mM, pH 8.5), followed by adding NAS solution (10% in DMSO, m/v) to perform the conjugation. The amount of NAS used is at 20:1 molar ratio (NAS to protein), and the conjugation is achieved by keeping the reaction at 4°C for 1 h. The solution was then thoroughly dialyzed against pH 7.0 phosphate buffer (20 mM) with a dialysis tubing membrane (MWCO = 10 kDa, Sigma-Aldrich) to remove any unreacted NAS. Acryloylated enzyme solutions were store at 4°C for further uses.

The average number of acryloyl groups conjugated onto the enzymes was determined by measuring the residual (unreacted) lysine on the enzyme molecule with a fluoresamine assay. Briefly, fluoresamine was first dissolved in anhydrous DMSO to make a 3 mg/mL stock solution. Native enzyme and its acryloylated counterpart were prepared as 1 mg/mL solutions with 0.1 M phosphate buffer (pH = 7.0), respectively. The native and the acryloylated enzymes were then diluted with 0.1 M phosphate buffer (pH = 7) to make a series of solutions with concentrations 0.00781, 0.01563, 0.03125, 0.0625, 0.125, 0.25, 0.5, and 1 mg/mL; pipette 100 μL of each solution to an

opaque 96-well plate, respectively. 30 µL of the fluoresamine solution was then added into each well; the plate was then incubated for 1 h at room temperature (25°C). After the incubation, fluorescence intensity (Ex = 360 nm, Em = 465 nm) was read with a plate reader. The number of residual lysine was then estimated by comparing the fluorescent intensity of the acryloylated and the native enzymes. The number of acryloyl groups conjugated onto the enzymes is listed in Table 2-2.

Table 2-2 Average number of acryloyl groups conjugated to the enzymes

Enzyme	Total No. of Lys	Unreacted Lys (%)	Average No. of acryloyl groups conjugated
HRP	5	0%	5.0
GOx	15	2.7%	14.6
Invertase	26	29.6%	18.3
AOx	38	70.7%	11.6
Catalase	28	40%	16.8

2.2.2.4 Synthesis of multiple-enzyme nanocomplexes

Enzymes (HRP, GOx and Inv) were acryloxylated respectively by reacting with N-acryloxysuccinimide (NAS). The conjugation was achieved by adding NAS (10% in DMSO) to the enzyme solution (5 mg/mL, pH 8.5, 20 mM sodium carbonate buffer) at 20:1 molar ratio (NAS to protein) and reacting for 1 h at 4°C. The solution was then thoroughly dialyzed against pH 7.0 phosphate buffer (20 mM) with a dialysis tubing membrane (MWCO = 10 kDa, Sigma-Aldrich). Then equal moles of the acryloxylated enzymes were mixed with the corresponding DNA inhibitors and incubated at room temperature for 30 min. During this process, DNA-inhibitors and enzymes self-assemble and form the DNA-enzyme complexes as illustrated in Figure 2-4.

For the polymerization step, acrylamide (AAm) and bis-methacrylamide (BIS) were first prepared as 10% (w/v) stock solution in DI-water and anhydrous DMSO, respectively; then were added into the solution containing DNA-enzymes complex (AAm/protein, 6000:1, n/n; BIS/protein, 1000:1, n/n). The final enzyme concentration was tuned to 1 mg/mL by diluting with phosphate buffer (50mM, pH 7.0). Polymerization was initiated by the addition of ammonium persulfate (APS/protein, 500:1, n/n) and tetramethylethylenediamine (TEMED/APS, 2:1, w/w) and kept at room temperature for 2 h. After the polymerization, the solution was dialyzed against PBS to remove unreacted monomers and by-products.

After dialysis, the sample solution was then heated to 37°C for 10 min, and purified using a size exclusion chromatography (Sepharose-6B) to remove DNA-inhibitors or un-encapsulated enzymes. The purification with size exclusion chromatography was achieved by passing sample through a Sepharose-6B column by gravity. Sepharose column was prepared by pipette 5 mL of Sepharose 6B beads into a glass column. Before pipetting, Sepharose bottle was shaken gently to spread the beads evenly throughout the solution. The column was then pre-equilibrated with phosphate-buffered saline (PBS). After equilibration, sample was loaded in the column, and then eluted with PBS. Because the fractionation range of Sepharose-6B is 10,000-4,000,000 Da, encapsulated proteins (nProtein) are too big to enter the pores of Sepharose beads, as a result, eluted first during the elution. Eluted solution was collected in a volume of 100 μL per fraction, and the absorbance at 280 nm of each fraction was measured with a UV/Vis meter by using elution buffer (PBS) as background. Figure 2-5 shows the elution curve of n(HRP-GOx), which is a typical elution curve of protein nanocapsules/nanocomplexes. Fractions of encapsulated proteins were collected, combined, and then condensed using centrifugal filtration. Protein nanocomplexes solution was stored at 4°C for further studies.
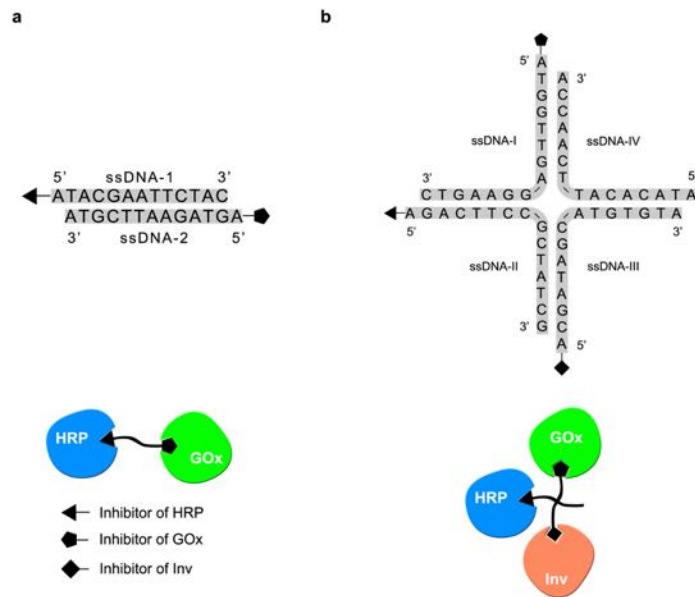
Figure 2-4 DNA-inhibitor scaffolds and DNA-enzymes complex for the syntheses of n(HRP-GOx) (**a**) *and n(HRP-GOx-Inv)* (**b**).
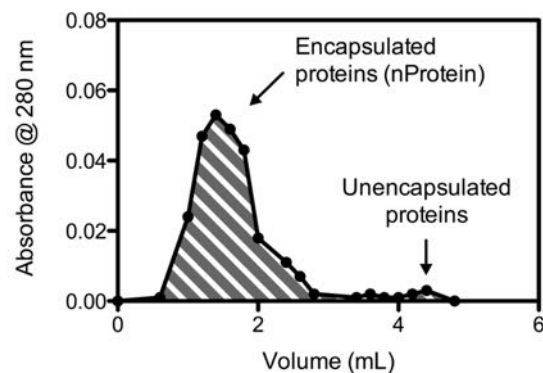
Figure 2-5 Elution curve of n(HRP-GOx)

2.2.2.5 Synthesis of dual fluorescence-labeled n(HRP-RhB-GOx-FITC)

Rhodamine-B-labeled horseradish peroxidase (HRP-RhB) and fluorescein isothiocyanate-labeled glucose oxidase (GOx-FITC) were prepared by following the protocol provided by the manufacturer of fluorescence dyes. Fluorescent dyes, RhB and FITC, were first dissolved in anhydrous DMSO to get 10 mg/mL stock solution, respectively. Then 50 µL of dye solutions were added

gradually into 2 mL enzyme solutions (10 mg protein/mL, pH=8.2, sodium carbonate, 100 mM). The reactions were carried out overnight at 4°C. Labeled proteins were then dialyzed against phosphate buffer (20 mM, pH = 7), condensed by centrifugal filtration (MWCO = 10 kDa) and stored at 4°C for further use. The concentration and dye/protein ratio (D/P) of HRP-RhB and GOx-FITC were determined by the extinction coefficients of 102,000 $M^{-1}cm^{-1}$ at 403 nm (HRP), 44,100 $M^{-1}cm^{-1}$ at 280 nm (GOx) and 108,000 $M^{-1}cm^{-1}$ at 555 nm (RhB), 81,000 $M^{-1}cm^{-1}$ at 495 nm (FITC).

Enzyme nanocomplex n(HRP-RhB-GOx-FITC) was prepared from HRP-RhB, GOx-FITC and HRP/GOx DNA-inhibitor scaffold using the procedure similar to that for the synthesis of n(HRP-GOx). After the preparation, such dual fluorescence-labeled ENs were further purified by gel filtration (Sepharose-6B). The first band, which has a strong absorbance at 555 nm, was collected, condensed and stored at 4°C for fluorescence characterizations.

2.2.2.6 Synthesis of Au-nanoparticle labeled ENs

Excess amounts of Au-nanoparticles (mono-sulfo-N-hydroxy-succinimido Au-nanoparticles) were reacted with native HRP and GOx (3:1, n/n, Au/enzyme) in 1xPBS buffer for 1 hr, respectively. The excess gold nanoparticles was then removed by gel filtration (Superdex-75). Concentrations of the Au-nanoparticles, HRP and GOx were then determined by the UV/vis spectra based on their molar extinction coefficients (nanogold, 155,000 $M^{-1}cm^{-1}$ at 420 nm, HRP, 102,000 $M^{-1}cm^{-1}$ at 403 nm, GOx, 11,200 $M^{-1}cm^{-1}$ at 453 nm). The resulted Au-labeled HRP/GOx MCENs contain an AuNP/HRP ratio of 0.83 and AuNP/GOx ratio of 0.95. The Au-labeled HRP and GOx were then used to prepare dual AuNP labeled ENs by using the same protocol for the preparation of n(HRP-GOx). After the preparation, the sample was purified by size exclusion chromatography

(Sepharose-6B). The first colored band having absorbance at 420 nm was collected and stored at 4°C for the transmission electron microscopy (TEM) observation.

2.2.2.7 Synthesis of ssDNA-alcohol oxidase (ssDNA-AOx) and ssDNA-Catalase (ssDNA-Cat) conjugates

Alcohol oxidase (AOx) and catalase (Cat) were dissolved in 50 mM sodium phosphate buffer (pH=7.4, 0.15 M NaCl) with a concentration of 2 mg/mL, respectively. N-succinimidyl 3-(2-pyridyldithio) propionate (SPDP) stock solution was first prepared as a 2 mM DMSO solution, followed by reacting with enzymes by gradual addition of 25 µL of SPDP solution into 1 mL enzyme solutions. The reaction was kept at 4°C under stirring for 4 h. After the reaction, SPDP-modified enzymes were purified by gel filtration (Superdex-75) using 50 mM sodium phosphate, 0.15 M NaCl, 10 mM EDTA, pH 7.2 as eluting buffer. In the meanwhile, ssDNA-1' and ssDNA-2' were reduced with dithiothreitol (DTT) and purified by gel filtration (Superdex-75) immediately. After the purification, reduced ssDNA-1' and ssDNA-2' were then added into SPDP-activated Cat and AOx solutions at a molar ratio of 1.2/1 (ssDNA to enzyme), respectively. The mixture was kept at 4°C overnight for a complete conjugation, and then add NAS (NAS/protein, 20:1, n/n) into the mixture to anchor acryloxyl groups to the ssDNA-enzyme conjugates. The samples were then purified by dialysis against 1xPBS with a dialysis tubing membrane (MWCO ~ 10 kDa).

2.2.2.8 Synthesis of n(GOx-Cat) and n(AOx-Cat)

ssDNA-2-glucosamine (ssDNA inhibitor for GOx) was first mixed with equal amount of acryloxylated ssDNA-1' conjugated Cat and acryloxylated GOx (1:1:1, n/n/n). The mixture was heated to 37°C for 10 min and then cooled down with an ice bath. After recovering to room temperature, the enzyme complex solution was first diluted to 1 mg/mL protein with phosphate buffer (50 mM,

pH=7.0). AAm (6000:1, n/n, acrylamide/protein) and BIS (1000:1, n/n, BIS/protein) were then added into the reaction solution. *In-situ* polymerization was initiated by the addition of APS (500:1, n/n, APS/protein) and TEMED (2:1, w/w, TEMED/APS). After dialysis against 1xPBS, the sample was heated to 37°C for 10 min and immediately passed through a size exclusion column (Sepharose 6B). The first eluted band having absorbance at 280 nm was collected and condensed to get a stock solution of n(GOx-Cat), which was kept at 4°C for further use.

The preparation of n(AOx-Cat) is similar to that of n(GOx-Cat) mentioned above. Equal amount (1:1, n/n) of acryloxylated ssDNA-1' conjugated Cat and ssDNA-2' conjugated AOx was mixed together and tuned to a concentration of 1 mg/mL protein with phosphate buffer (50 mM, pH=7.0). Polymerization was then performed using the same procedure used to make n(GOx-Cat). After the polymerization, the reaction mixture was passed through a size exclusion column (Sepharose 6B) to remove unreacted monomers and by-products. n(AOx-Cat) was then condensed and aliquoted to 100μL/tube for *in-vitro* and *in-vivo* tests.

Note that n(AOx-Cat) can also be prepared by directly conjugating the two enzymes. Native AOx and Cat were first desalted by dialysis thoroughly against phosphate buffer (0.1M, pH 7.0), following by diluting to 2 mg/mL with the same buffer, respectively. AOx was then activated with 3-(2-Pyridyldithio)propionic acid N-hydroxysuccinimide ester (SPDP, Sigma-Aldrich), which was achieved by adding SPDP DMSO solution (10% DMSO) into AOx solution (2 mg/mL) with a molar ratio of 10:1 (n/n, SPDP/AOx). The activation was performed for 2 h at 4°C, following by dialysis against phosphate buffer (0.1M, pH=7). Cat was activated with 2-Iminothiolane hydrochloride (Traut's reagent, Sigma-Aldrich), which was achieved by adding Traut's reagent (2

mg/mL in DI-water) into Cat solution (2 mg/mL). Reaction was performed at 4°C for 2 h, follow-ing by dialysis against phosphate-EDTA buffer (0.1M phosphate, 1 mM EDTA, pH=7) to remove unreacted reagents. Conjugation of AOx and Cat was then achieved by mixing equal mole of ac-tivated AOx and Cat (1:1, n/n) and incubated for 2 h at 4°C. After conjugation, NAS was added into conjugated AOx-Cat solution (20:1, n/n, NAS/protein) to derive acryloxyl groups on the sur-face of enzymes. After dialysis against phosphate buffer (50 mM, pH 7.0), AOx-Cat solution was diluted to 1 mg protein/mL with phosphate buffer (50 mM, pH 7.0), following by encapsulation with the same protocols described above.

2.2.2.9 Synthesis of n(AOx), n(Cat), and n(GOx)

n(GOx), n(AOx) and n(Cat) were synthesized using the method we reported previously.[1] Briefly, the enzymes were first acryloxylated by reacting with NAS (20:1, NAS/protein, n/n), followed by *in-situ* polymerization as described above. The AAm/BIS/APS/protein ratio was kept at 6000:1000:500:1 (mole ratio), while the TEMED/APS ratio is kept at 2:1 (w/w). After dialysis against 1xPBS, these single-enzyme nanocapsules were purified by size exclusion chromography (Sepharose-6B) and stored at 4°C for further use.

2.2.2.10 Synthesis of PEG-lipo(AOx+Cat)

The PEGylated liposomes were made from 1,2-distearoyl-sn-glycero-3-phosphoethanolamine-N-[methoxy(polyethylene glycol)-2000] (PEG2000-DSPE), hydrogenated L-α-phosphatidylcholine, hydrogenated (Soy) (HSPC) and cholesterol, of which composition (PEG2000-DSPE:HSPC:cho-lesterol = 1:3:1, m/m/m) is similar to that of the commercial PEGylated liposomes (Doxil). PEG2000-DSPE, HSPC and cholesterol were first dissolved in chloroform to get stock solutions with concentrations of 3.73 mg/mL, 11.17 mg/mL, and 3.73 mg/mL, respectively. AOx and Cat

were dispersed in PBS with the concentration of 2 mg/mL. A lipid film was then prepared on the inner wall of a flask by mixing 600 μL of PEG2000-DSPE, 600 μL HSPC, and 600 μL cholesterol solutions and drying the solvent using a rotary evaporator. The lipid film was further dried in vacuum overnight. The lipid film was then dissolved with 200 μL of ethanol, and immediately added into 2 mL of protein solution (500 μL of AOx stock solution, 160 μL of Cat solution, and 1340 μL of PBS). As-formed lipid-protein solution was stirred for 1 h at 4°C, and then pass through a 0.22 μm filter for 5 times. The PEG-lipo(AOx+Cat) solution was then dialyzed against PBS for 12 h with a dialysis membrane (MWCO = 10 kDa). After dialysis, PEG-lipo(AOx+Cat) solution was purified again with a size exclusion column (Sepharose-6B) by following the same method as the purification of enzyme nanocomplexes to remove unencapsulated AOx and Cat. Fractions containing PEG-lipo(AOx+Cat) were collected, combined, and condensed by centrifugal filtration. The sample was stored at 4°C for in vivo studies and further characterizations. All liposome samples used in animal studies were prepared 1 day before injection. The hydrodynamic size of PEG-lipo(AOx-Cat) particles is determined by DLS and the mean size is 60 nm (Figure 2-6).
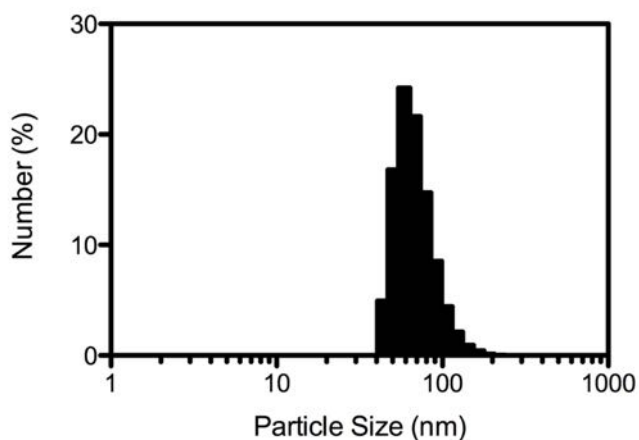
Figure 2-6 Size distribution of PEG-lipo(AOx-Cat)

2.2.2.11 Determination of enzyme concentrations

Enzyme concentrations of single protein nanocapsules, including n(HRP), n(GOx), n(Inv), n(AOx), n(Cat), were determined using BCA micro-assay. Before tests, two BCA reagents were prepared using the following recipes. Reagent A was prepared by dissolving 0.1 g bicinchoninic acid disodium salt hydrate (BCA), 0.32 g sodium carbonate, 0.01 g tartate acid in 10 mL DI-water, following by tuning the pH to 11.25 with 1 M NaOH solution. Reagent B was prepared by dissolving 0.2 g $CuSO_4 \bullet 5H_2O$ in 5 mL DI-water. BCA working solution (BWS) was prepared by mixing 50 volume of Reagent A and 1 volume of Reagent B together.

Standard curves of each enzyme were established using native enzyme with a series of enzyme concentrations (0.0078125, 0.015625, 0.03125, 0.0625, 0.125, 0.25, 0.5, 1 mg/mL). This was achieved by repeating 2-fold dilutions of 1 mg/mL enzyme solution with PBS in a 384-well plate. BCA assays were conducted by adding 10 μL of native enzyme solutions with different concentrations into each well of 384-well plate respectively, following by the addition of 10 μL of BCA working solution (BWS). In the meanwhile, 10 μL of enzyme nanocapsule solution was also added into the same plate, following by the addition of 10 μL of BWS. The plate was then incubated at 65°C for 1 h. Absorbance at 550 nm of each well was read out by using a plate reader. Concentration of the encapsulated enzyme was calculated by using its absorbance at 550 nm and the standard curve established at the same condition.

For ENs such as n(AOx-Cat), the concentration of encapsulated enzymes is measured by its enzymatic activity. Similar to the BCA assay, we first established the relationship between the activities and enzyme concentrations by their activity assays using the native (untreated) enzymes, respectively. Take n(AOx-Cat) as an example, the relationship between AOx concentration and its

activity was established by measuring the decreasing rates of its substrate under a series concentration of native AOx. The decreasing rates were achieved by incubating 1 μL of AOx solution with 200 μL 5% allyl alcohol PBS solution at room temperature, following by monitoring the absorbance at 233 nm. Meanwhile, the standard curve of decreasing rate of substrate vs. Cat concentration was established with the similar method by using hydrogen peroxide as substrate (incubate 1 μL of Cat solution with 200 μL of 0.5% H_2O_2 PBS solution, and monitor the absorbance at 240 nm of reaction solution). Two activity assays were then performed with the same amount of n(AOx-Cat) as enzyme, respectively. Reaction rates coming from AOx and Cat assays were then correlated with the standard curves of AOx and Cat to determine the concentrations of AOx and Cat in n(AOx-Cat) solution.

2.2.3 TEM and DLS studies of ENs

TEM samples were prepared by drop-coating of 2 μL n(HRP-GOx) solution onto carbon-coated copper grids. Droplets of samples were contacted with the grids for 45 s, then excess amount of samples was removed. The grid was then rinsed, and stained with 1% sodium phosphotungstate at pH 7.0. For better imaging, silver enhancement of AuNPs was performed prior to observation with TEM. Briefly, AuNP-labeled n(HRP-GOx) solution was first contacted with a TEM grid for 45s. After rinsing with deionized water, the grid was floated on a drop of freshly prepared silver enhancement reagent (Nanoprobe, NY) for 1 min. The grid was then rinsed again, followed by staining with 1% sodium phosphotungstate at pH 7.0. This process resulted in the formation of negatively-stained n(HRP-GOx) with 3~4 nm silver-coated AuNPs inside. DLS Measurements were taken at 90° scattering angle. Results show that the centered hydrodynamic diameters of ENs are 18 nm for n(HRP-GOx), 37 nm for n(HRP-GOx-Inv), 17 nm for n(GOx-Cat), and 24 nm for n(AOx-Cat) (Figure S6).
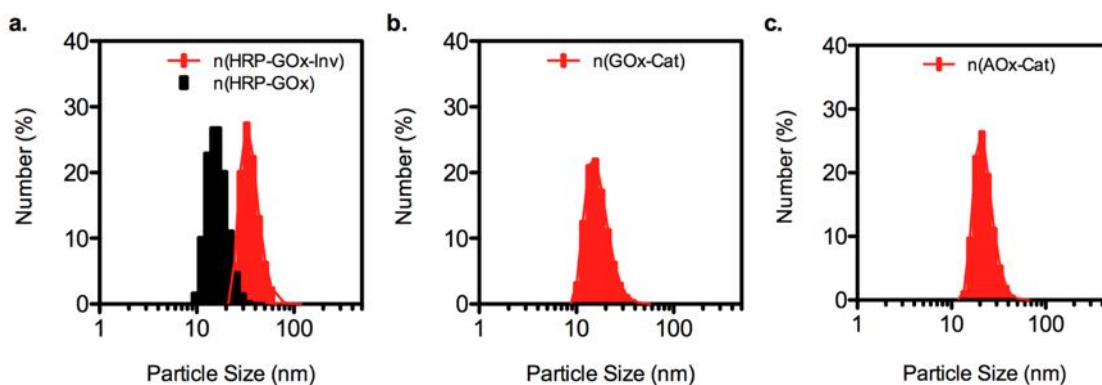
*Figure 2-7 Size distribution of **a.** n(HRP-GOx) (~18 nm) (black) and n(HRP-GOx-Inv) (~37 nm)(red); **b.** n(GOx-Cat) (~17 nm); and **c.** n(AOx-Cat) (~24 nm).*

2.2.4 Activity assays and stability of ENs

Overall activities of the enzyme complexes, n(HRP-GOx) and n(HRP-GOx-Inv), were assessed by monitoring the oxidation rate of *o*-Dianisidine (ODS). Briefly, a phosphate buffer (0.1M, pH = 7.0) containing 0.2 mM *o*-Dianisidine, 500 pM of ENs and a specific amount of substrate (glucose for n(HRP-GOx) or sucrose for n(HRP-GOx-Inv)), were incubated at 25˚C for 5 min. During the incubation, absorbance at 460 nm was recorded continuously with a UV/vis spectrometer. The absorption curve was plotted *versus* time and ΔA_{460}/min from the linear potion of the curve was calculated. The activity assays were repeated with a series of appropriate concentrations of substrate to get a series of catalytic rates to obtain K_M^{app} and k_{cat}^{app} by the Lineweaver–Burk plot. Similar assays were also performed with free enzymes mixture (free HRP/GOx, and free HRP/GOx/Inv) as the control experiments.

Similar activity assays were also performed in polyethylene glycol (PEG, M_w~3000) solutions with a series of PEG concentrations (0%, 5%, 10%, 15%, 20%, 25%, 30%, 35%, m/v) to simulate the viscous environment within the cells or blood stream. Briefly, certain amount of PEG was first

added into phosphate buffer (0.1M, pH=7.0) to get a stock PEG solution. Then enzyme nanocomplexes (or their corresponding free enzymes mixtures) and ODS were added and mixed thoroughly to get an assay solution with an enzyme concentration of 500 pM, and ODS concentration of 0.2 mM. 145 µL of as-prepared assay solution was then passaged into a transparent 96-well plate. Substrates (glucose for n(HRP-GOx), and sucrose for n(HRP-GOx-Inv) were dissolved in PEG solution to get 10% substrate solutions (w/v). Then 5 µL of substrate solution was added into each well of reaction solution. Plate was then shaken for 30 s and further incubated for 5 min. Absorbance at 450 nm of each sample was then read out with a plate reader.

Table 2-3 Kinetic parameters of HRP/GOx and HRP/GOx/Invertase free enzyme systems and their corresponding ENs

System	$K_M^{app}(mM)$	k_{cat}^{app}	
		s^{-1}	%
Free HRP/GOx	53.30±0.44	244.6±23.2	100
n(HRP-GOx)	361.85±0.37	1262.0±18.6	515.9±7.6
Free HRP/GOx/Inv	53.30±3.54	65.3±2.5	100
n(HRP-GOx-Inv)	224.90±13.64	1008.7±61.2	1542.5±93.5

Thermal stability was conducted using the following procedure: Solutions of n(HRP-GOx), n(HRP-GOx-Inv), free HRP/GOx mixture, and free HRP/GOx/Inv mixture (~0.1 mg/mL protein, in 10 mM phosphate buffer, pH 7.0) were first incubated at 65°C for certain periods (5 – 60 min), followed by quenching on ice bath and recovering to room temperature. Activity assays were performed with these samples to determine the residual activities of ENs and their corresponding free enzymes mixtures.

2.2.5 Kinetic studies of H_2O_2 generation and elimination

The kinetic studies of H_2O_2 generation and elimination were performed with the following procedure. D-glucose was dissolved in PBS buffer at concentration of 2 mg/mL; then 3,3',5,5'-tetramethylbenzidine (TMB) solution (10% w/v in DMSO) and HRP stock solution (1 mg/mL in PBS) were added to obtain final concentrations of TMB at 0.5 mM and HRP at 1 μg/mL. n(GOx), mixture of n(GOx) and n(Cat), or n(GOx-Cat) was then added respectively to the Glucose-TMB-HRP solution to a final concentration of GOx content of 0.3 μg/mL. The reaction mixtures were vortexed and aliquots of 30 μL were transferred into a 96-well plate after 2, 5, 10, 20, 30, 50, 70, and 90 min (3 aliquots per time point). Immediately after the aliquots were taken out, 30 μL H_2SO_4 solution (160 mM) per well was added to terminate the enzymatic reaction. After collecting all the samples, the absorbance at 450 nm was read with a plate reader. All data were acquired from three independent experiments performed triplicated.

To relate the H_2O_2 concentration with the absorbance, a standard absorbance curve *vs* H_2O_2 concentration was obtained using the method described below. Firstly, H_2O_2 stock solution (30%, m/v) was diluted with PBS to a series of concentrations (0.05, 0.1, 0.2, 0.4, 0.6, 0.8, and 1 ppm). Pure PBS buffer (1x) was used as blank. Subsequentially, TMB and HRP were added into pure PBS buffer and H_2O_2-PBS solutions, respectively. The reactions were incubated for 30 min at room temperature to allow the complete conversion of H_2O_2. After the incubation, reaction solutions were transferred into a 96-well plate with 30 μL per well, following by the addition of 30 μL of H_2SO_4 solution (160 mM). The plate was then mounted into a plate reader to measure the absorbance at 450 nm. The absorbance of samples was plotted versus H_2O_2 concentration (Figure 2-8). This curve is then used as the standard curve to calculate H_2O_2 generation during GOx-catalyzed reaction.
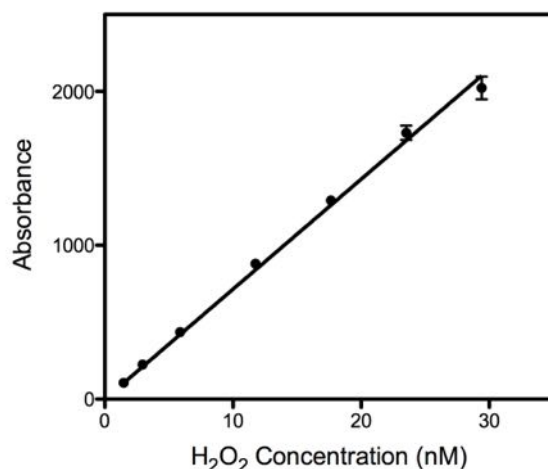
Figure 2-8 Standard curve represents the relationship between absorbance and H_2O_2 concentration. Data represent average; errors come from three independent experiments performing triplicated.

2.2.6 Cell viability assay

Cell viabilities in the presence glucose oxidation reaction catalyzed by n(GOx-Cat), n(GOx), or mixture n(GOx) of n(Cat) was tested in HeLa cells. HeLa cells were seeded into a 96-well plate (10^4 cells/well, 100 μL/well) and cultured in DMEM (normal level of glucose in medium, with 10% FBS) for a day prior to exposure to the nanoparticles. Same amounts (0.7 mg/mL, 2 μL) of n(GOx), mixture of n(GOx) and n(Cat), and n(GOx-Cat) were then added into the wells and incubated at 37°C for 5 h.

Cell viabilities in the presence of alcohol oxidation reaction catalyzed by n(AOx-Cat), native AOx, n(AOx), n(Cat), and mixture of n(AOx) and n(Cat) were tested using a similar procedure. Nanocapsules or native AOx (2 μg/well) were first incubated with the cells (10k cells) for 1 hr. Then equal amount of ethanol (3 μL) was added into each well and incubated with cells for another 5 h at 37°C.

60

After incubation, CellTiter-Blue (20 μL) was added into each well and further incubated for 3 h. The plate was then placed on a shaking table at 150 rpm for 5 min to thoroughly mix the solution. Viable cells reduce CellTiter Blue and show fluorescent reddish color. Quantification of the cell viability was achieved by measuring the fluorescence intensities with a plate reader (Ex = 535 nm, Em = 585 nm).
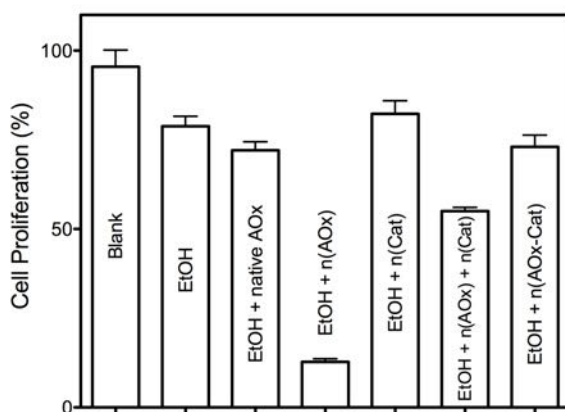
Figure 2-9 Viability of the cells treated with EtOH in the presence of n(AOx-Cat), native AOx mixture of n(AOx) and n(Cat), or n(Cat).

2.2.7 *In-vivo* studies of alcohol antidotes and prophylactics

Alcohol antidote studies: Male C57B6 mice of 8-10 week old from Jackson Laboratory (Bar Harbor, ME) were used for the studies. 18 mice were divided into six groups and fasted for 12 hours prior to the studies. All mice were fed with an alcohol liquid diet at dosage of 6 mg ethanol/bodyweight (g). The mice were intoxicated and slept with 20 min of feeding. 30 min after feeding, these intoxicated mice were tail-vein injected with PBS (control), native AOx, n(AOx), mixture of n(AOx) and n(Cat), Lipo(AOx+Cat), and n(AOx-Cat), respectively. The dose of enzyme was maintained at ~ 65 μg AOx and ~ 21 μg Cat per mouse; the volume of PBS or enzyme solutions was maintained at 150 μL per mouse. Blood samples (~10 μl) were taken from tails at 45, 90 180,

and 300 min post injection, and the blood alcohol concentrations were determined using an ethanol assay kits purchased from BioVision, CA, USA or Analox Instruments, IL, USA.

Alcohol prophylactic studies: 24 Male mice (C57B6) were divided into 6 groups and gavaged with the alcohol diet at dose of 6 mg ethanol/bodyweight (g). The doses of native AOx, n(Cat), n(AOx), mixture of n(AOx) and n(Cat), or n(AOx-Cat) were maintained at 65 µg AOx and 21 µg Cat per animal. Another group of mice were fed with isocaloric diet without ethanol and used as the control group. BACs were determined using the same method mentioned above. The levels of plasma alanine aminotransferase (ALT) were determined 6 to 8 hours after the alcohol gavage following the methods described previously.[252]

GOx-induced tissue damage in mice: Male mice (C57B6) were anesthetized using ketaime (85 mg/kg) combined with xylazine (10 mg/kg), which were intramuscularly injected into the posterior thighs. Hairs on the back of animals were then removed using an animal shaver. n(GOx), n(Cat) and n(GOx-Cat) were delivered into the skin via two cutaneous injections, respectively, at 0 and 24 hours with a dosage of 35 µg nanocapsule dispersed in 50 µl PBS buffer per group per injection. Equal volumes of hydrogen peroxide (H_2O_2) solution and PBS buffer were injected at different spots of the back of the same animals, respectively, as the positive and negative controls. The animals were anesthetized at 24 hours following the second injection; pieces of skin tissues were then sampled, fixed and processed for H&E staining and fluorescent TUNEL staining using an *in-situ* Cell Death Detection Kit from Roche. H&E images were captured with a Nikon Eclipse E600 microscope and confocal fluorescence images were obtained with a Nikon PCM2000 confocal laser-scanning microscope according to previous methods.[253,254]

Blood alcohol concentration (BAC) reduction studies were also conducted by gavaging mice with ethanol-containing diet followed by tail-vein injection of native AOx, n(AOx), n(Cat), mixture of n(AOx) and n(Cat), or n(AOx-Cat). Male C57B6 mice of 8-10 week old from the Jackson Laboratory (Bar Harbor, ME) were used in these studies. 24 mice were divided into 7 groups, and fed with alcohol liquid diet (6 g of EtOH/kg body weight) after fasted for 8-12 h. Equivalent amount (65 µg of AOx, and 21 µg of Cat) of native AOx, n(AOx), n(Cat), n(AOx)+n(Cat) mixture, and n(AOx-Cat) were injected to 5 groups of alcohol-fed animals via tail-vein injection 30 min after alcohol feeding, respectively. 4 alcohol-fed mice were injected with 150 µL of PBS to use as the control group. For the negative control, 4 mice were fasted for 8-12 h, then fed with isocarloric diet without EtOH. BAC and ALT of mice were determined with the same methods for mice administrated orally (detailed method are described in Methods part of the manuscript). Similar BAC reduction effect and ALT levels were obtained in comparison with those obtained by oral administration (Figure 2-10). Dose-dependence of BAC reduction for n(AOx-Cat) was also conducted (Figure 2-11). All animals were treated in accordance with the Guide for Care and Use of Laboratory Animals approved by local committee.

In these *in-vivo* studies, BACs were adjusted against the body weights of individual mice by using the formula, $BAC_{adj} = BAC_i \times (BWT_i/BWT_{ave})$, where BAC_j is the adjusted BAC, BAC_i and BWT_i are the blood alcohol level and bodyweight of individual mouse, respectively; BWT_{ave} is the average mouse weight of all animals in each set of experiment. Statistical analyses were performed using the Bonferroni post-test following a two-way ANOVA for BACs and the Newman-Keuls post-test following a one-way ANOVA for ALT data. $P < 0.05$ or less was considered significant.
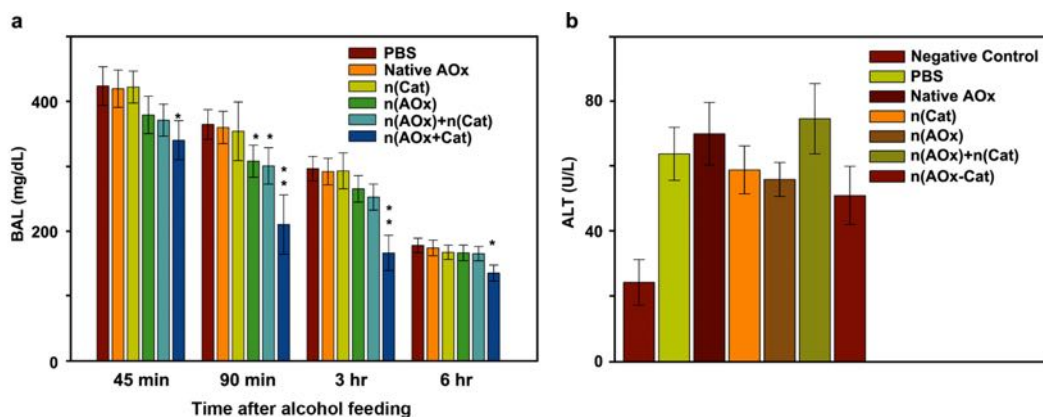
*Figure 2-10 Blood alcohol concentration (BAC) (**a**) and plasma alanine aminotransferase (ALT) (**b**) of mice gavaged with ethanol-containing diet followed by tail-vein injection of PBS (control), native AOx, n(AOx), n(Cat), mixture of n(AOx) and n(Cat), and n(AOx-Cat)). For mice treated with n(AOx-Cat), BAC decreases significantly before 3 hr (*P < 0.05; **P < 0.01, 4 mice used in each group), compared to the mice injected with PBS only. All the animals treated with alcohol show higher ALT levels; a tendency of lower ALT is also observed for the mice treated with n(AOx-Cat).*
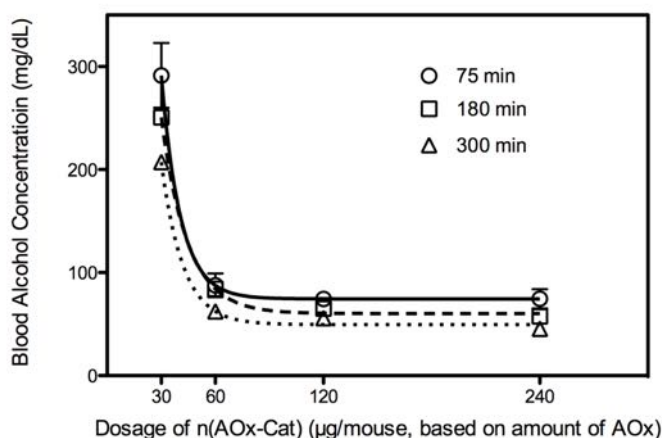
Figure 2-11 BAC of intoxicated mice injected with different doses of n(AOx-Cat) per mouse. Before the injection, mice were fasted for 12 hours and gavaged with the alcoholic liquid diet at 6 mg ethanol per gram of bodyweight. A series amount (30-240 μg AOx per mouse) of n(AOx-Cat) were then administrated to animals 30 min post alcohol feeding. The BAC was measured 75, 180, and 300 min after the injection of antidote. Due to a larger variation of animal weights in this experimental group of animals, the BAC was normalized with the body weight using the following equation: $BAC_{adj} =$

$BAC_i/\left[1 + ln2^{(BWT_{max}-BWT_i)}\right]$, *where BWT_{max} is the highest bodyweight among this group of animals.*
All values are expressed as means $\pm$ s.e.m. unless otherwise indicated.

2.2.8 Pharmacokinetics and bio-distribution of enzyme nanocomplexes in mice

2.2.8.1 Bio-distribution of ENs administrated orally

Bio-distribution and pharmacokinetics of ENs administrated orally was achieved by monitoring the residual activity of the ENs in plasma after gavage of Rhodamine B-labeled n(AOx). n(AOx) was first prepared with the method described above. Fluorescence labeling was achieved by incubating the nanocapsules with rhodamine B (RhB) isothiocyanate at 4°C, pH 8.0 overnight. RhB-labeled n(AOx) (RhB-n(AOx)) was purified by dialysis against PBS thoughtfully to remove excess RhB.
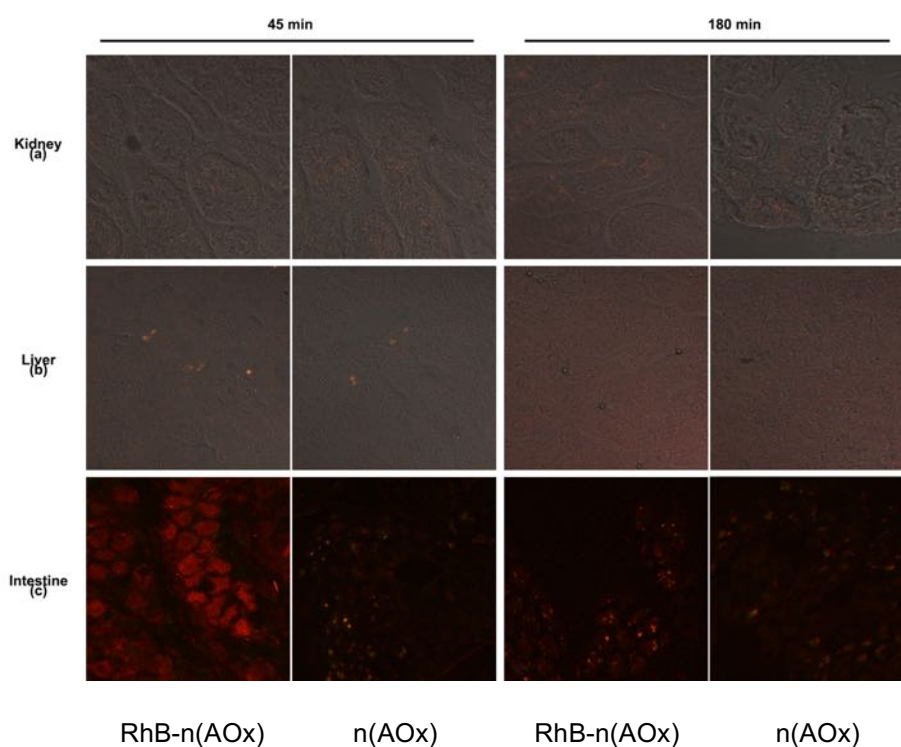
Figure 2-12 Confocal images of Kidney (a) Liver (b) and intestine (c) of animals treated with RhB-n(AOx) (red) and n(AOx) (no color).

65

Six male C57B6 mice of 8-10 week old from the Jackson Laboratory (Bar Harbor, ME) were used in these studies. Before administration of RhB-n(AOx), mice were fast for 6-8 hours. Animals were then divided to two 3-mouse groups, followed by gavage alcohol-free diet with 120 μL (1 mg/mL) of RhB-n(AOx), and 120 μL of non-labeled n(AOx) as control, respectively. Animals were then fed with water, and the blood samples (20 μL) were taken from tails at 30 min, 45 min and 180 min. After taking the blood sample, animals were sacrificed, and their tissues including liver, kidney, and intestine were taken and imaged with confocal microscope. Blood samples were first centrifuged at 20,000 rpm for 5 min to remove the blood cells. Residual activities of n(AOx) were determined by incubating 1 μL of plasma with 100 μL of assay solution (1% EtOH, 0.02 mg/mL HRP, and 0.5 mM TMB in 0.1 M phosphate buffer, pH = 7.0), and monitoring the absorbance change at 620 nm with a plate reader. A series of n(AOx) stock solutions with different concentrations (0.4688 μg/mL, 0.9375 μg/mL, 1.875 μg/mL, 3.75 μg/mL, 7.5 μg/mL, 15 μg/mL and 30 μg/mL) were then prepared and used to establish the relationships between reaction rates and concentrations of enzyme nanocomplex.

No activity can be detected in the plasma of n(AOx) or RhB-n(AOx) treated animals, indicating as-gavaged ENs were retained within the digestive tract. In order to confirm this observations, we also imaged the tissues taken at different time after oral administration of RhB-n(AOx). To avoid the interferences coming from the fluorescence from animal's tissue, we also imaged the tissues taken from animals that gavage with non-fluorescence labeled n(AOx) as controls. Images of livers and kidneys (Figure 2-12, a & b) showed no fluorescence intensity of rhodamine B, indicating that RhB-n(AOx) administrated orally did not enter the circulation system. In contrast, a strong fluorescence signal was observed in intestine 45 min post administration in RhB-n(AOx)-treated mice (Figure 2-12, c). This result indicated that ENs can partially attached on the intestine but not

entered the blood stream or internalized into cells. This feature could be useful for the development of drug needed to deliver orally.

2.2.8.2 Pharmacokinetics and bio-distribution of ENs administered systematically

Pharmacokinetics of ENs was achieved by monitoring the residual activity of ENs in plasma after the tail injection of the ENs. It should be noted that current AOx-activity assays are based on detection of H_2O_2 produced during the alcohol oxidation reaction. Such assays could not be used to determine the activity of AOx within the n(AOx-Cat) nanocomplexes, because as-generated H_2O_2 will be eliminated by the catalase (Cat) with the nanocomplexes. Thus, a similar enzyme nanocapsule, n(AOx), was employed in the pharmacokinetics studies (PK studies), since it has the same surface chemistry and similar particle size as n(AOx-Cat).

A standard cure was first established to relate the activity and concentration of n(AOx). Briefly, a series of n(AOx) concentrations (0.4688 µg/mL, 0.9375 µg/mL, 1.875 µg/mL, 3.75 µg/mL, 7.5 µg/mL, 15 µg/mL and 30 µg/mL) were used, of which activity were measured respectively by incubating 1 µL of the enzyme solution with 100 µL of assay solution (1% EtOH, 0.02 mg/mL HRP, and 0.5 mM 3,3′,5,5′-tetramethylbenzidine (TMB) in 0.1 M phosphate buffer, pH = 7.0). Their reaction rates can be achieved by monitoring the absorbance changes at 620 nm respectively using a plate reader.

Male C57B6 mice of 8-10 week old from the Jackson Laboratory (Bar Harbor, ME) were used in these studies. Before administration of n(AOx), mice were fast for 6-8 hours, followed by injected with 100 µL of n(AOx) (1 mg/mL, 3 out of 6 mice) and 100 µL of PBS (3 out of 6 mice) via tail vein, respectively. Animals were then fed with ordinary food and water, and the blood samples

(20 μL) were taken from tails at 45 min, 90 min, 180 min, 300 min, 600 min, and 1440 min. The blood samples were then centrifuged at 20,000 rpm for 5 min to remove the blood cells. Residual activities of n(AOx) were determined by incubating 1 μL of plasma with 100 μL of assay solution (1% EtOH, 0.02 mg/mL HRP, and 0.5 mM 3,3′,5,5′-tetramethylbenzidine (TMB) in 0.1 M phosphate buffer, pH = 7.0), and monitoring the absorbance change at 620 nm with a plate reader. Figure 2-13 shows the time-dependence of the equivalent plasma concentration of n(AOx), clearly showing decay of the enzyme concentration with time. From this PK profile, it is clear that no n(AOx) could be detected in the plasma within 1000 min after the injection. No activity can be detected in plasma after 1000 min.

Besides the PK study, we have also investigated the bio-distribution using the PET/CT technique. Briefly, we radioactively labeled n(AOx-Cat) using ^{18}F-SFB. ^{18}F-SFB was prepared using synthesis module TRACER lab FX$_{FN}$ (GE Medical System). n(AOx-Cat) (1 mg/mL) was added into freshly prepared ^{18}F-SFB solution, and reacted at 60°C for 30 min in borate buffer (100 mM, pH 8.5). After removal of free ^{18}F-SFB by repeated centrifuging and washing steps, ^{18}F-n(AOx-Cat) (^{18}F-ENs) were re-dispersed with PBS and passed through a 0.22 mm filter (Millipore) into a sterile multi-dose vial for in vivo studies. PET scans and image analysis were performed using a microPET/CT model scanner (Inveon, Siemens). Mice (BLAC) were injected with ^{18}F-ENs via tail vein at the dose of ~ 3.7 MBq/animal. For dynamic PET, 120-min scans were started 20 min post the injection. The images were reconstructed using a two-dimensional ordered-subsets expectation maximum algorithm and no correction was applied for attenuation or scatter. For each microPET scan, regions of interest were drawn over major organs using vendor software on decay-corrected

whole-body coronal images. The standard uptake value was normalized by body weight. The distribution of ^{18}F-ENs in the animal was shown in Figure 2-14. By continuously monitoring the local radiation intensities at liver, kidney, lung, and spleen with PET/CT, dynamic distribution of ENs is shown in Figure 2-15.
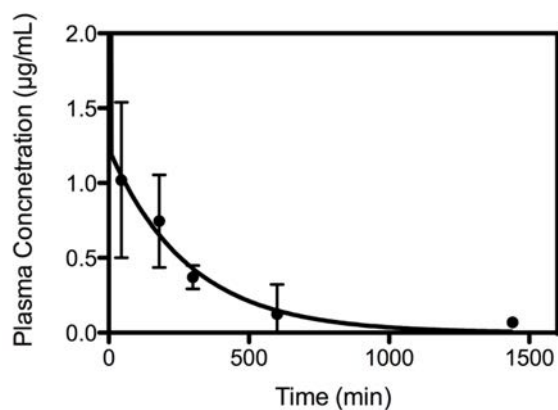
Figure 2-13 Residual concentration of n(AOx) in the plasma of enzyme nanocomplex-treated mice.
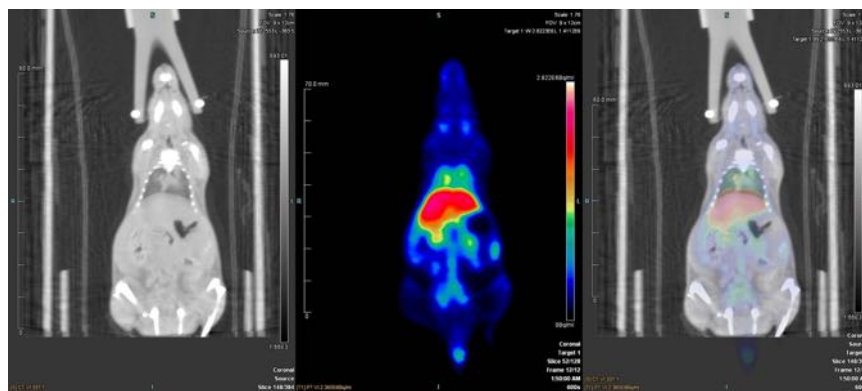
Figure 2-14 CT, PET and PET/CT images of a mouse, injected with ^{18}F-n(AOx-Cat). PET image were acquired with a 120-min dynamic PET scan started at 20 min post injection of ^{18}F-ENs.
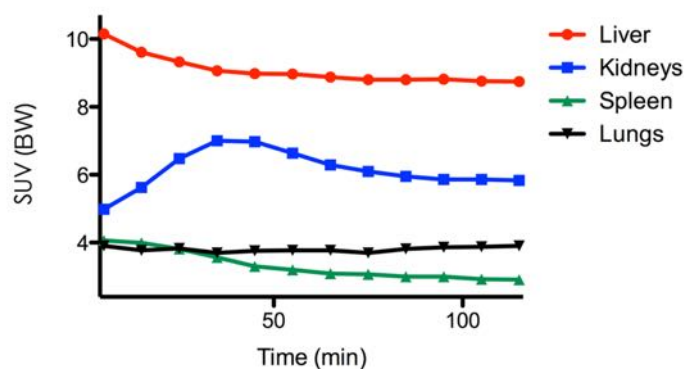
Figure 2-15 Residual concentration of ^{18}F-n(AOx-Cat) in the organs of EN-treated mouse. Quantifications of ^{18}F-n(AOx-Cat) in liver (red), kidney (blue), lung (black), and spleen (green) were achieved by monitoring the local radiation intensity with PET/CT.

2.3 Results and discussions

Successful construction of the enzyme nanocomplexes was demonstrated using horseradish peroxidase (HRP) and glucose oxidase (GOx) as the model enzymes. Figure 2-16a shows a transmission electron microscopic (TEM) image of n(HRP-GOx) with an average diameter of 30±7 nm. To justify the double-enzyme architecture, each HRP and GOx molecule was labelled with a single 1.4-nm gold nanoparticle. As shown in Figure 2-16b, most gold-labelled enzyme nanocomplexes contain two gold nanoparticles, indicating that each nanocomplex indeed contains two enzyme molecules. Considering the specific bindings between the enzymes and their inhibitors linked to the DNA scaffolds, it is reasonable to conclude that such double-enzyme architecture is constructed by one HRP and one GOx molecule.
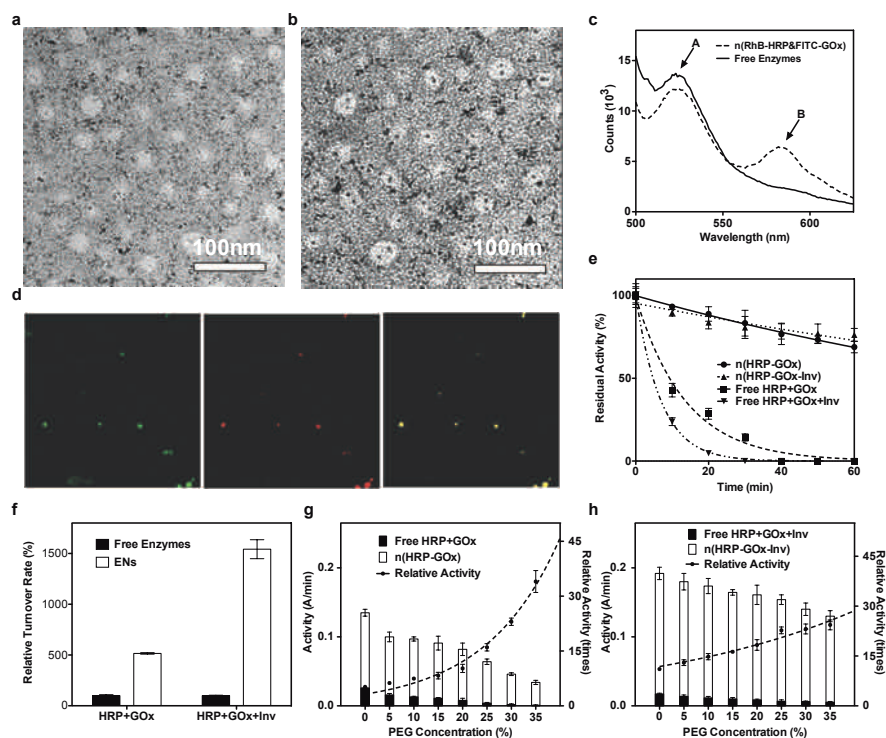
*Figure 2-16 **The Structure and Enhanced Activity and Stability of Enzyme Nanocomplexes**. **a, b.** Transmission electron micrograph showing the uniform size of n(HRP-GOx) (**a**) and n(HRP-GOx) prepared by labelling HRP and GOx with single gold nanoparticles (**b**). **c**, Fluorescence spectra of n(HRP-GOx) and a mixture of n(HRP) and n(GOx) with the same protein content. GOx and HRP were pre-labelled with FITC and RhB, respectively. The spectrum was recorded at Ex=450nm. **d**, Confocal microscope images of n(FITC-labelled GOx) (left; Ex=488nm, Em=510-530nm), n(RhB-labelled HRP) (middle; Ex=532nm, Em=570-600nm), and n(RhB labelled HRP-FITC labelled GOx) (right; Ex=488nm; Em=570-600nm). **e**, Activity change of n(HRP-GOx), n(HRP-GOx-Inv) and their native-enzyme-mixture counterparts during incubation at 65°C. **f**, The turnover rates of n(HRP-GOx) and n(HRP-GOx-Inv) with corresponding free enzyme mixtures. **g**, The activity of n(HRP-GOx) and a mixture containing the same amount of free HRP and GOx in the presence of increasing concentrations of poly(ethylene glycol) (PEG) in phosphate buffer (50 mM, pH 7.0). **h**, The activity of n(HRP-GOx-Inv) and a mixture containing the same amount of free HRP, GOx and Inv as the complex in the presence of increasing PEG concentrations. Relative activities were normalized by the activities of the free-enzyme mixtures with the same enzyme content and PEG concentration.*

71

Such nanocomplex architecture spatially defines the constituent enzymes within close proximity. Using Rhodamine-B-labelled HRP (HRP-RhB) and fluorescein-isothiocyanate-labelled GOx (GOx-FITC) as an example, Figure 2-16c compares the fluorescence spectra of their mixture (equal molar ratio) and the corresponding dual-enzyme nanocomplexes. Since FITC and RhB possess excitation maximums at 495 and 540 nm, respectively, the mixture of GOx-FITC and HRP-RhB only exhibits the FITC emission centered at 520 nm under 450 nm excitation. For comparison, the nanocomplex exhibits intense emissions from both FITC and RhB (centered at 520 nm and 585 nm, respectively). This observation indicates an effective Föster resonance energy transfer (FRET) from GOx-FITC to HRP-RhB, confirming the HRP and GOx molecules are closely associated within a short distance (< 10 nm).[255] Figure 2-16d further shows fluorescence microscopic images of the nanocomplex showing co-localization of GOx-FITC and HRP-RhB. Upon excitation at 488 nm, FRET emission at 580 nm was also detected at the same position further confirming their close association.

Such close-proximity architecture endows the nanocomplexes with significantly enhanced catalytic efficiency, which was demonstrated by consecutive reactions of sucrose and glucose mediated by invertase (Inv), GOx and HRP. Glucose added or generated was oxidized, producing H_2O_2 that further oxidizes *o*-dianisidine *via* the HRP-mediated reaction. Figure 2-16f compares the turnover rates (*o*-dianisidine oxidation rates) of n(HRP-GOx) and n(HRP-GOx-Inv) with those of their native-enzyme mixtures with same enzyme content. Compared with the native enzyme mixtures, n(HRP-GOx) and n(HRP-GOx-Inv) show elevated turnover rates by 5 and 15 folds in phosphate buffer, respectively. To simulate the viscous environment within cell or blood stream,[256] poly(ethylene glycol) (PEG) was added to the reaction medium. The relative turnover rates increase with increasing the PEG concentration. When 35 wt-% PEG was added, 34-fold and 24-

fold increase in turnover rate was achieved for n(HRP-GOx) and n(HRP-GOx-Inv), respectively (Figure 2-16g & h). Moreover, both the nanocomplexes retain over 70% activities after incubation at 65 °C for 60 minutes, whereas their mixture counterparts lose more than 98% activities, indicating the nanocomplexes possess significantly enhanced stability (Figure 2-16e).

This unique architecture also affords the nanocomplexes with complementary functions. Oxidases, for example, are being used or proposed for various therapeutics;[37] oxidase-mediated reactions, however, produce toxic hydrogen peroxide (H_2O_2). Nevertheless, through constructing oxidase-catalase nanocomplexes, such toxic intermediates can be eliminated effectively. Exemplified using GOx, cells incubated with n(GOx) in glucose-containing media lose more than 90% viability; adding n(Cat) into the media increases the viability to 42%. In contrast, the cells with n(GOx-Cat) exhibit much higher viability (~ 91%), which is similar to the control, owning to the effective H_2O_2 elimination (Figure 2-17a). The net rates of H_2O_2 production were quantified using glucose-containing buffer solutions, to which the enzyme nanocapsules were added and their temporal H_2O_2-concentration profiles were obtained, respectively (Figure 2-17b). Consistently, the net rate of H_2O_2 production for the n(GOx-Cat) system is 5-fold lower compared with those with the n(GOx)/n(Cat) mixture or n(GOx).
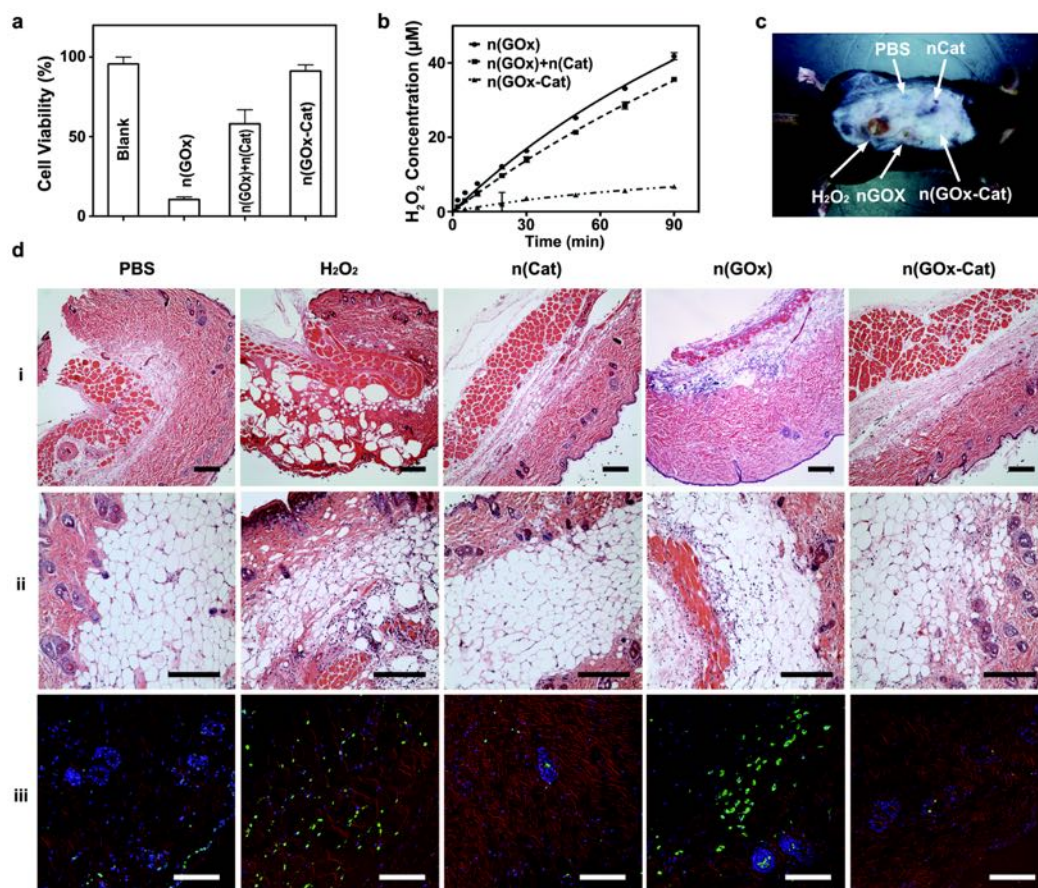
*Figure 2-17 **In-vivo Detoxifying Capability of the Catalase-Containing Enzyme Nanocomplexes. a,** Cell viability assays after treated with n(GOx), mixture of n(GOx) and n(Cat), and n(GOx-Cat). Cell proliferation rates were normalized with those of the untreated cells. **b,** H_2O_2 concentration in glucose oxidation reaction catalysed by n(GOx), n(GOx)+n(Cat) or n(GOx-Cat). The system with n(GOx), the mixture of n(GOx) and n(Cat), and n(GOx-Cat) shows a rate of 0.434±0.004 µM/min, 0.388±0.005 µM/min, and 0.075±0.007 µM/min, respectively. **c,** Photograph of a mouse cutaneously injected with PBS, n(Cat), H_2O_2, n(GOx), and n(GOx-Cat) at different sites. **d,** Micrograph of mouse skin tissue at the injection sites. **(i) & (ii)** Hematoxylin and eosin (H&E) stain **(iii)** Immunohistology stain with TUNEL assay (green), Cy3-conjugated monoclonal α-smooth muscle actin antibody (red) and DAPI (blue). The scale bars indicate a distance of 100 µm.*

Such nanocapsules were then cutaneously injected to a mouse at different sites, respectively. Equal volumes of H_2O_2 solution (3% w/v) and phosphate buffer saline (PBS) were used as the positive and negative control, respectively (Figure 2-17c). Skin lesions were observed in H_2O_2-

treated and n(GOx)-treated sites 48 hours after injection. In contrast, skin damages were not observed in the spots injected with PBS, n(Cat), or n(GOx-Cat). The skin tissues at the injection sites were sectioned and stained with hematoxylin and eosin (H&E) and TUNEL staining kit. H_2O_2 administration caused tearing and ballooning in the dermis of the skin; n(GOx) administration resulted in similar tissue ballooning and neutrophil infiltration albeit to a milder extent, indicating pathophysiological response and injury due to the generated H_2O_2. No tissue damages were observed in the spots injected with PBS, n(Cat) and n(GOx-Cat) (Figure 2-17d, i&ii). Consistently, cell apoptosis was evident in the skin tissue treated with either H_2O_2 or n(GOx), whereas the cell death in n(Cat)- or n(GOx-Cat)-treated skin tissues was minimal and comparable to that of PBS treated sample (Figure 2-17d, iii).

The capability of making robust enzyme nanocomplexes with enhanced and complimentary functions offers a novel platform for various applications. For example, alcohol consumption is a millennium-old component of human civilization with unique social functions. Excessive consumption and abuse of alcohol, however, associate with a series of organ injuries and social problems. To date, although alcohol prophylactic does exist in the market, their efficacies have not been documented yet. For alcohol antidote, although various colloidal antidotes[257,258] were developed for drug overdosing, such antidotes may not be sufficient for alcohol intoxication. Recently, γ-aminobutyric-acid-based receptor antagonists were explored to resist the alcohol intoxication effect but with side effects.[259] Based on the nanocomplexes of alcohol oxidase (AOx) and catalase, we demonstrated a design of alcohol prophylactic and antidote.

For the prophylactic studies, mice were gavaged with alcoholic diet containing native AOx, n(AOx), n(Cat), mixture of n(AOx) and n(Cat), or n(AOx-Cat). All mice were intoxicated and

slept within 20 min after feeding; the group with n(AOx-Cat) woke up 1-2 hours earlier than the other groups. The blood alcohol concentration (BAC) of the mice administered with n(AOx-Cat) was reduced by 10.1%, 31.8% and 36.8%, respectively, at 45 min, 90 min and 3 hours after feeding (Figure 2-18a). Significantly less BAC reductions were observed in those with n(AOx) (< 8.5%) or with the mixture of n(AOx) and n(Cat) (< 10.6%). Insignificant BAC reduction was observed for those with n(Cat) or native AOx. All alcohol-fed animals show increased plasma alanine aminotransferase (ALT) level; nevertheless, the mice treated with n(AOx-Cat) had a tendency of lower ALT levels (Figure 2-18b). Most nanocomplexes were retained on the intestine surface and no nanocomplexes could be detected in the liver and kidney (Figure 2-12).
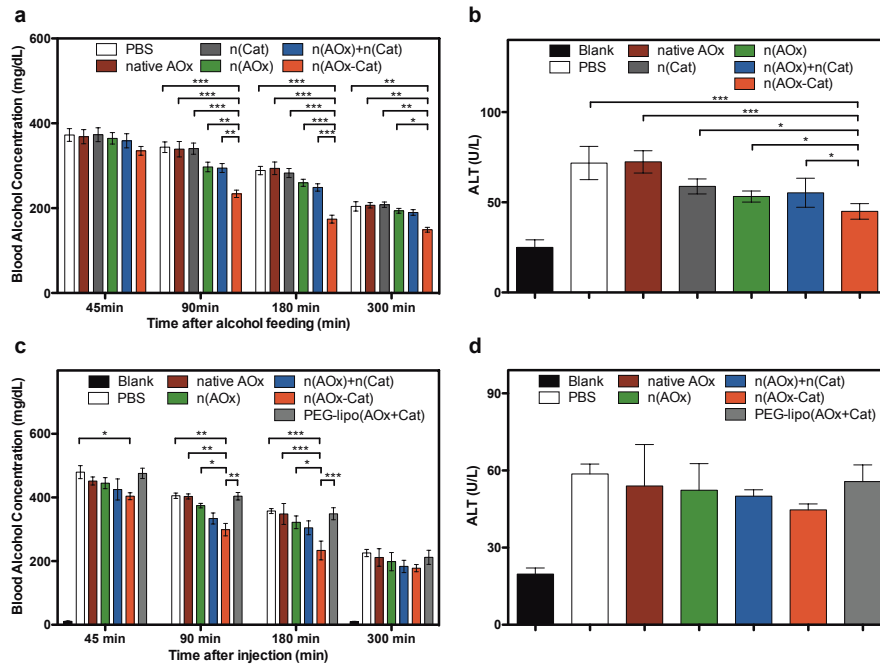
Figure 2-18 **Efficacy of n(AOx-Cat) as Prophylactic and Antidote for Alcohol Intoxication.** *Animals in Blank group are feed with normal diet without alcohol and used as baseline group. Four mice were used in each group. Data are presented as mean ± SEM and the significance levels (P values) are labelled using * (P < 0.05), ** (P < 0.01) and *** (P < 0.001), respectively.* **a, b.** *Blood alcohol concentration (BAC)* **(a)** *and plasma alanine aminotransferase (ALT)* **(b)** *in mice after gavage with alcohol diet containing PBS,*

*native AOx, n(Cat), n(AOx), a mixture of n(AOx) and n(Cat), or n(AOx-Cat) with equivalent amount of enzymes. The amount of AOx and Cat used was fixed at 65 µg and 21 µg, respectively; while the alcohol dosage was fixed at 6 mg ethanol/bodyweight (g). **c, d.** BAC **(c)** and ALT **(d)** of intoxicated mice after injection with PBS, native AOx, lipo(AOx+Cat), or n(AOx-Cat). Thirty minutes before the injection, mice were gavaged with the alcohol diet at 6 mg ethanol per gram of the bodyweight. The volume of PBS and the enzyme solutions injected was maintained at 150 µL; the dose of enzyme injected was maintained at 65 µg AOx or 21 µg Cat per mouse. Three mice were used in each group.*

For the antidote studies, PBS, native AOx, n(AOx), mixture of n(Cat) and n(AOx), n(AOx-Cat) were tail-vein injected to intoxicated mice, respectively. The mice treated with n(AOx-Cat) show the lowest ALT level (Figure 2-18d) and the most significant BAC reduction of 15.8%, 26.1%, 34.7%, and 21.3% at 45 min, 90 min, 3 h, and 6 h after the injection, respectively (Figure 2-18c). Liposome has been considered as the most promising approach for protein delivery; insignificant BAC reduction, however, was observed for the liposomes co-entrapping AOx and Cat. Dose-dependence study suggests BAC rapidly decreases with increasing n(AOx-Cat) dose from 30-60 µg AOx per animal and then remains almost constant with further increasing doses (Figure 2-11). Upon nanocomplex injection, blood concentration of the nanocomplexes rapidly decreases (Figure 2-13). Dynamic PET/CT scan suggests that the nanocomplexes are accumulated in the liver shortly after the injection, while the accumulation in kidney increases with time reaching the peak level after ~ 40 min (Figure 2-14 and Figure 2-15).

Both the prophylactic and antidote studies suggest n(AOx-Cat) is more effective than the mixture of n(AOx) and n(Cat) for BAC and ALT reduction. The unique n(AOx-Cat) architecture enables effective removal of toxic H_2O_2 (Figure 2-9) and prevents the AOx from being inactivated by the H_2O_2 generated.[260] Moreover, the H_2O_2 elimination process regenerates molecular oxygen ensur-

ing a fast alcohol oxidation kinetics leading to more significant BAC reduction. The alcohol oxidation process also generates another toxic intermediate, acetaldehyde. More effective ALT reduction and complete liver protection will rely on effective removal of acetaldehyde; unfortunately, neither active enough aldehyde dehydrogenase nor aldehyde oxidase (ADOx) is available. Better prophylactic and antidote are anticipated, when active enough ADOx becomes available for the construction of n(AOx-ADOx-Cat) triple-enzyme nanocomplexes.

2.4 Conclusion

To conclude, we have demonstrated a design of robust enzyme nanocomplexes with improved efficiency, enhanced stability, complementary and synergic functions by precisely assembling and stabilizing multiple enzymes within a nano-space. Considering the vast library of enzymes that is currently or potentially available, novel classes of enzyme nanocomplexes could be built for a broad range of applications. Moreover, through judiciously choosing the constituent enzymes and harvesting their synergic and complementary effects, we foresee the creation of novel families of enzyme machineries with programmable function possibly beyond evolution.

Chapter 3. Phosphorylcholine polymer nanocapsules prolong the circulation time and reduce the immunogenicity of therapeutic proteins

3.1 Introduction

Proteins are essential parts of organisms participating in virtually every process within the cells; from the perspective of disease mechanism, protein therapy represents a tremendous opportunity for the modern medicine. An increasing number of protein therapeutics have been approved for clinical use and many more are being developed;[1,2,261] nonetheless, broad adaption of protein therapy remains challenging mainly due to the difficulties, such as poor protein stability in non-physiological and proteolytic environments, insufficient ability to enter cells and other compartments of the body, rapid clearance, and immune responses against the therapeutic proteins administrated.[262–264] Particularly, throughout evolution, complex living organisms have perfected their defense mechanisms against foreign particles such as pathogens, exogenous proteins and particles. As a result, proteins injected intravenously are often cleared out rapidly with undesired accumulation commonly in the liver, spleen or kidney.[154,205,265]

Extensive efforts have been made to improve the efficacy of protein therapeutics. At present, the most widely-applied approach is modifying the proteins with poly(ethylene glycol) (PEG), which leads to improved protein stability, prolonged circulation time, and reduced immune response.[266–268] However, ~25% of the patients have already possessed or started to develop the anti-PEG antibodies prior to or after the first administration of PEG-modified proteins nowadays, which results that PEG-based protein therapeutics injected are subsequently opsonized by the circulating antibodies and cleared rapidly, resulting in an accelerated blood clearance and reduced efficacy.[269–271] Another type of approaches for avoiding the rapid clearance is achieved by bonding nanostructures

with zwitterionic polymers such as phosphobetaine-, sulfobetaine-, and carboxybetaine-based polymers.[272–279] Compared to PEG and other hydrophilic polymers that achieve hydration via hydrogen bonding, zwitterionic polymers bind water molecules much more strongly via electrostatically induced hydration,[280,281] resulting a unique surface that resists non-specific protein absorption. Due to their outstanding biocompatibility and protein-adsorption-resistant ability, such polymers have been explored as antifouling coatings for blood-contacting devices, drug delivery carriers, and contrast agents for imaging.[274,282–287] Recently, conjugation of proteins and zwitterionic polymers have also been investigated, and the resulting conjugates exhibited similar pharmacokinetics kinetic profiles as pegylated protein conjugates[288] without compromise their biological activities.[289] All these evidences imply that zwitterionic polymers could potentially become the next-generation biomaterials that boost the development of protein therapeutics.

Towards better protein therapeutics, it is of paramount importance to design therapeutics that can evade the clearance mechanisms, mainly the mononuclear phagocyte system (MPS).[290–292] From an anatomo-physiological perspective, intravenously injected therapeutics are transported to the heart, continue on to the pulmonary circulation, return to the left ventricles, and pumped into the system circulation.[293] In the blood stream, these therapeutic particles may adhere with the plasma proteins, such as lipoproteins, apolipoproteins and proteins of complement. It has been known that charged, highly hydrophobic, irregular or low-curvature surface generally promotes the opsonizing process.[294] The opsonization with the lipoproteins and apolipoproteins compels the particles trafficking toward the hepatocytes and tissues rich in lipoprotein receptors; while the opsonization with the complement proteins enables the recognition and clearance by the phagocytic cells via phagocytosis.[295,296] Minimizing the adhesion with the plasmas proteins and weakening the

interactions with macrophages, therefore, could lead to protein therapeutics with evading capability.
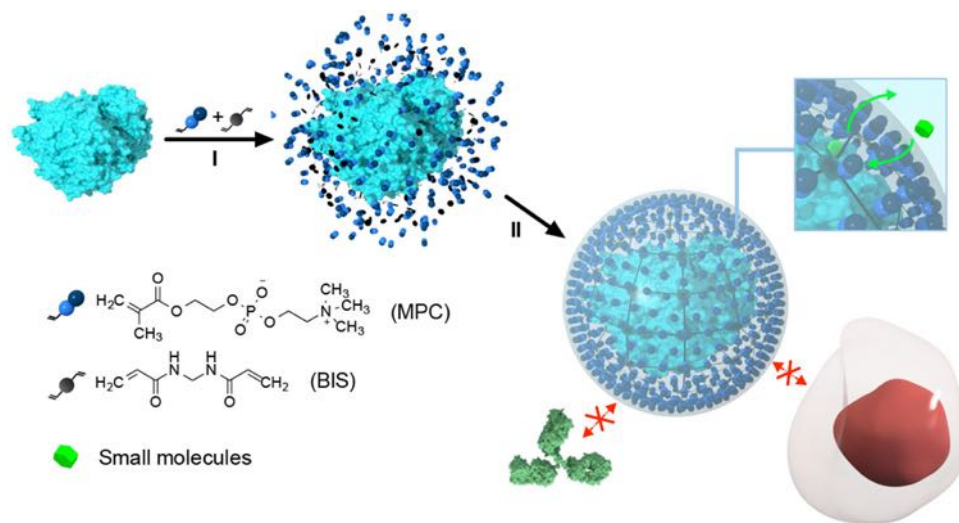
*Figure 3-1 Schematic illustration of the synthesis of stealth protein nanocapsules by (**I**) enriching 2-methacryloyloxyethyl phosphorycholine (MPC, monomer) and N,N'-methylenebis(acrylamide) (BIS, crosslinker) around a protein molecule, and (**II**) in situ polymerization of the monomer and crosslinker forming a thin shell of poly(2-methacryloxyloxyethyl phosphorycholine) (PMPC) around the protein molecule. The PMPC shells are permeable to small-size substrates ensuring effective enzymatic reactions occurred within the protein cores; such zwitterionic shells also resist the adsorption of proteins and phagocytosis, endowing the nanocapsules with stealth capability.*

Rooting from the defense mechanism, we envision that stealth protein therapeutics could be made by coating individual protein molecules with a thin layer of zwitterionic polymer to resist non-specific protein absorption. As illustrated in Figure 3-1, using 2-methacryloyloxyethyl phosphorycholine (MPC) as the monomer and N,N′-methylenebisacrylamide (BIS) as the crosslinker, a thin layer of crosslinking polyMPC (PMPC) can be readily grown around the protein molecules through *in situ* polymerization.[49,204] Compared to direct conjugation of zwitterionic polymer chains to the protein surfaces, this in situ polymerization approach encapsulate the protein with

crosslinked PMPC, which completely replaces the protein surface with the zwitterionic polymer and thus provides better shielding effects from serum protein adsorption under blood flow. This simple technique enables the synthesis of a family of stealth nanocapsules denoted as n(Protein), where Protein within the parentheses is the protein being encapsulated.

3.2 Methods, experiments, and characterizations

3.2.1 Materials and Instruments

Reagents and solvents were purchased from Sigma-Aldrich (St. Louis, MO) and used as received without further purification unless otherwise noted. U87 and J774A.1 cells were purchased from American Type Culture Collection (ATCC). The Dulbecco's Modified Eagle Medium (DMEM) growth medium and Penicillin/streptomycin were obtained from Invitrogen (Carlsbad, CA). Fetal Bovine Serum (FBS) was obtained from Lonza Walkerrsville Inc. (Walkerrsville, MD). CellTitra Blue cell viability kit was purchased from Promega (Madison, WI). Fluorescence dyes including Rhodamine B isothiocyanate and Fluorescein isothiocyanate were obtained from Sigma-Aldrich (St. Louis, MO). Proteins including human transferrin (Tf), ovalbumin (OVA), horseradish peroxidase (HRP), glucose oxidase (GOx), and alcohol oxidase (AOx) were purchased from Sigma-Aldrich (St. Louis, MO). Uricase (UOx) was purchased from Worthington Biochemical Corporation (Lakewood, NJ). Bovine serum albumin (BSA) was purchased from Equitech-Bio Inc (Kerrville, TX). Male BALB/C (6-8 weeks) mice were purchased from Jackson Laboratory (Bar Harbor, ME). Male Kun Ming (KM) mice (6-8 weeks) were purchased from the Chinese Academy of Sciences Research Institute in Shanghai, China. 2-Methacryloyloxyethyl phosphorylcholine (MPC), acrylamide, acrylic acid, N-hydroxylsuccinimide ester, N,N'-methylenebisacrylamide, ammonium persulfate, and N,N,N',N'-tetramethylethylenediamine were purchased from Sigma-

Aldrich and used without further purification. N-(3-Aminopropyl) methacrylamide hydrochloride was purchased from Polymer Science, Inc. Bicinchoninic acid disodium salt hydrate (BCA) and copper sulfate were purchased from Sigma-Aldrich and used as received. Phenyl-Sepharose CL-4B, Sepharose-6B, and Sephadex G-25 were purchased from Sigma-Aldrich.

UV-Visible spectra were acquired with a DU730 spectrometer (Beckman Coulter, Inc.). Dynamic light scattering (DLS) studies of the nanocapsules were performed on Zetasizer Nano instrument (Malvern Instruments Ltd., United Kingdom) equipped with a 10 mW helium-neon laser ($\lambda = 632.8$ nm) and thermoelectric temperature controller. Transmission electron microscope (TEM) images were obtained on Tecnai T12 electron microscope (FEI) operating with an acceleration voltage of 120 kV. Fluorescence intensities were measured with a Fujifilm BAS-5000 plate reader. Cells were observed and photographed with a Carl Zeiss Axio Observer inverted fluorescence micro-scope. Flow cytometry analysis was achieved using a BD LSRFortessa cell analyzer. SPECT/CT images were accessed using an Inveon system (Siemens Preclinical Solutions).

3.2.2 Synthesis of the nanocapsules

3.2.2.1 Fluorescence-labeling of ovalbumin (OVA) and transferrin (Tf)

For the imaging purposes, OVA and Tf were fluorescene-labeled with rhodamine B (RhB) and fluorescence (FITC), respectively. Briefly, the proteins were first dissolved with water and dia-lyzed against sodium carbonate buffer (20 mM, pH 8.5) to remove any ammonium sulfate that usually exists in the stock protein powder. After dialysis, the proteins were diluted to 5 mg/ml with sodium carbonate buffer (20 mM, pH 8.5). Rhodamine B isothiocyanate (RhB-TIC) and fluorescence isothiocyanate (FITC) were dissolved with DMSO to make 1% (m/v) stock solutions, respectively. Then RhB-ITC and FITC stock solutions were added into OVA and Tf solutions at

a molar ratio of 5:1 (Dye:Protein), respectively. The reactions were kept at 4°C for overnight; as-formed samples were dialyzed against sodium carbonate buffer (20 mM, pH 8.5) to remove the unconjugated dye.

3.2.2.2 Acryloxylation of the proteins

Acryloxylation of the proteins used in this work was achieved with the same methods described in Chapter 1, Section 2.2.2.3 The number of acryloyl groups conjugated onto the proteins is listed in Table 3-1.

Table 3-1 Average number of acryloyl groups conjugated to the proteins

Protein	Total No. of Lys	Unreated Lys (%)	Average No. of acryloyl groups conjugated
EGFP	20	42.24%	11.55
OVA	20	22.27%	15.55
HRP	5	13.71%	4.32
GOx	15	44.47%	8.33
UOx	26	34.69%	16.98
AOx	38	53.15%	17.80
Tf	58	68.27%	18.40
BSA	59	71.64%	16.73

3.2.2.3 Synthesis of n(EGFP), n(OVA), n(HRP), n(GOx), n(UOx), n(AOx), n(Tf), and n(BSA)

After acryloxylation, the proteins were encapsulated with PMPC using an *in situ* polymerization method. 2-methacryloyloxyethyl phosphorylcholine (MPC) and bis-methacrylamide (BIS) were first prepared as 10% (m/v) stock solution in DI-water and anhydrous DMSO, respectively. Then MPC and BIS were added into the solution of the proteins being encapsulated with a specific molar

ratio (listed in Table S2). The final protein concentration was tuned to 1 mg/mL by diluting with phosphate buffer (50mM, pH 7.0). Polymerization was initiated by the addition of ammonium persulfate (APS) and tetramethylethylenediamine (TEMED) and kept at 4°C for 2 h. After the polymerization, the solution was dialyzed against PBS to remove unreacted monomers and by-products. The detailed synthesis parameters of n(EGFP), n(OVA), n(HRP), n(GOx), n(UOx), n(AOx), n(Tf), and n(BSA) were listed in Table 3-2.

Table 3-2 Synthesis parameters of various PMPC protein nanocapsules

Sample	Protein	MPC	BIS	APS	TEMED
n(EGFP)	1	3000	400	250	500
n(OVA)	1	3000	400	400	800
n(HRP)	1	3000	400	300	600
n(GOx)	1	16000	2400	800	1600
n(UOx)	1	10000	1400	600	1200
n(AOx)	1	80000	11000	4000	8000
n(Tf)	1	3000	400	400	800
n(BSA)	1	3000	400	400	800

* All numbers indicate the molar ratios.

3.2.2.4 Synthesis of positively charged n(EGFP)(+)

The synthesis of positively charged n(EGFP)(+) is similar as that of n(EGFP). Instead of using MPC solely as monomer, mixture of MPC and N-(3-Aminopropyl) methacrylamide hydrochloride (APm) with a molar ratio of 9:1 was employed as monomer in the polymerization step. The final molar ratio of monomer to EGFP was kept as 3000:1. After tuning the EGFP concentration to 1.0 mg/mL with phosphate buffer (50mM, pH 7.0), the polymerization step was initiated using

APS/TEMED (1:250:500, EGFP:APS:TEMED, n/n/n), and the reaction was kept at 4°C for 2 h. The reaction solution was then dialyzed against PBS to remove reaction by products.

3.2.2.5 Synthesis of PAAM-n(EGFP)

The PAAM-n(EGFP) was prepared using the method we described before. Acrylamide (AAm) was employed as monomer for the encapsulation of EGFP. Briefly, acryloxyl-EGFP was first mixed with AAm and BIS at specific ratio (EGFP:AAm:BIS = 1:2000:300, n/n/n). After tuning the protein concentration to 1.0 mg/mL with phosphate buffer (50mM, pH 7.0), the reaction was initiated using APS/TEMED (EGFP:APS:TEMED = 1:250:500, n/n/n). The reactions were kept at room temperature for 2 h. The reaction solution was then dialyzed against PBS to remove reaction by products.

3.2.2.6 Synthesis of positively charged PAAM-n(EGFP)(+)

The preparation of positively charged PAAM-n(EGFP)(+) was achieved with a similar method as the synthesis of PAAM-n(EGPF). The mixture of AAm and APm with a molar ratio of 9:1 was employed as monomer for the encapsulation. After mixing the monomers with EGFP, the final molar ratio of EGFP and two monomers is 1:1800:200 (EGFP:AAm:APm). After tuning the protein concentration to 1.0 mg/mL with phosphate buffer (50mM, pH 7.0), the polymerization step was initiated using APS/TEMED (EGFP:APS:TEMED = 1:250:500, n/n/n), and the reactions were kept at 4°C for 2 h. The reaction solution was then dialyzed against PBS to remove reaction by products.

3.2.2.7 Purification of the protein nanocapsules

After dialysis, protein nanocapsules were passed through columns by gravity to remove unencap-sulated proteins. Based on the different physical properties, PMPC protein nanocapsules n(Pro-tein) and PAAM-based protein nanocapsules were purified with hydrophobic interaction column (Phenyl-Sepharose CL-4B) and size exclusion column (Sepharose-6B), respectively. For the pu-rification of n(Protein), the column was prepared by pipette 5 mL of Phenyl-Sepharose CL-4B into a glass column. Before loading the samples, the column was pre-equilibrated with 2.5 M sodium sulfate. The nanocapsules were first mixed with sodium sulfate powder to make the final concen-tration of sodium sulfate to 2.5 M. Then, the samples were loaded onto the column and eluted with 2.5 M sodium sulfate solution. Since the nanocapsules possess a super-hydrophilic surface, their binding affinity to the column is much weaker than the native protein, especially in such a condition with high salt concentration (2.5 M sodium sulfate). Thus, encapsulated protein will eluted with 2.5 M sodium sulfate, whereas the native protein binds on the column. The elution with 2.5 M sodium sulfate was collected and condensed using centrifugal filtration. The sample was then dialyzed against PBS to remove the sodium sulfate, and stored at 4°C for further studies.

The purification of PAAM-n(Protein) was achieved using the method we described before. It was achieved by passing the samples through a Sepharose-6B column by gravity. Sepharose column was prepared by pipette 5 mL of Sepharose 6B beads into a glass column. The column was then pre-equilibrated with PBS. After equilibration, the samples were loaded in the column, and then eluted with PBS. Because the fractionation range of Sepharose-6B is 10,000-4,000,000 Da, en-capsulated proteins (PAAM-n(Protein)) are too big to enter the pores of the Sepharose beads, as a result, eluted first during the elution. Eluted solution was collected in a volume of 100 μL per fraction, and the absorbance at 280 nm of each fraction was measured with a UV/Vis meter by

using elution buffer (PBS) as background. Fractions of the encapsulated proteins (first A280 peak) were collected, combined, and then condensed using centrifugal filtration. Protein nanocapsule solution was stored at 4°C for further studies.

3.2.2.8 Determination of the protein concentrations

Protein concentrations of protein nanocapsules, including n(OVA), n(EGFP), n(EGFP)(+), PAAM-n(EGFP), PAAM-n(EGFP)(+), n(HRP), n(GOx), n(UOx), n(AOx), and n(Tf), were determined using BCA micro-assay. Before the tests, two BCA reagents were prepared using the following recipes. Reagent A was prepared by dissolving 0.1 g bicinchoninic acid disodium salt hydrate (BCA), 0.32 g sodium carbonate, 0.01 g tartate acid in 10 mL DI-water, following by tuning the pH to 11.25 with 1 M NaOH solution. Reagent B was prepared by dissolving 0.2 g $CuSO_4 \cdot 5H_2O$ in 5 mL DI-water. BCA working solution (BWS) was prepared by mixing 50 volume of Reagent A and 1 volume of Reagent B together.

Standard curves of each protein were established using the native protein with a series of concentrations (0.0078125, 0.015625, 0.03125, 0.0625, 0.125, 0.25, 0.5, 1 mg/mL). This was achieved by repeating 2-fold dilutions of 1 mg/mL protein solution with PBS in a 384-well plate. BCA assays were conducted by adding 10 μL of native protein solutions with different concentrations into each well of 384-well plate, respectively, following by the addition of 10 μL of BCA working solution (BWS). In the meanwhile, 10 μL of protein nanocapsule solution was also added into the same plate, following by the addition of 10 μL of BWS. The plate was then incubated at 65°C for 1 h. Absorbance at 550 nm of each well was read out by using a plate reader. Concentration of the encapsulated protein was calculated by using its absorbance at 550 nm and the standard curve established at the same condition.

3.2.3 TEM and DLS studies of the protein nanocapsules

TEM samples were prepared by drop-coating of 2 μL n(EGFP) solution and n(OVA) onto carbon-coated copper grids, respectively. Droplets of the samples were contacted with the grids for 45 s, then excess amount of samples was removed with Kimwipes. The grid was then rinsed, and stained with 1% sodium phosphotungstate at pH 7.0. The grid was then rinsed again, followed by the removal of excess staining agent with kimwipes. The grids were dried under vacuum and observed with a FEI Tecnai T12 transmission electron microscope.

DLS Measurements were achieved with a Malvern Zetasizer Nano instrument, with scattering angle at 173°. The particle sizes acquired from DLS were summarized in Figure 3-2.
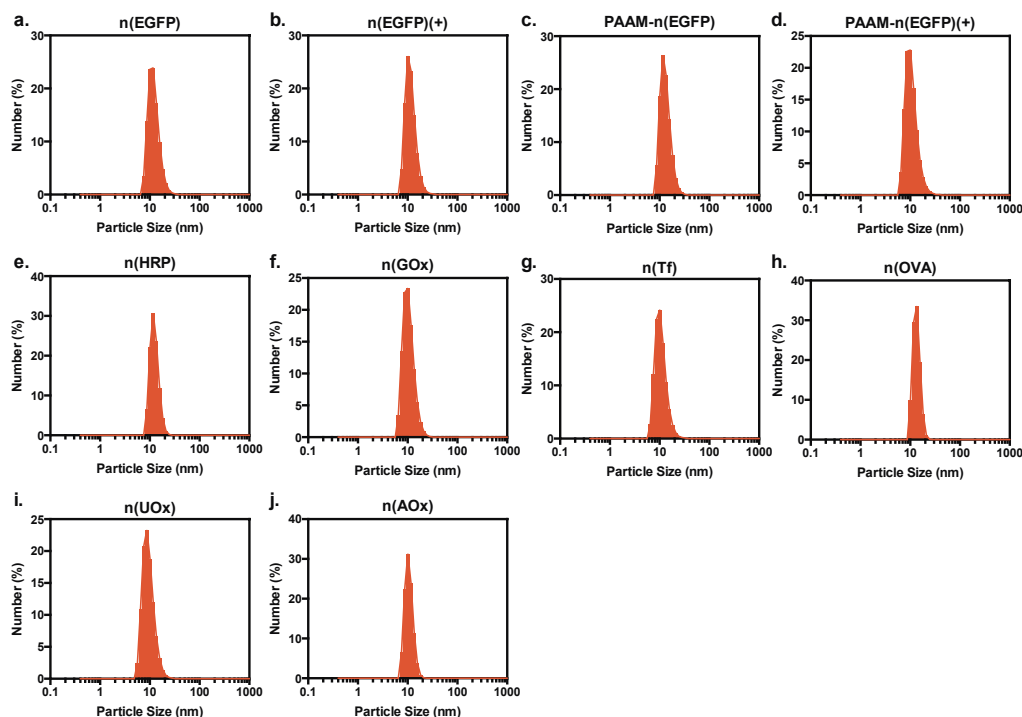
*Figure 3-2 Size distribution of **a**, n(EGFP) (mean diameter: 12.16 nm), **b**, n(EGFP)(+) (mean diameter: 11.62 nm), **c**, PAAM-n(EGFP) (mean diameter: 13.25 nm), **b**, PAAM-n(EGFP)(+) (mean diameter: 10.82 nm), **e**, n(HRP) (mean diameter: 12.46 nm), **f**, n(GOx) (mean diameter: 10.61 nm), **g**, n(Tf) (mean diameter:*

10.78 nm), **h***, n(OVA) (mean diameter: 13.46 nm),* **i***, n(UOx) (mean diameter: 9.556 nm), and* **j***, n(AOx) (mean diameter: 10.68 nm).*

3.2.4 Activity assays and stability of n(HRP), n(GOx), n(UOx) and n(AOx)

The activity of native native HRP, n(HRP), GOx, n(GOx), native AOx, and n(AOx) were determined with a method similar to that described in Chapter 1, Section 2.2.4 . Briefly, the initial reaction rates were determined by monitoring the oxidation rates of TMB of GOx and AOx when incubating with the assay solutions with different concentrations of substrates, respectively. For native GOx and n(GOx), the assay solutions were prepared by mixing TMB (0.5 mM), native HRP (0.001 mg/mL), and different amount of D-gluocose (0.005%, 0.010%, 0.015%, 0.020%, 0.030%, 0.040%, m/v) in 0.1 M phosphate buffer (pH 7.0). For native AOx and n(AOx), the assay solutions were composed by TMB (0.5 mM), native HRP (0.001 mg/mL), and different amount of ethanol (0.0025%, 0.005%, 0.0075%, 0.010%, 0.020%, 0.030%, m/v) in 0.1 M phosphate buffer (pH 7.0). The measurements were achieved by monitoring the A655 of the reaction solutions during the incubation of 1 µL of native enzyme or n(Protein) (0.5 mg/mL for native GOx and n(GOx), 1 mg/mL for native AOx and n(AOx)) with their corresponding assay solutions.

Table 3-3 Kinetic parameters of n(HRP), n(GOx), n(UOx), n(AOx) and their native enzyme counterparts

Sample	$K_M^{app}(mM)$	$k_{cat}^{app}\ (s^{-1})$	k_{cat}^{app}/K_M^{app}	
			$mM^{-1}s^{-1}$	%
native HRP	0.0925±0.0213	4.03×10^2	4356.7±989.0	100±22.7
n(HRP)	0.121±0.0340	4.80×10^2	3966.9±1114.7	91.1±28.1
native GOx	18.00±6.21	87.9	4.883±1.684	100±34.5
n(GOx)	21.56±6.70	77.6	3.600±1.119	73.7±31.1
native UOx	0.0219±0.0017	3.36	153.4±11.8	100±7.7
n(UOx)	0.0259±0.0043	3.59	138.6±22.9	90.4±16.5
native AOx	3.109±0.720	18.8	6.047±1.428	100±23.61

n(AOx)	5.120±1.433	23.4	4.570±1.279	75.6±28.00

Native UOx and n(UOx) activities were determined by monitoring the decrease of A290 with UV-spectrometer during the incubation of 1 μL native UOx or n(UOx) (0.714 mg/mL) with a series urate solutions (pH = 8, 0.1 M borate buffer, urate concentrations: 0.005%, 0.010%, 0.015%, 0.020%, 0.030%, 0.040%, m/v). The initial rates were achieved by plotting the absorption at 290 nm versus time and calculating the ΔA290/min from the linear potion of the curve.

Thermal stability of native UOx and n(UOx) was conducted using the following procedure: the solutions of native UOx and n(UOx) (0.714 mg/mL, 10 mM phosphate buffer, pH 7.0) were first incubated at 37℃ for certain periods (1-120 hr), followed by quenching on ice bath and recovering to room temperature. UOx activity assays were then performed with these samples to determine the residual activities of native UOx and n(UOx).

The stability of native UOx and n(UOx) against protease was conducted using the following protocol: the solutions of native UOx and n(UOx) (0.714 mg/mL, 10 mM borate buffer, pH 8.0, 10 mM Ca^{2+}) were mixed with trypsin stock solution (10 mg/mL) to bring the final trypsin concentration to 0.1 mg/mL. The control groups of native UOx and n(UOx) solutions were prepared by mixing the stock solutions with same volume of PBS as that of trypsin solution. The preparation of these four solution were performed in an ice bath to avoid the activation of trypsin. After the preparation, the four solutions were incubated at 37°C for certain periods (20 - 180 min), followed by quenching on ice bath. UOx activity assays were then performed with these samples to determined the residual activities of native UOx and n(UOx).

3.2.5 Quantification of the protein adsorption

Protein adsorption was quantified using the following method. 10 µL of PBS (negative control), n(EGFP) (1 mg/mL), PAAM-n(EGFP) (1 mg/mL), and native EGFP (1 mg/mL) were mixed with 30 µL of mouse whole serum and incubated at 37°C for 30 min, respectively. After incubation, samples were filtered and washed with PBS for 3 times with centrifugal filtration (molecular weight cut-off, MWCO = 100 kDa) to remove any unabsorbed serum proteins. After reconstituting with 50 µL of PBS, the amount of EGFP in each sample was determined by measuring the absorbance at the wavelength of 450 nm with a nanodrop. To better quantify the amount of serum proteins adsorbed, specific amounts of native EGFP were added to the samples respectively to ensure the same EGFP concentrations among all the samples. Finally, the amount of protein adsorbed was determined by measuring the overall protein concentration of each sample with BCA assay using BSA as the standard. Statistical analysis were performed using the Tukey post-test following a one-way ANOVA. $P < 0.05$ or less was considered significant.

3.2.6 Cell viability assay

The toxicity of n(Protein), including n(EGFP), n(OVA), n(UOx), and n(AOx) was evaluated by measuring the cell viability after the incubation of U87 cells with different amount of n(Protein) (0.01 mg/mL, 0.05 mg/mL, 0.10 mg/mL, 0.20 mg/mL) for 24 h. For better comparison, the toxicities of native EGFP, OVA, UOx, and AOx were also tested with the same method. U87 cells were seeded into a 96-well plate (10^4 cells/well, 100 µL/well) and cultured in DMEM (normal level of glucose in medium, with 10% FBS) for a day prior to exposure to the samples. After the addition of n(Protein)s and their native counterparts respectively, cells were further incubated for 24 h. After incubation, CellTiter-Blue (20 µL) was added into each well and further incubated for 3 h. The plate was then placed on a shaking table at 150 rpm for 5 min to thoroughly mix the

solution. Viable cells reduce CellTiter Blue and show fluorescent reddish color. Quantification of the cell viability was achieved by measuring the fluorescence intensities with a plate reader (Ex = 535 nm, Em = 585 nm). The viability of untreated cells was used as 100% during the data analysis.
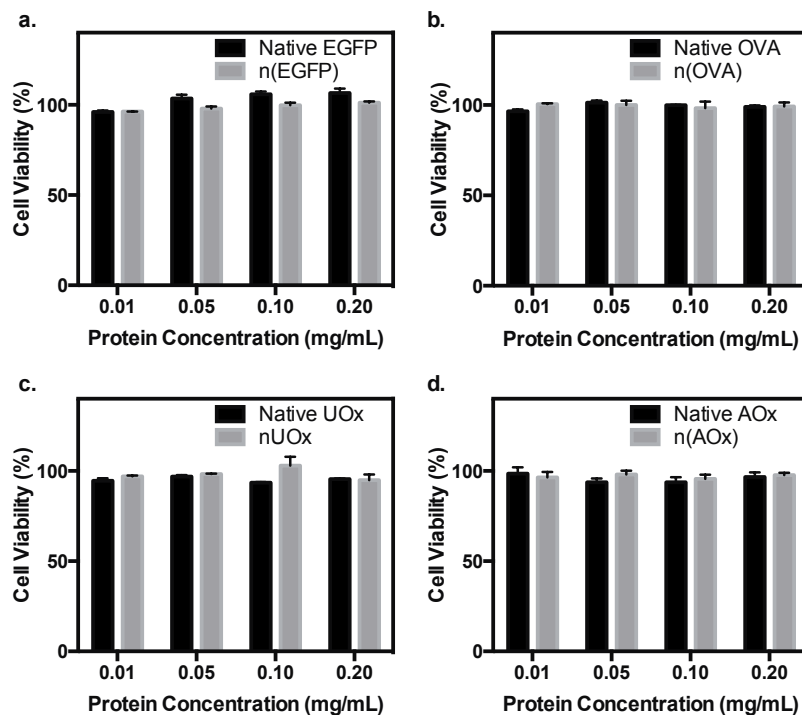
Figure 3-3 Viability of the cells treated with n(EGFP), n(OVA), n(UOx), and n(AOx) and their corresponding native proteins at different concentrations.

3.2.7 Cell uptake of EGFP nanoparticles with different surface properties

To evaluate the effect of surface in cell internalization, we encapsulated EGFP with PAAM and PMPC to obtain PAAM-n(EGFP) (zeta potential ζ = -3.38 mV) and n(EGFP) (zeta potential ζ = -0.222 mV), respectively, and also prepared positively charged PAAM-n(EGFP)(+) (zeta potential ζ = +1.27 mV) and n(EGFP)(+) (zeta potential ζ = +1.08 mV) by introducing APm during the polymerization. The study was achieved by incubating U87 cells with the EGFP nanocapsules.

93

U87 cells were seeded into a 96-well plate (10^4 cells/well, 100 μL/well) and cultured in DMEM (normal level of glucose in medium, with 10% FBS) for a day prior to exposure to the samples. EGFP nanocapsules, including PAAM-n(EGFP), PAAM-n(EGFP)(+), n(EGFP), and n(EGFP)(+), were then added to the cells (10 μg/well) and incubated at 37°C for 4 hrs. After the incubation, cells were rinsed with PBS (1X) for three times to remove the excess samples and culture medium. Fluorescence intensity of the cells were read out using a plate reader (Fujifilm BAS-5000). After the measurement of the fluorescence, the cells were lysed with cell lysis buffer, and the total protein concentration of each well of cells was determined with BCA assay using BSA as standard. The fluorescence intensity of each well was then normalized with the corresponding protein concentration. All the statistical analyses were performed using the Tukey post-test following a one-way ANOVA. $P < 0.05$ or less was considered significant.

The study on the receptor-mediated endocytosis of Tf was achieved by incubating fluorescence-labeled native Tf and n(Tf) with U87 cells, and then evaluating the uptake by measuring the cellular fluorescence intensity. Briefly, U87 cells were plated in a 96-well plate at 5k cells/well one day prior to the exposure to the native Tf and n(Tf). After incubation at 37°C for 4 hrs, the cells were rinsed with PBS (1X) for three times. Fluorescence intensity of the cells were read out using a plate reader (Fujifilm BAS-5000). After the measurement, the cells were lysed with cell lysis buffer, and the total protein concentration of each well of the cells was determined with BCA assay using BSA as standard. The fluorescence intensity of each well was then normalized with the corresponding total protein concentration. The cell-uptake of EGFP nanocapsule with different surface charges was achieved with the similar method, which is detailed in the supplementary information. All the statistical analyses were performed using the Tukey post-test following a one-way ANOVA. $P < 0.05$ or less was considered significant.

94

Phagocytosis was studied using J774A.1 mouse macrophage, which were cultured according to the standard protocol (DMEM with 10% FBS, 37°C, 5% carbon dioxide) and plated into a 96-well plate (5k cells/well) one day prior to the studies. Since the J774A.1 cells have complement receptor (C3R) expressed, complement activation was tested by pre-incubating native OVA and n(OVA) with mouse whole serum at 37°C for 30 min. The macrophage were then incubated with the native OVA or n(OVA) for 1 hr, rinsed with PBS (1X) for three times, and observed using a fluorescence microscope (Carl Zeiss Axio Observer) after staining with Hoechst 33342 20 min prior to the observation. The cells were also cultured in a 24-well plate at the density of 30k cells/well and exposed to the samples. After detaching the cells by scraping, phagocytosis levels were accessed with flow cytometry analysis (BD LSRFortessa cell analyzer). All flow cytometry data were analyzed using FlowJo.
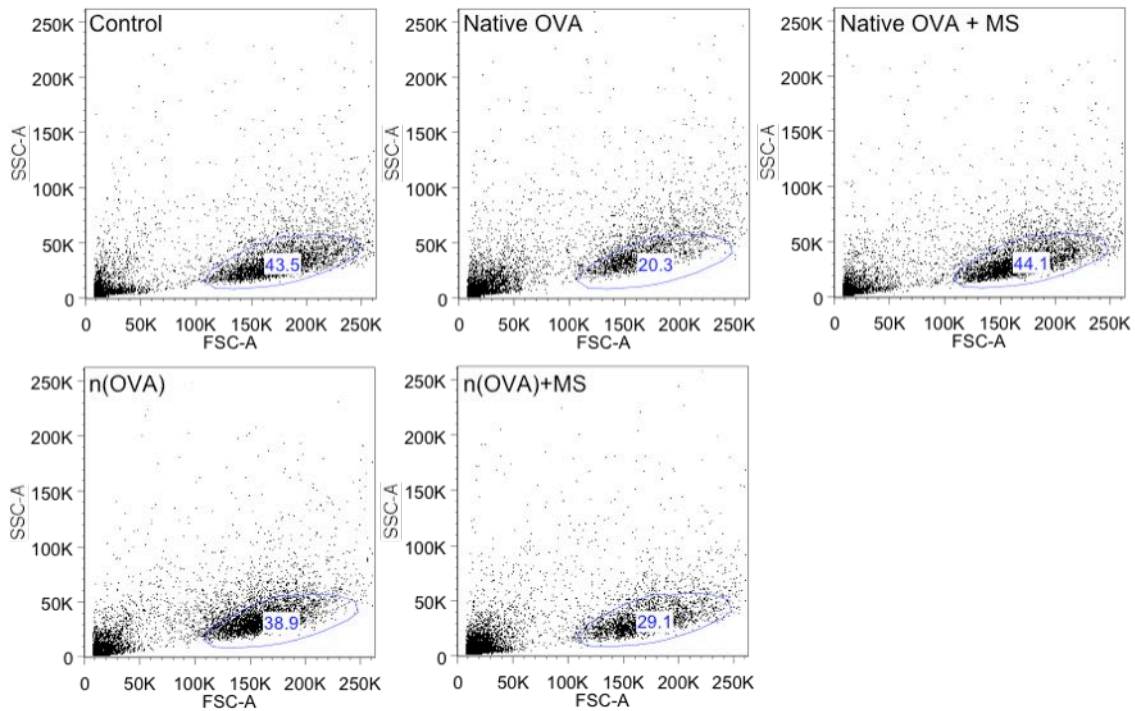
Figure 3-4 Dot plots indicating the ungated cells and gates used in the flow cytometry analysis

95

Table 3-4 FACS results of macrophages after exposure to OVA and n(OVA)

Sample	Events	%Gated	%RhB -	%RhB +	Mean Fluorescence	% Robust CV
Control/mock	10000	43.5	99.8	0.207	217	54.9
native OVA	10000	20.3	5.03	95	2558	51.3
native OVA + MS	10000	44.1	0.159	99.8	5229	49.8
n(OVA)	10000	38.9	63.7	36.3	810	45.4
n(OVA) + MS	14508	29.1	48.2	51.8	946	48.5
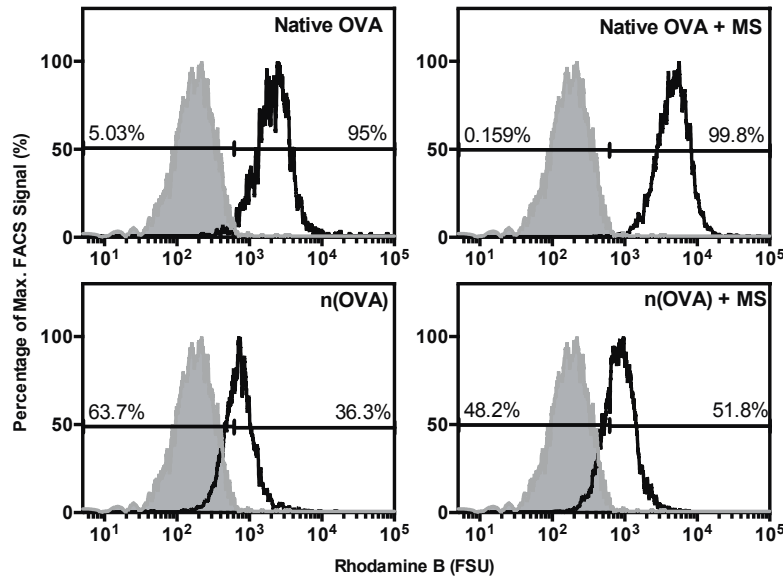
Figure 3-5 Fluorescence-assisted cell sorting (FACS) analysis of macrophage cells after 1 hr incubation with native OVA, native OVA+MS, n(OVA), and n(OVA)+MS.

3.2.8 Engulfment of n(OVA) by human blood peripheral cells (PBMCs)

Native OVA and n(OVA) were first labeled with rhodamine B for observation and quantification.

Human PBMCs were obtained without identifying information from the UCLA Center for AIDS

Research (CFAR) Virology Core Laboratory in accordance with UCLA Institutional Review Board (IRB) approved protocols along with an IRB-approved written consent form. PBMCs from 5 donors were isolated from leukopacks by Ficoll 48 hours before transduction. Half of the cells were cultured in RPMI medium, 20% FBS, 1% GPS (L-Glutamine/penicillin/streptomycin) to maintain the quiescent status for 2 days, while the other half were stimulated in RPMI medium, 20% FBS, 1% GPS with 20 units/ml IL-2 and 25 μg/mL PHA for 2 days. PBMCs were plated into a 48-well plate at a density of 1×10^5 cells per well in Opti-MEM medium. The PBMCs were transduced with PBS, native OVA, and n(OVA) respectively for 4 hrs. The cells were washed in FACS buffer twice and fixed with 2% formaldehyde in PBS. Fluorescent intensity was examined on LSRFortessa (BD Biosciences). The data were analyzed by FlowJo (TreeStar) software. In the live cell gate, lymphocyte population was isolated based on FSC-A vs FSC-H plot and FSC-A vs SSC-A plot. The fluorescent analysis was performed within lymphocyte populations. The rhodamine B positive gate (RhB +) was set based on the PBS treated control sample.
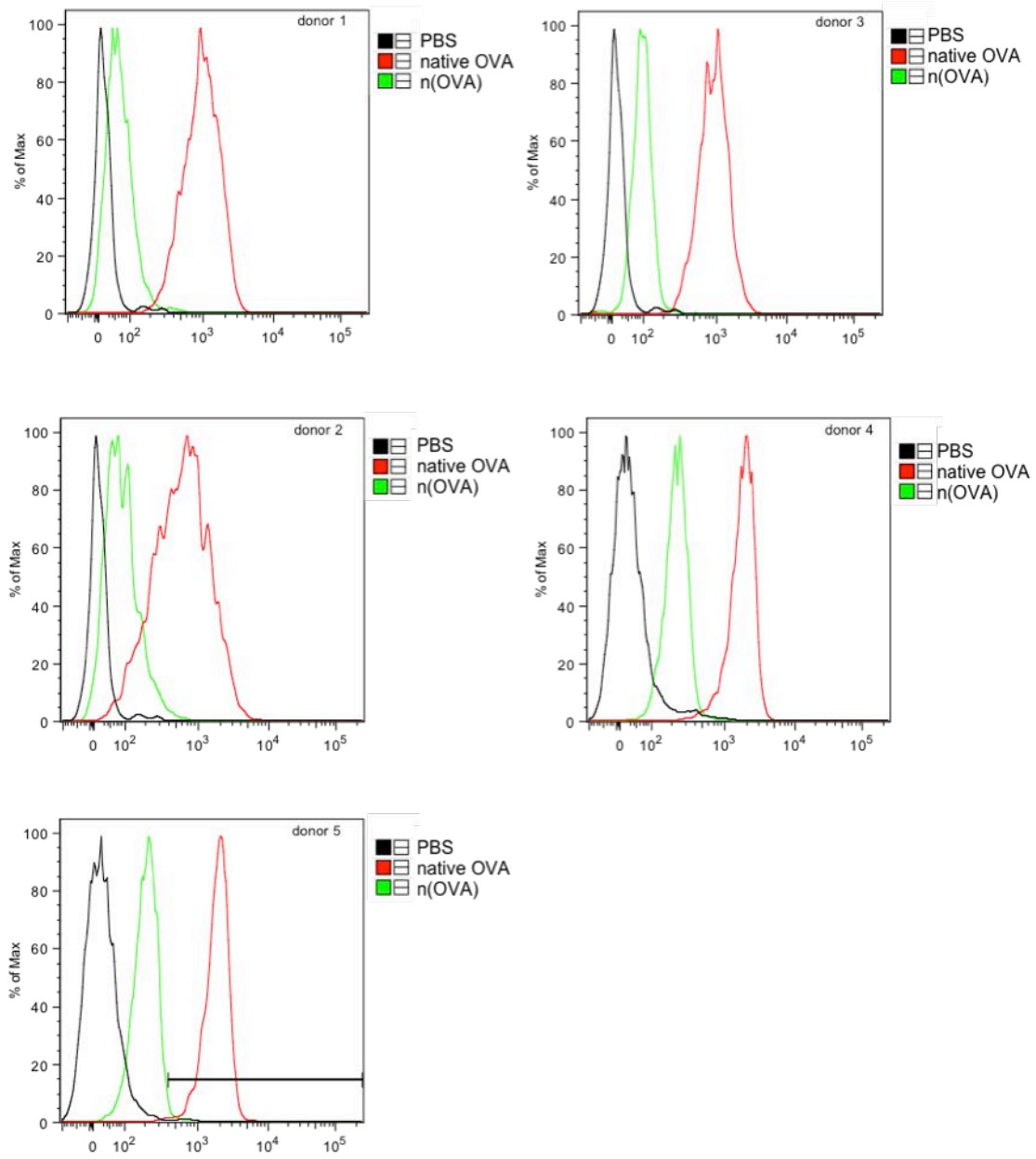
Figure 3-6 FACS analysis of quiescent PBMCs after 4 hr incubation with native OVA and n(OVA).
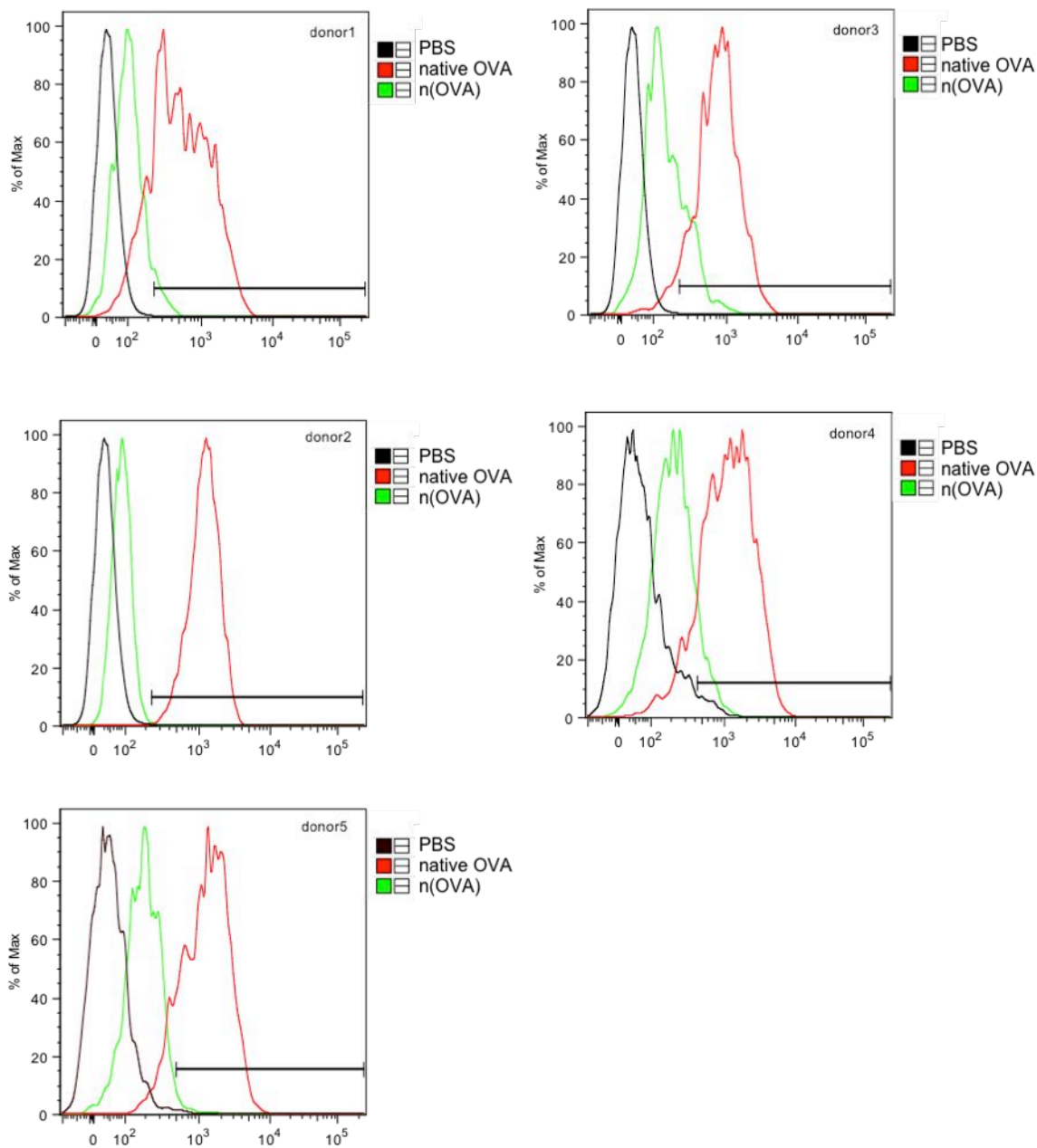
Figure 3-7 FACS analysis of stimulated PBMCs after 4 hr incubation with native OVA and n(OVA).

3.2.9 Pharmacokinetics studies of n(UOx) in mice

Pharmacokinetics (PK) profiles of native UOx and n(UOx) were accessed by monitoring the residual UOx activity in plasma after intravenous administration. Briefly, 30 mice (BALB/c) were

divided into 2 groups and injected with native UOx and n(UOx) via tail vein at a dosage of 2 Units/kg body weight, respectively. As a negative control, another 15 mice were injected with 100 µL of PBS. The blood samples (~ 20 µL) were then taken from the tails at 1 h, 24 h, 48 h, 72 h, and 120 h after the injection. The blood samples were then centrifuged at 20 krpm for 5 min to remove the blood cells, and the UOx activity in the plasma was measured using a UOx enzyme activity assay. Residual UOx activities of were determined by incubating 5 µL of plasma with 250 µL of assay solution (0.12 M uric acid in 0.1 M borate buffer, pH = 8.5), and monitoring the absorbance change at 290 nm with a plate reader. A series of native UOx stock solutions with different concentrations (0.000778 Units/mL, 0.001556 Units/mL, 0.003125 Units/mL, 0.00625 Units/mL, 0.0125 Units/mL, 0.025 Units/mL and 0.05 Units/mL) were then prepared and used to establish the relationships between reaction rates and UOx concentrations.

The analysis of the PK data was achieved by fitting the data using a one-phase exponential decay model with the constraints of Y0 < 0.03 (maximum UOx concentration cannot be higher than 0.03 Units/mL) and Plateau = 0. All data analysis was achieved using Graphpad Prism.

Table 3-5 Pharmacokinetics parameters of native UOx and nanocapsules

Parameters	native UOx	n(UOx)
$k\,(h^{-1})$	0.4338±0.06449	0.01604±0.002424
$t_{1/2}\,(h)$	1.598±0.2376	43.22±6.531
$\tau\,(h)$	2.305±0.3427	62.35±9.422

3.2.10 Therapeutic effect of uricase in reducing the serum uric acid level

The therapeutic effect of native UOx and n(UOx) was accessed by monitoring the serum uric acid level of mice after intravenous administration. Briefly, 45 mice (BALB/c) were divided into 3 groups and injected with PBS (100 uL), native UOx (2 Units/kg body weight) and n(UOx) (2 Units/kg body weight) via tail vein, respectively. The blood samples (~ 20 μL) were then taken from the tails at 1 h, 24 h, 48 h, 72 h, and 120 h after the injection. The blood samples were then centrifuged at 20 krpm for 5 min to remove the blood cells, and the concentration of serum uric acid was measured using a uric acid kit with KHB310 biochemical analyzer (Shanghai Kehua Bio., China).

3.2.11 Biodistribution of n(EGFP), n(BSA), PAAM-n(BSA) and PAAM-n(BSA)(+)

The biodistributions of n(EGFP), n(BSA), PAAM-n(BSA), and PAAM-n(BSA)(+) in mice were accessed using Single-photon emission computed tomography (SPECT) / X-ray computed tomography (CT) imaging method. To allow tracing the samples after injection, n(EGFP), n(BSA), PAAM-n(BSA), and PAAM-n(BSA)(+) were radioactively labeled with ^{125}I using the iodogen method before the injection. Samples were then injected into mice (KM) via tail vein at a dosage of 100 μL (~ 0.1 mg protein) per animal, respectively. Animals were then imaged at 3 h, 24 h, 72 h, 120 h, and 168 h after the administration. For the imaging, animals were first anesthetized with intraperitoneal injection of 100 μL of sodium pentobarbital (2.5%), and then imaged with CT (~ 7 min on average), following by SPECT scanning (~ 24 min on average). The details parameters used in CT and SPECT scanning were described as follow. CT: frame resolution, 256×512; tube votage, 45 kVp; current, 0.15 mA; exposure time, 500 ms/frame. Real-time 3D reconstructions of the collected images were performed using Nucline software (v1.02, Mediso, Hungary). SPECT: for high-resolution, conical collimators with 9-pinhole plates; energy peak, 28 keV; window width,

10%; resolution, 1 mm/pixel; matrix, 256×256; projections, 24; scan time, 60 s/projection. Three-dimensional ordered subset expectation maximization images were reconstructed using HiSPECT (Bioscan, USA). The reconstruction algorithm included four subsets and the sixth-order iterative method, with a resolution of 0.4 mm/pixel.
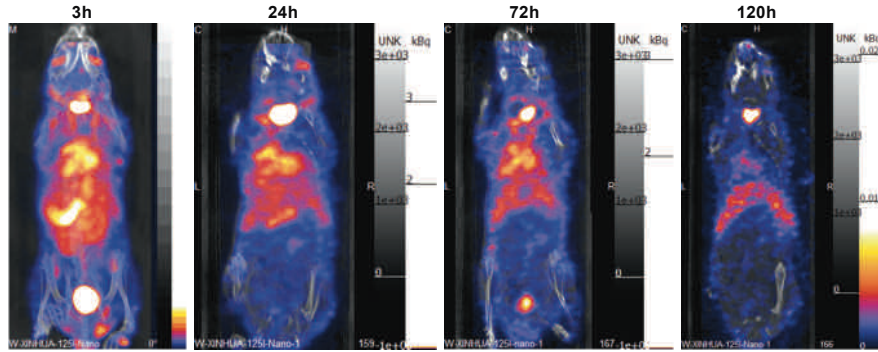
Figure 3-8 SPECT/CT images of n(BSA) acquired at 3h, 24h, 72h, and 120h.
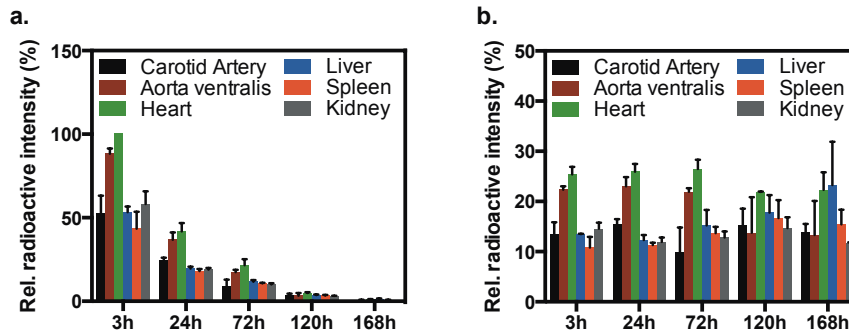
Figure 3-9 Biodistributions of n(BSA). ***a****, Quantitative analysis of the relative amount of ^{125}I-n(BSA) in blood and organs at different time. All the radioactive intensities were normalized with the intensity of heart at 3 h of each animal.* ***b****, Histogram summarizing the relative amount of n(BSA) distributed in blood and other major organs comparing to the total amount of n(BSA) at different time after the injection.*
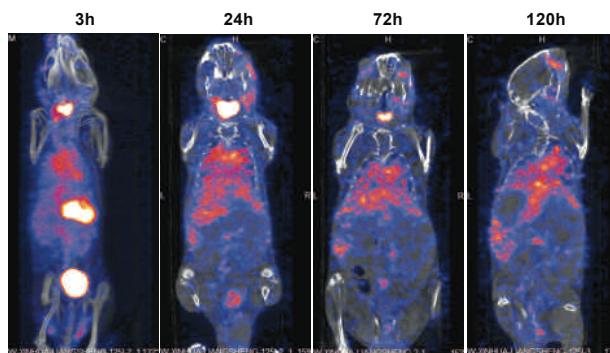
Figure 3-10 SPECT/CT images of PAAM-n(BSA) acquired at 3h, 24h, 72h, and 120h.
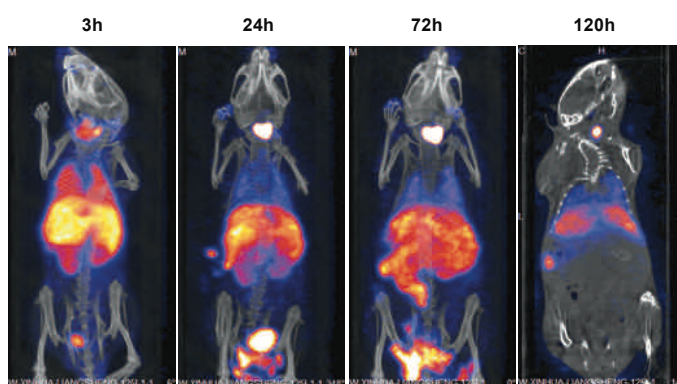
Figure 3-11 SPECT/CT images of positively charged PAAM-n(BSA)(+) acquired at 3h, 24h, 72h, and 120h.

3.2.12 Immunogenicity studies of n(OVA)

Immunogenicity of n(OVA) was accessed by measuring the serum concentration of IgG, IgE, OVA-specific IgG (OVA-sIgG), and OVA-specific IgE (OVA-sIgE) in mice after the injection of n(OVA). Briefly, 3 groups of mice (BALB/C, 5 animals per group) were administrated with PBS (blank control), 100 µg of native OVA (positive control), and 100 µg of n(OVA) (the weight indicates the weight of OVA protein) via tail vein, respectively. Blood samples were then taken from each animal 15-day post injection. The blood samples were then centrifuged to remove the blood cells, and the concentrations of IgE, IgG, OVA-sIgE, OVA-sIgG were determined with ELISA assays.

3.2.13 Accelerated clearance of native UOx and n(UOx)

Twelve male BALB/c mice were randomly divided into two groups. Animals in each group were dosed with native UOx and n(UOx), respectively, by intravenous route at 2 Units/kg body weight. The dosing volume was 8 mL/kg body weight. All animals were injected three times with 7-day interval. The blood samples were collected one hour after each injection. The blood samples were then centrifuged at 20 krpm for 5 min to remove the blood cells, and the plasma UOx levels were determined with uricase activity assay.

3.3 Results and discussions

Exemplified by the nanocapsules of enhanced green fluorescence n(EGFP) and ovalbumin n(OVA), Figure 3-12**a** and **b** respectively shows their TEM images revealing a uniform size of 25±5 nm. Since EGFP and OVA molecules have a similar size of ~8 nm, the average thickness of the PMPC shell is estimated to be 8-11 nm (also see the dynamic light scattering (DLS) in Figure 3-2). Figure 3-12**c** compares the enzyme activities of the nanocapsules of horseradish peroxidase n(HRP), glucose oxidase n(GOx), uricase n(UOx) and alcohol oxidase n(AOx) with their native enzyme counterparts, indicating that the nanocapsules retain more than 75% of their native enzyme activities (Table 3-3). The nanocapsules also show enhanced stability against thermal denature and proteolysis. As an example, Figure 3-12**d** compares the enzyme activity of n(UOx) with native UOx after incubation at 37°C for 5 days, where the native UOx lost more than 50% activity whereas n(UOx) still retained 85% of its activity. Figure 3-12**e** further compares the activity of n(UOx) with native UOx after incubation with protease trypsin, where the native UOx completely lost its activity within 40 min of incubation whereas n(UOx) still retained more than 95% of the activity even after 90 min of incubation.

Besides stablizing the proteins, the PMPC shells also prevent the nanocapsules from being opso-nized by the plasmas proteins, internalized by the cells, and uptaked by phagocytic cells. As ex-ample, after incubating n(EGFP) and native EGFP with mouse serum at 37°C for 30 min, n(EGFP) shows absence of protein adsorption whereas the native EGFP shows significant protein adsorption (Figure 3-12**f**). To confirm the anti-opsonization ability observed does arise from the PMPC shells, EGFP nanocapsules denoted as PAAM-n(EGFP) were also synthesized under a similar condition but using acrylamide (AAM) as the monomer, which do exhibit a significant adsorption of the serum proteins (Figure 3-12**f**).
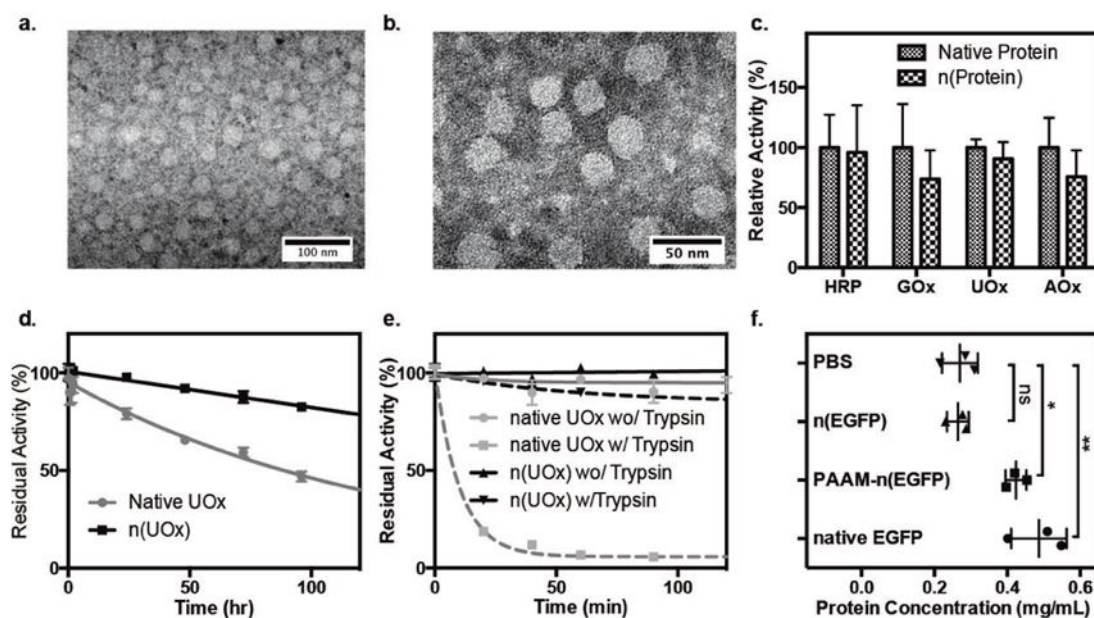
*Figure 3-12 **a, b,** Transmission electron microscopic (TEM) images of (**a**) n(EGFP) and (**b**) n(OVA) show-ing a uniform size of 25±5 nm. **c,** comparison of the enzyme activities of the nanocapsules of n(HRP), n(GOx), n(UOx), and n(AOx) and their native counterparts. **d,** Residual activities of native UOx and n(UOx) after incubating at 37°C for 5 days. **e,** Residual enzyme activities of native UOx and n(UOx) after incubation with 0.1 mg/mL trypsin at 37°C. **f,** Quantitative measurements of serum proteins adsorbed by n(EGFP), PAAM-n(EGFP), and native EGFP after incubation with mouse whole serum. Data represent mean ± standard error of the mean (s.e.m.) (**c, d, e**) and mean ± standard derivation (s.d.) (**f**) from three independent experiments.*
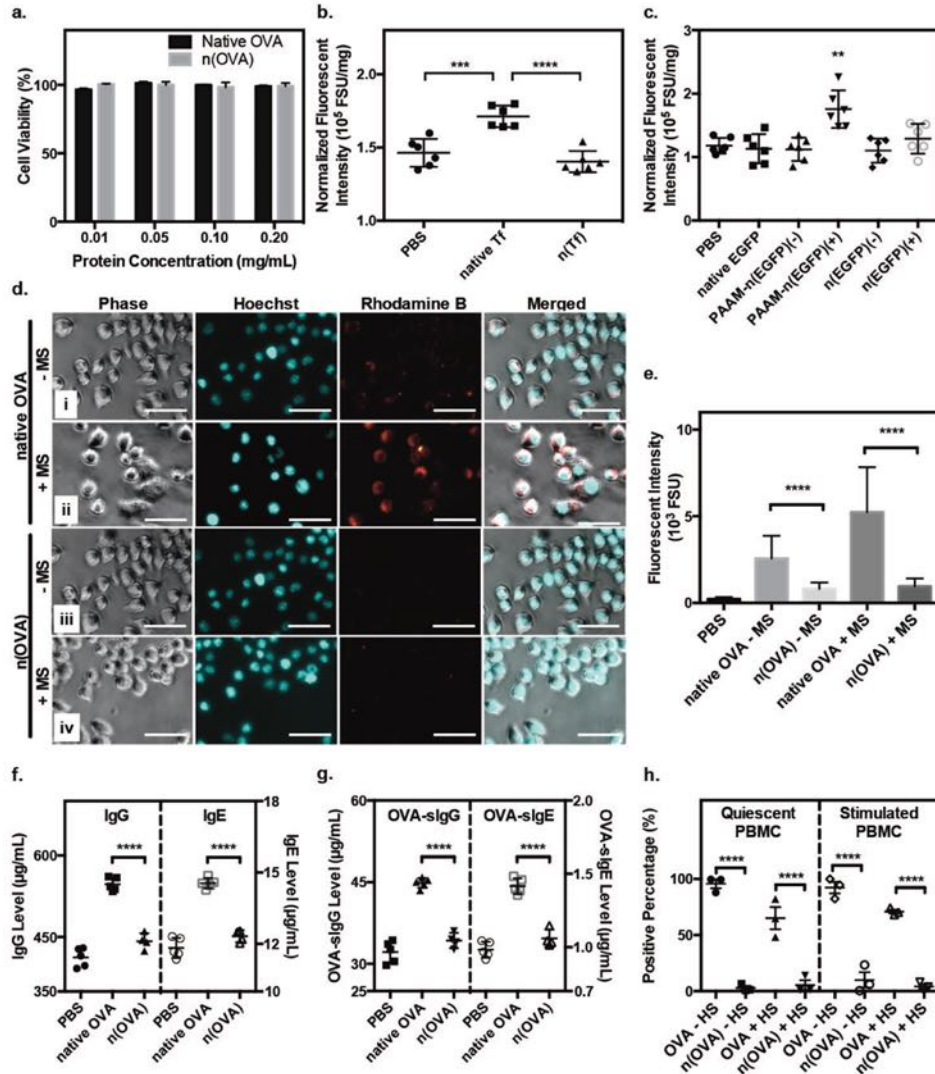
*Figure 3-13 **a**, Cell viability assays after incubating with native OVA or n(OVA) for 24 hrs. Cell viabilities were normalized with those of the untreated cells cultured in the same condition. The viability was assayed with CellTiter Blue. **b**, Receptor-mediated endocytosis level of native transferrin (Tf) and n(Tf) by U87 cells. **c**, Cell uptake level of native EGFP, positively charged (+) and negatively charged (-) n(EGFP) and PAAM-n(EGFP). **d**, Fluorescence images of J774A.1 mouse macrophages 1-hr after incubation with native OVA (**i, ii**) or n(OVA) (**iii, iv**) with (+MS) and without (-MS) pre-incubation with mouse serum (MS). Pre-incubation with mouse serum enhances the phagocytosis of native OVA but not n(OVA). Cells were stained with Hoechst 33342 for imaging the nuclei. Scalebar: 50 μm. **e**, Histogram comparing the mean fluorescent intensity accessed from fluorescence-assisted cell sorting (FACS) analysis of the macrophages after incubating with native OVA, native OVA+MS, n(OVA), and n(OVA)+MS. **f, g**, Comparison of the levels of IgG, IgE, OVA-specific IgG (OVA-sIgG), and OVA-sIgE of the mice treated with PBS, native OVA or n(OVA). **h**, Quantitative analysis of the uptake of OVA and n(OVA) by both quiescent and stimulated human*

106

The avoiding of cell internalization was demonstrated using U87 cells, which can effectively internalize transferrin (Tf) through receptor-mediated endocytosis. As shown in Figure 3-13**b**, in comparison with native transferrin that exhibits a significant uptake, incubation n(Tf) with U87 cells shows a negligible n(Tf) uptake, suggesting that the PMPC shells do prevent the internalization. For further investigation, native EGFP, n(EGFP) and PAAM-n(EGFP) with negative or positive surface charge were incubated with U87 cells, respectively (Figure 3-13**c**). As expected, native EGFP and the negatively charged nanocapsules exhibit negligible internalization. In contrast to the positively charged PAAM-n(EGFP) (zeta potential $\zeta \sim 1.27$ mV) exhibiting a significant cell uptake, n(EGFP) with similar surface charge ($\zeta \sim 1.08$ mV) shows a negligible uptake that is comparable with the negative control (PBS) and the native EGFP. In addition, HeLa cells incubated with the nanocapsules or their native enzyme counterparts for 24 h showed similar cell viabilities and unnoticeable cytotoxicity (Figure 3-13**a**, Figure 3-3).

The evaded phagocytosis was demonstrated using J744A.1 mouse macrophages. Native OVA and n(OVA) labeled with rhodamine B (RhB) were respectively incubated with the macrophages with and without pre-incubating with mouse serum. For native OVA, the macrophages show intense fluorescent signal indicating an effective phagocytosis (Figure 3-13**d, i, ii**). The macrophages with the pre-incubated OVA showed more intense fluorescence, suggesting the pre-incubation opsonizes the OVA and enhances the phagocytosis. For n(OVA), no significant phagocytosis could be

observed with or without the pre-incubation, confirming the anti-opsonization and anti-phagocy-tosis ability (Figure 3-13**d, iii, iv**). Further fluorescence-activated cell sorting (FACS) analysis confirms a 5.2-fold and 2.5-fold lower of n(OVA) uptake than the native OVA with and without the pre-incubation, respectively (Figure 3-13**e**, Figure 3-5 and Table 3-4).

To evaluate the stealth capability of the nanocapsules against the human adaptive immune system, we also tested n(OVA) using quiescent and stimulated human peripheral blood mononuclear cells (PBMCs) with and without a pre-incubation with human serum (Figure 3-13**h**). PBMCs consist mainly of monocytes, lymphocytes and dendritic cells of both myeloid and plasmacytoid origins, constituting an essential component of the human peripheral immune system.[297] Similar to the phagocytosis observed, n(OVA) with and without the pre-incubation shows a near absence of up-take by both the quiescent and stimulated PBMCs, in comparison with the native OVA (near 100% uptake with the pre-incubation or 75% uptake without the pre-incubation). The ability to evade the adaptive immune system could significantly reduce the immunogenicity. Figure 3-13**f** com-pares the IgG and IgE levels of the mice (BALB/C) treated with phosphate buffered saline (PBS, 1X), native OVA, and n(OVA), respectively. The mice treated with native OVA expressed high levels of IgG and IgE, whereas no significant elevation in the IgG and IgE levels could be observed in n(OVA)-treated group. Similar result (Figure 3-13**g**) was also observed for the OVA-specific IgG and IgE levels (OVA-sIgG and OVA-sIgE), confirming the evading ability of the nanocap-sules from the adaptive immune system (Figure 3-13**g**).

The stealth ability endows the nanocapsules with significantly prolonged circulating time and ab-sence of accumulation within any organ or tissue. Figure 3-14**a** shows SPECT-CT images of a

mice during 5 days post tail-vein injection of ^{125}I-labeled n(EGFP). Intense radioactivity was recorded in the heart, artery and veins without any obvious accumulation in the liver, kidney and spleen. Further quantitative analysis of the SPECT images was used to examine their spatiotemporal distribution in the major organs and tissues (Figure 3-14**b**). Spatially, most n(EGFP) remain in the circulation system (e.g., carotid artery, aorta ventralis and heart) 3 h after the injection; more than 20% of the n(EGFP) are circulating in the blood stream 72 h post the injection, and significant concentration of n(EGFP) was still observed 120 h post the injection. As known, intravenously administrated exogenous particles tend to be cleaned out from the blood stream with a preferred accumulation in the organs such as liver and spleen.[29,298] Without the stealth capability, PAAM-nanocapsules consistently shows a rapid clearance with accumulation in the liver shortly after the injection (Figure 3-10**,** Figure 3-11). Figure 3-14**c** further displays the radioactive intensities in the carotid artery, aorta ventralis, heart, liver, spleen, and kidney after normalizing with the total radioactive intensities. Unchanged relative intensities are observed in the organs and tissues, further confirming an absence of accumulation within any of the organs.
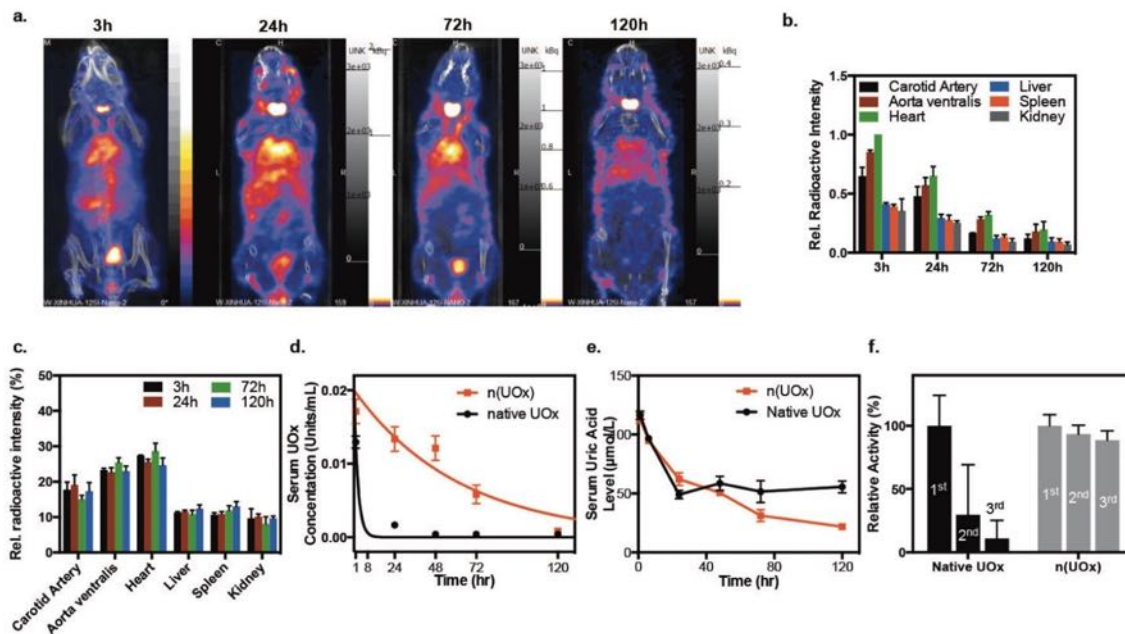
*Figure 3-14 **a,** Single-photon emission computed tomography / x-ray computed tomography (SPECT/CT) images of a mice after intravenous administration of radioactive ^{125}I-labeled n(EGFP). **b,** Quantitative analysis of the relative amount of n(EGFP) in blood and the organs at different time. All the radioactive intensities were normalized with the intensity of the heart at 3 h for each animal. **c,** Histogram summarizing the relative distribution of n(EGFP) in the blood and other major organs. The relative intensities were normalized by the total amount of n(EGFP) at 3 h, 24 h, 72 h and 120 h after the injection. **d,** Pharmaco-kinetic (PK) profiles of native UOx and n(UOx) after a systemic administration. **e,** Temporal evolution of the serum uric acid levels after administration of native UOx or n(UOx). **f,** Serum UOx activities after repetitive administration of native UOx or n(UOx). Serum UOx activities are normalized with the mean enzymatic activity after the first administration. Data represent mean ± s.e.m. from n independent experiments (n=3 for **b, c,** n=15 for **d, e,** n=6 for **f**).*

Such a stealth technology affords a novel class of protein therapeutics for treatments of metallic enzyme deficiency (e.g., gout and phenylketonuria)[141,299] and cancer (e.g., acute lymphoblastic leukemia),[300–302] where small-molecule metabolites can effectively transport cross the PMPC shells and decomposed by the encapsulated enzymes. Exampled by n(UOx) that can breakdown uric acid for chronic gout treatment, Figure 3-14**d** compares the serum UOx concentrations of the mice injected with n(UOx) or native UOx. For the native UOx, the serum enzyme concentration

rapidly decreases due to a rapid clearance; for the n(UOx), significantly higher serum enzyme concentration is retained due to a slower eliminating rate. Further analysis using the one-compartment model suggests that the elimination half-lives of n(UOx) is ~ 43.22 h, which is 27 fold longer than that of the native UOx (~ 1.598 h) (Table 3-5). Figure 3-14**e** further compares the serum uric acid concentrations after the injection. Injection of native UOx reduces the uric acid concentration from 116.4 to 49.1 μmol/mL within 24 h, which slightly rebounds and maintains at 55.6 μmol/mL for 96 hours. For comparison, injection of n(UOx) steadily reduces the uric acid level to 21.8 μmol/mL 120 h after the administration.

Besides the prolonged circulation time, the nanocapsules also exhibit reduced immunogenicity. **Figure 4f** compares the relative serum UOx activity after three consecutive administrations of native UOx or n(UOx). For the native UOx, the 2nd and 3rd injection provided ~ 29.7% and 10.8% activity of that of the 1st injection due to the accelerated blood clearance. In contrast, repetitive injection of n(UOx) afforded similar serum activities (93.5% for the 2nd and 83.7% for the 3rd injection), confirming the evading capability from the adaptive immune system.

3.4 Conclusion

To conclude, we have developed a stealth delivery platform by coating protein molecules with a shell of protein-adsorption-resistant polymer, affording a novel class of protein therapeutics with enhanced protein stability, prolonged half-life and reduced immunogenicity. This platform can also be extended for delivery of non-protein drugs, such as small molecular drugs and gene-based drugs, which may significantly impact the field of medicines. Furthermore, targeting delivery has been considered as a dream technology for cancer treatment; however, without the stealth capability, most of the drugs administrated are cleared out even before they can reach the target sites. In

this aspect, achieving long circulation is a precondition towards targeting delivery and this stealth platform makes one step closer.

Chapter 4. Delivery of Intact Transcription Factor by Using Self-Assembled Supramolecular Nanoparticles

4.1 Introduction

Protein delivery has been considered as the most straight- forward strategy for modulating cellular behavior without the safety concerns and expression performance issues associated with gene deliver approaches.[303–311] Two major challenges remain to be overcome in order to enable practical applications in biology and medicine 1) how to foster cellular uptake of protein molecules and 2) how to retain their stabilities and functions over the delivery process.[312–314] Recently, attempts have been made to develop a variety of delivery vectors, including liposomes,[25,315,316] polymer micelles,[176,317–321] and nanoparticle,[186,204,322–327] to enhance the uptake of protein molecules in target cells, and at the same time, to stabilize the encapsulated proteins. Owing to the time-consuming procedures employed in optimization of delivery materials, significant endeavors have been made in search of better delivery systems, although there has been limited progress in the field to date. Alternatively, recombinant technology[328] can be utilized to conjugate cell-penetrating peptides[329–333] (CPPs) onto protein molecules, this is the most commonly used protein delivery system with improved delivery efficiency. In this case, the major bottlenecks associated with the complicated procedure of generating recombinant proteins and the lack of protection mechanism against protein denature need to be solved.

Transcription factor (TF) is a protein responsible for regulating gene transcription in cellular circuitry.[334] In general, TFs contain one or more DNA-binding domains (DBDs), which recognize matching DNA sequences adjacent to the genes they regulate. Apparently, highly efficient delivery

of TFs can provide a powerful technology for modulating cellular behavior. One of the most important in-vitro applications that required highly efficient TF delivery is the generation of human induced pluripotent stem cells (hiPSCs) which has recently been demonstrated by introducing CPPs- fused reprogramming TFs (i.e., OCT4, SOX2, KLF4, and c- MYC)[335] into human somatic cells. The resulting hiPSCs have the potential to revolutionize regenerative medicine.[336,337] However, the high costs of the four reprogramming TFs in their recombinant forms, means it is unlikely that this approach can be used for large-scale hiPSCs generation without further improvement in the delivery performance of the reprogram- ming proteins. Therefore, it is crucial to develop a new type of vector capable of delivering intact (unmodified) TFs in a highly efficient manner.

Previously, we demonstrated a convenient, flexible, and modular self-assembly approach for the preparation of supramolecular nanoparticles (SNPs) from a small collection of molecular building blocks through a multivalent molecular recognition based on adamantane (Ad) and b-cyclodextrin (CD) motifs. Such a self-assembly synthetic strategy enables control upon the sizes, surfaces chemistry, zeta potentials, and payloads of the resulting SNPs, which open up many interesting opportunities for biomedical applications, for example, positron emission tomography (PET) imaging,[338] magnetic resonance imaging (MRI),[339] photothermal treat- ment of cancer cells,[340] and highly efficient gene delivery.[341,342]

Considering the unique role of TF, we attempted to explore the use of SNPs as a new type of nanoscale vector for delivering intact (unmodified) TFs with an efficiency superior to that of existing approaches. Our idea is to achieve the encapsulation of a TF into cationic SNP vectors by

introducing anionic characteristics to the TF. A DNA plasmid with a matching recognition sequence specific to a TF can be employed to form an anionic TF·DNA complex, which can be subsequently encapsulated into SNPs, resulting in TF- encapsulated SNPs (TF·DNA SNPs).

4.2 Methods, experiments, and characterizations

4.2.1 Materials and instruments

Reagents and solvents were purchased from Sigma-Aldrich (St. Louis, MO) and used as received otherwise noted. 1-Admantanamine (Ad) hydrochloride and β-cyclodextrin (β-CD) were purchased from TCI America (San Francisco, CA). 1st-Generation polyamidoamine dendrimer (PAMAM) with 1,4-diaminobutane core and amine terminals in 20% wt methanol solution was purchased from Dendritic Nanotechnologies, Inc (Mount pleasant, MI). N-hydroxysuccinimide (SCM) and maleimido (MAL) hetero-functionalized polyethylene glycol (SCM-PEG-MAL, MW = 5 kDa) was obtained from NANOCS Inc (New York, NY). Arginine-glycine-aspartic- cystein (RGDC) peptide and TAT peptide (CGRKKRRQRRR) were purchased from GenScript Corp (Piscataway, NJ). CD-grafted branched polyethylenimine (CD-PEI), Ad-grafted PAMAM (Ad-PAMAM), Ad-grafted polyethylene glycol (Ad-PEG), Ad-grafted PEG-RGD (Ad-PEG-RGD), and Ad-grafted PEG-TAT (Ad-PEG-TAT) were prepared via the method previously reported by our group.[342] 4',6-diamidino-2-phenylindole (DAPI), Phosphate-Buffered Saline (PBS) and Dulbecco's Modified Eagle Medium (DMEM) were obtained from Invitrogen (Carlsbad, CA). Cy^{TM}5 monofunctional dye (Cy5-NHS) was purchased from GE Healthcare. Transcription factor, GAL4-VP16, was purchased from Jena Bioscience (Jena, Germany). HeLa cell line was obtained from American Type Culture Collection. CellTitra Blue cell viability kit was purchased from Promega (Madison, WI).

Hydrodynamic size and Zeta potential of transcription factor encapsulated supramolecular nano-particles (**TF•DNA⊂SNPs**) were acquired using a Zetasizer Nano instrument (Malvern Instruments Ltd., UK). UV-vis absorption of Cy5-labeled **TF•DNA⊂SNPs** was determined by Nanodrop 2000c (Thermo Scientific). Transmission electron microscopy (TEM) images were obtained on Philips CM 120 electron microscopy operating with an acceleration voltage 120 kV. Cell imaging was performed on a Nikon TE2000S inverted fluorescent microscopy with a CCD camera (Photomatrix, Cascade II), X-Cite 120 Mercury lamp, automatic stage, and a filter for fluorescent channel (Cy5). Fluorescence intensity and bioluminescence of cell lysate were measured by a Fujifilm BAS-5000 plate reader. Bioluminescence images were acquired by using a cooled charge-coupled device (CCD) camera (IVIS, Xenogen).

4.2.2 ConstructionofpG5E4T-FlucandpG5E4Tplasmidvectors

pG5E4T-Fluc plasmid was constructed according to literature method.[343] Briefly, five copies of 17-bp GAL4 binding sites were placed on 23-base upstream of the TATA box of the E4 gene of adenovirus (G5E4T). Then, this G5E4T sequence was amplified by PCR with the primers to attach *Sac*I and *Xho*I sites on up- and down-streams, respectively. Then, pG5E4T-Fluc plasmid was constructed by digesting *Sac*I and *Xho*I sites of PCR-amplified fragments and introducing into pGL3-Basic vector (Promega).

For constructing pG5E4T plasmid, pG5E4T-Fluc plasmid was digested with SacI and NcoI sites to remove Fluc coding sequence, blunted and self-ligated by using DNA Ligation Kit (Takara).

4.2.3 Synthesis of Cy5 labeled TF

The preparation of Cy5 labeled TF (**Cy5-TF**) was basically following the protocol coming along with $Cy^{TM}5$ monofunctional dye (Cy5-NHS) from GE Healthcare. 1 tube of Cy5-NHS was first dissolved in 1 mL anhydrous DMSO to achieve a 1 mg/mL Cy5-SCM stock solution. Then 0.4 μL Cy5-NHS was then added gradually into 10 μL $NaHCO_3$ (pH=8.2) containing 400 ng GAL4-VP16 (**TF**) and mixed thoroughly. The mixture was incubated under rocking for 0.5 h. Then the reaction mixture was adjusted to 20 μL and unconjugated Cy5 was removed by dialysis against PBS with a Dispo-Biodialyzer (Sigma). The UV/Vis was used to monitor the purification process. The dialysis was terminated when we observed the absorption (650 nm) of solution in the dialysis cassette keep constant.

4.2.4 Preparation of transcription factor encapsulated supramolecular nanoparticles

A two-step self-assembly was employed to achieve the transcription factor encapsulated supramolecular nanoparticles (**TF•DNA⊂SNPs**). Firstly, GAL4-VP16 (200 ng) was incubated with pG5E4T-Fluc (2 μg) at 4°C for 30 min to generate **TF•DNA** complex. Secondly, 1 μL **CD-PEI** (4.3 μg) was gradually added into a 19 μL PBS solution containing **TF•DNA** complex (GAL4-VP16: 200 ng, pG5E4T-Fluc: 2μg), **Ad-PEG** (5.94 μg), **Ad- PEG-RGD** (0.297 μg), **Ad-PEG-TAT** (0.535 μg) and **Ad-PAMAM** (0.528 μg). The **TF•DNA⊂SNPs** were obtained by briefly vortexing mixing, followed by incubation at 4°C for 30 min.

4.2.5 Zeta potential (ζ) Measurements

Zeta potential of **TF•DNA⊂SNPs** was determined by photon correlation spectroscopy using a Zetasizer Nano instrument, (Malvern Instruments, Malvern, Worcestershire, UK). The measurements were performed at 25°C with a detection angle of 90°, and the raw data were subsequently correlated to zeta potential by the Zetasizer software program. The zeta potentials were averaged by three independent measurements. Through multivalent Ad/CD recognition interactions, the ammonium groups in **CD-PEI** and **Ad-PAMAM** endow the TFs with positive charges. After the encapsulation, the weak ionic TF, GAL4-VP16 (pI ~ 5.5), turned to cationic **TF•DNA⊂SNPs** with a zeta potential about + 12.9±1.85 mV.

4.2.6 Transmission Electron Microscope (TEM)

Transmission electron microscope was used for directly examining the morphology and sizes of **TF•DNA⊂SNPs**. The studies were carried out on a Philips CM 120 electron microscope, operating at an acceleration voltage of 120 kV. TEM samples were prepared by performing drop-coating of 2 μl **TF•DNA⊂SNPs** solutions onto carbon-coated copper grids. After contacting the droplets with copper grids for 45 s, excess amount of droplets were removed by filter papers. Subsequently, the surface-deposited **TF•DNA⊂SNPs** were stained with 2% uranyl acetate for 30 s before the TEM studies.
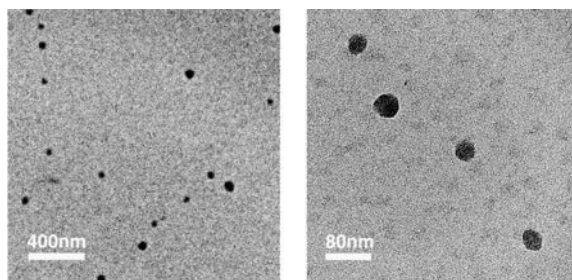
Figure 4-1 Transmission Electron Microscope (TEM) images of TF•DNA ⊂SNPs.

4.2.7 *In vitro* cell internalization

Cell internalization studies were assessed via fluorescence microscopic technique. HeLa cells were plated into a 24-well plate the day before exposure to Cy5 labeled **TF•DNA⊂SNPs**. After incubation with Cy5 labeled **TF•DNA⊂SNPs** for 12 h, cells were washed with PBS for 3 times and then fixed with 4% formaldehyde for 15 min. Nucleus staining was performed by using DAPI according to manufacture's protocol. Fluorescence images of treated cells (Figure 4-2) indicated the co-localization of cell-nuclei and **TF**, suggesting successful delivery of **TF** into cell-nuclei by **TF•DNA⊂SNPs**.
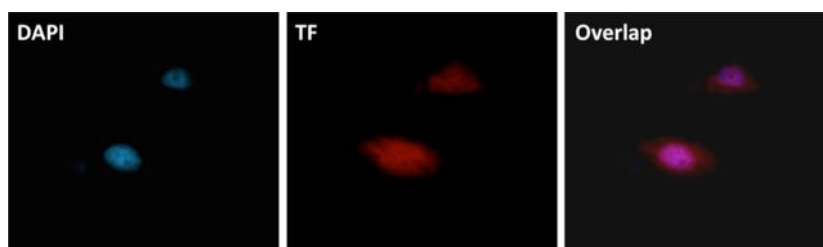
Figure 4-2 Fluorescence images of HeLa cells after the treatment with Cy5 labeled TF•DNA⊂SNPs

4.2.8 Quantification of TF•DNA⊂SNPs delivery efficiency

The delivery efficiency was determined by qualification the fluorescence intensity of HeLa cells after uptaking nanoparticles. In order to evaluate the performance of **TF•DNA⊂SNPs**, equivalent amount of **TF** (Cy5 labeling GAL4-VP16), **TF•DNA**, and **TAT-TF** were used as control to compare with **TF•DNA⊂SNPs**. GAL4-VP16 (**TF**) was first labeled with Cy5-NHS and then encapsulated into **TF•DNA⊂SNPs** with the methods described above. TAT-TF-Cy5 was synthesis by conjugation of TAT-NHS with Cy5-GAL4-VP16. TF DNA was prepared by mixing GAL4-VP16 (200 ng) and pG5E4T-Fluc (2μg) in 20 μL PBS. HeLa cells were seed into a 96-well plate the day

before exposure to the nanoparticles. 1 µL of **TF**, **TF•DNA**, **TAT-TF** and **TF•DNA⊂SNPs** (each contains exact 10 ng Cy5-TF) was then incubated with HeLa cells for 12 h. After removal of nanoparticles, cells were washed with PBS for 3 times and then fixed with 4% formaldehyde PBS solution. Fluorescence intensity of each group was then quantified by using a plate reader (Ex = 535 nm, Em = 585 nm). HeLa cells incubated with **TF•DNA⊂SNPs** were also imaged by a fluo-rescence microscopy.

4.2.9 Characterization of TF activity after delivery via TF•DNA⊂SNPs

In order to determine the TF (GAL4-VP16) activity after delivery, we quantified the luciferase expression by measuring the bioluminescence intensity of **TF•DNA⊂SNPs**-treated cells. **TF•DNA⊂SNPs** were prepared in using the method described above. HeLa cells were seed into a black 96-well plate the day before exposure to the **TF•DNA⊂SNPs** and control experiments (PBS, **TF•DNA⊂SNPs**, and **DNA⊂SNPs**). A series amount of **TF•DNA⊂SNPs** and controls (i.e., 0.1 µL, 0.5 µL, 1 µL, 2 µL, 5 µL, and 10 µL; for **TF•DNA⊂SNPs** and **TF•DNA**, the concentration of **TF** is 10 ng/µL, the concentration of **DNA** is 100 ng/µL; for **DNA⊂SNPs**, the concentration of **DNA** is 100 ng/µL) was then added into HeLa cells, respectively. After 12-h incubation, cells were washed and incubated with fresh medium for another 24 h to allow the luciferase expression that was activated by **TF**. To quantify the luciferase expression, cells were lysed and then incubated with 100 µL luciferin substrate (Promega, E1500) at room temperature for 2 min. Bioluminescence intensities were then measured by both the plate reader (Fujifilm BAS-5000) and the CCD camera (IVIS, Xenogen).

4.2.10 TF-dosage dependent study

In order to confirm the release of TF in **TF•DNA⊂SNPs**-treated cells, and the TF-dosage dependent expression of luciferase, the control experiments were carried out as described below. A newly constructed **pG5E4T** plasmid vector (with only have GAL4 binding sequence but without luciferase reporter gene), was used as the matching DNA (to confer negative charges to TF) in this study. Using similar methods as described in section 5.3, we prepared **TF•pG5E4T⊂SNPs** in order to achieve the delivery of TF. HeLa cells were first seeded into a black 96-well plate the day before treatments. pG5E4T-Fluc plasmid (1 μg)-encapsulated SNP and a series amount (1ng, 5ng, 10ng, 20ng, 50ng, 100ng) of **TF•pG5E4T⊂SNPs** were added to each well simultaneously. After 12-h incubation, cells were washed and incubated with fresh medium for another 24 h to allow the expression of luciferase.
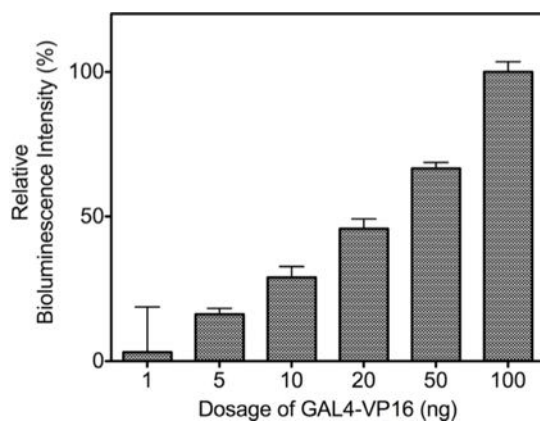
Figure 4-3 Dosage dependence between bioluminescence intensity and the amount of GAL4-VP16 delivered by TF•pG5E4T ⊂SNPs

Quantification of luciferase expression was achieved by performing luciferase assay on lysed cells. As illustrated in Figure 4-3, strong bioluminescence signal proved the activation of luciferase expression by **TF**, suggesting that the TFs were successfully released from **TF•pG5E4T⊂SNPs** after

internalization. Meanwhile, bioluminescence intensity increased with the dosage of **TF•pG5E4T⊂SNPs** in presence of the fixed amount of pG5E4T-Fluc delivered into cells, indicating that the expression level is dominated by the amount of TF delivered via **TF•pG5E4T⊂SNPs**.

4.2.11 Cytotoxicity of TF•DNA⊂SNPs

The cytotoxicity of **TF•DNA⊂SNPs** was assessed by the MTT assay using PBS as control. HeLa cells were seed into a 96-well plate the day before exposure to the **TF•DNA⊂SNPs**. **TF•DNA⊂SNPs** with different concentrations were incubated with cells for 24 h. After incubation, CellTiter-Blue (20 μL) was added into each well and incubated for 3 h. The plate was then placed on a shaking table, 150 rpm for 5 min to thoroughly mix the solution, and then fluorescence intensities were measured with a plate reader (Ex = 535 nm, Em = 585 nm). As shown in Figure 4-4, the **TF•DNA⊂SNPs** have no toxicity at all.
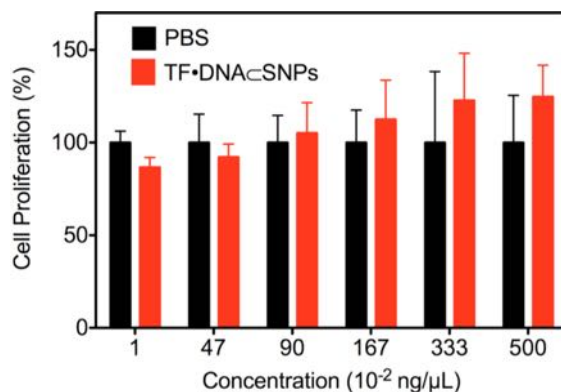
Figure 4-4 Cytotoxicity evaluation of TF•DNA ⊂SNPs

4.3 Results and discussions

In this work, we introduce a new type of protein delivery system capable of highly efficient transduction of intact TFs. In this proof-of-concept study, a mammalian orthogonal fusion TF, GAL4-

VP16 was chosen to serve as a model TF. Since GAL4-VP16 is an artificial transcription factor, there should be no background concentration in the mammalian cells employed in the delivery studies. To facilitate the encapsulation of the model TF into the SNP vectors, a DNA plasmid (i.e., pG5E4T-Fluc) that contains five tandem copies of GAL4-VP16 matching recognition sequences and a conjugated luciferase reporter was designed. The incorporation of multivalent recognition sequences enhances dynamic binding between GAL4-VP16 and pG5E4T-Fluc, allowing improved encapsulation and dynamic releasing of the intact TF. In addition, the conjugated luciferase reporter can be specifically activated by GAL4-VP16, providing a real-time readout reflecting the activities of the TF after its intracellular delivery.
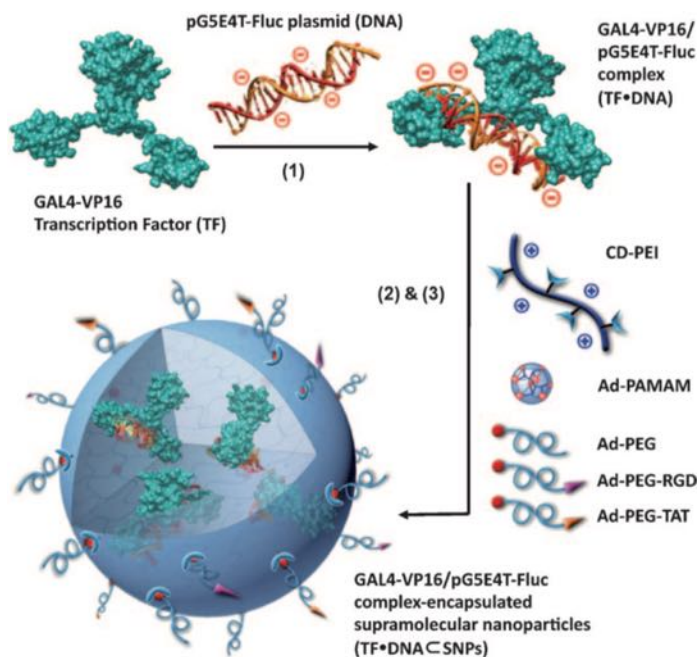
Figure 4-5 Schematic representation of the self-assembly approach for the preparation of transcription factor-incorporated supramolecular nanoparticles (TF·DNA ⊂SNPs).

As shown in Figure 4-5, three types of molecular recognition mechanisms were employed to facilitate the preparation of TF-encapsulated SNP (TF·DNA⊂SNPs). First, the specific binding (the

dissociate constant $K_d = 10$ nm)[344] between GAL4-VP16 (TF) and pG5E4T-Fluc (DNA) led to the formation of an anionic TF·DNA complex. Second, the Ad/CD-based molecular recognition ($K = 1.1*10^5$ m^{-1})[345,346] was utilized to form the SNP vectors with cationic hydrogel cores. Third, electrostatic interactions assist the incorporation of TF·DNA into SNPs to give TF·DNA⊂SNPs. The preparation of TF·DNA⊂SNPs can be accomplished by simply mixing TF·DNA complex with other five functional building blocks (i.e., CD-PEI : CD-grafted branched polyethylenimine, Ad-PAMAM : Ad-grafted polyamidoamine dendrimer, Ad-PEG : Ad-grafted polyethylene glycol, Ad-PEG-RGD : Ad-grafted polyethylene glycol with RGD targeting ligand, and Ad-PEG-TAT: Ad-grafted polyethylene glycol with TAT-based CPP). Among the three ligand compounds, Ad-PEG plays a role of a capping/solvation reagent that can not only confine continuous propagation of the TF·DNA-encapsulated PEI/PAMAM hydrogel networks, but also impart desired water solubility, structural stability, and passivation performance to the resulting TF·DNA⊂SNPs. In addition, Ad-PEG-RGD and Ad-PEG-TAT, which were incorporated onto the surfaces of TF·DNA⊂SNPs during the one-pot mixing process,[342] enable delivery specificity (to recognize a certain population of cells with avb3-integrin receptors) and cell transfusion capability (to foster internalization through membrane and releasing from endosome trapping), respectively, of TF·DNA⊂SNPs. The previous study revealed a set of optimal synthetic parameters[341] that produce DNA-encapsulated SNPs which have good gene transfection performance. Additionally, the results suggested that the presence of both 5% RGD and 9% TAT ligands is a crucial factor in the enhanced efficiency. In this study, we took the advantage of these optimal synthetic parameters for the preparation of TF·DNA⊂SNPs. We were able to demonstrated unprecedented performance for delivery intact

TF when TF·DNA⊂SNPs is compared with the conventional CPPs-based protein delivery strategy. Moreover, the intra- cellular TF delivered by TF·DNA⊂SNPs retained its bioactivity, which was confirmed by monitoring the bioluminescence intensity of the SNP-treated cells.

The model plasmid pG5E4T-Fluc and all other molecular building blocks (i.e. CD-PEI, Ad-PAMAM, Ad-PEG, Ad- PEG-RGD, and Ad-PEG-TAT), were synthesized and characterized as described in Section 4.2 . The model transcription factor, GAL4-VP16 was obtained from commercial sources. pG5E4T-Fluc is orthogonal to mammalian genome, thus cannot be activated to express luciferase in the absence of GAL4-VP16.[347] Prior to the preparation of TF·DNA⊂SNP, GAL4-VP16 was incubated with a slight excess amount of pG5E4T-Fluc (GAL4-VP16/pG5E4T-Fluc=1: 0.35 n/n, each pG5E4T-Fluc contains five tandem copies of GAL4-VP16 recognition sequences thus might accommodate more than one TF) for 30 min at 4ºC to generate TF·DNA. Subsequently, TF·DNA⊂SNPs were prepared by slowly adding CD-PEI (4.32 mg) in 1 mL phosphate-buffered saline (PBS, pH 7.2) into a 19 mL of PBS solution containing TF·DNA complex (200 ng GAL4-VP16 and 2 mg pG5E4T-Fluc), Ad-PEG (5.94 mg), Ad-PEG-RGD (0.297 mg), Ad-PEG-TAT (0.535 mg), and Ad-PAMAM (0.528 mg). After a brief stirring, the mixture was incubated at 4ºC for another 30 min. To determine hydrodynamic size of the resulting TF·DNA⊂SNPs, we performed dynamic light scattering (DLS) measurements (Figure 4-6b), indicating a uniform size of 50±3 nm. In parallel, the morphology of TF·DNA⊂SNPs was characterized by transmission electron microscopy (TEM), suggesting homogeneous, narrow size- distributed spherical nanoparticles with size of 40±3 nm (Figure 4-6a).
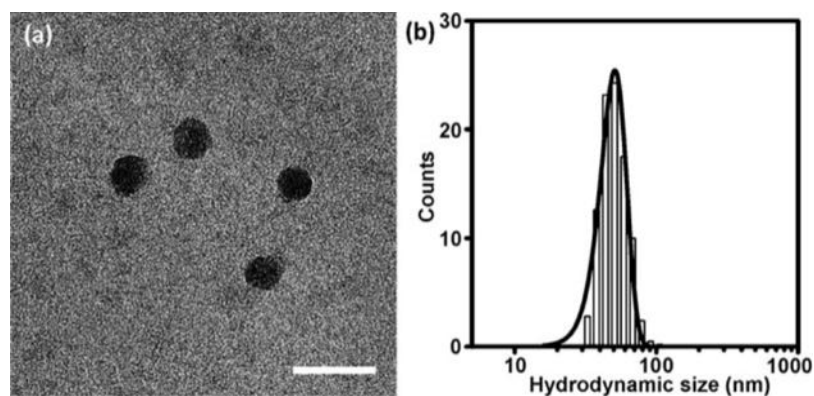
Figure 4-6 a) Transmission electron microscopy (TEM) micrographs of TF·DNA⊂SNPs. Scale bar: 80 nm. b) Histograms summarize the hydrodynamic size distribution obtained from DLS measurement of (50±3) nm TF·DNA⊂SNPs.

To examine the delivery performance of TF·DNA⊂SNPs, we perform their cell uptake studies using by incubating TF·DNA⊂SNPs (10 ng TF per well) with HeLa cells in a 96-well plate (10^4 cells per well). Again, GAL4-VP16 was labeled by Cy5 dye to allow quantitative monitoring of the delivery performance of TF·DNA⊂SNPs. Control experiments based on Cy5-labeled-TF alone (TF), Cy5-labeled- TF·DNA complex and Cy5-labeled-TF with TAT-conjugation (TAT-TF) were carried out in parallel under the same experimental conditions. After incubation for various periods (i.e., 0.5, 1, 2, 6, 12, and 24 h) and removal of non-uptake reagents in the media, the delivery performances of individual studies were quantified by measuring their fluorescence intensities in a plate reader (Fujifilm BAS-5000). As shown in Figure 4-7b, Cy5-labeled TF·DNA⊂SNPs exhibited dramatically enhanced delivery performance in contrast to those observed in the control studies. It is noteworthy that the delivery efficiency of TF·DNA SNPs was approximately five- times greater than that of TAT-TF, which was commonly used as a standard method for TF delivery. The time-dependent uptake studies (Figure 4-7c) of TF·DNA SNPs revealed that accumulation of the fluorescence signals increased with the incubation time and

126

reached saturation at 12 h. Fluorescence micrographs (Figure 4-7d) indicated that localization of

Cy5-labeled TF in the cell nuclei, suggesting that the TF molecules were delivered to cell nuclei,

where TF functioned as a regulator by controlling the translation of specific gene(s). This result

was also confirmed by the co-localization of Cy5-labeled TF and 4 ,6-diamidino-2-phenylindole

(DAPI) stained cell nuclei using fluorescence microscopy (Section 4.2.7).
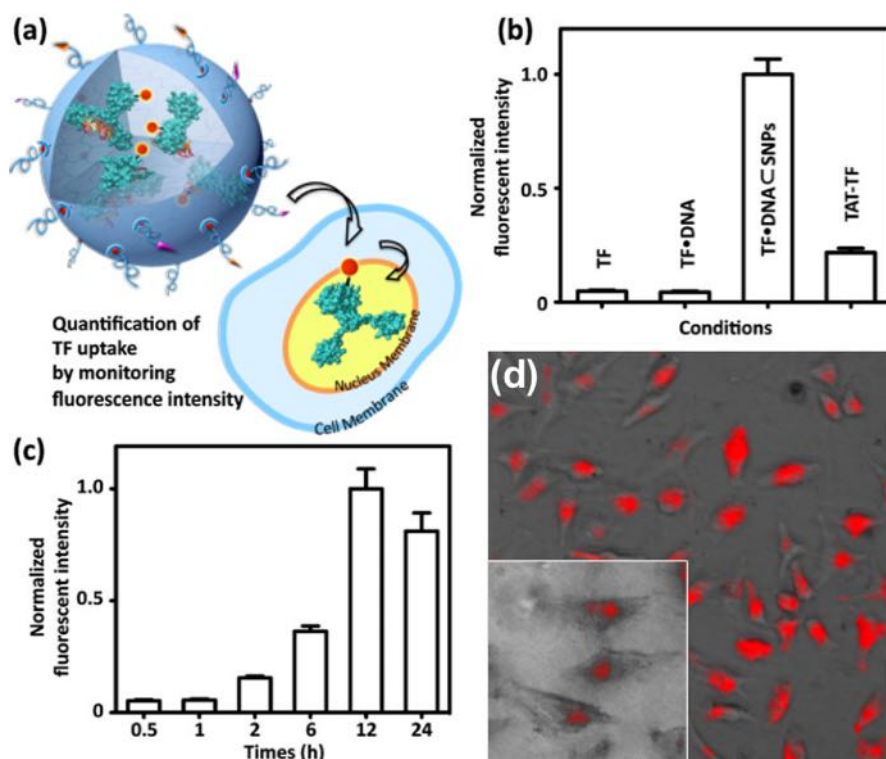
Figure 4-7 a) Quantification studies on the delivery performance of TF·DNA ⊂SNPs. b) Delivery efficiency of Cy5-labeled TF·DNA SNPs, Cy5-labeled-TF alone (TF), Cy5-labeled-TF·DNA complex, and Cy5-labeled-TF with TAT-conjugation (TAT-TF). c) Time-dependent uptake studies of TF·DNA ⊂SNPs. d) Fluorescence micrographs of HeLa cells after incubating with TF·DNA SNPs for 12 h. Cy5-labeled TF was localized in the cell nuclei, where TF functioned as a regulator to control the translation of a specific gene.

To confirm that the GAL4-VP16 (TF) retained its activity after delivery, we quantified the lucif-

erase expression by measuring the bioluminescence intensity of SNP-treated cells (Figure 4-8).

Again, the pG5E4T-Fluc (DNA) used in our study contains a luciferase reporter that can be specifically activated by GAL4-VP16. Therefore, the activity of GAL4-VP16 is reflected in the bioluminescence intensity of SNP-treated cells as a result of luciferase expression. After the incubation of HeLa cells with SNPs and the control reagents (including SNP vector, TF·DNA, and DNA⊂SNPs), the cells were lysed for quantification of bioluminescence. After incubation with luciferin for 2 min, the bioluminescence intensities were recorded by both a plate reader (Figure 4-8b) and a cooled charge-coupled device (CCD) camera (IVIS, Xenogen; Figure 4-8c).
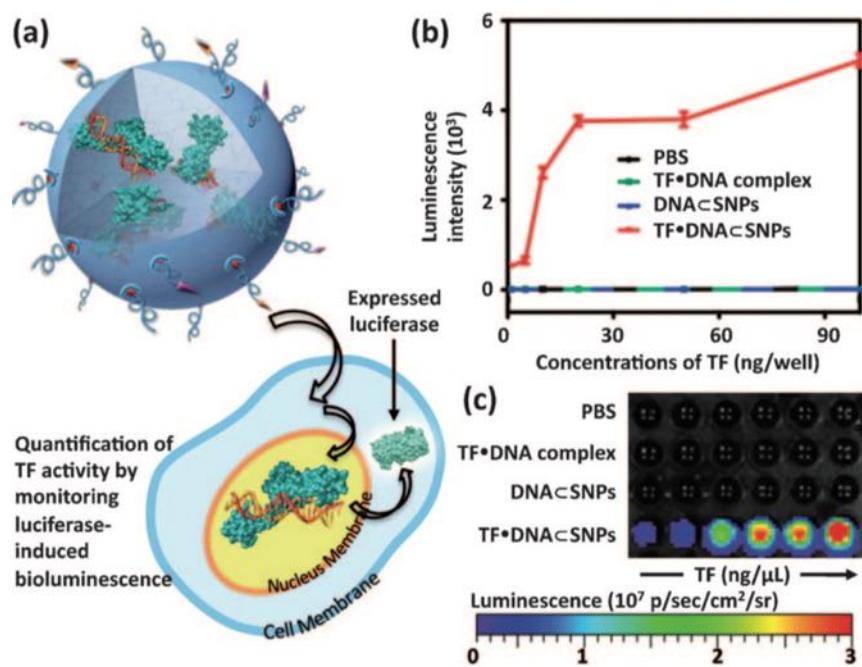
Figure 4-8 a) Bioluminescence study on TF·DNA⊂SNPs-treated cells. The activity of GAL4-VP16 can be reflected in the bioluminescence intensity as a result of luciferase expression. b) Dose-dependent profile and c) bioluminescence imaging of TF·DNA⊂SNPs-treated cells along with the controlled experiments based on TF·DNA complex and DNA⊂SNPs. Error bars in (b) were obtained from three independent experiments.

Compared to the background-level bioluminescence intensities observed from the control experiments, that observed for TF·DNA SNPs-treated cells is significantly higher, suggesting that the

GAL4-VP16 retains its activity to trigger the luciferase expression after intracellular delivery. The dose-dependent studies (Figure 4-8b) indicated that bioluminescence intensities of the SNP-treated cells increased with the TF dosages. In addition, we also conducted a set of control studies, where the functional gene (pG5E4T-Fluc) and TF are delivered separately using the respective SNP-based delivery systems at different ratios. We were able to observe very similar bioluminescent outcomes as shown in Figure 4-8, validating the release of TF from the SNP vector, as well as the dominance of TF amount to the expression level of luciferase (Section 4.2.10). Moreover, the cell viability assays carried out at different doses of TF·DNA $\subset$ SNPs indicated that the TF·DNA SNPs exhibit negligible toxicity. (Section 4.2.11)

4.4 Conclusion

In conclusion, we have successfully demonstrated the feasibility of applying TF·DNA $\subset$ SNPs for delivery of intact (unmodified) transcription factor (TF) in a highly efficient manner. The uniqueness of our self-assembly synthetic strategy for the preparation of TF·DNA $\subset$ SNPs has to do with the combined use of three types of molecular recognition mechanisms, including 1) specific binding between TF and matching DNA plasmid for formation of an anionic TF·DNA complex, 2) the Ad/CD-based molecular recognition for generation of SNP vectors with cationic hydrogel cores, and 3) electrostatic interactions that facilitate encapsulation of anionic TF·DNA into SNPs. We believe such a TF delivery approach provides a powerful method for manipulating cellular behaviors. A potential application is for generating human induced pluripotent stem cells (hiPSCs), which required the delivery of four reprogramming TFs. We note that, in conjunction with the use of a miniaturized high-throughput screening platform[348–352] and biological assays,[353–355] to achieve

hiPSCs generation in a highly efficient manner, it is feasible to optimize the ratios of the four

reprogramming TFs, something that could be possible through the use of TF·DNA⊂SNPs.

Chapter 5. A High-Throughput Platform for Formulating and Screening Multifunctional Nanoparticles Capable of Simultaneous Delivery of Genes and Transcription Factors

5.1 Introduction

Nowadays, researches have a wide variety of techniques for delivery genes and proteins. Among the existing delivery systems, nanoparticles (NPs) have been regarded as promising non-viral vectors for delivering either a gene[336,337,356–359] or a protein[360–363] into specific types of cells or tissues.[364] The conventional approaches employed for optimization of NP delivery systems required empirical and multiple optimization cycles to repeat design/synthesis/assays processes. Given the fact that enormous complexity of a biological system, it is unlike such a time and cost consuming developmental pipeline could lead to a crucial breakthrough in the search of optimal delivery vectors.

Combining microfluidic technologies[348,351,365–368] with supramolecular synthetic strategy,[341,350,369–371] we demonstrated herein a high-throughput approach for formulating and screening multifunctional nanoparticles (MFNPs) that are capable of simultaneous delivery of gene and functional proteins with superb efficiency and controllable stoichiometry among individual payloads (Figure 5-1). As illustrated in Figure 5-1a, this approach utilized two microfluidic systems including a digital droplet generator (DDG)[348,372] and a microfluidic cell culture array[373,374]. To enable the capability of on-chip synthesis of MFNPs using the DDG, we have developed a modular assembly system based on the supramolecular synthetic strategy[369,371] (Figure 5-1b). By utilizing the molecular recognition between adamantane (Ad) and β-cyclodextrin (CD), a combinatorial library of

DNA and proteins-encapsulated MFNPs was generated by the DDG *via* systematically altering the ratios among the four functional modules. By coupling the DDG and the cell culture array, all the MFNPs in the library could be exposed to cells respectively for the screening of the synthetic parameters that facilitated an optimal delivery performance. Using the identified parameters, the MFNPs, which consists a pair of functionally complementary protein and gene[371,375] (GAL4-VP16 and pG5E4T-Fluc), were synthesized and facilitate a successful co-delivery of the protein and gene allowing them to function synergistically both *in vitro* and *in vivo*.
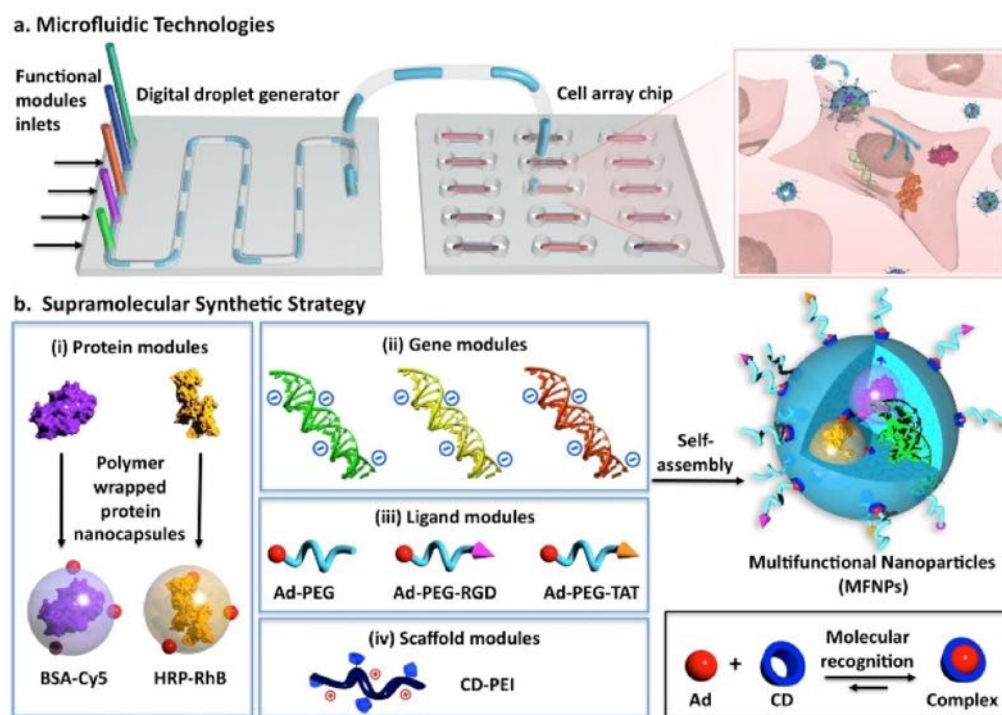
Figure 5-1 A high-throughput approach for formulating and screening multifunctional nanoparticles (MFNPs) for simultaneous delivery of genes and proteins. a) Two microfluidic systems, i.e.*, a digital droplet generator and a microfluidic cell array chip were employed for formulating and screening of MFNPs capable of simultaneous delivery of genes and functional proteins with superb efficiency and controllable stoichiometry among individual payloads. b) Our supramolecular synthetic strategy, based on an adamantane (Ad) and β-cyclodextrin (CD) molecular recognition system, allows a convenient, flexible and modular*

generation of a combinatorial library of genes and proteins-encapsulated MFNPs by systematically alter-ing the mixing ratio of among the four functional modules, including (i) protein modules, (ii) gene modules, (iii) ligand modules (Ad-PEG, Ad-PEG-RGD and Ad-PEG-TAT), and (iv) a scaffold module (CD-PEI).

5.2 Methods, experiments, and characterizations

5.2.1 Materials and instruments

Reagents and solvents were purchased from Sigma-Aldrich (St. Louis, MO) and used as received without further purification otherwise noted. Branched polyethylenimine (PEI, MW = 10 kD) was purchased from Polysciences Inc (Washington, PA). Polymers contain primary, secondary and tertiary amine groups in approximately 25/50/25 ratio. 1st-generation polyamidoamine dendrimer (PAMAM) with 1, 4-diaminobutane core and amine terminals in a 20% wt methanol solution was purchased from Dendritic Nanotechnologies, Inc (Mount pleasant, MI). 1-Adamantanamine (Ad) hydrochloride and α-cyclodextrin (α-CD) were purchased from TCI America (San Francisco, CA). N-hydroxysuccinimide (SCM) and maleimido (MAL) hetero-functionalized polyethylene glycol (SCM-PEG-MAL, MW = 5 kD) was obtained from NANOCS Inc (New York, NY). Phosphate-buffered saline (PBS, 1X, pH 7.2 ± 0.05) for sample preparation. 6-Mono-tosyl-cyclodextrin (6-OTs-α-CD) was prepared following the literature reported method.[376] Octa-Ad-grafted polyami-doamine dendrimer (Ad-PAMAM), CD-grafted branched polyethylenimine (CD-PEI) and Ad-grafted polyethylene glycol (Ad-PEG) were prepared as the methods we reported previously.[377] Dry CH_2Cl_2 was obtained by refluxing over CaH_2 and freshly distilled before use. NIH 3T3 (mouse embryonic fibroblast cell line), U87 (human brain glioblastoma cell line), HeLa (human cervix epithelial carcinoma cells), MCF7 (human breast adenocarcinoma cells) and HDF-2 (human dermal fibroblast cells) were purchased from American Type Culture Collection (ATCC). The Dulbecco's Modified Eagle Medium (DMEM), Earl's Modified Eagle's Medium (EMEM) growth

medium and Penicillin/streptomycin were obtained from Invitrogen (Carlsbad, CA). Fetal Bovine Serum (FBS), EGFP-encoded plasmid (pMAX EGFP®, 4.3 kb) and mCherry-encoded plasmid (4.8 kb) were obtained from Lonza Walkerrsville Inc (Walkerrsville, MD). EGFP-siRNA was obtained from Invitrogen (Carlsbad, CA). RGD (RGDC) and TAT peptides (CGRKKRRQRRR) were purchased from GenScript Corp. (Piscataway, NJ). Cy5™ monofunctional dye (Cy5-NHS) was purchased from GE Healthcare. Transcription factor, GAL4-VP16, was purchased from Jena Bioscience (Jena, Germany). CellTitra Blue cell viability kit was purchased from Promega (Madison, WI). N-(3-Aminopropyl) methacrylamide hydrochloride for production of single-protein nano-capsules was purchased from Polymer Science, Inc.

Dynamic light scattering and zeta potentials of multifunction nanoparticles (MFNPs) were measured on Zetasizer Nano instrument (Malvern Instruments Ltd., United Kingdom). Transmission electron microscope (TEM) images were measured on Philips CM 120 electron microscope operating with an acceleration voltage of 120 kV. Cell imaging, gene transfection and protein transduction studies were performed on a Nikon TE2000S inverted fluorescent microscope with a CCD camera (Photomatrix, Cascade II), X-Cite 120 Mercury lamp, automatic stage, and filters for three fluorescent channels (W1 (EGFP), W2 (RhB) and W3 (Cy5)). Fluorescence and bioluminescence intensities were measured by a Fujifilm BAS-5000 plate reader. Bioluminescence images were acquired by using a cooled charge-coupled device (CCD) camera (IVIS, Xenogen).

5.2.2 Synthesis of protein nanocapsules

1 mg of BSA-Cy5 in 0.5-mL sodium carbonate buffer (pH=8.5, 50 mM) was reacted with 0.1 mg N-acryloxysuccinimide in 5-µL DMSO for 1 h at room temperature. Subsequentially, the reaction

solution was dialyzed against phosphate buffer (pH=7.0, 20 mM) thoroughly. To 1 mL acryloy-lated BSA-Cy5 solution at 1 mg/mL, in situ polymerization from the surface of protein was achieved by adding 1.8 mg acrylamide and 0.6-mg N-(3-aminopropyl)methacrylamide as mono-mer, 0.5 mg glycerol dimethacrylate as degradable crosslinker, and 0.4 mg ammonium persulfate and 1 μL N,N,N',N'-tetramethylethylenediamine as initiator system. After reacting for 1 hour at room temperature under a nitrogen atmosphere, the reaction solution was dialyzed against phos-phate buffer saline (PBS) to remove unreacted monomers and initiators. Meanwhile, 1 mg 1-ada-mantane acetate acid (Ad) was activated by reacting with 1.5 mg N-(3-Dimethylaminopropyl)-N'-ethylcarbodiimide hydrochloride and 0.7 mg N-hydroxysuccinimide in 1 mL anhydrous DMSO for 2 h at room temperature. 30 μL activated Ad was then added in 1 mL BSA-Cy5 nanocapsule solution (1 mg/mL) and incubated at room temperature for 2 h to achieve Ad-conjugation. Finally, the product was purified with size exclusion chromatography, and the concentration was deter-mined by the absorption of Cy5 and D/P ratio.

Other protein modules, including horseradish peroxidase (HRP), Rhodamine B-labeled HRP (HRP-RhB) and GAL4-VP16 Ad-conjugated nanocapsules, were synthesized in using the similar method as that of BSA-Cy5 Ad-conjugated nanocapsules. HRP-RhB was synthesized by modify-ing the proteins using a conjugating technique. For the synthesis of HRP and HRP-RhB nanocap-sules, stabilizer 4-dimethylaminoantipyrine (1:10 weight ratio to HRP) was added into the reaction systems in the polymerization step.

5.2.3 Fabrication and operation of the microfluid system

5.2.3.1 Fabrication of the digital droplet generator

The digital droplet generator employed in this study was fabricated by the standard multi-layer soft lithography technology using polydimethylsiloxane (PDMS) materials. The basic working mechanism of the digital droplet generator, as well as its applications in supramolecular nanoparticle synthesis and protein labeling have been reported in the literatures.[352] Two different sets of silicon molds composed of photoresist-patterned microstructures for fluidic layer and control layer were individually fabricated by standard photolithographic process. The fluidic layer mold utilized for fabrication of the fluidic channels was made by patterning 50-μm thick positive photoresist (AZ 50XT) on the silicon wafer (channel width: 200 μm, channel height: 50 μm). The control layer mold utilized for the control channels was made by patterning negative photoresist (SU8-2050) on the silicon wafer (channel width: 100 μm, channel height: 40 μm). In order to achieve reliable performance of the valves, the width of the control channel was set at 300 μm in sections where the valve modules are located.

Before fabricating the PDMS microfluidic chips, all molds were pretreated by exposure to trimethylsilyl chloride (TMSCl) vapor for 10 minutes. Well-mixed PDMS pre-polymer (GE RTV615 A and B, total 36 g, mixing ratio A: B = 5:1) was poured onto the fluid layer molds to give 6 mm-thick fluidic layers. Another portion of PDMS pre-polymer (GE RTV615, total 10 g, mixing ratio A:B = 20:1) was mixed and then spin-coated on the control layer molds at 1500 RPM for 60 s. The fluidic and control layers were cured at 80°C oven for 15 minutes and 18 minutes, respectively. After baking, the fluidic layers were peeled off from the mold, aligned onto the corresponding control layers, and then baked at 80°C for at least 6 h to bond them. The assembled layers were peeled off from the control layer molds when the fluidic and control layers were bonded together.

Holes were then punched to form ports connected to the fluidic layer channels for reagent inlets and outlets, and ports connected to the control layer channels for valve actuation with hydraulic fluid. Adhesion of the layers to a clean glass microscope slides to seal the control channels were achieved by oxygen plasma bonding. the digital droplet generators were baked in an oven at 80°C for 72 h to restore the intrinsic hydrophobicity of PDMS surfaces needed to minimize the residue lost on channel walls when moving aqueous droplets.

5.2.3.2 Control interface

The pneumatic control system consists of two sets of 48-channel manifolds (electronic solenoid valves, SMC Series S070). The hydraulic valves embedded in the digital droplet generator are actuated by pressurizing the corresponding control channel, filled with water at 60 psi. When the manifold was activated, pressure was transferred from the solenoids to the chip via PTFE tubing (0.022" inner diameter, Cole Parmer) connected to 22-gauge stainless steel tubes and the valve in control layer would close the corresponding fluidic channel. All the valves were automatically controlled through a self-fabricated control system by a software program written in LabView (National Instruments).

5.2.3.3 Formulation of multi-function nanoparticles (MFNPs)

A schematic diagram (Figure 5-2) is shown to summarize the process for the preparation of a given category of MFNPs in a combinatorial library. In synthesis chip, the central microchannel is partitioned by hydraulic valves into multiple confined plug regions for systematically altering the mixing ratios among all building molecules. We note that a PBS solution is utilized to control the dilutions of building molecules (scaffold module and function module) and protein/gene cargos that could lead to the changes in the resulting transfection and transduction performance of MFNPs.

Herein, we take the synthesis of MFNPs containing pEGFP, BSA-Cy5 and HRP-RhB as an example. MFNPs with other different genes or proteins can be prepared with similar method. The preparation of MFNPs containing pEGFP, BSA-Cy5 and HRP-RhB is achieved with 8 steps. Step 1 and step 2 are applied to introduce vacuum (10.8 psi) to individual plug regions in order to accelerate the filling of all the building molecules (i.e. scaffold module: CD-PEI (**1**); function modules: Ad-PEG (**2**), Ad-PEG-RGD (**3**), Ad-PEG-TAT (**4**); protein modules: BSA-Cy5 (**5**), HRP-RhB (**6**); gene module: pEGFP (**7**)) and PBS. It takes about 150 ms to complete these two steps. In Step 3 (ca. 50 ms), several partition valves are closed (in red) to define the volumes of the plug regions that affect the mixing ratios among all building molecules. In step 4 (ca. 150 ms), several inlet valves that control the access to all building molecules and PBS are open, thus the regents are synchronously filled into the defined plug regions with the help of a 30-psi backpressure. In step 5 (ca. 50 ms), all of the inlet valves are closed. In step 6 (50 ms), all the partition valves are open, leading to a long/continuous plug region containing the resulting reagent mixture (200 nL in volume). In step 7 (4.5 s), a trap valve at the right end of the microchannel is open. Consequently, the 200-nL reagent mixture for the given MFNPs formulation is delivered into a PFPE storage tube using a peristaltic pump. Finally (step 8, ca. 50 ms), the valves at both ends of the microchannel are closed to prepare a new reaction cycle starting over from step 1. All the reagents inside the droplets can be homogeneously mixed prior to arrival of the PFPE storage tube. By systematic altering the amount of scaffold module (CD-PEI: 0.01, 0.02, 0.03, 0.04 and 0.05 µg), protein modules (BSA-Cy5: 0.013, 0.026, 0.039, 0.052 and 0.065 µg), (HRP-RhB: 0.009, 0.018, 0.027, 0.036 and 0.045 µg), the fixed amount of the function modules (Ad-PEG: 0.1 µg, Ad-PEG-RGD: 0.005 µg and Ad-PEG-TAT: 0.009 µg) and gene module (10 ng), a combinatorial library of MFNPs with 375 different formulations can be achieved within 1 hour. Once the droplets are incubated for the

138

desired period (30 minutes), they are loaded into the cell culture array chip by an electronic, handheld pipette (Thermo Fisher Scientific, Hudson, New Hampshire).
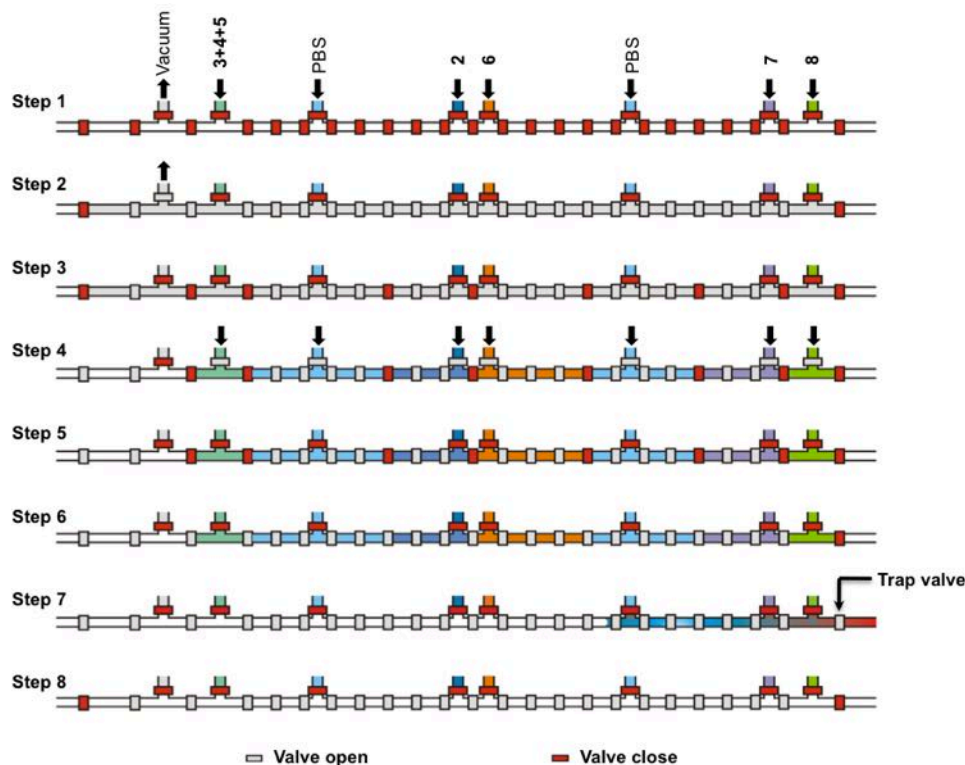
Figure 5-2 Schematic diagram of the preparation of a given category of MFNPs in a combinatorial library using the digital droplet generator

5.2.3.4 Fabrication of cell culture array chip

The cell array chip consists of 24 (3 x 8) cell culture chambers, each with dimensions of 8 mm (l) x 1 mm (w) x 120 μm (h) for a total volume of 960 nL. The cell array chip is fabricated by directly attaching a polydimethylsiloxane (PDMS)-based microfluidic component onto a commercial poly-Llysine (PLL)-coated glass slide (Polysciences, Inc., Philadelphia, PA). The PDMS based micro-fluidic component was fabricated using a soft lithography method. Well-mixed PDMS precursors (Sylgard 184, A:B = 10:1 ratio) were poured onto a silicon wafer replicate of photolithographically

defined microchannel patterns. After vacuum degassing and curing at 80 $^{\circ}$C, the microfluidic component was peeled off the replicate, followed by introduction of holes with pipette tip size-matched diameters at the ends of the microchannels. To attach the microfluidic component to a PLL-coated glass slide, we prepared a 1-3 μm-thick adhesive PDMS layer by spin coating a 1: 4 mixture of toluene and PDMS precursors (Sylgard 184, A:B = 5:1 ratio) onto a glass substrate. Through contact printing, the adhesive PDMS layer was directly transferred to the PDMS-based microfluidic component, followed by direct attachment onto a PLL-coated glass slide. The assembled chip was then baked in an 80 $^{\circ}$C vacuum oven for 24 h. Prior to cell culture, the cell array chips were sterilized by exposure to UV light for 15 min.

5.2.4 Comparison of MFNPs formulation and screening by the digital droplet generator and conventional pipetting

The employed digital droplet generator exhibits profound advantages, including faster operation throughput, uniform control upon the sizes of MFNPs, error-proof and significantly improved reproducibility, over those observed for pipette-based manual operation.

Table 5-1 Comparison of MFNPs formulation and screening by the digital droplet generator and conventional pipetting

	Digital Droplet Generator	Pipetting
Throughput	375 conditions/h	<20 conditions/h
Size distribution	Excellent (PDI[a]: <0.05)	Good (PDI[a]: 0.10~0.20)
Operation error	No	Possible
Reproducibility	High	Modest

[a]PDI: The polydispersity index obtained from DLS measurements. The experiments were repeated 3-4 times independently to determine the size distribution, operation error and reproducibility.

5.2.5 Screening of MFNPs

To test the throughput capability of the platform for formulating and screening MFNPs, three categories of MFNPs with different ligand decorations were prepared in the digital droplet generator. The entire 375 MFNP formulations were automatically prepared within 1 h, and then incubated in the PTFE tubes for 30 min at room temperature. Subsequently, the individual MFNP were introduced into individually addressed cell culture chambers (containing NIH 3T3 cells, ca. 5x 10^3 cells/chamber) in the cell culture array chip. After incubating the MFNP-treated cells (5% CO_2) at 37^oC for 24 h, the transfection and transduction efficiencies of each MFNP was quantified by fluorescence microscopy-based single cell image cytometry. A 3D plot and its corresponding 2D cross sections (Fig. S2a and b) were used to summarize the transfection and transduction efficiencies of the MFNPs library. Regarding the operation rate of the microfluidic cell culture array, it takes less than 1 s to introduce a specific type of MFNP into an individually addressed cell culture chamber using an electronic, handheld pipette (Thermo Fisher Scientific, Hudson, New Hampshire).

5.2.6 Correlations between structures of MFNPs and delivery performance

To gain insight on how the structures of MFNPs affect the observed delivery performance, three sets of synthetic parameters that led to high (★), medium (★) and low (★) delivery performances (see the image cytometry data that reflect transfection/transduction efficiencies in Figure 5-3) were chosen for scale-up preparation (200 droplets, 40 μL for each data point) of the respective MFNPs. Transmission electron microscopy (TEM) was employed to examine the morphology and sizes of the MFNPs, indicating that three distinct sizes of 100 ± 4, 210 ± 9 and 480 ± 13 nm MFNPs were

obtained from the chosen synthetic parameters (Table 5-1). These results were confirmed by dynamic light scattering measurements (Figure 5-4). We also characterized the zeta potentials of these MFNPs, which cover a range from 7.2±2.5 to 21.7±3.8 mV (Figure 5-5).
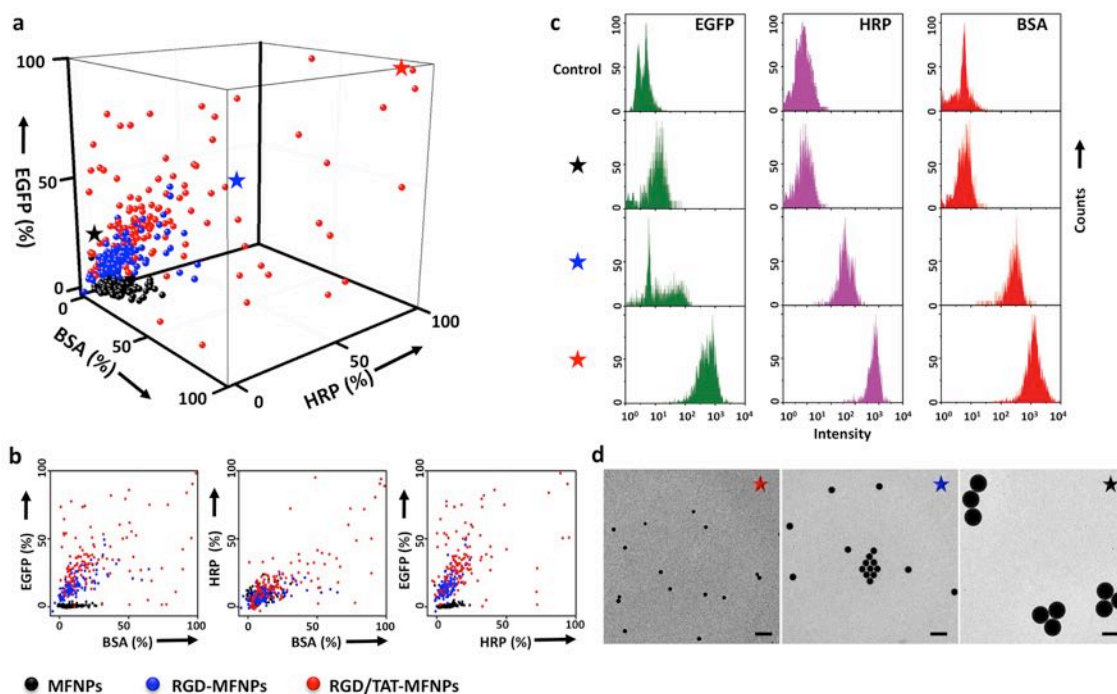
Figure 5-3 a, A 3D profile of gene transfection (EGFP) and transduction performance (BSA and HRP) of three categories of MFNPs produced by the digital droplet generator. b, The XY, YZ and XZ projections of the transfection/transduction data of the 3D profile of gene transfection and transduction performance. c, Image cytometry data showed high (★), medium (★) and low (★) delivery performances. d, Transmission electron microscopy (TEM) was employed to examine the morphology and sizes of the MFNPs.
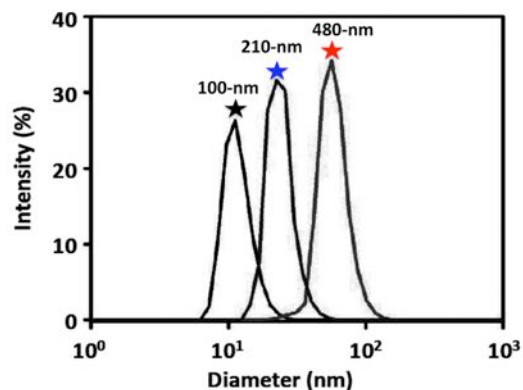
Figure 5-4 Hydrodynamic sizes of MFNPs with high (★), medium (★) and low (★) delivery performance were measured by DLS in PBS buffer.
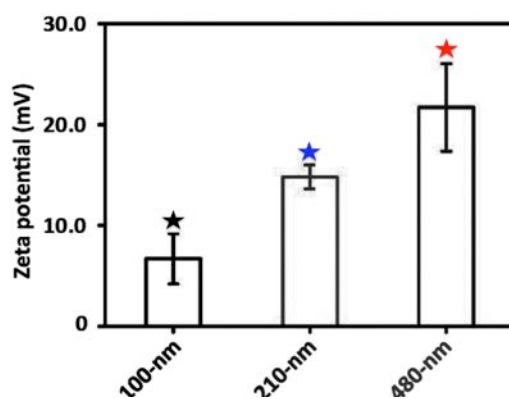
Figure 5-5 Zeta potentials variations of MFNPs with high (★), medium (★) and low (★) delivery performance were measured in PBS buffer.

5.2.7 HRP activity assay

The activity of intracellular HRP delivered by MFNPs was assessed by monitoring the oxidation of o-Dianisidine catalyzed by the lysated MFNP-treated cells. Briefly, NIH 3T3 cells were firstly incubated with MFNPs containing HRP for certain time (usually 12 or 24 h). After incubation, cells were rinsing with PBS for three times to wash away all HRP that are not taken by cells. Cells were then lysed by adding cell lysis buffer (Sigma-Aldrich, US) and then add 100-μL PBS into each well. To evaluate the residual activity of HRP inside cells, certain amount of o-Dianisidine

143

DMSO solution (50 mM) and 5-μL of 0.1% H2O2 were added into cell lysate. The plate was placed on a shake table, 150 rpm for 30 s to mix thoroughly. During reaction, the cell lysate turned from clear to yellow then to dark brown, indicating the oxidation of o-Dianisidine catalyzed by HRP. The activity of HRP can be further quantified by measuring the absorbance (460 nm) of the reaction mixture.

5.2.8 GAL4-VP16 activity assay

In order to determine the GAL4-VP16 activity after delivery, we quantified the luciferase expression by measuring the bioluminescence intensity of MFNP-treated NIH 3T3 cells. MFNPs were prepared in using the method described in the main text (page 5). NIH 3T3 cells were seed into a 96-well plate the day before exposure to the MFNPs and control groups (PBS, pG5E4T-Fluc, and GAL4-VP16). After 12-h incubation, cells were washed and incubated with fresh medium for another 24 h to allow the luciferase expression that was activated by GAL4-VP16. To quantify the luciferase expression, cells were lysed and then incubated with 100-μL luciferin substrate (Promega, E1500) at room temperature for 2 min. Bioluminescence intensities were then measured by both the plate reader (Fujifilm BAS-5000) and the CCD camera (IVIS, Xenogen).

5.2.9 Stability studies of 100-nm MFNPs

In order to understand the dynamic stability of the optimal 100-nm MFNPs indentified from the large-scale screening, we employed real-time DLS measurements to monitor their size variation (i) at different pH values (pH 3.8-9.2) and temperatures (25, 37 and 60°C), (ii) in the presence of 10% serum, and (iii) at different storage times in presence of physiological salt concentrations. The results were summarized in Figure 5-6.
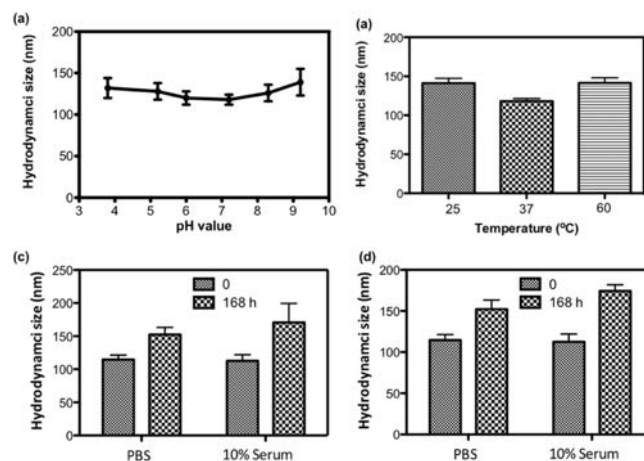
Figure 5-6 a. pH-dependent size varations of 100-nm MFNPs in the respective buffer solution with pH values ranging from 3.8 to 9.2; b. Temperature-dependent size variation of 100-nm MFNPs in PBS buffer with different temperatures at 25, 37 and 60 °C; c. Hydrodynamic size of 100-nm MFNPs in either the presence or absence of 10% serum containing PBS buffer; d. Hydrodynamic size of GAL4-VP16 encapsulated MFNPs in either the presence or absence of 10% serum containing PBS buffer. Error bars are obtained from triplicated experiments.

5.2.10 Biodegradability of GAL4-VP16-encapsulated MFNPs in serum

The biodegradability of GAL4-VP16-encapsulated MFNPs in serum was investigated to understand their properties in vivo environment. The prepared GAL4-VP16-encapsulated MFNPs were incubated in the serum for different time scales. The GAL4-VP16 activity was quantified by measuring the bioluminescence intensity of MFNP-treated NIH 3T3 cells.
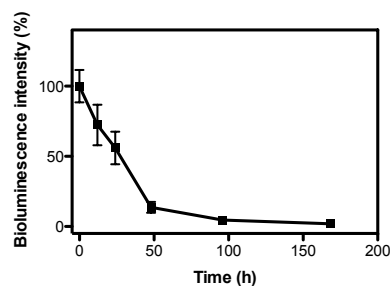
Figure 5-7 Biodegradability of GAL4-VP16 encapsulated MFNPs from 0 to 168 h in serum. Error bars are obtained from triplicated experiments.

5.2.11 Microscope settings, imaging processing and data analyzing

The cell array chip was mounted onto a Nikon TE2000S inverted fluorescent microscope with a CCD camera (Photomatrix, Cascade II), X-Cite 120 Mercury lamp, automatic stage, and filters for three fluorescent channels (W1 (EGFP), W2 (RhB) and W3 (Cy5)). Following image acquisition, MetaMorph (Molecular Devices, Version 7.5.6.0) was used to quantify EGFP expression, RhB and Cy5 fluorescence intensity of cells. The Multi-Wavelength Cell Scoring module of the Metamorph software allows image analysis. A cell counting application in the module allows us to calculate the total cell number. In order to determine the gene transfection efficiency, the EGFP-expressed cell number was counted by the MetaMorph program that distinguishes the transfected cells from the non-transfected cells. The EGFP fluorescence intensity of non-transfected cells are 200~300 pixels higher than the background. The cells with EGFP fluorescence intensity 300 pixels higher than the background are recognized as the transfected cells. The gene transfection efficiency was obtained by the EGFP-expressed cell number divided by the total cell number. The protein transduction efficiency was quantified by the fluorescence intensities of fluorophores labeled in the proteins nanocapsules in the transduced cells.

5.2.12 Cell viability assay
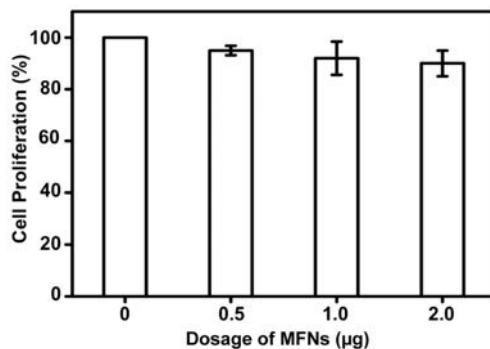
Figure 5-8 Cytotoxicity of different dosages of 100-nm MFNPs determined by MTT assay after 24 h incubation with NIH 3T3 cells. Error bars are obtained from triplicated experiments.

146

The cytotoxicity of 100-nm MFNPs was assessed by the MTT assay. NIH 3T3 cells were seeded into a 96-well plate (10^4 cells/well), the 100-nm MFNPs with different concentrations were incubated with cells for 24 h. After incubation, CellTiter-Blue (20 µL) was added into each well and incubated for 3 h. The plate was then placed on a shaking table, 150 rpm for 5 min to thoroughly mix the solution, and then fluorescence intensities were measured with a plate reader (Ex = 535 nm, Em = 585 nm). As shown inFigure 5-8, there was no significant fluorescence intensity differences between the treated and non-treated cells, which suggested that the toxicity of 100-nm MFNPs are negligible.

5.2.13 In vivo bioluminescence imaging

To monitor the bioluminescent signals of co-delivered pG5E4T-FLuc and GAL4-VP16 *in vivo*, the immune competent female nu/nu nude mice were anesthetized and injected with 100 µL of luciferin substrate via intraperitoneal. Mice were placed in a light-tight chamber of the IVIS imaging system and bioluminescent light signals from whole-body imaging were acquired repetitively until the maximum peak of photon numbers were obtained with the cooled charged-coupled device optical imaging system (Xenogen, Alameda, CA). The intensity of imaging signals from regions of interest (ROIs) were selected, measured, and analyzed in total photons/second and maximum photons/second/ cm2/steradian using LIVING IMAGE Optical Imaging Software (Xenogen). *Ex vivo* experiments were performed after treatment of the mice with MFNPs (containing pG5E4T-Fluc and GAL4-VP16) 168 h. The mice were sacrificed and liver, heart, kidney, lung and spleen were collected for imaging.

5.2.14 Pathological study and blood chemistry assay

Pathological studies were evaluated in immune competent female nu/nu mice. Animals were injected with 100-nm MFNPs into the tail vein. Animals were sacrificed at 168 h after treatment. Livers were collected, formalin fixed, sections H & E (hematoxilin (stains nucleus) and eosin (stains cytoplasm)) stained, and pathologically examined by UCLA phathological core facility.

The 100-nm MFNP-treated mice were scarified 168 h post-injection. Blood was collected from the junction of the submandibular and facial vein by puncture with a 22 gauge needle into a sodium citrate containing serum tube (transaminases, creatinine). Transaminases (ALT/AST) and creatinine were measured by using a Cobas Mira (Roche) autoanalyzer at diagnostic laboratory, division of laboratory animal medicine, UCLA.

5.3 Results and discussions

As illustrated in Figure 5-1b, the modular assembly system consists the following modules. The gene module can be any DNA or RNA of interest. The scaffold modules is cyclodextran-linked poly(ethylenimine) (CD-PEI); and the function modules are a series of poly(ethylene glycol) (PEG) derivatives, of which one end-group is terminated with an Adamantane (Ad) group and the other end is terminated with a methyl group (Ad-PEG) or a functional peptide, such as RGD[340] (Ad-PEG-RGD) and TAT[339] (Ad-PEG-TAT). The protein module includes a library of protein nanocapsules, which were made by encapsulating protein within a thin layer of degradable polymer of which surface was linked with adamantane (Ad) groups. This strategy yields generally applicable protein modules whose assembly properties are not affected by the core protein. Driven by electrostatic interactions between the CD-PEI (positive charged) and the gene molecules (negative charged), as well as the molecular recognition between Ad and CD, genes and proteins can

148

be effectively incorporated together to form MFNPs with various functional molecules (Ad-PEG, Ad-PEG-TAT, and Ad-PEG-RGD) on their surface in order to stabilize the structure, as well as confer delivery specificity and cell transfusion capability. Apparently, the gene and protein payloads are encapsulated inside the self-assembled MFNPs, avoiding potential degradation[378] over the delivery process. It is worth noting that the protein nanocapsules also act as a crosslinker to maintain the structure of MFNPs since there are multiple Ad groups on their surface. Since the polymeric shell of protein nanocapsules is ready to be degraded during the endocytosis, the structure of MFNPs cannot maintain after entering the cells, leading to an effective release of the protein and gene payloads intracelluarly.

As one of the key feature, this platform is capable to rapidly determine the optimal formulation of MFNPs with desired delivery efficiency. To test this capability, two types of fluorescence-labeled proteins, Cy5 labeled bovine serum albumin (BSA-Cy5) and rhodamin B-labeled horseradish peroxidase (HRP-RhB), and EGFP-encode DNA plasmid were employed for the preparation of MFNPs in the digital droplet generator. By modulating the inlet of functional module, three categories of MFNPs with different surface ligands were synthesized. The 1st category of MFNPs bear Ad-PEG, Ad-PEG-RGD and Ad-PEG-TAT with pre-identified ratios[369]; the 2nd category contained Ad-PEG and Ad-PEG-RGD; and 3rd category was decorated with only Ad-PEG. Each category contains 125 formulations of MFNPs that were prepared by systematically altering the concentration of CD-PEI, BSA-Cy5, and HRP-RhB. As a result, 375 formulations of MFNPs were prepared automatically with 1h. After 30-min incubation, each MFNP droplet (0.2 μL) was then automatically diluted with 1.8-μL of Opti-MEM media to 2 μL, and introduced into an individually addressed cell culture chamber (containing NIH 3T3 cells, *ca.* 5×10^3 cells/chamber) in the cell culture array chip. After incubating the MFNPs-treated cells (5% CO_2) in the cell array chip at 37

°C for 24 h, the transfection and transduction efficiencies of each MFNPs formulation were quantified by fluorescence microscopy-based single-cell image cytometry.[373] A 3D plot (Figure 5-9a) were used to summarize the transfection and transduction efficiencies of the MFNPs library, revealing that an optimal transfection/transduction performance was achieved using RGD/TAT-MFNPs (3rd category) with a specific composition, *i.e.*, CD-PEI = 20 ng, BSA-Cy5 = 39 ng and HRP-RhB = 27 ng in 200-nL PBS. Figure 2b shows the fluorescence images of cells treated with optimal MFNPs, indicating the successful transfection of EGFP-encode DNA plasmid and the successful transduction of both two proteins.
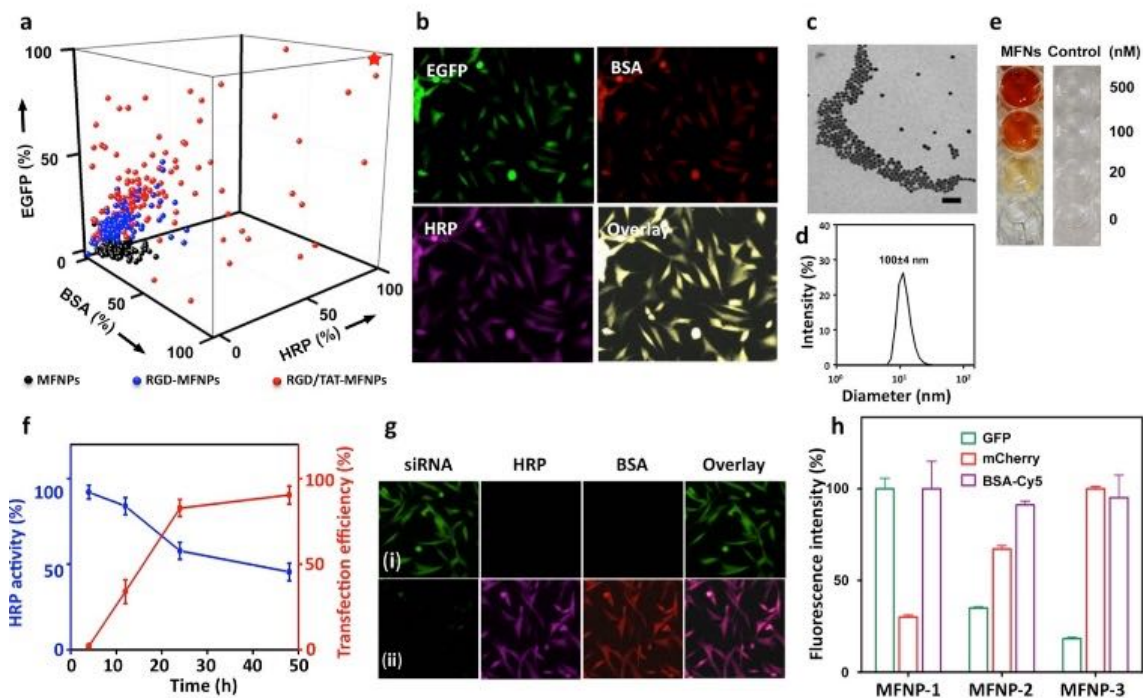
Figure 5-9 Optimization of MFNPs for simultaneous delivery of genes and proteins. a) A 3D profile of gene transfection (EGFP) and transduction performance (BSA-Cy5 and HRP-RhB) of three categories of MFNPs produced by the digital droplet generator. Red dots represent 125 data points observed for the 1st category: RGD/TAT-MFNPs; Blue dots (125 data points) for the 2nd category: RGD-MFNPs; Black dots (125 data points) for 3rd category: MFNPs. b) A set of synthetic parameters that resulted in high (★) delivery performance (see the fluorescence micrographs that reflect transfection/transduction outcomes)

were chosen for scale-up preparation (200 droplets, 40 µL for each set) of the respective RGD/TAT-MFNPs. c) Transmission electron microscopy (TEM) was employed to examine the morphology and sizes of the RGD/TAT-MFNPs, scale bars: 400 nm. d) Dynamic light scattering (DLS) was employed to measure MFNPs hydrodynamic sizes in PBS buffer. The distinct MFNP size of 100 ± 4 nm was obtained from the chosen synthetic parameters. Error bars are based on the standard deviation of three independent experimental results. e) A colorimetric assay was employed for quantifying intracellular enzymatic activity of HRP delivered by the MFNPs using o-Dianisidine (3,3'-dimethoxybenzidine) (50 mM) as chromogenic substrates and H_2O_2 as an oxidizer. Different concentrations of 100-nm RGD/TAT-MFNPs with encapsulated HRP amounts from 0 to 500 nM were added into individual wells in a 96-well plate. The orange color indicated that the HRP remained its biological activity after transduction. f) The time-dependent in vitro co-delivery performance of the optimal 100-nm RGD/TAT-MFNPs were monitored in parallel by quantifying fluorescent signals associated with EGFP expression and colorimetric readouts correlated to HRP activity, respectively. The highest co-delivery performance was achieved after treatment of cells for 24-48 h. g) Fluorescence images of U87-EGFP cells before (i) and after (ii) transduction with MFNPs containing siRNA silencing enhanced green fluorescence protein, BSA-Cy5 and HRP-RhB. Intense cellular fluorescence signals from HRP-RhB and BSA-Cy5, as well as significantly reduced green fluorescence intensity due to the silencing of EGFP expression by siRNA, suggest successful demonstration of simultaneous delivery of gene and proteins. h) Quantification of the fluorescence intensity of NIH 3T3 cells after the incubation with MFNPs containing BSA-Cy5, EGFP and mCherry plasmids with different ratios. The amount of BSA-Cy5 was kept constant in three groups of MFNPs. Molar ratios of plasmids of EGFP to mCherry were 4:1 (MFNP-1), 1:1 (MFNP-2), and 1:4 (MFNP-3), respectively. One-way ANOVA, post-hoc Tukey test, P< 0.01). No difference is present among the BSA-Cy5 transduction efficiency. GFP and mCherry transfection efficiencies are statistically different from among the three groups.

To gain insight on how the structural property of RGD/TAT-MFNPs affect the observed co-delivery performance, the optimal synthetic parameters (Figure 5-9a, ★) was chosen for scale-up preparation (200 droplets, 40 µL). Transmission electron microscopy (TEM, Figure 5-9c) images indicates that the RGD/TAT-MFNPs are spherical morphology with diameters of 100 ± 4 nm, which was also confirmed by dynamic light scattering measurements (Figure 2d). We also characterized the zeta potentials of the 100-nm RGD/TAT-MFNPs as 7.2±2.5 mV (Figure 5-5). Furthermore, a colorimetric assay was employed for quantifying the enzymatic activity of MFNP-encapsulated

HRP intracellular by using o-Dianisidine (3,3′-dimethoxybenzidine) as chromogenic substrates (Figure 5-9e). The time-dependent *in vitro* transfection and transduction performance of 100-nm RGD/TAT-MFNPs were monitored in parallel by quantifying fluorescent signals associated with EGFP expression and colorimetric readouts correlated to HRP activity, respectively. As shown in Figure 5-9f, the highest co-delivery performance was achieved at 24 to 48 h after MFNP-treatment. Moreover, the other two formulations that led to sub-optimal delivery performances of RGD/TAT-MFNPs were also carefully examined (Figure 5-3). TEM images indicated that the size of those two sub-optimal MFNPs were larger than 200 nm (Figure 5-3d), which is unfavorable for high-performance delivery.

To test the general applicability of the MFNP vectors, the optimal synthetic parameter identified above was employed for delivery of two protein modules (*i.e.*, HRP-RhB and BSA-Cy5) and a short-interfering siRNA for silencing of enhanced green fluorescence protein (EGFP). After treating EGFP-expressing brain tumor cells (EGFP-U87) with these MFNPs, we were able to observe the suppression of EGFP expression, as well as simultaneous transduction of both HRP-RhB and BSA-Cy5 in EGFP-expressing brain tumor cells (EGFP-U87) (Figure 5-9g). Finally, we examined the feasibility of controlling stoichiometry among individual payloads in MFNP vectors. As an example, a protein module (*i.e.*, BSA-Cy5) and two gene modules (*i.e.*, pEGFP and mCherry plasmids) were encapsulated into MFNP vectors at different pEGFP/pmCherry ratios (1: 4, 1: 1, and 4: 1, n/n) and a fixed BSA-Cy5 quantity, resulting in three different MFNP formulations denoted as MFNP-1, 2, and 3, respectively. As shown in Figure 5-9h, the fluorescence intensity coming from expressed EGFP and mCherry is proportional to the amount of pEGFP and pmCherry plasmid carried by the MFNPs, confirming that the ratio of payloads being delivered can be controlled

with MFNP. Moreover, all three types of MFNPs carried the same amount of BSA-Cy5, as a result, cells exposed with them exhibit similar fluorescent intensities of BSA-Cy5, confirming an excellent reproducibility of BSA-Cy5 transduction (Figure 5-9h). Moreover, the MFNPs are quite stable in various conditions, which was confirmed by a series of studies (Figure 5-6).
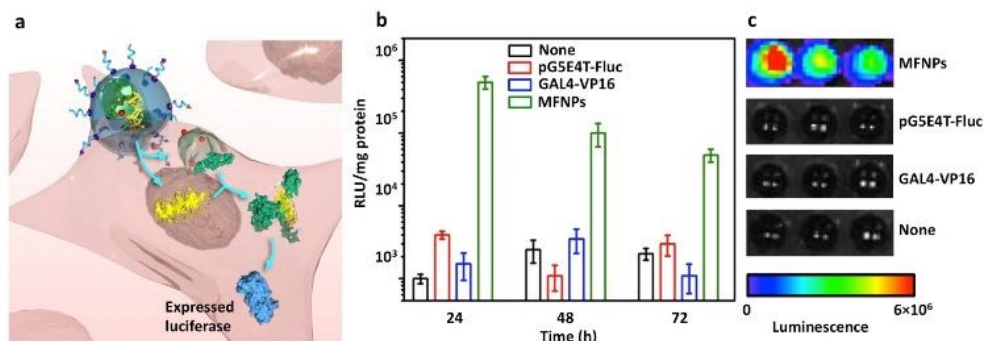
Figure 5-10 Co-delivery of functionally complementary gene and protein in cells. a) The optimal synthetic parameters identified from the screening were employed for the preparation of 100-nm MFNPs for simultaneous delivery of functionally complementary protein (GAL4-VP16) and gene (pG5E4T-Fluc). The delivery efficiency can be reflected in the bioluminescence intensity as a result of luciferase expression of pG5E4T-Fluc specifically activated by GAL4-VP16. b) Time-dependent luciferase expression and c) bioluminescence imaging of the 100-nm MFNPs-treated cells along with the control experiments based on pG54ET-Fluc plasmid and GAL4-VP16. Error bars were obtained from three independent experiments. One way ANOVA, post-hoc Tukey test, $P < 0.05$). No difference is present among the control groups. Statistically difference was found from between positive and control groups.

The uniqueness of the high-efficient co-delivery vector is that it could simultaneously introduce functionally complementary protein and gene that lead to synergistic outcomes for regulating cellular circuitry. As an example (Figure 5-10a), GAL4-VP16 (a transcription factor fusion protein) and pG5E4T-Fluc (a plasmid vector that contains GAL4-VP16 matching recognition sequences and a luciferase reporter) were chosen for conducting in vitro and in vivo studies. After intracel-

lular delivery of GAL4-VP16 and pG5E4T-Fluc, the luciferase reporter in pG5E4T-Fluc was specifically activated by GAL4-VP16, generating a real-time readout reflecting a synergistic outcome of the co-delivered payloads. By using the previous optimized synthetic parameters, 10 droplets (2 µL in total volume) containing desired MFNPs were generated from CD-PEI (0.2 µg), Ad-PEG (10.0 µg), Ad-PEG-RGD (0.5 µg), Ad-PEG-TAT (0.9 µg), pG5E4T-Fluc (0.1 µg) and GAL4-VP16 (0.66 µg) in the digital droplet generator. The resulting MFNPs were introduced into a 96-well plate (containing NIH 3T3 cells, *ca*. 1×10^4 cells/well) along with control systems, including pG54ET-Fluc plasmid, and the protein module containing GAL4-VP16. After incubating (5% CO_2) at 37 ^{o}C for 24, 48 and 72 h, the cells were lysed for quantification of bioluminescence using either a plate reader (Figure 5-10b) or a cooled charge-coupled device (CCD) camera (IVIS, Xenogen) (Figure 5-10c). Compared to the background-level bioluminescence intensities observed for the control experiments, the bioluminescence intensity of the MFNPs-treated cells was significantly higher, suggesting that the MFNPs are capable to deliver both pG54ET-Fluc and GAL4-VP16 simultaneously into the cells with a much higher performance than the direct use of the protein and the gene.
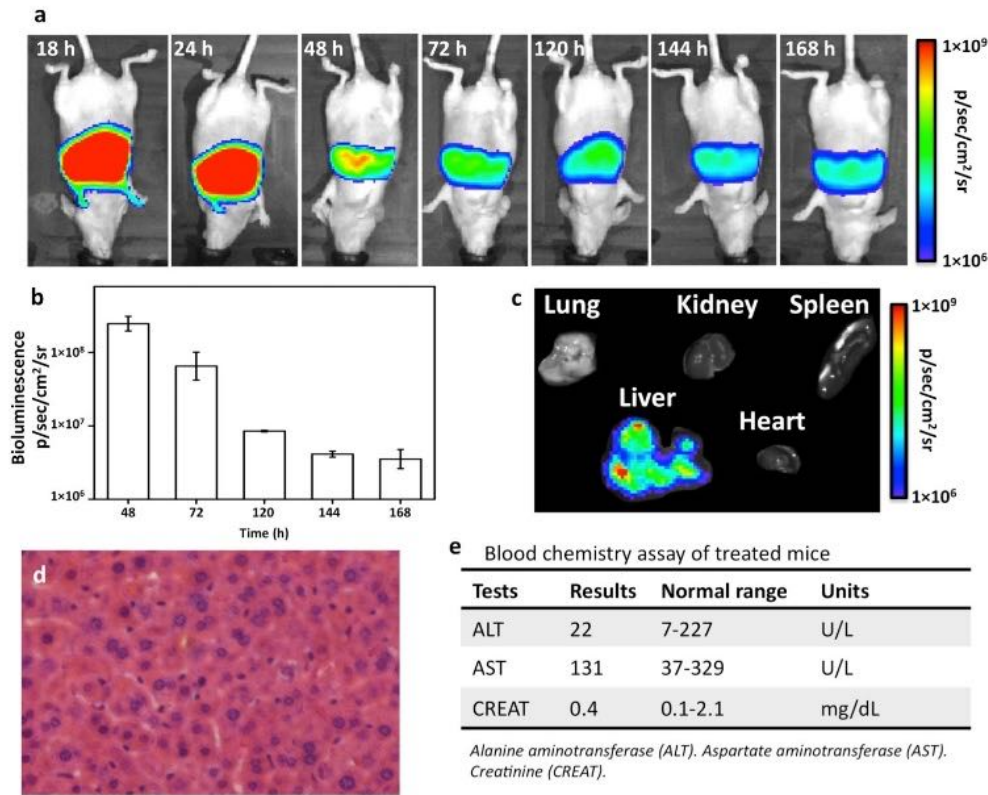
Figure 5-11 Monitoring in vivo synergetic effects of the co-delivered gene and protein. In vivo experiments were performed by injection of 100-nm MFNPs (containing 1 µg pG5E4T-Fluc and 6.6 µg Ad-n-GAL4-VP16) into nu/nu nude mice via tail veins. a) The bioluminescence imaging indicated that 100-nm MFNPs were delivered into hepatocytes efficiently and the liver showed strong bioluminescence signal. b) The bioluminescence was quantified from 48 to 168 h post MFNP treatments. Quantitative data were not available due to the saturated bioluminescence within 48 h post treatment. There are the significant differences of bioluminescence intensity at different time points (One way ANOVA test, P< 0.01, n=4). c) Ex vivo experiments of 100-nm MFNPs-treated mice were performed after 168 h post injection and the results were consistent with bioluminescence imaging data. The in vivo cytotoxicity of the optimal co-delivery vector was evaluated by both histological study and blood chemistry assay. d) H&E stained liver sections from nude mice treated with 100-nm MFNPs after 168 h post injection. There was no hepatocytes necrosis or excessive lymphoid infiltrates were observed. e) Blood chemistry assay was carried out and the results indicated that no significant difference in any blood parameter was observed between treated and normal control mice.

Finally, the *in vivo* experiments were performed by injection of the MFNPs that encapsulated pG54ET-Fluc (1 µg) and GAL4-VP16 (6.6 µg) into nu/nu nude mice *via* tail veins. As illustrated

in Figure 5-11a, strong bioluminescent signal was observed from the liver of the treated animal, indicating that the MFNPs were delivered into hepatocytes efficiently. The intensity of the signal at 168 h post injection was decreased two-fold magnitude compared to that at 48 h post injection (Figure 5-11b). *Ex vivo* results were consistent with bioluminescent imaging data (Figure 5-11c). The *in vivo* cytotoxicity of the optimal co-delivery system was evaluated by both histological study and blood chemistry assay. The mice treated with the MFNPs did not show any hepatocytes necrosis or excessive lymphoid infiltrates (Figure 5-11d). In addition, the blood chemistry assay indicated that no significant difference in any blood parameter between treated and normal control mice. Furthermore, no liver toxicity as indicated by elevated liver enzymes (ALT/AST) or kidney toxicity as indicated by elevated creatinine levels was observed (Figure 5-11e), suggesting the liver toxicity or kidney toxicity of the MFNPs is negligible.

5.4 Conclusion

In conclusion, we have demonstrated a high-throughput technology that provides a universal platform for formulating and screening multifunctional nanoparticles (MFNPs) capable of high-efficient simultaneous delivery of genes and proteins with flexibility in payload selection, accuracy in payload control. Further work on the application of this technology in immunotherapy and stem cell reprogramming are under way.

Chapter 6. Summary and Perspectives

Protein therapy, which delivers therapeutic proteins to correct disorders, has been considered as the safest and most direct approach for treating diseases. However, its applications are highly limited by the lack of efficient strategies for protein delivery, resulting the fast clearance of therapeutic proteins after administration in vivo. Decades of efforts in this fields result in the development of various strategies and carriers for protein delivery, including various liposomal carriers, self-assembled polymeric nanostructures, direct conjugation of cationic polymers or hydrophilic polymers for the purposes of intracellular delivery and systemic delivery of therapeutic proteins respectively. From the molecular perspective, such carriers are designed to shield the enzymes from the surrounding, which creates a new surface surrounding the protein molecule to interact with outer environment instead of the original surface of the proteins. Such strategies not only confer proteins unique features such as high membrane permeability, long plasma half-life, as well as reduced possibilities of proteolysis, immune activation and immune clearance. However, clinical application of protein therapeutics other than mAbs remains rare, indicating several essential problems have not yet been resolved properly by current delivery systems. Novel delivery strategies, especially the systems designed and optimized specially for protein delivery, are still demanded to fulfill the requirements of clinical application of protein therapy in diseases treatments.

At year 2010, our group demonstrated a novel strategy for protein delivery by encapsulating single protein molecule into a thin layer of polymer network, in order to endow new features and unique surface properties to any protein. One major advantage of this system is, the encapsulation process is achieved by in-situ polymerization of monomers and crosslinkers in protein solution, which

provides countless potentials for easily engineering of the surface properties of the resulting protein nanocapsules. Based on this techonology, our group and many other research groups have been developed various systems that have covered most areas for the applications of proteins, including protein intracellular delivery, systemic delivery and long circulation of proteins, co-delivery of multiple proteins, as well as applications such as siRNA and miRNA delivery. During the past five years, my Ph.D. research also worked on exploring the potential of this system to resolve real-life problems in the application of proteins and enzymes for therapeutic purposes. In these thesis, four of my work were discussed in detail, demonstrating several practical methods to solve common challenges in protein delivery including

(a) intracellular delivery of proteins without compromising their biological functions;

(b) high-through synthesis and optimization of nanostructures for efficient co-delivery of multiple proteins intracellularly;

(c) systemic delivery of multiple proteins with highly synergistical functions;

(d) prolonging the plasma half-life and reducing immunogenicity of any protein.

The abovementioned work not only demonstrate some well designed systems to solve several essential problems in protein delivery, they also provide solid fundamental for solving other issues especially for targeted delivery, which has been the ultimate goal for the broad field of nanomedicine. With the rapid advances in the protein-engineering technologies, understanding of disease mechanism at the molecular (enzyme) level, and the development of more advanced carriers, one can expect that increasing number of protein therapeutics will be developed and widely applied to curing diseases in the near future.

References

1.	Krejsa, C., Rogge, M. & Sadee, W. Protein therapeutics: new applications for pharmacogenetics. *Nat. Rev. Drug Discov.* **5,** 507–521 (2006).

2.	Leader, B., Baca, Q. J. & Golan, D. E. Protein therapeutics: a summary and pharmacological classification. *Nat. Rev. Drug Discov.* **7,** 21–39 (2008).

3.	Dimitrov, D. in *Therapeutic Proteins* (eds. Voynov, V. & Caravella, J. A.) **899,** 1–26 (Humana Press, 2012).

4.	Reichert, J. M. Antibody-based therapeutics to watch in 2011. *mAbs* **3,** 76–99 (2011).

5.	Reichert, J. M. Metrics for antibody therapeutics development. *mAbs* **2,** 695–700 (2010).

6.	Dimitrov, D. S. Therapeutic antibodies, vaccines and antibodyomes. *mAbs* **2,** 347–356 (2010).

7.	Longo, N. *et al.* Single-dose, subcutaneous recombinant phenylalanine ammonia lyase conjugated with polyethylene glycol in adult patients with phenylketonuria: an open-label, multicentre, phase 1 dose-escalation trial. *Lancet* **384,** 37–44 (2014).

8.	Ganson, N. J., Kelly, S. J., Scarlett, E., Sundy, J. S. & Hershfield, M. S. Control of hyperuricemia in subjects with refractory gout, and induction of antibody against poly(ethylene glycol) (PEG), in a phase I trial of subcutaneous PEGylated urate oxidase. *Arthritis Res Ther* **8,** (2006).

9.	Sarkissian, C. N. *et al.* A different approach to treatment of phenylketonuria: Phenylalanine degradation with recombinant phenylalanine ammonia lyase. *Proc. Natl. Acad. Sci.* **96,** 2339–2344 (1999).

10.	Sherman, M. R., Saifer, M. G. P. & Perez-Ruiz, F. PEG-uricase in the management of treatment-resistant gout and hyperuricemia. *Adv. Drug Deliv. Rev.* **60,** 59–68 (2008).

11.	Bomalaski, J. S. & Clark, M. A. Serum uric acid-lowering therapies: where are we heading in management of hyperuricemia and the potential role of uricase. *Curr. Rheumatol. Rep.* **6,** 240–247 (2004).

12.	Hernandez, C. P. *et al.* Pegylated arginase I: a potential therapeutic approach in T-ALL. *Blood* **115,** 5214–5221 (2010).

13.	Hershfield, M. S. PEG-ADA replacement therapy for adenosine deaminase deficiency: an update after 8.5 years. *Clin. Immunol. Immunopathol.* **76,** S228–32 (1995).

14.	Müller, H. J. & Boos, J. Use of l-asparaginase in childhood ALL. *Crit. Rev. Oncol. Hematol.* **28,** 97–113 (1998).

15.	Porter, D. W., Nealley, E. W. & Baskin, S. I. In vivo detoxification of cyanide by cystathionase γ-lyase. *Biochem. Pharmacol.* **52,** 941–944 (1996).

16.	Turrens, J. F., Crapo, J. D. & Freeman, B. A. Protection against oxygen toxicity by intravenous injection of liposome-entrapped catalase and superoxide dismutase. *J. Clin. Invest.* **73,** 87–95 (1984).

17.	Vilanova, E. & Sogorb, M. A. The Role of Phosphotriesterases in the Detoxication of Organophosphorus Compounds. *Crit. Rev. Toxicol.* **29,** 21–57 (1999).

18.   Bomalaski, J. S., Holtsberg, F. W., Ensor, C. M. & Clark, M. A. Uricase formulated with polyethylene glycol (uricase-PEG 20): Biochemical rationale and preclinical studies. *J. Rheumatol.* **29,** 1942–1949 (2002).

19.   CLEMEDSON, C. J., HULTMAN, H. I. & SORBO, B. The antidote effect of some sulfur compounds and rhodanese in experimental cyanide poisoning. *Acta Physiol. Scand.* **32,** 245–251 (1954).

20.   COHEN, J. A. & WARRINGA, M. Purification and Properties of Dialkylfluorophosphatase. *Biochim. Biophys. Acta* **26,** 29–39 (1957).

21.   Frankenberg, L. Enzyme therapy in cyanide poisoning: Effect of rhodanese and sulfur compounds. *Arch. Toxicol.* (1980).

22.   Jackson, C. J. *et al.* Pharmacokinetics of OpdA, an organophosphorus hydrolase, in the African green monkey. *Biochem. Pharmacol.* **80,** 1075–1079 (2010).

23.   Nucci, M. L., Olejarczyk, J. & Abuchowski, A. Immunogenicity of polyethylene glycol-modified super-oxide dismutase and catalase. *J. Free Radic. Biol. Med.* **2,** 321–325 (1986).

24.   Müller, H.-J. *et al.* Pharmacokinetics of native Escherichia coli asparaginase (Asparaginase medac) and hypersensitivity reactions in ALL-BFM 95 reinduction treatment. *Br. J. Haematol.* **114,** 794–799 (2001).

25.   Torchilin, V. P. Recent advances with liposomes as pharmaceutical carriers. *Nat. Rev. Drug Discov.* **4,** 145–160 (2005).

26.   Gombotz, W. R. & Pettit, D. K. Biodegradable Polymers for Protein and Peptide Drug Delivery. *Bioconjug. Chem.* **6,** 332–351 (1995).

27.   Duncan, R. The dawning era of polymer therapeutics. *Nat. Rev. Drug Discov.* **2,** 347–360 (2003).

28.   Veronese, F. M. & Pasut, G. PEGylation, successful approach to drug delivery. *Drug Discov. Today* **10,** 1451–1458 (2005).

29.   Petros, R. A. & DeSimone, J. M. Strategies in the design of nanoparticles for therapeutic applications. **9,** 615–627 (2010).

30.   Vellard, M. The enzyme as drug: application of enzymes as pharmaceuticals. *Curr. Opin. Biotechnol.* **14,** 444–450 (2003).

31.   Abuchowski, A., Karp, D. & Davis, F. F. Reduction of plasma urate levels in the cockerel with polyethylene glycol-uricase. *J. Pharmacol. Exp. Ther.* **219,** 352–354 (1981).

32.   Caliceti, P. & Veronese, F. M. Pharmacokinetic and biodistribution properties of poly(ethylene glycol)-protein conjugates. *Adv. Drug Deliv. Rev.* **55,** 1261–1277 (2003).

33.   Fuertges, F. & Abuchowski, A. The clinical efficacy of poly (ethylene glycol)-modified proteins. *J. Controlled Release* (1990).

34.   Savoca, K. V., Davis, F. F. & Palczuk, N. C. Induction of tolerance in mice by uricase and monomethoxypolyethylene glycol-modified uricase. *Int. Arch. Allergy Appl. Immunol.* **75,** 58–67 (1984).

35.   Davis, S., Park, Y. K., Abuchowski, A. & Davis, F. F. Hypouricaemic effect of polyethyleneglycol modified urate oxidase. *The Lancet* (1981).

36. NISHIMURA, H., Ashihara, Y., MATSUSHIMA, A. & INADA, Y. Modification of yeast uricase with polyethylene glycol: disappearance of binding ability towards anti-uricase serum. *Enzyme* **24,** 261–264 (1979).

37. Kelly, S. J. *et al.* Diabetes insipidus in uricase-deficient mice: a model for evaluating therapy with poly(ethylene glycol)-modified uricase. *J. Am. Soc. Nephrol. JASN* **12,** 1001–1009 (2001).

38. YASUDA, Y., FUJITA, T., TAKAKURA, Y., HASHIDA, M. & SEZAKI, H. Biochemical and Biopharmaceutical Properties of Macromolecular Conjugates of Uricase with Dextran and Polyethylene-Glycol. *Chem. Pharm. Bull. (Tokyo)* **38,** 2053–2056 (1990).

39. Caliceti, P., Schiavon, O. & Veronese, F. M. Immunological properties of uricase conjugated to neutral soluble polymers. *Bioconjug. Chem.* **12,** 515–522 (2001).

40. Caliceti, P., Schiavon, O. & Veronese, F. M. Biopharmaceutical properties of uricase conjugated to neutral and amphiphilic polymers. *Bioconjug. Chem.* **10,** 638–646 (1999).

41. Schiavon, O., Caliceti, P., Ferruti, P. & Veronese, F. M. Therapeutic proteins: a comparison of chemical and biological properties of uricase conjugated to linear or branched poly(ethylene glycol) and poly(N-acryloylmorpholine). *Farmaco* **55,** 264–269 (2000).

42. Tan, Q. Y., Wang, N., Yang, H., Chen, L. & Xiong, H. R. Preparation and characterization of lipid vesicles containing uricase. *... Deliv.* (2010).

43. Tan, Q. Y. *et al.* Characterization, stabilization and activity of uricase loaded in lipid vesicles. *Int. J. Pharm.* **384,** 165–172 (2010).

44. Magnani, M., Mancini, U., Bianchi, M. & Fazi, A. Comparison of uricase-bound and uricase-loaded erythrocytes as bioreactors for uric acid degradation. *... Use Resealed Erythrocytes ...* (1992).

45. Ihler, G., Lantzy, A., Purpura, J. & Glew, R. H. Enzymatic degradation of uric acid by uricase-loaded human erythrocytes. *J. Clin. Invest.* **56,** 595–602 (1975).

46. Dapergolas, G., Neerunjun, E. D. & Gregoriadis, G. Penetration of target areas in the rat by liposome-associated bleomycin, glucose oxidase and insulin. *Febs Lett.* (1976).

47. Taverna, R. D. & Langdon, R. G. Glucose transport in white erythrocyte ghosts and membrane-derived vesicles. *Biochim. Biophys. Acta* **298,** 422–428 (1973).

48. Rossi, L., Bianchi, M. & Magnani, M. Increased glucose metabolism by enzyme-loaded erythrocytes in vitro and in vivo normalization of hyperglycemia in diabetic mice. *Biotechnol. Appl. Biochem.* **15,** 207–216 (1992).

49. Liu, Y. *et al.* Biomimetic enzyme nanocomplexes and their use as antidotes and preventive measures for alcohol intoxication. *Nat. Nanotechnol.* **8,** 187–192 (2013).

50. Hershfield, M. S. *et al.* Treatment of adenosine deaminase deficiency with polyethylene glycol-modified adenosine deaminase. *N. Engl. J. Med.* **316,** 589–596 (1987).

51. Gamez, A., Wang, L., Straub, M., Patch, M. G. & Stevens, R. C. Toward PKU enzyme replacement therapy: PEGylation with activity retention for three forms of recombinant phenylalanine hydroxylase. *Mol. Ther. J. Am. Soc. Gene Ther.* **9,** 124–129 (2004).

52. Gamez, A. *et al.* Development of pegylated forms of recombinant Rhodosporidium toruloides phenylalanine ammonia-lyase for the treatment of classical phenylketonuria. *Mol. Ther. J. Am. Soc. Gene Ther.* **11,** 986–989 (2005).

53. Hoskins, J. A. *et al.* Enzymatic control of phenylalanine intake in phenylketonuria. *Lancet* **1,** 392–394 (1980).

54. Bourget, L. & Chang, T. M. Phenylalanine ammonia-lyase immobilized in semipermeable microcapsules for enzyme replacement in phenylketonuria. *Febs Lett.* **180,** 5–8 (1985).

55. Nakaoka, R., Tabata, Y., Yamaoka, T. & Ikada, Y. Prolongation of the serum half-life period of superoxide dismutase by poly (ethylene glycol) modification. *J. Controlled Release* (1997).

56. Veronese, F. M., Caliceti, P., Schiavon, O. & Sergi, M. Polyethylene glycol-superoxide dismutase, a conjugate in search of exploitation. *Adv. Drug Deliv. Rev.* **54,** 587–606 (2002).

57. ODA, T. *et al.* Oxygen Radicals in Influenza-Induced Pathogenesis and Treatment with Pyran Polymer-Conjugated Sod. *Science* **244,** 974–976 (1989).

58. Perez, Y., Valdivia, A., Gomez, L., Simpson, B. K. & Villalonga, R. Glycosidation of Cu,Zn-Superoxide Dismutase with End-Group Aminated Dextran. Pharmacological and Pharmacokinetics Properties. *Macromol. Biosci.* **5,** 1220–1225 (2005).

59. Xiong, Y., Qi, J. & Yao, P. Amphiphilic Cholic-Acid-Modified Dextran Sulfate and its Application for the Controlled Delivery of Superoxide Dismutase. *Macromol. Biosci.* **12,** 515–524 (2012).

60. Caliceti, P., Schiavon, O. & Morpurgo, M. Physico-Chemical and Biological Properties of Monofunctional Hydroxy Teriminating Poly (N-Vinylpyrrolidone) Conjugated Superoxide Dismutase. *J. Bioact. ...* (1995).

61. Onaca, O. *et al.* SOD Antioxidant Nanoreactors: Influence of Block Copolymer Composition on the Nanoreactor Efficiency. *Macromol. Biosci.* **10,** 531–538 (2010).

62. Simone, E. A. *et al.* Loading PEG-catalase into filamentous and spherical polymer nanocarriers. *Pharm. Res.* **26,** 250–260 (2009).

63. Hu, P. & Tirelli, N. Scavenging ROS: Superoxide Dismutase/Catalase Mimetics by the Use of an Oxidation-Sensitive Nanocarrier/Enzyme Conjugate. *Bioconjug. Chem.* **23,** 438–449 (2012).

64. Suntres, Z. E. Liposomal Antioxidants for Protection against Oxidant-Induced Damage. *J. Toxicol.* **2011,** 1–16 (2011).

65. Stone, W. L. & Smith, M. Therapeutic uses of antioxidant liposomes. *Mol. Biotechnol.* **27,** 217–230 (2004).

66. Shuvaev, V. V., Tliba, S., Nakada, M., Albelda, S. M. & Muzykantov, V. R. Platelet-endothelial cell adhesion molecule-1-directed endothelial targeting of superoxide dismutase alleviates oxidative stress caused by either extracellular or intracellular superoxide. *J. Pharmacol. Exp. Ther.* **323,** 450–457 (2007).

67. Shuvaev, V. V. *et al.* Targeted Detoxification of Selected Reactive Oxygen Species in the Vascular Endothelium. *J. Pharmacol. Exp. Ther.* **331,** 404–411 (2009).

68. Muro, S. & Muzykantov, V. R. Targeting of antioxidant and anti-thrombotic drugs to endothelial cell adhesion molecules. *Curr. Pharm. Des.* **11,** 2383–2401 (2005).

69. Papahadjopoulos, D. *et al.* Sterically Stabilized Liposomes - Improvements in Pharmacokinetics and Antitumor Therapeutic Efficacy. *Proc. Natl. Acad. Sci. U. S. A.* **88,** 11460–11464 (1991).

70. BARNARD, M. L., BAKER, R. R. & MATALON, S. Mitigation of Oxidant Injury to Lung Microvasculature by Intratracheal Instillation of Antioxidant Enzymes. *Am. J. Physiol.* **265,** L340–L345 (1993).

71. PADMANABHAN, R. V., GUDAPATY, R., LIENER, I. E., SCHWARTZ, B. A. & HOIDAL, J. R. Protection Against Pulmonary Oxygen-Toxicity in Rats by the Intratracheal Administration of Liposome-Encapsulated Superoxide-Dismutase or Catalase. *Am. Rev. Respir. Dis.* **132,** 164–167 (1985).

72. WALTHER, F. J., DAVIDCU, R. & LOPEZ, S. L. Antioxidant Surfactant Liposomes Mitigate Hyperoxic Lung Injury in Premature Rabbits. *Am. J. Physiol.* **269,** L613–L617 (1995).

73. Jubeh, T. T., Antler, S., Haupt, S., barenholz, Y. & Rubinstein, A. Local prevention of oxidative stress in the intestinal epithelium of the rat by adhesive liposomes of superoxide dismutase and tempamine. *Mol. Pharm.* **2,** 2–11 (2005).

74. Vorauer-Uhl, K., Furnschlief, E., Wagner, A., Ferko, B. & Katinger, H. Topically applied liposome encapsulated superoxide dismutase reduces postburn wound size and edema formation. *Eur. J. Pharm. Sci.* **14,** 63–67 (2001).

75. Petrikovics, I. *et al.* Characterization of liposomal vesicles encapsulating rhodanese for cyanide antagonism. *Drug Deliv.* **16,** 312–319 (2009).

76. Petrikovics, I. *et al.* Optimization of liposomal lipid composition for a new, reactive sulfur donor, and in vivo efficacy studies on mice to antagonize cyanide intoxication. *J. Drug Deliv.* **2011,** 928626 (2011).

77. Leung, P., Cannon, E. P., Petrikovics, I., Hawkins, A. & Way, J. L. In vivo studies on rhodanese encapsulation in mouse carrier erythrocytes. *Toxicol. Appl. Pharmacol.* **110,** 268–274 (1991).

78. Petrikovics, I. *et al.* Nano-intercalated rhodanese in cyanide antagonism. *Nanotoxicology* **4,** 247–254 (2010).

79. Novikov, B. N., Grimsley, J. K., Kern, R. J., Wild, J. R. & Wales, M. E. Improved pharmacokinetics and immunogenicity profile of organophosphorus hydrolase by chemical modification with polyethylene glycol. *J. Control. Release Off. J. Control. Release Soc.* **146,** 318–325 (2010).

80. Petrikovics, I. *et al.* Long circulating liposomes encapsulating organophosphorus acid anhydrolase in diisopropylfluorophosphate antagonism. *Toxicol. Sci. Off. J. Soc. Toxicol.* **57,** 16–21 (2000).

81. Petrikovics, I. *et al.* Antagonism of paraoxon intoxication by recombinant phosphotriesterase encapsulated within sterically stabilized liposomes. *Toxicol. Appl. Pharmacol.* **156,** 56–63 (1999).

82. Petrikovics, I. *et al.* In vitro studies on sterically stabilized liposomes (SL) as enzyme carriers in organophosphorus (OP) antagonism. *Drug Deliv.* **7,** 83–89 (2000).

83. Budai, M. *et al.* Physicochemical characterization of stealth liposomes encapsulating an organophosphate hydrolyzing enzyme. *J. Liposome Res.* **19,** 163–168 (2009).

84. Han, Z.-K., Liu, Z.-N., Yuan, L., Zhang, P.-S. & Zhao, M. Preparation of paraoxonase-1 liposomes and studies on their in vivo pharmacokinetics in rats. *Clin. Exp. Pharmacol. Physiol.* (2014). doi:10.1111/1440-1681.12275

85. Pei, L. *et al.* Encapsulation of Phosphotriesterase Within Murine Erythrocytes. *Toxicol. Appl. Pharmacol.* **124,** 296–301 (1994).

86. McGuinn, W. D. *et al.* The Encapsulation of Squid Diisopropylphosphorofluoridate-Hydrolyzing Enzyme Within Mouse Erythrocytes. *Fundam. Appl. Toxicol.* **21,** 38–43 (1993).

87. Petrikovics, I. *et al.* Enzyme-based intravascular defense against organophosphorus neurotoxins: Synergism of dendritic-enzyme complexes with 2-PAM and atropine. *Nanotoxicology* **1,** 85–92 (2007).

88. Suthiwangcharoen, N. & Nagarajan, R. Enhancing Enzyme Stability by Construction of Polymer Enzyme Conjugate Micelles for Decontamination of Organophosphate Agents. *Biomacromolecules* **15,** 1142–1152 (2014).

89. Wei, W. *et al.* Construction of Robust Enzyme Nanocapsules for Effective Organophosphate Decontamination, Detoxification, and Protection. *Adv. Mater.* **25,** 2212–2218 (2013).

90. Yoshimoto, M., Sato, M., Yoshimoto, N. & Nakao, K. Liposomal encapsulation of yeast alcohol dehydrogenase with cofactor for stabilization of the enzyme structure and activity. *Biotechnol. Prog.* **24,** 576–582 (2008).

91. Lizano, C., Sanz, S., Luque, J. & Pinilla, M. In vitro study of alcohol dehydrogenase and acetaldehyde dehydrogenase encapsulated into human erythrocytes by an electroporation procedure. *BBA - Gen. Subj.* **1425,** 328–336 (1998).

92. Lizano, C., Perez, M. T. & Pinilla, M. Mouse erythrocytes as carriers for coencapsulated alcohol and aldehyde dehydrogenase obtained by electroporation - In vivo survival rate in circulation, organ distribution and ethanol degradation. *Life Sci.* **68,** 2001–2016 (2001).

93. Magnani, M. *et al.* Invivo Accelerated Acetaldehyde Metabolism Using Acetaldehyde Dehydrogenase-Loaded Erythrocytes. *Alcohol Alcohol* **25,** 627–637 (1990).

94. Magnani, M., Fazi, A., MANGANI, F., Rossi, L. & Mancini, U. Methanol Detoxification by Enzyme-Loaded Erythrocytes. *Biotechnol. Appl. Biochem.* **18,** 217–226 (1993).

95. Dinndorf, P. A., Gootenberg, J., Cohen, M. H., Keegan, P. & Pazdur, R. FDA drug approval summary: Pegaspargase (Oncaspar (R)) for the first-line treatment of children with acute lymphoblastic leukemia (ALL). *Oncologist* **12,** 991–998 (2007).

96. Ashihara, Y., Kono, T., Yamazaki, S. & INADA, Y. Modification of E. coli L-asparaginase with polyethylene glycol: disappearance of binding ability to anti-asparaginase serum. *Biochem. Biophys. ...* (1978).

97. Park, Y. K., Abuchowski, A., Davis, S. & DAVIS, F. Pharmacology of Escherichia-Coli-L-Asparaginase Polyethylene-Glycol Adduct. *Anticancer Res.* **1,** 373–376 (1981).

98.   HO, D. *et al.* Clinical-Pharmacology of Polyethylene-Glycol L-Asparaginase (Peg-L-Ase). *Proc. Am. Assoc. Cancer Res.* **26,** 152–152 (1985).

99.   Taylor, C. W., Dorr, R. T., Fanta, P., Hersh, E. M. & Salmon, S. E. A phase I and pharmacodynamic evaluation of polyethylene glycol-conjugated L-asparaginase in patients with advanced solid tumors. *Cancer Chemother. Pharmacol.* **47,** 83–88 (2001).

100. Pinheiro, J. *et al.* Drug monitoring of low-dose PEG-asparaginase (Oncaspar (TM)) in children with relapsed acute lymphoblastic leukaemia. *Br. J. Haematol.* **113,** 115–119 (2001).

101. Graham, M. L. Pegaspargase: a review of clinical studies. *Adv. Drug Deliv. Rev.* **55,** 1293–1302 (2003).

102. CRUZ, M., Gaspar, M. M., LOPES, F., JORGE, J. S. & PEREZSOLER, R. Liposomal L-Asparaginase - in-Vitro Evaluation. *Int. J. Pharm.* **96,** 67–77 (1993).

103. Gaspar, M. M., Perez-Soler, R. & Cruz, M. E. Biological characterization of L-asparaginase liposomal formulations. *Cancer Chemother. Pharmacol.* **38,** 373–377 (1996).

104. Jorge, J. C., Perez-Soler, R., Morais, J. G. & Cruz, M. E. Liposomal palmitoyl-L-asparaginase: characterization and biological activity. *Cancer Chemother. Pharmacol.* **34,** 230–234 (1994).

105. ALPAR, H. O. & LEWIS, D. A. Therapeutic Efficacy of Asparaginase Encapsulated in Intact Erythrocytes. *Biochem. Pharmacol.* **34,** 257–261 (1985).

106. Kravtzoff, R. *et al.* Tolerance evaluation of L-asparaginase loaded in red blood cells. *Eur. J. Clin. Pharmacol.* **51,** 221–225 (1996).

107. Kravtzoff, R. *et al.* Improved pharmacodynamics of L-asparaginase loaded in human red blood cells. *Eur. J. Clin. Pharmacol.* **49,** 465–470 (1996).

108. Kwon, Y. M. *et al.* L-Asparaginase encapsulated intact erythrocytes for treatment of acute lymphoblastic leukemia (ALL). *J. Control. Release Off. J. Control. Release Soc.* **139,** 182–189 (2009).

109. Wolf, M., Wirth, M., Pittner, F. & Gabor, F. Stabilisation and determination of the biological activity of L-asparaginase in poly(D,L-lactide-co-glycolide) nanospheres. *Int. J. Pharm.* **256,** 141–152 (2003).

110. Morrow, K. *et al.* Anti-leukemic mechanisms of pegylated arginase I in acute lymphoblastic T-cell leukemia. *Leukemia* **27,** 569–577 (2013).

111. SHERWOOD, R. F. *et al.* Enhanced Plasma Persistence of Therapeutic Enzymes by Coupling to Soluble Dextran. *Biochem. J.* **164,** 461–464 (1977).

112. SAKURAGAWA, N., SHIMIZU, K., KONDO, K., KONDO, S. & NIWA, M. Studies on the Effect of Peg-Modified Urokinase on Coagulation-Fibrinolysis Using Beagles. *Thromb. Res.* **41,** 627–635 (1986).

113. KAJIHARA, J., SHIBATA, K., NAKANO, Y., NISHIMURO, S. & KATO, K. Physicochemical Characterization of Peg-Ppg Conjugated Human Urokinase. *BBA - Gen. Subj.* **1199,** 202–208 (1994).

114. Tan, H. *et al.* PEG-urokinase nanogels with enhanced stability and controllable bioactivity. *Soft Matter* **8,** 2644–2650 (2012).

115. PIZZO, S. V. Preparation, Invivo Properties and Proposed Clinical Use of Polyoxyethylene-Modified Tissue Plasminogen-Activator and Streptokinase. *Adv. Drug Deliv. Rev.* **6,** 153–166 (1991).

116. Koide, A., Suzuki, S. & Kobayashi, S. Preparation of polyethylene glycol-modified streptokinase with disappearance of binding ability towards anti-serum and retention of activity. *Febs Lett.* **143,** 73–76 (1982).

117. BRUCATO, F. H. & PIZZO, S. V. Catabolism of Streptokinase and Polyethylene Glycol-Streptokinase - Evidence for Transport of Intact Forms Through the Biliary System in the Mouse. *Blood* **76,** 73–79 (1990).

118. Rajagopalan, S., Gonias, S. L. & PIZZO, S. V. A nonantigenic covalent streptokinase-polyethylene glycol complex with plasminogen activator function. *J. Clin. Invest.* **75,** 413–419 (1985).

119. Kim, I. S., Choi, H. G., Choi, H. S., Kim, B. K. & Kim, C. K. Prolonged systemic delivery of streptokinase using liposome. *Arch. Pharm. Res.* **21,** 248–252 (1998).

120. Schuber, F., Kichler, A., Boeckler, C. & Frisch, B. Liposomes: from membrane models to gene therapy. *Pure Appl. Chem.* **70,** 89–96 (1998).

121. SCHERPHOF, G. L., DIJKSTRA, J., SPANJER, H. H., Derksen, J. T. & ROERDINK, F. H. Uptake and intracellular processing of targeted and nontargeted liposomes by rat Kupffer cells in vivo and in vitro. *Ann. N. Y. Acad. Sci.* **446,** 368–384 (1985).

122. Immordino, M. L., Dosio, F. & Cattel, L. Stealth liposomes: review of the basic science, rationale, and clinical applications, existing and potential. *Int. J. Nanomedicine* **1,** 297–315 (2006).

123. Klibanov, A. L., Maruyama, K., Torchilin, V. P. & Huang, L. Amphipathic polyethyleneglycols effectively prolong the circulation time of liposomes. *Febs Lett.* **268,** 235–237 (1990).

124. Whiteman, K. R., Subr, V., Ulbrich, K. & Torchilin, V. P. Poly(Hpma)-coated liposomes demonstrate prolonged circulation in mice. *J. Liposome Res.* **11,** 153–164 (2001).

125. Torchilin, V. P. *et al.* Amphiphilic poly-N-vinylpyrrolidones: synthesis, properties and liposome surface modification. *Biomaterials* **22,** 3035–3044 (2001).

126. Metselaar, J. M. *et al.* A novel family of L-amino acid-based biodegradable polymer-lipid conjugates for the development of long-circulating liposomes with effective drug-targeting capacity. *Bioconjug. Chem.* **14,** 1156–1164 (2003).

127. Takeuchi, H., Kojima, H., Yamamoto, H. & Kawashima, Y. Evaluation of circulation profiles of liposomes coated with hydrophilic polymers having different molecular weights in rats. *J. Control. Release Off. J. Control. Release Soc.* **75,** 83–91 (2001).

128. Szilasi, M., Budai, M. & Budai, L. Nanoencapsulated and microencapsulated enzymes in drug antidotal therapy. *Toxicol. Ind. ...* (2012).

129. Gauthier, M. A. & Klok, H.-A. Polymer-protein conjugates: an enzymatic activity perspective. *Polym. Chem.* **1,** 1352–1373 (2010).

130. Jevsevar, S., Kunstelj, M. & Porekar, V. G. PEGylation of therapeutic proteins. *Biotechnol. J.* **5,** 113–128 (2010).

131. Humphreys, D. P. *et al.* Alternative antibody Fab' fragment PEGylation strategies: combination of strong reducing agents, disruption of the interchain disulphide bond and disulphide engineering. *Protein Eng. Des. Sel.* **20,** 227–234 (2007).

132. Kinstler, O., Molineux, G., Treuheit, M., Ladd, D. & Gegg, C. Mono-N-terminal poly(ethylene glycol)-protein conjugates. *Adv. Drug Deliv. Rev.* **54,** 477–485 (2002).

133. Veronese, F. M. *et al.* Site-specific pegylation of G-CSF by reversible denaturation. *Bioconjug. Chem.* **18,** 1824–1830 (2007).

134. Fontana, A., Spolaore, B., Mero, A. & Veronese, F. M. Site-specific modification and PEGylation of pharmaceutical proteins mediated by transglutaminase. *Adv. Drug Deliv. Rev.* **60,** 13–28 (2008).

135. Sato, H. Enzymatic procedure for site-specific pegylation of proteins. *Adv. Drug Deliv. Rev.* **54,** 487–504 (2002).

136. DeFrees, S. *et al.* GlycoPEGylation of recombinant therapeutic proteins produced in Escherichia coli. *Glycobiology* **16,** 833–843 (2006).

137. Veronese, F. M., Caliceti, P. & Schiavon, O. Branched and linear poly(ethylene glycol): Influence of the polymer structure on enzymological, pharmacokinetic, and immunological properties of protein conjugates. *J. Bioact. Compat. Polym.* **12,** 196–207 (1997).

138. Fishburn, C. S. The pharmacology of PEGylation: Balancing PD with PK to generate novel therapeutics. *J. Pharm. Sci.* **97,** 4167–4183 (2008).

139. Hamidi, M., Rafiei, P. & Azadi, A. Designing PEGylated therapeutic molecules: advantages in ADMET properties. *Expert Opin. Drug Discov.* **3,** 1293–1307 (2008).

140. Aiuti, A. Advances in gene therapy for ADA-deficient SCID. *Curr. Opin. Mol. Ther.* **4,** 515–522 (2002).

141. Schlesinger, N., Yasothan, U. & Kirkpatrick, P. Pegloticase. *Nat. Rev. Drug Discov.* **10,** 17–18 (2011).

142. Ensor, C. M., Holtsberg, F. W., Bomalaski, J. S. & Clark, M. A. Pegylated arginine deiminase (ADI-SS PEG(20,000) (mw)) inhibits human melanomas and hepatocellular carcinomas in vitro and in vivo. *Cancer Res.* **62,** 5443–5450 (2002).

143. Nevozhay, D. *et al.* Antitumor properties and toxicity of dextran-methotrexate conjugates are dependent on the molecular weight of the carrier. *Anticancer Res.* **26,** 1135–1143 (2006).

144. Mehvar, R. Dextrans for targeted and sustained delivery of therapeutic and imaging agents. *J. Control. Release Off. J. Control. Release Soc.* **69,** 1–25 (2000).

145. WILEMAN, T. E., FOSTER, R. L. & ELLIOTT, P. Soluble Asparaginase-Dextran Conjugates Show Increased Circulatory Persistence and Lowered Antigen Reactivity. *J. Pharm. Pharmacol.* **38,** 264–271 (1986).

146. Melton, R. G., Wiblin, C. N. & FOSTER, R. L. Covalent linkage of carboxypeptidase G< sub> 2 to soluble dextrans—I: Properties of conjugates and effects on plasma persistence in mice. *Biochem. ...* (1987).

147. Zinderman, C. E., Landow, L. & Wise, R. P. Anaphylactoid reactions to Dextran 40 and 70: Reports to the United States Food and Drug Administration, 1969 to 2004. *J. Vasc. Surg.* **43,** 1004–1009 (2006).

148. Ahmad, Z., Shah, A., Siddiq, M. & Kraatz, H.-B. Polymeric micelles as drug delivery vehicles. *RSC Adv.* **4,** 17028–17038 (2014).

149. Savic, R., Luo, L. B., Eisenberg, A. & Maysinger, D. Micellar nanocontainers distribute to defined cytoplasmic organelles. *Science* **300,** 615–618 (2003).

150. Yi, X. *et al.* Pluronic-modified superoxide dismutase 1 attenuates angiotensin II-induced increase in intracellular superoxide in neurons. *Free Radic. Biol. Med.* **49,** 548–558 (2010).

151. HAAF, F., SANNER, A. & STRAUB, F. Polymers of N-Vinylpyrrolidone - Synthesis, Characterization and Uses. *Polym. J.* **17,** 143–152 (1985).

152. RAVIN, H. A., SELIGMAN, A. M. & FINE, J. Polyvinyl Pyrrolidone as a Plasma Expander - Studies on Its Excretion, Distribution and Metabolism. *N. Engl. J. Med.* **247,** 921–929 (1952).

153. VONSPECHT, B. U. & BRENDEL, W. Preparation and Properties of Trypsin and Chymotrypsin Coupled Covalently to Poly(N-Vinylpyrrolidone). *Biochim. Biophys. Acta* **484,** 109–114 (1977).

154. Pisal, D. S., Kosloski, M. P. & Balu-Iyer, S. V. Delivery of therapeutic proteins. *J. Pharm. Sci.* **99,** 2557–2575 (2010).

155. Monfardini, C. & Veronese, F. M. Stabilization of substances in circulation. *Bioconjug. Chem.* **9,** 418–450 (1998).

156. Veronese, F. M., VISCO, C., MASSAROTTO, S., BENASSI, C. A. & Ferruti, P. New Acrylic Polymers for Surface Modification of Enzymes of Therapeutic Interest and for Enzyme Immobilization. *Ann. N. Y. Acad. Sci.* **501,** 444–448 (1987).

157. Veronese, F. M., LARGAJOLLI, R., VISCO, C., Ferruti, P. & MIUCCI, A. Surface Modification of Proteins by Covalent Binding of Acrylic Polymers. *Appl. Biochem. Biotechnol.* **11,** 269–277 (1985).

158. RANUCCI, E. *et al.* Synthesis and Molecular-Weight Characterization of Low-Molecular-Weight End-Functionalized Poly(4-Acryloylmorpholine). *Macromol. Chem. Phys.* **195,** 3469–3479 (1994).

159. Zelphati, O. *et al.* Intracellular delivery of proteins with a new lipid-mediated delivery system. *J. Biol. Chem.* **276,** 35103–35110 (2001).

160. Dalkara, D., Zuber, G. & Behr, J. P. Intracytoplasmic delivery of anionic proteins. *Mol. Ther.* **9,** 964–969 (2004).

161. van der Gun, B. T. F. *et al.* Serum insensitive, intranuclear protein delivery by the multipurpose cationic lipid SAINT-2. *J. Controlled Release* **123,** 228–238 (2007).

162. Iwaoka, S., Nakamura, T., Takano, S., Tsuchiya, S. & Aramaki, Y. Cationic liposomes induce apoptosis through p38 MAP kinase-caspase-8-Bid pathway in macrophage-like RAW264.7 cells. *J. Leukoc. Biol.* **79,** 184–191 (2006).

163. Sapra, P. & Allen, T. M. Internalizing antibodies are necessary for improved therapeutic efficacy of antibody-targeted liposomal drugs. *Cancer Res.* **62,** 7190–7194 (2002).

164. Park, J. W. *et al.* Tumor targeting using anti-her2 immunoliposomes. *J. Controlled Release* **74,** 95–113 (2001).

165. Pirollo, K. F. *et al.* Tumor-targeting nanocomplex delivery of novel tumor suppressor RB94 chemosensitizes bladder carcinoma cells in vitro and in vivo. *Clin. Cancer Res.* **14,** 2190–2198 (2008).

166. Lee, R. & Low, P. Delivery of Liposomes into Cultured Kb Cells Via Folate Receptor-Mediated Endocytosis. *J. Biol. Chem.* **269,** 3198–3204 (1994).

167. Visser, C. C. *et al.* Targeting liposomes with protein drugs to the blood-brain barrier in vitro. *Eur. J. Pharm. Sci.* **25,** 299–305 (2005).

168. Torchilin, V. P., Rammohan, R., Weissig, V. & Levchenko, T. S. TAT peptide on the surface of liposomes affords their efficient intracellular delivery even at low temperature and in the presence of metabolic inhibitors. *Proc. Natl. Acad. Sci. U. S. A.* **98,** 8786–8791 (2001).

169. Furuhata, M., Kawakami, H., Toma, K., Hattori, Y. & Maitani, Y. Intracellular delivery of proteins in complexes with oligoarginine-modified liposomes and the effect of oligoarginine length. *Bioconjug. Chem.* **17,** 935–942 (2006).

170. Sawant, R. M. *et al.* 'SMART' drug delivery systems: Double-targeted pH-responsive pharmaceutical nanocarriers. *Bioconjug. Chem.* **17,** 943–949 (2006).

171. Hasadsri, L., Kreuter, J., Hattori, H., Iwasaki, T. & George, J. M. Functional Protein Delivery into Neurons Using Polymeric Nanoparticles. *J. Biol. Chem.* **284,** 6972–6981 (2009).

172. Bayele, H. K. *et al.* Protein transduction by lipidic peptide dendrimers. *J. Pharm. Sci.* **95,** 1227–1237 (2006).

173. Santra, S., Kaittanis, C. & Perez, J. M. Cytochrome c Encapsulating Theranostic Nanoparticles: A Novel Bifunctional System for Targeted Delivery of Therapeutic Membrane-Impermeable Proteins to Tumors and Imaging of Cancer Therapy. *Mol. Pharm.* **7,** 1209–1222 (2010).

174. Kim, S. H., Jeong, J. H., Joe, C. O. & Park, T. G. Folate receptor mediated intracellular protein delivery using PLL-PEG-FOL conjugate. *J. Controlled Release* **103,** 625–634 (2005).

175. Lee, Y. *et al.* A protein nanocarrier from charge-conversion polymer in response to endosomal pH. *J. Am. Chem. Soc.* **129,** 5362–5363 (2007).

176. Lee, Y. *et al.* Charge-Conversional Polyionic Complex Micelles-Efficient Nanocarriers for Protein Delivery into Cytoplasm. *Angew. Chem. Int. Ed.* **48,** 5309–5312 (2009).

177. Dalkara, D., Chandrashekhar, C. & Zuber, G. Intracellular protein delivery with a dimerizable amphiphile for improved complex stability and prolonged protein release in the cytoplasm of adherent cell lines. *J. Controlled Release* **116,** 353–359 (2006).

178. Heffernan, M. J. & Murthy, N. Disulfide-Crosslinked Polyion Micelles for Delivery of Protein Therapeutics. *Ann. Biomed. Eng.* **37,** 1993–2002 (2009).

179. Futami, J. *et al.* Intracellular delivery of proteins into mammalian living cells by polyethylenimine-cationization. *J. Biosci. Bioeng.* **99,** 95–103 (2005).

180. Kitazoe, M., Futami, J., Nishikawa, M., Yamada, H. & Maeda, Y. Polyethylenimine-cationized beta-catenin protein transduction activates the Wnt canonical signaling pathway more effectively than cationic lipid-based transduction. *Biotechnol. J.* **5,** 385–392 (2010).

181. Murata, H. *et al.* Denatured and reversibly cationized p53 readily enters cells and simultaneously folds to the functional protein in the cells. *Biochemistry (Mosc.)* **45,** 6124–6132 (2006).

182. Schmid, G. Large Clusters and Colloids - Metals in the Embryonic State. *Chem. Rev.* **92,** 1709–1727 (1992).

183. Brust, M., Walker, M., Bethell, D., Schiffrin, D. & Whyman, R. Synthesis of Thiol-Derivatized Gold Nanoparticles in a 2-Phase Liquid-Liquid System. *J. Chem. Soc.-Chem. Commun.* 801–802 (1994). doi:10.1039/c39940000801

184. Templeton, A. C., Wuelfing, M. P. & Murray, R. W. Monolayer protected cluster molecules. *Acc. Chem. Res.* **33,** 27–36 (2000).

185. Giljohann, D. A. *et al.* Gold Nanoparticles for Biology and Medicine. *Angew. Chem. Int. Ed Engl.* **49,** 3280–3294 (2010).

186. Ghosh, P. *et al.* Intracellular delivery of a membrane-impermeable enzyme in active form using functionalized gold nanoparticles. *J. Am. Chem. Soc.* **132,** 2642–2645 (2010).

187. Vivero-Escoto, J. L., Slowing, I. I., Wu, C.-W. & Lin, V. S.-Y. Photoinduced Intracellular Controlled Release Drug Delivery in Human Cells by Gold-Capped Mesoporous Silica Nanosphere. *J. Am. Chem. Soc.* **131,** 3462–+ (2009).

188. Slowing, I. I., Trewyn, B. G. & Lin, V. S.-Y. Mesoporous silica nanoparticles for intracellular delivery of membrane-impermeable proteins. *J. Am. Chem. Soc.* **129,** 8845–8849 (2007).

189. Lai, C. Y. *et al.* A mesoporous silica nanosphere-based carrier system with chemically removable CdS nanoparticle caps for stimuli-responsive controlled release of neurotransmitters and drug molecules. *J. Am. Chem. Soc.* **125,** 4451–4459 (2003).

190. Park, C., Lee, K. & Kim, C. Photoresponsive Cyclodextrin-Covered Nanocontainers and Their Sol-Gel Transition Induced by Molecular Recognition. *Angew. Chem.-Int. Ed.* **48,** 1275–1278 (2009).

191. Angelos, S., Yang, Y.-W., Patel, K., Stoddart, J. F. & Zink, J. I. pH-responsive supramolecular nanovalves based on cucurbit[6]uril pseudorotaxanes. *Angew. Chem.-Int. Ed.* **47,** 2222–2226 (2008).

192. Liu, R., Zhao, X., Wu, T. & Feng, P. Tunable Redox-Responsive Hybrid Nanogated Ensembles. *J. Am. Chem. Soc.* **130,** 14418–+ (2008).

193. Patel, K. *et al.* Enzyme-responsive snap-top covered silica nanocontainers. *J. Am. Chem. Soc.* **130,** 2382–2383 (2008).

194. Yang, Q. *et al.* pH-responsive carrier system based on carboxylic acid modified mesoporous silica and polyelectrolyte for drug delivery. *Chem. Mater.* **17,** 5999–6003 (2005).

195. Kam, N. W. S. & Dai, H. Carbon nanotubes as intracellular protein transporters: generality and biological functionality. *J. Am. Chem. Soc.* **127,** 6021–6026 (2005).

196. Kam, N. W. S., Jessop, T. C., Wender, P. A. & Dai, H. J. Nanotube molecular transporters: Internalization of carbon nanotube-protein conjugates into mammalian cells. *J. Am. Chem. Soc.* **126,** 6850–6851 (2004).

197. Lu, Q. *et al.* RNA polymer translocation with single-walled carbon nanotubes. *Nano Lett.* **4,** 2473–2477 (2004).

198. Bianco, A. *et al.* Cationic carbon nanotubes bind to CpG oligodeoxynucleotides and enhance their immunostimulatory properties. *J. Am. Chem. Soc.* **127,** 58–59 (2005).

199. Pantarotto, D. *et al.* Functionalized carbon nanotubes for plasmid DNA gene delivery. *Angew. Chem.-Int. Ed.* **43,** 5242–5246 (2004).

200. Pantarotto, D., Briand, J. P., Prato, M. & Bianco, A. Translocation of bioactive peptides across cell membranes by carbon nanotubes. *Chem. Commun.* 16–17 (2004). doi:10.1039/b311254c

201. Kam, N. W. S., O'Connell, M., Wisdom, J. A. & Dai, H. J. Carbon nanotubes as multifunctional biological transporters and near-infrared agents for selective cancer cell destruction. *Proc. Natl. Acad. Sci. U. S. A.* **102,** 11600–11605 (2005).

202. Kam, N. W. S., Liu, Z. A. & Dai, H. J. Carbon nanotubes as intracellular transporters for proteins and DNA: An investigation of the uptake mechanism and pathway. *Angew. Chem.-Int. Ed.* **45,** 577–581 (2006).

203. Yan, M., Ge, J., Liu, Z. & Ouyang, P. Encapsulation of Single Enzyme in Nanogel with Enhanced Biocatalytic Activity and Stability. *J. Am. Chem. Soc.* **128,** 11008–11009 (2006).

204. Yan, M. *et al.* A novel intracellular protein delivery platform based on single-protein nanocapsules. *Nat. Nanotechnol.* **5,** 48–53 (2009).

205. Moghimi, S. M., Hunter, A. C. & Murray, J. C. Long-Circulating and Target-Specific Nanoparticles: Theory to Practice. *Pharmacol. Rev.* **53,** 283–318 (2001).

206. Owens, D. E. & Peppas, N. A. Opsonization, biodistribution, and pharmacokinetics of polymeric nanoparticles. *Int. J. Pharm.* **307,** 93–102 (2006).

207. Choi, H. S. *et al.* Renal clearance of quantum dots. *Nat. Biotechnol.* **25,** 1165–1170 (2007).

208. Gu, Z. *et al.* Protein Nanocapsule Weaved with Enzymatically Degradable Polymeric Network. *Nano Lett* **9,** 4533–4538 (2009).

209. Wen, J. *et al.* Controlled Protein Delivery Based on Enzyme-Responsive Nanocapsules. *Adv. Mater.* **23,** 4549–4553 (2011).

210. Liang, S. *et al.* Phosphorylcholine polymer nanocapsules prolong the circulation time and reduce the immunogenicity of therapeutic proteins. *Nano Res.* 1–10 (2016). doi:10.1007/s12274-016-0991-3

211. Choi, H. K., Mount, D. B. & Reginato, A. M. Pathogenesis of gout. *Ann. Intern. Med.* **143,** 499–516 (2005).

212. Pittman, J. R. & Bross, M. H. Diagnosis and management of gout. *Am. Fam. Physician* **59,** 1799–+ (1999).

213. Pacher, P., Nivorozhkin, A. & Szabo, C. Therapeutic effects of xanthine oxidase inhibitors: Renaissance half a century after the discovery of allopurinol. *Pharmacol. Rev.* **58,** 87–114 (2006).

214. Borges, F., Fernandes, E. & Roleira, F. Progress towards the discovery of xanthine oxidase inhibitors. *Curr. Med. Chem.* **9,** 195–217 (2002).

215. Lin, W. *et al.* A novel zwitterionic copolymer with a short poly(methyl acrylic acid) block for improving both conjugation and separation efficiency of a protein without losing its bioactivity. *J. Mater. Chem. B* **1,** 2482–2488 (2013).

216. Ihler, G. M., Glew, R. H. & Schnure, F. W. Enzyme loading of erythrocytes. in (1973).

217. Tan, Q. Y. *et al.* Preparation and characterization of lipid vesicles containing uricase. *Drug Deliv.* **17,** 28–37 (2010).

218. Giblett, E. R., Anderson, J. E., Cohen, F., Pollara, B. & Meuwissen, H. J. Adenosine-deaminase deficiency in two patients with severely impaired cellular immunity. *Lancet* **2,** 1067–1069 (1972).

219. Hirschhorn, R., Vawter, G. F., Kirkpatrick, J. A. & Rosen, F. S. Adenosine deaminase deficiency: frequency and comparative pathology in autosomally recessive severe combined immunodeficiency. *Clin. Immunol. Immunopathol.* **14,** 107–120 (1979).

220. Polmar, S. H., Wetzler, E. M., Stern, R. C. & Hirschhorn, R. Restoration of in-vitro lymphocyte responses with exogenous adenosine deaminase in a patient with severe combined immunodeficiency. *Lancet* **2,** 743–746 (1975).

221. Polmar, S. H. *et al.* Enzyme replacement therapy for adenosine deaminase deficiency and severe combined immunodeficiency. *N. Engl. J. Med.* **295,** 1337–1343 (1976).

222. Scriver, C. R. *The metabolic and molecular bases of inherited disease.* (McGraw-Hill Companies, 1995).

223. Stiehm, E. R., Ochs, H. D. & Winkelstein, J. A. *Immunologic Disorders in Infants and Children.* (Gulf Professional Publishing, 2004).

224. Erlandsen, H., Patch, M. G., Gamez, A., Straub, M. & Stevens, R. C. Structural studies on phenylalanine hydroxylase and implications toward understanding and treating phenylketonuria. *Pediatrics* **112,** 1557–1565 (2003).

225. Kruszyna, R., Kruszyna, H. & Smith, R. Comparison of Hydroxylamine, 4-Dimethylaminophenol and Nitrite Protection Against Cyanide Poisoning in Mice. *Arch. Toxicol.* **49,** 191–202 (1982).

226. ATKINSON, A., RUTTER, D. A. & SARGEANT, K. Enzyme Antidote for Experimental Cyanide Poisoning. *Lancet* **2,** 1446–1446 (1974).

227. Lee, Y. W., Stanish, I., Rastogi, V., Cheng, T. C. & Singh, A. Sustained enzyme activity of organophosphorus hydrolase in polymer encased multilayer assemblies. *Langmuir* **19,** 1330–1336 (2003).

228. KIDD, J. G. Regression of transplanted lymphomas induced in vivo by means of normal guinea pig serum. II. Studies on the nature of the active serum constituent: histological mechanism of the regression: tests for effects of guinea pig serum on lymphoma cells in vitro: discussion. *J. Exp. Med.* **98,** 583–606 (1953).

229. Kravtzoff, R., ROPARS, C., LAGUERRE, M., Muh, J. P. & Chassaigne, M. Erythrocytes as carriers for L-asparaginase. Methodological and mouse in-vivo studies. *J. Pharm. Pharmacol.* **42,** 473–476 (1990).

230. Balcao, V. M., Mateo, C., Fernandez-Lafuente, R., Malcata, F. X. & Guisan, J. M. Structural and functional stabilization of L-asparaginase via multisubunit immobilization onto highly activated supports. *Biotechnol. Prog.* **17,** 537–542 (2001).

231. Ho, D. *et al.* Clinical-Pharmacology of Polyethylene Glycol-L-Asparaginase. *Drug Metab. Dispos.* **14,** 349–352 (1986).

232. Jin, H. *et al.* Ultrasound-triggered thrombolysis using urokinase-loaded nanogels. *Int. J. Pharm.* **434,** 384–390 (2012).

233. Park, Y. J., Liang, J. F., Yang, Z. Q. & Yang, V. C. Controlled release of clot-dissolving tissue-type plasminogen activator from a poly(L-glutamic acid) semi-interpenetrating polymer network hydrogel. *J. Control. Release Off. J. Control. Release Soc.* **75,** 37–44 (2001).

234. MUCKLOW, J. C. Thrombolytic Treatment - Streptokinase Is More Economical Than Alteplase. *Br. Med. J.* **311,** 1506–1506 (1995).

235. Gillis, J. C. & Goa, K. L. Streptokinase - A pharmacoeconomic appraisal of its use in the management of acute myocardial infarction. *Pharmacoeconomics* **10,** 281–310 (1996).

236. Schoffelen, S. & Hest, J. C. M. van. Multi-enzyme systems: bringing enzymes together in vitro. *Soft Matter* **8,** 1736–1746 (2012).

237. Conrado, R. J., Varner, J. D. & DeLisa, M. P. Engineering the spatial organization of metabolic enzymes: mimicking nature's synergy. *Curr. Opin. Biotechnol.* **19,** 492–499 (2008).

238. Yan, W., Aebersold, R. & Raines, E. W. Evolution of organelle-associated protein profiling. *J. Proteomics* **72,** 4–11 (2009).

239. Matsumoto, R. *et al.* A liposome-based energy conversion system for accelerating the multi-enzyme reactions. *Phys. Chem. Chem. Phys. PCCP* **12,** 13904–13906 (2010).

240. van Dongen, S. F. M., Nallani, M., Cornelissen, J. J. L. M., Nolte, R. J. M. & van Hest, J. C. M. A three-enzyme cascade reaction through positional assembly of enzymes in a polymersome nanoreactor. *Chem. Weinh. Bergstr. Ger.* **15,** 1107–1114 (2008).

241. Wilner, O. I. *et al.* Enzyme cascades activated on topologically programmed DNA scaffolds. *Nat. Nanotechnol.* **4,** 249–254 (2009).

242. Niemeyer, C. M., Koehler, J. & Wuerdemann, C. DNA-Directed Assembly of Bienzymic Complexes from In Vivo Biotinylated NAD(P)H:FMN Oxidoreductase and Luciferase. *ChemBioChem* **3,** 242–245 (2002).

243. Fierobe, H.-P. *et al.* Degradation of Cellulose Substrates by Cellulosome Chimeras SUBSTRATE TARGETING VERSUS PROXIMITY OF ENZYME COMPONENTS. *J. Biol. Chem.* **277,** 49621–49630 (2002).

244. Kristensen, C. *et al.* Metabolic engineering of dhurrin in transgenic Arabidopsis plants with marginal inadvertent effects on the metabolome and transcriptome. *Proc. Natl. Acad. Sci. U. S. A.* **102,** 1779–1784 (2005).

245. Dueber, J. E. *et al.* Synthetic protein scaffolds provide modular control over metabolic flux. *Nat. Biotechnol.* **27,** 753–759 (2009).

246. Wanders, R. J. A. & Waterham, H. R. Biochemistry of mammalian peroxisomes revisited. *Annu. Rev. Biochem. Vol 79* **75,** 295–332 (2006).

247. Schrader, M. & Fahimi, H. D. Mammalian peroxisomes and reactive oxygen species. *Histochem. Cell Biol.* **122,** 383–393 (2004).

248. Sheikh, F. G., Pahan, K., Khan, M., Barbosa, E. & Singh, I. Abnormality in catalase import into peroxisomes leads to severe neurological disorder. *Proc. Natl. Acad. Sci.* **95,** 2961–2966 (1998).

249. Scism, R. A. & Bachmann, B. O. Five-component cascade synthesis of nucleotide analogues in an engineered self-immobilized enzyme aggregate. *Chembiochem Eur. J. Chem. Biol.* **11,** 67–70 (2010).

250. Bäumler, H. & Georgieva, R. Coupled enzyme reactions in multicompartment microparticles. *Biomacromolecules* **11,** 1480–1487 (2010).

251. Stempfer, G., Höll-Neugebauer, B., Kopetzki, E. & Rudolph, R. A fusion protein designed for noncovalent immobilization: stability, enzymatic activity, and use in an enzyme reactor. *Nat. Biotechnol.* **14,** 481–484 (1996).

252. Ji, C. & Kaplowitz, N. Betaine decreases hyperhomocysteinemia, endoplasmic reticulum stress, and liver injury in alcohol-fed mice. *Gastroenterology* **124,** 1488–1499 (2003).

253. Ji, C., Deng, Q. & Kaplowitz, N. Role of TNF-α in ethanol-induced hyperhomocysteinemia and murine alcoholic liver injury. *Hepatology* **40,** 442–451 (2004).

254. Ji, C. *et al.* Liver-specific loss of glucose-regulated protein 78 perturbs the unfolded protein response and exacerbates a spectrum of liver diseases in mice. *Hepatology* **54,** 229–239 (2011).

255. Selvin, P. R. The renaissance of fluorescence resonance energy transfer. *Nat. Struct. Mol. Biol.* **7,** 730–734 (2000).

256. Ellis, R. J. Macromolecular crowding: obvious but underappreciated. *Trends Biochem. Sci.* **26,** 597–604 (2001).

257. Jamaty, C. *et al.* Lipid emulsions in the treatment of acute poisoning: a systematic review of human and animal studies. *Clin. Toxicol.* **48,** 1–27 (2010).

258. Bertrand, N., Bouvet, C., Moreau, P. & Leroux, J.-C. Transmembrane pH-Gradient Liposomes To Treat Cardiovascular Drug Intoxication. *ACS Nano* **4,** 7552–7558 (2010).

259. Shen, Y. *et al.* Dihydromyricetin As a Novel Anti-Alcohol Intoxication Medication. *J. Neurosci.* **32,** 390–401 (2012).

260. Averbakh, A. Z. *et al.* Flavin-dependent alcohol oxidase from the yeast Pichia pinus. Spatial localization of the coenzyme FAD in the protein structure: hot-tritium bombardment and ESR experiments. *Biochem. J.* **310 (Pt 2),** 601–604 (1995).

261. Christian, D. A. *et al.* Polymersome carriers: from self-assembly to siRNA and protein therapeutics. *Eur. J. Pharm. Biopharm. Off. J. Arbeitsgemeinschaft Für Pharm. Verfahrenstechnik EV* **71,** 463–474 (2009).

262. Baker, M., Reynolds, H. M., Lumicisi, B. & Bryson, C. J. Immunogenicity of protein therapeutics: The key causes, consequences and challenges. *Self/Nonself* **1,** 314–322 (2010).

263. Manning, M. C., Chou, D. K., Murphy, B. M., Payne, R. W. & Katayama, D. S. Stability of protein pharmaceuticals: an update. *Pharm. Res.* **27,** 544–575 (2010).

264. Manning, M. C., Patel, K. & Borchardt, R. T. Stability of Protein Pharmaceuticals. *Pharm. Res.* **06,** 903–918 (1989).

265. Albanese, A., Tang, P. S. & Chan, W. C. W. The effect of nanoparticle size, shape, and surface chemistry on biological systems. *Annu. Rev. Biomed. Eng.* **14,** 1–16 (2012).

266. Harris, J. M. & Chess, R. B. Effect of pegylation on pharmaceuticals. *Nat. Rev. Drug Discov.* **2,** 214–221 (2003).

267. Knop, K., Hoogenboom, R., Fischer, D. & Schubert, U. S. Poly(ethylene glycol) in Drug Delivery: Pros and Cons as Well as Potential Alternatives. *Angew. Chem. Int. Ed.* **49,** 6288–6308 (2010).

268. Harris, J. M. & Veronese, F. M. Peptide and protein pegylation II-clinical evaluation. *Adv Drug Deliv Rev* **55,** 1259–1260 (2003).

269. Armstrong, J. K. *et al.* Antibody against poly(ethylene glycol) adversely affects PEG-asparaginase therapy in acute lymphoblastic leukemia patients. *Cancer* **110,** 103–111 (2007).

270. Veronese, F. M. Peptide and protein PEGylation. *Biomaterials* **22,** 405–417 (2001).

271. Ishihara, T. *et al.* Accelerated Blood Clearance Phenomenon Upon Repeated Injection of PEG-modified PLA-nanoparticles. *Pharm. Res.* **26,** 2270–2279 (2009).

272. Ishihara, K. *et al.* Hemocompatibility of human whole blood on polymers with a phospholipid polar group and its mechanism. *J. Biomed. Mater. Res.* **26,** 1543–1552 (1992).

273. Ishihara, K. *et al.* Why do phospholipid polymers reduce protein adsorption? *J. Biomed. Mater. Res.* **39,** 323–330 (1998).

274. Zhang, L. *et al.* Zwitterionic hydrogels implanted in mice resist the foreign-body reaction. *Nat. Biotechnol.* **31,** 553–556 (2013).

275. Lowe, A. B. & McCormick, C. L. Synthesis and Solution Properties of Zwitterionic Polymers. *Chem. Rev.* **102,** 4177–4190 (2002).

276. Zhang, Z., Chen, S., Chang, Y. & Jiang, S. Surface Grafted Sulfobetaine Polymers via Atom Transfer Radical Polymerization as Superlow Fouling Coatings. *J. Phys. Chem. B* **110,** 10799–10804 (2006).

277. Zhang, Z. *et al.* Nonfouling Behavior of Polycarboxybetaine-Grafted Surfaces: Structural and Environmental Effects. *Biomacromolecules* **9,** 2686–2692 (2008).

278. Vaisocherová, H. *et al.* Ultralow Fouling and Functionalizable Surface Chemistry Based on a Zwitterionic Polymer Enabling Sensitive and Specific Protein Detection in Undiluted Blood Plasma. *Anal. Chem.* **80,** 7894–7901 (2008).

279. Jiang, S. & Cao, Z. Ultralow-Fouling, Functionalizable, and Hydrolyzable Zwitterionic Materials and Their Derivatives for Biological Applications. *Adv. Mater.* **22,** 920–932 (2009).

280. Chen, S., Zheng, J., Li, L. & Jiang, S. Strong Resistance of Phosphorylcholine Self-Assembled Monolayers to Protein Adsorption: Insights into Nonfouling Properties of Zwitterionic Materials. *J. Am. Chem. Soc.* **127,** 14473–14478 (2005).

281. He, Y. *et al.* Molecular Simulation Studies of Protein Interactions with Zwitterionic Phosphorylcholine Self-Assembled Monolayers in the Presence of Water. *Langmuir* **24,** 10358–10364 (2008).

282. Iwasaki, Y. & Ishihara, K. Phosphorylcholine-containing polymers for biomedical applications. *Anal. Bioanal. Chem.* **381,** 534–546 (2004).

283. Matsuno, R. & Ishihara, K. Integrated functional nanocolloids covered with artificial cell membranes for biomedical applications. *Nano Today* **6,** 61–74 (2011).

284. Matsuno, R. & Ishihara, K. Molecular-Integrated Phospholipid Polymer Nanoparticles with Highly Biofunctionality. *Macromol. Symp.* **279,** 125–131 (2009).

285. Zhu, Y. *et al.* A Robust Graft-to Strategy To Form Multifunctional and Stealth Zwitterionic Polymer-Coated Mesoporous Silica Nanoparticles. *Biomacromolecules* **15,** 1845–1851 (2014).

286. Liu, J. *et al.* PEGylation and Zwitterionization: Pros and Cons in the Renal Clearance and Tumor Targeting of Near-IR-Emitting Gold Nanoparticles. *Angew. Chem. Int. Ed.* **52,** 12572–12576 (2013).

287. Liu, P., Skelly, J. D. & Song, J. Three-dimensionally presented anti-fouling zwitterionic motifs sequester and enable high-efficiency delivery of therapeutic proteins. *Acta Biomater.* **10,** 4296–4303 (2014).

288. Lewis, A., Tang, Y., Brocchini, S., Choi, J. & Godwin, A. Poly(2-methacryloyloxyethyl phosphorylcholine) for Protein Conjugation. *Bioconjug. Chem.* **19,** 2144–2155 (2008).

289. Keefe, A. J. & Jiang, S. Poly(zwitterionic)protein conjugates offer increased stability without sacrificing binding affinity or bioactivity. *Nat. Chem.* **4,** 59–63 (2012).

290. Romberg, B., Hennink, W. E. & Storm, G. Sheddable coatings for long-circulating nanoparticles. *Pharm. Res.* **25,** 55–71 (2008).

291. Mastrobattista, E., van der Aa, M. A. E. M., Hennink, W. E. & Crommelin, D. J. A. Artificial viruses: a nanotechnological approach to gene delivery. *Nat. Rev. Drug Discov.* **5,** 115–121 (2006).

292. Yang, W. *et al.* Poly(carboxybetaine) nanomaterials enable long circulation and prevent polymer-specific antibody production. *Nano Today* **9,** 10–16 (2014).

293. Bertrand, N. & Leroux, J.-C. The journey of a drug-carrier in the body: An anatomo-physiological perspective. *J. Control. Release Off. J. Control. Release Soc.* **161,** 152–163 (2012).

294. Champion, J. A., Katare, Y. K. & Mitragotri, S. Particle shape: A new design parameter for micro- and nanoscale drug delivery carriers. *J. Controlled Release* **121,** 3–9 (2007).

295. Ruddy, S., Gigli, I. & Austen, K. F. The Complement System of Man. *N. Engl. J. Med.* **287,** 489–495 (1972).

296. Müller-Eberhard, H. J. Molecular organization and function of the complement system. *Annu. Rev. Biochem. Vol 79* **57,** 321–347 (1988).

297. *Roitt's essential immunology*. (Wiley-Blackwell, 2011).

298. Dancey, J. E. & Chen, H. X. Strategies for optimizing combinations of molecularly targeted anticancer agents. *Nat. Rev. Drug Discov.* **5,** 649–659 (2006).

299. Vockley, J. *et al.* Phenylalanine hydroxylase deficiency: diagnosis and management guideline. *Genet. Med. Off. J. Am. Coll. Med. Genet.* **16,** 188–200 (2014).

300. Pieters, R. *et al.* L-asparaginase treatment in acute lymphoblastic leukemia. *Cancer* **117,** 238–249 (2011).

301. Appel, I. M. *et al.* Pharmacokinetic, pharmacodynamic and intracellular effects of PEG-asparaginase in newly diagnosed childhood acute lymphoblastic leukemia: results from a single agent window study. *Leukemia* **22,** 1665–1679 (2008).

302. Rytting, M. Peg-asparaginase for acute lymphoblastic leukemia. *Expert Opin. Biol. Ther.* **10,** 833–839 (2010).

303. Kost, T. A., Condreay, J. P. & Jarvis, D. L. Baculovirus as versatile vectors for protein expression in insect and mammalian cells. *Nat. Biotechnol.* **23,** 567–575 (2005).

304. Cross, B. C. S., Sinning, I., Luirink, J. & High, S. Delivering proteins for export from the cytosol. *Nat. Rev. Mol. Cell Biol.* **10,** 255–264 (2009).

305. Brasnjevic, I., Steinbusch, H. W. M., Schmitz, C. & Martinez-Martinez, P. Delivery of peptide and protein drugs over the blood–brain barrier. *Prog. Neurobiol.* **87,** 212–251 (2009).

306. Tessmar, J. K. & Göpferich, A. M. Matrices and scaffolds for protein delivery in tissue engineering. *Adv. Drug Deliv. Rev.* **59,** 274–291 (2007).

307. Galán, J. E. & Wolf-Watz, H. Protein delivery into eukaryotic cells by type III secretion machines. *Nature* **444,** 567–573 (2006).

308. Leader, B., Baca, Q. J. & Golan, D. E. Protein therapeutics: a summary and pharmacological classification. *Nat. Rev. Drug Discov.* **7,** 21–39 (2008).

309. Protein transduction: an alternative to genetic intervention? *Publ. Online 29 January 2001 Doi101038sjgt3301383* **8,** (2001).

310. Cao, Z. *et al.* Reversible Cell-Specific Drug Delivery with Aptamer-Functionalized Liposomes. *Angew. Chem. Int. Ed.* **48,** 6494–6498 (2009).

311. Muth, T. R. & Caplan, M. J. Transport Protein Trafficking in Polarized Cells. *Annu. Rev. Cell Dev. Biol.* **19,** 333–366 (2003).

312. Cicerone, M., Giri, J., Shaked, Z. 'ev & Roberts, C. Protein stability — An underappreciated but critical need for drug delivery systems. *Adv. Drug Deliv. Rev.* **93,** 1 (2015).

313. Haidar, Z. S., Hamdy, R. C. & Tabrizian, M. Protein release kinetics for core-shell hybrid nanoparticles based on the layer-by-layer assembly of alginate and chitosan on liposomes. *Biomaterials* **29,** 1207–1215 (2008).

314. Tokuriki, N. & Tawfik, D. S. Protein Dynamism and Evolvability. *Science* **324,** 203–207 (2009).

315. Cheong, I. *et al.* A bacterial protein enhances the release and efficacy of liposomal cancer drugs. *Science* **314,** 1308–1311 (2006).

316. Brannon-Peppas, L. Nanoparticle and targeted systems for cancer therapy. *Adv. Drug Deliv. Rev.* (2004).

317. Lee, Y. *et al.* Efficient Delivery of Bioactive Antibodies into the Cytoplasm of Living Cells by Charge-Conversional Polyion Complex Micelles. *Angew. Chem. Int. Ed.* **49,** 2552–2555 (2010).

318. De Cock, L. J. *et al.* Polymeric Multilayer Capsules in Drug Delivery. *Angew. Chem. Int. Ed.* **49,** 6954–6973 (2010).

319. van Dongen, S. F. M. *et al.* Cellular Integration of an Enzyme-Loaded Polymersome Nanoreactor. *Angew. Chem. Int. Ed.* **49,** 7213–7216 (2010).

320. Amidi, M., Mastrobattista, E., Jiskoot, W. & Hennink, W. E. Chitosan-based delivery systems for protein therapeutics and antigens. *Adv. Drug Deliv. Rev.* **62,** 59–82 (2010).

321. George, M. & Abraham, T. E. Polyionic hydrocolloids for the intestinal delivery of protein drugs: Alginate and chitosan - a review. *J. Control. Release Off. J. Control. Release Soc.* **114,** 1–14 (2006).

322. Li, H. *et al.* A Protease-Based Strategy for the Controlled Release of Therapeutic Peptides. *Angew. Chem. Int. Ed.* **49,** 4930–4933 (2010).

323. Skwarczynski, M. *et al.* Polyacrylate Dendrimer Nanoparticles: A Self-Adjuvanting Vaccine Delivery System. *Angew. Chem. Int. Ed.* **49,** 5742–5745 (2010).

324. Huang, Y. *et al.* Synthetic Skin-Permeable Proteins Enabling Needleless Immunization. *Angew. Chem. Int. Ed.* **49,** 2724–2727 (2010).

325. Brown, S. D. *et al.* Gold Nanoparticles for the Improved Anticancer Drug Delivery of the Active Component of Oxaliplatin. *J. Am. Chem. Soc.* (2010). doi:10.1021/ja908117a

326. Liu, J., Stace-Naughton, A., Jiang, X. & Brinker, C. J. Porous nanoparticle supported lipid bilayers (protocells) as delivery vehicles. *J. Am. Chem. Soc.* **131,** 1354–1355 (2009).

327. Ghosh, P., Han, G., De, M., Kim, C. K. & Rotello, V. M. Gold nanoparticles in delivery applications. *Adv. Drug Deliv. Rev.* **60,** 1307–1315 (2008).

328. Fothergill-Gilmore, L. in *Protein Biotechnology* (ed. Franks, F.) 467–487 (Humana Press, 1993).

329. Asoh, S. & Ohta, S. PTD-mediated delivery of anti-cell death proteins/peptides and therapeutic enzymes. *Adv. Drug Deliv. Rev.* **60,** 499–516 (2008).

330. Fittipaldi, A. & Giacca, M. Transcellular protein transduction using the Tat protein of HIV-1. *Adv. Drug Deliv. Rev.* **57,** 597–608 (2005).

331. Wadia, J. S. & Dowdy, S. F. Transmembrane delivery of protein and peptide drugs by TAT-mediated transduction in the treatment of cancer. *Adv. Drug Deliv. Rev.* **57,** 579–596 (2005).

332. Abbing, A. *et al.* Efficient intracellular delivery of a protein and a low molecular weight substance via recombinant polyomavirus-like particles. *J. Biol. Chem.* **279,** 27410–27421 (2004).

333. Console, S., Marty, C., García-Echeverría, C., Schwendener, R. & Ballmer-Hofer, K. Antennapedia and HIV transactivator of transcription (TAT) 'protein transduction domains' promote endocytosis of high molecular weight cargo upon binding to cell surface glycosaminoglycans. *J. Biol. Chem.* **278,** 35109–35114 (2003).

334. Kumagai, Y. & Sumi, D. Arsenic: Signal transduction, transcription factor, and biotransformation involved in cellular response and toxicity. *Annu. Rev. Pharmacol. Toxicol.* **47,** 243–262 (2007).

335. Kim, D. *et al.* Generation of human induced pluripotent stem cells by direct delivery of reprogramming proteins. *Cell Stem Cell* **4,** 472–476 (2009).

336. Maherali, N. & Hochedlinger, K. Guidelines and Techniques for the Generation of Induced Pluripotent Stem Cells. *Cell Stem Cell* **3,** 595–605 (2008).

337. Takahashi, K. & Yamanaka, S. Induction of pluripotent stem cells from mouse embryonic and adult fibroblast cultures by defined factors. *Cell* **126,** 663–676 (2006).

338. Wang, H. *et al.* A supramolecular approach for preparation of size-controlled nanoparticles. *Angew. Chem. Int. Ed Engl.* **48,** 4344–4348 (2009).

339. Chen, K.-J. *et al.* A small MRI contrast agent library of gadolinium(III)-encapsulated supramolecular nanoparticles for improved relaxivity and sensitivity. *Biomaterials* **32,** 2160–2165 (2011).

340. Wang, S. *et al.* Photothermal effects of supramolecularly assembled gold nanoparticles for the targeted treatment of cancer cells. *Angew. Chem. Int. Ed Engl.* **49,** 3777–3781 (2010).

341. Wang, H. *et al.* A Rapid Pathway Toward a Superb Gene Delivery System: Programming Structural and Functional Diversity into a Supramolecular Nanoparticle Library. *ACS Nano* **4,** 6235–6243 (2010).

342. Wang, H. *et al.* A small library of DNA-encapsulated supramolecular nanoparticles for targeted gene delivery. *Chem. Commun.* **46,** 1851–1853 (2010).

343. Iyer, M. *et al.* Two-step transcriptional amplification as a method for imaging reporter gene expression using weak promoters. Available at: http://www.pnas.org. (Accessed: 13th April 2016)

344. Rodgers, K. K. & Coleman, J. E. DNA binding and bending by the transcription factors GAL4(62*) and GAL4(149*). *Protein Sci.* **3,** 608–619 (1994).

345. Ludden, M. J. W., Sinha, J. K., Wittstock, G., Reinhoudt, D. N. & Huskens, J. Control over binding stoichiometry and specificity in the supramolecular immobilization of cytochrome c on a molecular printboard. *Org. Biomol. Chem.* **6,** 1553–1557 (2008).

346. Rekharsky, M. V. & Inoue, Y. Complexation Thermodynamics of Cyclodextrins. *Chem. Rev.* **98,** 1875–1918 (1998).

347. Sadowski, I., Ma, J., Triezenberg, S. & Ptashne, M. GAL4-VP16 is an unusually potent transcriptional activator. *Nature* **335,** 563–564 (1988).

348. Lee, C.-C. *et al.* Multistep Synthesis of a Radiolabeled Imaging Probe Using Integrated Microfluidics. *Science* **310,** 1793–1796 (2005).

349. Wang, J. *et al.* Integrated Microfluidics for Parallel Screening of an In Situ Click Chemistry Library. *Angew. Chem.* **118,** 5402–5407 (2006).

350. Lin, W.-Y., Wang, Y., Wang, S. & Tseng, H.-R. Integrated microfluidic reactors. *Nano Today* **4,** 470–481 (2009).

351. Wang, Y. *et al.* An integrated microfluidic device for large-scale in situ click chemistry screening. *Lab. Chip* **9,** 2281–2285 (2009).

352. Liu, K. *et al.* A digital microfluidic droplet generator produces self-assembled supramolecular nanoparticles for targeted cell imaging. *Nanotechnology* **21,** 445603 (2010).

353. Kamei, K. *et al.* An integrated microfluidic culture device for quantitative analysis of human embryonic stem cells. *Lab. Chip* **9,** 555–563 (2009).

354. Kamei, K. *et al.* Microfluidic image cytometry for quantitative single-cell profiling of human pluripotent stem cells in chemically defined conditions. *Lab. Chip* **10,** 1113–1119 (2010).

355. Sun, J. *et al.* A Microfluidic Platform for Systems Pathology: Multiparameter Single-Cell Signaling Measurements of Clinical Brain Tumor Specimens. *Cancer Res.* **70,** 6128–6138 (2010).

356. Darnell, J. Transcription factors as targets for cancer therapy. *Nat. Rev. Cancer* (2002).

357. Thomas, M. Role of transcription factors in cell replacement therapies for neurodegenerative conditions. *Regen. Med.* **5,** 441–450 (2010).

358. Yan, M. *et al.* A novel intracellular protein delivery platform based on single-protein nanocapsules. *Nat. Nanotechnol.* **5,** 48–53 (2010).

359. Ghosh, P. *et al.* Intracellular Delivery of a Membrane-Impermeable Enzyme in Active Form Using Functionalized Gold Nanoparticles. *J. Am. Chem. Soc.* **132,** 2642–2645 (2010).

360. Davis, M. E., Chen, Z. G. & Shin, D. M. Nanoparticle therapeutics: an emerging treatment modality for cancer. *Nat. Rev. Drug Discov.* **7,** 771–782 (2008).

361. Nie, S., Xing, Y., Kim, G. J. & Simons, J. W. Nanotechnology Applications in Cancer. *Annu. Rev. Biomed. Eng.* **9,** 257–288 (2007).

362. Zuris, J. A. *et al.* Cationic lipid-mediated delivery of proteins enables efficient protein-based genome editing in vitro and in vivo. *Nat. Biotechnol.* **33,** 73–80 (2015).

363. Kakizawa, Y. & Kataoka, K. Block copolymer micelles for delivery of gene and related compounds. *Adv. Drug Deliv. Rev.* **54,** 203–222 (2002).

364. Wang, Y., Gao, S., Ye, W.-H., Yoon, H. S. & Yang, Y.-Y. Co-delivery of drugs and DNA from cationic core–shell nanoparticles self-assembled from a biodegradable copolymer. *Nat. Mater.* **5,** 791–796 (2006).

365. Gabrielson, N. P. *et al.* Reactive and Bioactive Cationic α-Helical Polypeptide Template for Nonviral Gene Delivery. *Angew. Chem. Int. Ed.* **51,** 1143–1147 (2012).

366. Lee, K. *et al.* In vivo delivery of transcription factors with multifunctional oligonucleotides. *Nat. Mater.* **14,** 701–706 (2015).

367. Servick, K. Gene activation therapy prevents liver damage in mice. *Science* (2015). doi:10.1126/science.aab2549

368. Liu, Y. *et al.* Delivery of Intact Transcription Factor by Using Self-Assembled Supramolecular Nanoparticles. *Angew. Chem. Int. Ed.* n/a–n/a (2011). doi:10.1002/anie.201005740

369. Wang, J. *et al.* Integrated Microfluidics for Parallel Screening of an In Situ Click Chemistry Library. *Angew. Chem. Int. Ed.* **45,** 5276–5281 (2006).

370. Liu, K., Chen, Y.-C., Tseng, H.-R., Shen, C. K.-F. & Dam, R. M. Microfluidic device for robust generation of two-component liquid-in-air slugs with individually controlled composition. *Microfluid. Nanofluidics* **9,** 933–943 (2010).

371. Yoshida, J., Nagaki, A. & Yamada, T. Flash Chemistry: Fast Chemical Synthesis by Using Microreactors. *Chem. – Eur. J.* **14,** 7450–7459 (2008).

372. Marre, S. & Jensen, K. F. Synthesis of micro and nanostructures in microfluidic systems. *Chem. Soc. Rev.* **39,** 1183–1202 (2010).

373. deMello, A. J. Control and detection of chemical reactions in microfluidic systems. *Nature* **442,** 394–402 (2006).

374. Wang, H. *et al.* A Supramolecular Approach for Preparation of Size-Controlled Nanoparticles. *Angew. Chem. Int. Ed.* **48,** 4344–4348 (2009).

375. Wang, H. *et al.* A small library of DNA-encapsulated supramolecular nanoparticles for targeted gene delivery. *Chem. Commun.* **46,** 1851–1853 (2010).

376. Petter, R. C., Salek, J. S., Sikorski, C. T., Kumaravel, G. & Lin, F. T. Cooperative binding by aggregated mono-6-(alkylamino)-.beta.-cyclodextrins. *J. Am. Chem. Soc.* **112,** 3860–3868 (1990).

377. Wang, H. *et al.* A Supramolecular Approach for Preparation of Size-Controlled Nanoparticles. *Angew. Chem.* **121,** 4408–4412 (2009).

378. Stoffelen, C. & Huskens, J. Size-tunable supramolecular nanoparticles mediated by ternary cucurbit[8]uril host–guest interactions. *Chem. Commun.* **49,** 6740–6742 (2013).